DESIGN AND OPTIMISATION OF HIGH PERFORMANCE RESONATING MICRO-SCANNERS THROUGH A MULTIPHYSICS INVESTIGATION

Russell Farrugia

Department of Microelectronics & Nanoelectronics

Faculty of Information and Communication Technology

University of Malta

December 2019

Submitted in partial fulfilment of the requirements

for the degree of Doctor of Philosophy

Declaration of Authenticity

rfar0028

Russell Farrugia

Doctor of Philosophy (Faculty of ICT)

Title of Dissertation:

DESIGN AND OPTIMISATION OF HIGH PERFORMANCE MICRO-SCANNERS THROUGH A MULTIPHYSICS INVESTIGATION

(a) Authenticity of Dissertation

I hereby declare that I am the legitimate author of this dissertation and that it is my original work. No portion of this work has been submitted in support of an application for another degree or qualification of this or any other university or institution of higher education. I hold the University of Malta harmless against any third party claims with regard to copyright violation, breach of confidentiality, defamation and any other third party right infringement.

(b) Research Code of Practice and Ethics Review Procedure

I declare that I have abided by the University's Research Ethics Review Procedures. As a Ph.D. student, as per Regulation 49 of the Doctor of Philosophy Regulations, I accept that my thesis be made publicly available on the University of Malta Institutional Repository.

_____

RUSSELL FARRUGIA

_____

Date

In loving memory of my father, Pio

*"Nobody trusts a computer simulation except the guy who did it
and everybody trusts experimental data except the guy who did it"*

Ehsan B. Haghighi

List of Publications

The following is a list of peer-reviewed publications resulting from this research work.

Conference Papers

- R. Farrugia, I. Grech, O. Casha, J. Micallef and E. Gatt, "Analysis of dynamic deformation in 1-D resonating micro-mirrors", in the *Symposium on Design, Test, Integration and Packaging of MEMS/MOEMS*, Montpellier, France, 2016

- R. Farrugia, I. Grech, D. Camilleri, O. Casha, J. Micallef and E. Gatt, "Design optimization of a high frequency resonating micro-mirror with low dynamic deformation", in the *Symposium on Design, Test, Integration and Packaging of MEMS/MOEMS*, Budapest, Hungary, 2017

- R. Farrugia, B. Portelli, I. Grech, D. Camilleri, O. Casha, J. Micallef and E. Gatt, "Air damping analysis in resonating micro-mirrors", in the *Symposium on Design, Test, Integration and Packaging of MEMS/MOEMS*, Rome, Italy, 2018

- R. Farrugia, I. Grech, D. Camilleri, O. Casha, J. Micallef and E. Gatt, "CFD Analysis of Aerodynamic Drag on Resonating MEMS Micro-Scanners", in the *Symposium on Design, Test, Integration and Packaging of MEMS/MOEMS*, Paris, France, 2019

Journal Papers

- R. Farrugia, I. Grech, D. Camilleri, O. Casha, J. Micallef and E. Gatt, "Theoretical and finite element analysis of dynamic deformation in resonating micro-mirrors", *Microsystem Technologies* 24 (1), 445-455, 2018

- R. Farrugia, I. Grech, D. Camilleri, O. Casha, J. Micallef and E. Gatt, "Design optimization of a dynamically flat resonating micro-mirror for pico-projection applications", *Microsystem Technologies*, 1-13, 2018

- R. Farrugia, B. Portelli, I. Grech, D. Camilleri, O. Casha, J. Micallef, E. Gatt, "Air damping of high performance resonating micro-mirrors with angular vertical comb-drive actuators", *Microsystem Technologies*, 1-15, 2019

DESIGN AND OPTIMISATION OF HIGH PERFORMANCE RESONATING MICRO-SCANNERS THROUGH A MULTIPHYSICS INVESTIGATION

ABSTRACT

Resonating micro-scanners based on MEMS fabrication technologies have been extensively implemented in laser beam scanning systems for micro-display and imaging applications. The optical resolution obtained from laser beam scanning micro-mirrors for micro-display applications is dependent on the mirror size, the scanning frequency and scan angle amplitude. However, other factors need to be considered in the design of such devices, namely, the structural strength, dynamic deformation and the scanning efficiency. Understanding the structural, fluidic and electrostatic characteristics of resonant micro-scanners is crucial in order to maximize the optical performance of such devices.

In this dissertation, the multi-physical domains governing the micro-scanner operation will be evaluated using experimentally-validated computational fluid dynamics and finite element models. The numerical simulation models presented will be utilised (i) to investigate the validity of a number of analytical equations found in literature, (ii) to propose analytical equations with improved accuracy and range of validity for micro-scanner performance predictions and (iii) to develop and optimize novel micro-scanner designs. While micro-scanner designs with angular vertical comb actuation are the focus in this work, a number of research outcomes are also applicable to high frequency resonating micro-scanners employing other actuation methods. A detailed investigation is performed on the two principal limiting factors in micro-scanners for high performance applications: air damping and dynamic deformation.

Three-dimensional transient Navier–Stokes simulations are performed to analyse the complex air flow interactions of a high frequency scanning micro-mirror. The damping effects due to device thickness and the depth of the mirror cavity are also evaluated. It is shown that analytical damping models which are applicable to resonant MEMS devices, are not valid within the operating range of high performance micro-scanners. On the other hand good agreement in the overall quality factor is achieved between Navier-Stokes simulation and measurement results.

The inertia loading acting on the mirror plate, as the micro-scanner oscillates in out-of-plane rotation, results in the dynamic deformation of the mirror surface. A detailed analysis is presented on the micro-mirror design aspects contributing to dynamic deformation. An improved analytical equation for dynamic deformation predictions is proposed, which takes into consideration the two-dimensional mirror plate twist. A comparison among a number of layout designs was carried out with the aim of improving the dynamic deformation distribution on the mirror surface. A significant improvement in dynamic deformation was achieved with the inclusion of a gimbal-type structure between the mirror plate and the torsional beams.

A design optimization scheme based on numerical simulations and meta-modelling methodologies is introduced. The minimization of dynamic deformation is considered as one of the design objectives, which include output parameters related to micro-mirror optical performance, structural reliability and gas damping characteristics. The design optimization scheme was implemented in order to develop three high performance resonating micro-scanner prototypes using the SOIMUMPs MPW process. The simulations and measurements presented in this dissertation demonstrate that the optical performance of resonating micro-scanners fabricated from a single device layer can be maximized by incorporating the indirect-drive configuration and a gimbal-type mirror support structure.

Acknowledgements

TABLE OF CONTENTS

LIST OF FIGURES

LIST OF TABLES

NOMENCLATURE

Symbol	SI Units	Description
a	[-]	aperture shape factor
b_m	[m]	rectangular micro-mirror plate width
c_d	[kgm^2/s]	damping coefficient
c_{nl}	[kgm^2/s]	non-linear damping coefficient
f_0	[Hz]	micro-mirror torsional modal frequency
f_d	[Hz]	driving force frequency
f_g	[m]	comb finger gap
f_l	[m]	comb finger length
f_o	[m]	comb finger offset
f_s	[Hz]	micro-mirror scanning frequency
f_w	[m]	comb finger width
h	[m]	cavity depth
i	[A]	electrical current
I	[kgm^2]	effective moment of inertia
k_s	[Nm]	mechanical torsional stiffness coefficient
k_e	[Nm]	equivalent electrostatic stiffness coefficient
$l_{g,m}$	[m]	gimbal-mirror link length
l_s	[m]	torsion spring length
$nrmse$	[-]	root mean squared error as a percentage of full-scale
p	[Pa]	air pressure
s_j	[-]	design input parameters
t_f	[m]	reflective mirror metal layer thickness
t_m	[m]	silicon device layer thickness
$\boldsymbol{u}$	[m/s]	air velocity vector
w	[m]	dynamic micro-mirror plate deflection
w_g	[m]	gimbal frame width
$w_{g,m}$	[m]	gimbal-mirror link width
w_s	[m]	torsional spring width
C	[F]	capacitance
C_a	[-]	added mass coefficient
C_d	[-]	drag coefficient
E	[Pa]	Young's modulus
E_{loss}	[J]	micro-mirror energy loss over one oscillation cycle
$F(s)$	[-]	multi-criteria objective function for design optimization
$F_i(s)$	[-]	partial objectives for design optimization
G	[Pa]	shear modulus
J_s	[m^4]	polar moment of inertia
K	[m]	torsion factor
Kn	[-]	Knudsen number
L_m	[m]	rectangular micro-mirror plate length
L_s	[m]	torsion spring length
M	[Nm]	applied torsional spring moment
M_{comb}	[Nm]	overall dynamic aerodynamic moment acting on AVC structure
M_d	[Nm]	damping moment
M_i	[Nm]	inertial moment
M_{plate}	[Nm]	overall dynamic aerodynamic moment acting on mirror plate
M_{press}	[Nm]	pressure drag moment component
M_{visc}	[Nm]	viscous shear drag moments component
M_x, M_y	[Nm]	bending moment
M_{xy}	[Nm]	twisting moment
N	[-]	number of comb fingers
N_h	[-]	number of resolvable spots along a horizontal scan direction
N_v	[-]	number of resolvable spots along a vertical scan direction
Q	[-]	overall quality factor

Q_0	[-]	intercept of linear fit of Q-θ_{max}^2 relationship
Q_{nl}	[-]	slope of linear fit of Q-θ_{max}^2 relationship
R	[m]	micro-mirror plate radius
R_{def}	[m]	normalized dynamic deformation
Re	[-]	Reynolds number
Re_c	[-]	maximum Re of air flow surrounding AVC structure flow
Re_m	[-]	maximum Re on air flow surrounding mirror plate
V_d		micro-scanner drive voltage
δ	[m]	dynamic deformation
δ_{crit}	[m]	critical dynamic deformation based on the Rayleigh criterion
δ_{max}	[m]	peak-to-peak dynamic deformation
δ_{rms}	[m]	rms dynamic deformation
ε	[F/m]	electrical permittivity
θ	[°]	instantaneous micro-mirror scan angle
θ_{div}	[°]	divergence angle of the reflected laser beam
θ_{max}	[°]	micro-mirror scan angle amplitude
λ	[m]	optical wavelength
μ	[kg/m.s]	gas dynamic viscosity
μ_{eff}	[kg/m.s]	slip corrected gas dynamic viscosity
v	[-]	Poisson ratio
ρ	[kg/m^3]	air density
$\sigma_{1,2}$	[Pa]	maximum, minimum principal stress
τ_{crit}	[Pa]	critical shear stress
τ_{max}	[Pa]	maximum shear stress
ψ	[°]	gimbal-mirror link angle
ω_0	[rad/s]	angular torsional modal frequency
ω_d	[rad/s]	angular driving force frequency
ωs	[rad/s]	angular micro-mirror scanning frequency

ABBREVIATIONS

ADAS	Advanced Driver Assist Systems
AVC	Angular Vertical Comb
CFD	Computational Fluid Dynamics
DLP	Digital Light Processing
DMD	Digital Micro-Mirror Device
DOE	Design of Experiments
DRIE	Deep Reactive Ion Etching
EM	Electromagnetic
ES	Electrostatic
ET	Electrothermal
FE	Finite Element
FVM	Finite Volume Method
HUD	Head-Up Displays
KC	Keulegan and Carpenter
LBS	Laser Beam Scanning
LCoS	Liquid Crystal on Silicon
MEMS	Microelectromechanical Systems
N-S	Navier-Stokes
PE	Piezoelectric
PSD	Position Senstive Detector
PZT	Lead Zirconate Titanate
RSM	Response Surface Methodology
SLM	Spatial Light Modulators
SOI	Silicon-on-Insulator
STM	ST Microelectronics
SVC	Staggered Vertical Comb

1   INTRODUCTION

Throughout the past two decades, silicon-based scanning micro-mirrors have been broadly investigated for a number of light display and imaging applications. The potential of miniaturization, low energy consumption and reduced cost provides an incentive to replace macro-mirrors with MEMS micro-mirrors in a wide range of applications [1]. Initial research was directed towards imaging applications such as barcode scanners [2], fingerprint sensing and confocal microscopy [3, 4]. A recent increased interest in the development of high performance scanning micro-mirrors is driven by three factors: (i) a market demand for miniaturised image projection systems for consumer electronics, advanced driver assist systems (ADAS) and medical applications (ii) advances in microelectromechanical systems (MEMS) fabrication technologies and (iii) availability of compact and less expensive RGB laser diodes. The optical performance of micro-scanners is primarily defined by the scanning frequency, f_s, maximum mechanical scan angle, θ_{max} and the mirror aperture, D. As opposed to scanned imaging systems, the demands on f_s, θ_{max} and D for micro display applications such as hand-held projection systems [5, 6] and head-up displays (HUD) [7] are significant. Consequently, the development of high-speed micro-scanners demonstrating a greater motion range is still in progress [8]. An increase in the three main scanning performance characteristics is limited by power consumption, air damping losses, overall device footprint and non-planarity of the micro-mirror surface.

1.1   Dissertation Outline

The principle objective behind this dissertation is the design of high performance one-directional resonant micro-scanners for laser scanning display applications. In this work, a focus will be particularly given to the dynamic deformation and air damping characteristics of such devices under high scanning frequency and amplitude operation. Micro-scanner performance requirements largely define the resolution that can be achieved by the optical engine. Optical resolution requirements for micro-displays are discussed in more detail in Section 2.1.

Sections 2.2 and 2.3, demonstrate major advances in the field of one-directional micro-scanner design based on a number of MEMS technologies. However, a research lacuna still exists in the modelling of the non-linear dynamic response of a micro-scanner resonating in the torsional mode. The predictive capabilities of analytical and numerical models can only be improved if the physics leading to the observed non-linear behaviour

is well understood. An overview of the sources leading to non-linear response in MEMS is provided in Section 2.4. This study will focus on non-linear air damping in torsional micro-mirrors, which is addressed in Chapter 5.

The non-linearities of Section 2.4 largely determine the scanning performance of a resonating micro-mirror. However, the optical resolution produced by the laser scanning micro-mirror is also dependent on dynamic deformation. Dynamic flatness of the mirror surface is often neglected in the design process of a scanning micro-mirror. An introduction to dynamic deformation is provided in Section 2.6 and an extensive analysis is presented in Chapter 6.

As part of the research conducted, the correlation between measurements and numerical simulation results will be studied in order to validate the accuracy of finite element (FE) and computational fluid dynamics (CFD) models developed for the multi-physical analyses of resonating micro-scanners. Measurements will be performed on the resonant micro-scanner test case described in Section 2.7. Moreover, the accuracy of analytical and semi-empirical formulas will be compared against simplified FE and CFD models based on the experimentally-verified numerical simulation methods.

Finally, a design optimization scheme, based on electrostatic-mechanical-fluidic simulations, is proposed in Chapter 7. The minimization of micro-mirror dynamic deformation is considered as one of the main design objectives. The optimization scheme is eventually implemented in Chapter 8 to design and fabricate high performance micro-scanners using the SOIMUMPs multi-project wafer process. The predicted electro-mechanical micro-scanner performance is based on experimentally-verified FE simulations presented in Chapters 3 and 4. The micro-scanner prototypes and test case considered are electrostatically actuated via angular vertical comb structures as described in Section 2.2. Nonetheless, a number of research outcomes from this work are applicable to all scanning micro-mirrors oscillating in out-of-plane rotation.

In the following sections, an introduction to the field of micro-display technologies is presented. In particular, micro-scanning and display applications, competing technologies and different laser scanning architectures will be discussed.

1.2   Emerging Micro-Scanner Applications

Laser beam scanning (LBS) micro-mirrors based on MEMS fabrication technologies are being considered for a wide range of display and imaging applications. Reflective miniaturized laser projectors or pico-projectors is one growing field of applications for MEMS micro scanners. The screen size limitation of mobile devices for the direct exchange of multimedia contents can be overcome by embedded pico-projectors (see **Figure 1-1(a)**) [9]. HUD is another potential application for LBS. HUD (see **Figure 1-2(b)**) are intended to improve driver comfort and safety by projecting dashboard information directly in front of the driver through a real or virtual image on or in front of the windscreen [7, 10]. HUD are amongst a number of driver safety features currently being introduced in automobiles as part of ADAS. ADAS are one of the fastest-growing market segments in automotive electronics as a result of increased consumer safety concerns and more stringent road safety legislations. A fundamental feature of ADAS, such as lane departure warning and collision avoidance system, is LiDAR technology. LiDAR is used to obtain distance-to-target measurements by illuminating the target using a scanned pulsed-laser beam and measuring the time it takes for the reflected pulse to be detected by a sensor. Scanning MEMS micro-mirrors have also demonstrated superior beam steering capabilities for LiDAR at a fraction of the size and power required by traditional laser scanners [11, 12]. Another emerging automotive application of scanning micro-mirrors is high-power laser display for adaptive high-resolution vehicle headlamps [13]. The goal is to provide head lighting which can be adapted to a particular scenario (and driver) such as illuminating dark areas to increase contrast while reducing the light intensity projected on road signs to reduce glare [14].

In medical imaging, scanning micro-mirrors are being considered in endomicroscopy, for the realization of minimal invasive surgeries [15], and optical coherence tomography (OCT). OCT refers to the 2-D or 3-D imaging of an optical scattering medium such as biological tissue. With the use of micro-mirrors, better resolution is reported compared to other techniques such as magnetic resonance imagery (MRI), computed tomography (CT) and ultrasound [8].

<div align="center">(a)   (b)</div>

Figure 1-1: (a) embedded pico-projector [16]; (b) automotive head-up display [17]

1.3   **Micro-display Technologies**

Reflective micro-display technologies such as pico-projectors and HUD, generally refer to miniature display panels intended to be viewed indirectly via an optical system, which provides a magnified image of the panel [18]. Currently, the three main competitive technologies for miniaturized projection systems are digital micro-mirror devices (DMDs), liquid-crystal-on-silicon (LCoS) displays and MEMS laser beam scanning [19]. DMD and LCoS are both examples of spatial light modulators (SLM) whereby light is projected with equal intensity over the optical layer area of the display panel and an electric signal is applied to each pixel of the optical layer to achieve amplitude modulation of the incident light beam. DMDs, shown in **Figure 1-2**, are the core of the now mature Digital Light Processing (DLP) projection technology, developed by Texas Instruments. A DMD consists of a two-dimensional array of electrostatically actuated bistable MEMS micro-mirrors, mounted on torsional hinges. Each micro-mirror corresponds to an image pixel and the control of the pixel brightness is achieved by switching between two-tilt states to create either a bright pixel (ON state) or a dark pixel (OFF state) [20]. Currently, DLP chips enabling 4K UHD display resolution are commercially available and consist of an array with a diagonal size of 16.7 mm and a 5.4 μm micro-mirror pitch. The LCoS technology follows the same principle used in DMDs, however, the micro-mirrors are replaced with liquid crystals.
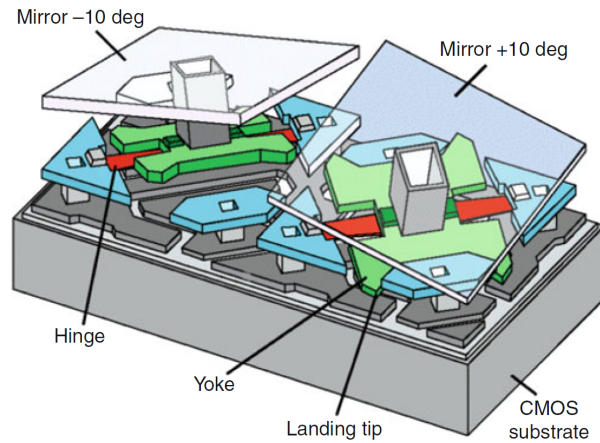
Figure 1-2: Two Digital Micro-Mirror Devices (DMDs) in opposite tilted states [18]

In laser scanning systems, a modulated laser source, having narrow divergence is scanned along a two-dimensional path, therefore generating one pixel at a time in a similar way as cathode ray tube (CRT) monitors. Therefore, the millions of micro-mirrors required in DMD projection systems are replaced by a more cost-effective single bi-axial scanning mirror. Consequently direct laser modulation in scanning systems shifts the architectural complexity from the optomechanics to the electronics [19]. The architecture typically consists of red, green and blue laser sources with their outputs combined into a single white beam using dichroic elements. The projected image is generated by synchronising all three lasers with the position of the scanning mirror. For each pixel, all three lasers are driven simultaneously at the level required for colour mixing, thus exploiting the high colour gamut of RGB lasers. Compared to a SLM, the main advantages of laser scanning are:

1) always-in-focus image: the projected laser beam creates a focussed image, which is independent of distance to the screen;
2) good power efficiency: given that the three lasers are driven at the required level for each pixel, a laser duty cycle of >90% is achieved compared to a maximum duty cycle of 33% with DMD and LCoS;
3) high contrast: lasers are completely off when generating a black pixel while with SLM the incident beam intensity is deflected.

Initially laser scanning was carried out by polygon scanners [21], acousto-optic scanners [22] and galvanometric scanners [23]. MEMS laser scanners have recently been considered for micro-display applications since they allow miniaturization, require low

power consumption, and are able to achieve acceptable optical performance by exploiting a high resonant frequency actuation. Another advantage compared to DMD is resolution scalability within the same device footprint. MEMS laser scanners can be classified according to (i) fabrication technology (bulk, surface or hybrid micromachining) (ii) operation principle (reflective mirror, refractive lens, diffraction grating) and (iii) actuation method (electrostatic, piezoelectric, electromagnetic or electrothermal). The most common MEMS scanners for high-resolution display applications are torsional micro-mirrors fabricated by bulk silicon micromachining. Torsional flexures provide repeatable and controllable motion, which can be simply integrated to the micro-mirror silicon layer [24]. The performance metrics and requirements of scanning MEMS micro-mirrors will be discussed in Section 2. In Section 2.2 the three main actuation principles will be introduced together with the current state-of-the-art micro scanners pertaining to each actuation method.

1.4   Laser Scanning Architecture

Beam steering for the projection of a two-dimensional image is typically performed using raster scanning or Lissajous scanning. Raster scanning, depicted in **Figure 1-3**, requires low frequency, quasi-static rotation in one axis to create the vertical scan lines and high frequency rotational motion along the second axis for the horizontal scan lines. In order to achieve high scanning frequencies together with large optical deflection amplitudes, the micro-mirror has to be operated at its torsional resonant mode, resulting in a narrowband, high gain response. Single micro-mirrors with bi-directional actuation, using this mixed mode operation (as shown in **Figure 1-4(a)**) have already been commercially developed [25]. However, the resulting bi-directional motion requires complex driving control to achieve uniform image resolution and illumination. Given that the design requirements for micro-mirror motion along each axis are different, a separate one-directional scanning micro-mirror for each scan direction, as in **Figure 1-4(b),** can result in improved performance, reliability and manufacturability [26].

One major disadvantage of raster scanning is the driving requirements for the slow-scanning micro-mirror in the absence of harmonics. In Lissajous scanning (see **Figure 1-3**), both axes are driven at resonance enabling larger scan angles to be achieved with a lower driving voltage. For best coverage, a high ratio between both resonant frequencies is required. This requires a slow-scanning micro-mirror with a low resonant frequency, near 60 Hz, making the projected image sensitive to vibrations [27]. A more

robust solution using two high scanning frequencies separated by the image refresh rate was also suggested. However, the proposed system is not intended for high-end applications [28]. Methods have also been developed in order to deduce the optical requirements for Lissajous scanning with the aim of optimizing the image quality [27, 29]. Lissajous scanning has been successfully implemented for a number of imaging applications such as endoscopic and confocal microscopy [3, 4], however it is not yet considered to be a suitable architecture for high quality displays [19].
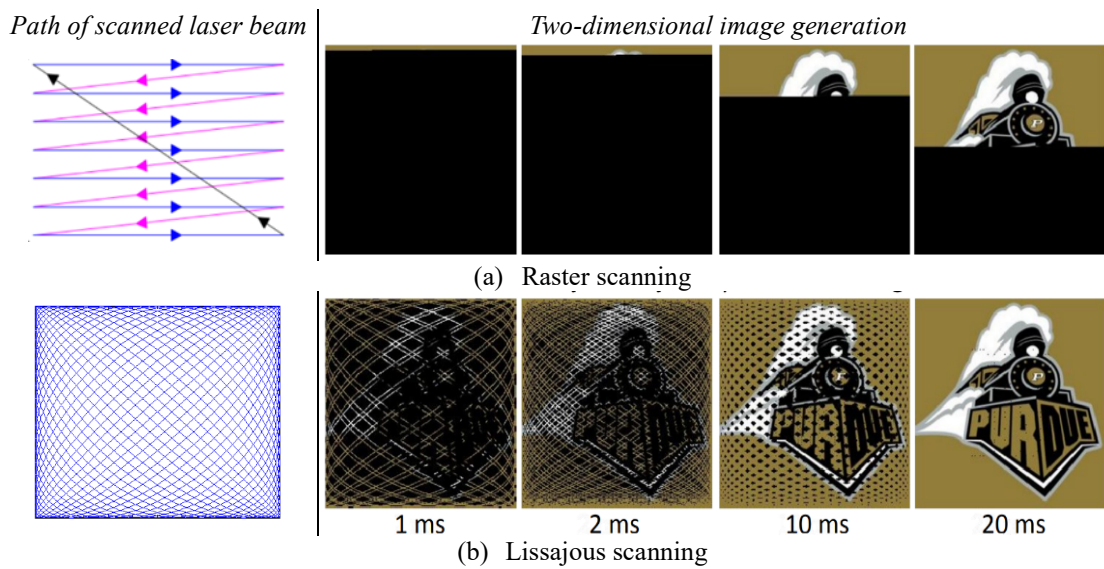
Figure 1-3: Comparison of (a) conventional raster beam-scanning and (b) Lissajous beam-scanning at different time points throughout the acquisition of a complete image acquired at a frame-rate of 25 Hz. (adapted from [30])
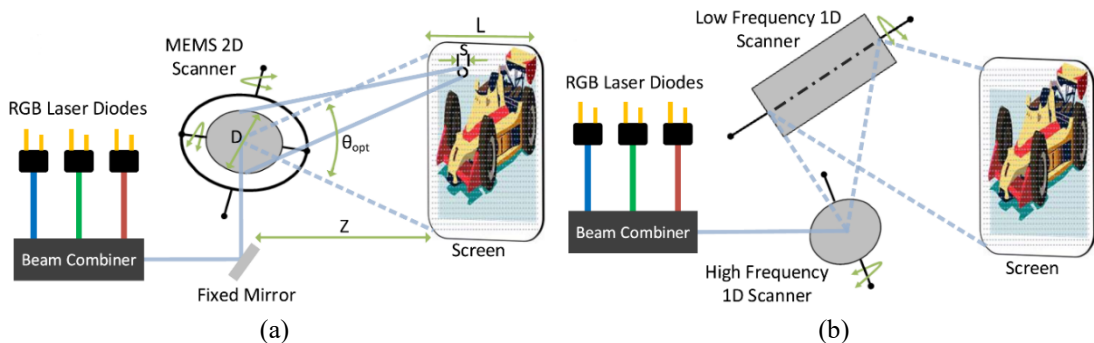
Figure 1-4: Bi-directional scanning mirror architectures using (a) a single bi-axial scanning mirror and (b) two separate mirrors for each scan direction [19]

2   LITERATURE REVIEW

This chapter presents an overview of the multi-physical operating principles behind resonating micro-scanners for laser beam scanning applications. Section 2.1 introduces the target performance metrics of the laser scanning devices on the basis of the theoretical optical resolution. Section 2.2 presents the modes of actuation which have been implemented for the operation of micro-mirrors at high scanning frequencies and a comparison of the highest performing resonating micro-scanners is presented in Section 2.3. A theoretical evaluation of the non-linear dynamic response in AVC-actuated resonating micro-scanners is given in Section 2.4. An introduction to the two main micro-scanner characteristics which will be addressed in this dissertation: dynamic deformation and air damping is presented in Section 2.5 and 2.6 respectively. Finally, a description of the resonant micro-scanner which will be used as a test case as part of numerical validation analyses will be provided in Section 2.7.

2.1   Optical Resolution

In the case where the aperture of an optical system is determined by the size and shape of the scanning micro-mirror, the reflected diffraction pattern (shown in **Figure 2-1** and known as an Airy pattern for circular apertures) consists of a central high intensity peak with a number of surrounding maxima.
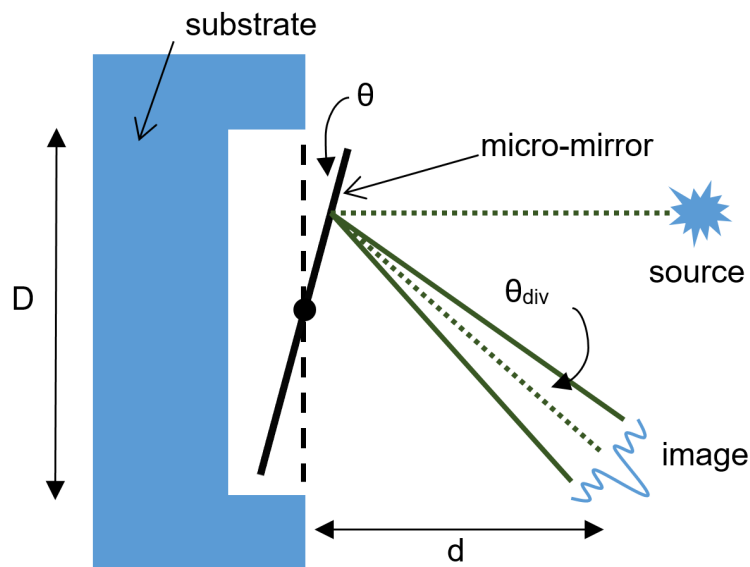
Figure 2-1: Cross-section of a tilting mirror used to image a point source; the dotted line from source to image denotes the path of the ray, but in reality, an optical system would generate a Gaussian beam (adapted from [31])

The width of the diffraction spot, Δx, is thus defined as the distance between the central maximum and the first minimum as given in (2.1) [31]:

$$\Delta x = a \frac{\lambda d}{D} \tag{2.1}$$

where a is the aperture shape factor (circular mirror: 1.22; square mirror: 1), λ is the longest system wavelength, d is the distance between the mirror and the image and D is the mirror aperture. From (2.1), the divergence angle, θ_{div}, due to diffraction can be deduced as in (2.2):

$$\theta_{div} \approx \arctan \frac{\Delta x}{d} \approx a \frac{\lambda}{D} \tag{2.2}$$

The distance between the central maximum and the first minimum (dark ring in the Airy disk) is a measure of the shortest distance possible between two adjacent diffraction spots for them to remain equally resolvable by the human eye. This is known as the Rayleigh criterion. For a reflective raster scanning system with a certain maximum mechanical scan angle, θ_{max}, the diffraction-limited resolution can be defined as the maximum number of resolvable spots or pixels, N_h and is given by (2.3).

$$N_h = \frac{4\theta_{max}}{\theta_{div}} = \frac{4\theta_{max}D}{a\lambda} \tag{2.3}$$

On the other hand, the number of resolvable spots in the vertical scan direction, N_v, can be calculated from the ratio of the horizontal scan frequency, f_s and the frame refresh rate, F_r as in (2.4). The frame refresh rate is normally set at the video frame rate (60 Hz) corresponding to the vertical scan frequency in raster micro-displays. Typically, two lines per scan cycle are written by the vertical scanner enabling the required f_s to be reduced by half. The vertical axis resolution is also dependent on the time fraction for vertical scanner retrace between successive frames, K_{rt}, which usually varies between 0.9 and 0.95 [32].

$$N_v = \frac{2f_s K_{rt}}{F_r} \tag{2.4}$$

From (2.3) and (2.4) it can be demonstrated that, at a fixed F_r, the image resolution is directly determined by the resonating micro-mirror characteristics: θ_{max}, D and f_s. The scanning requirements for a number of display formats are listed in **Table 2-1**. Scanner

design for high-resolution display applications entails a detailed understanding of how the various micro-mirror features interact. After selection of the $\theta_{max}.D$ product, trade-offs between the scan angle and mirror diameter/width need to be considered as shown in **Figure 2-2**. A large mirror facilitates beam alignment in the optical system. However, this also results in a D^4 increase in inertia, which corresponds to a reduction in the scanning frequency. Furthermore, increasing D results in a larger system size and higher dynamic deformation, which will be discussed in more detail in Section 2.6. On the other hand, a large θ_{max} would increase the torsional flexure stress and may be detrimental to stability and reliability of the micro scanner [24].

Table 2-1: $\theta_{max}.D$ and horizontal frequency requirements of various resolutions for displays using bidirectional raster scanning architecture [19]

Display Format	VGA	WVGA	SVGA	HD720	HD1080
N_h	640	854	800	1280	1920
N_v	480	480	600	720	1080
$\theta_{max}.D$ [°.mm]	7.0	9.4	8.8	14.1	21.1
f_s [kHz]	18	18	22.5	27	40.5
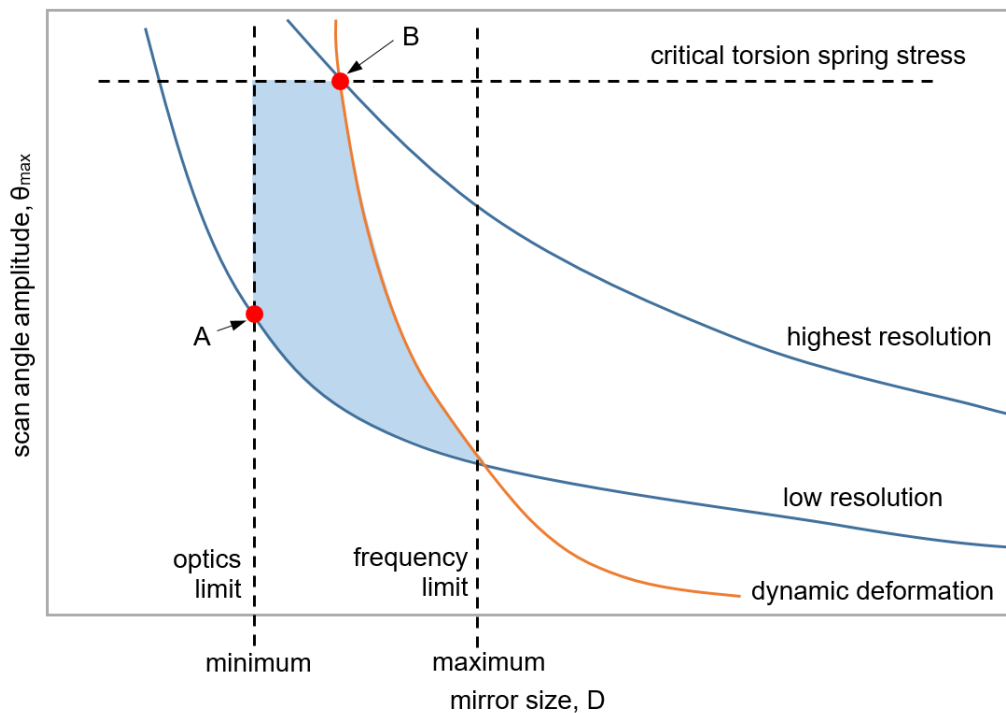
Figure 2-2: Optical resolution, torsional spring stress and dynamic deformation trade-offs for the design of resonating micro-mirrors; depicting a 2-D-slice from a multi-dimensional design space where A and B refer to the optimum operating points for low and high resolution scanning systems respectively (adapted from [24])

2.2   Actuation Principles

In order to achieve the scan angle required for high-resolution laser scanning displays, resonant micro-mirrors make use of their high mechanical quality factor, Q. However in order to overcome the damping losses when operated in atmospheric air, a high driving torque is required. This can be solved by encapsulating the micro-mirror in a vacuum package, which brings about additional fabrication costs. The three main actuation methods considered for resonant micro-mirrors are electrostatic (ES), piezoelectric (PE) and electromagnetic (EM) actuation. Micro-mirrors with electrothermal (ET) actuation have also been developed for a number of applications. However, the inherent slow dynamic response renders ET actuation not suitable for high frequency display systems [33, 34]. For MEMS laser scanning micro-mirrors intended for commercial use, the main aspects to consider are: resolution, drive voltage, power efficiency, compactness, robustness and fabrication simplicity.

2.2.1   Electrostatic Actuation

ES actuation is based on the principle of electrostatic attraction between two oppositely charged plates, depicted in **Figure 2-3** (Coulomb's law) where the electrostatic force, F_{es} between two plates is given by (2.5):

$$F_{es} = \frac{A \varepsilon V^2}{2 f_g^{\,2}} \tag{2.5}$$

where A is plate overlap area, V is the potential difference, ε is the dielectric permittivity of the medium and f_g is the gap between the two plates.
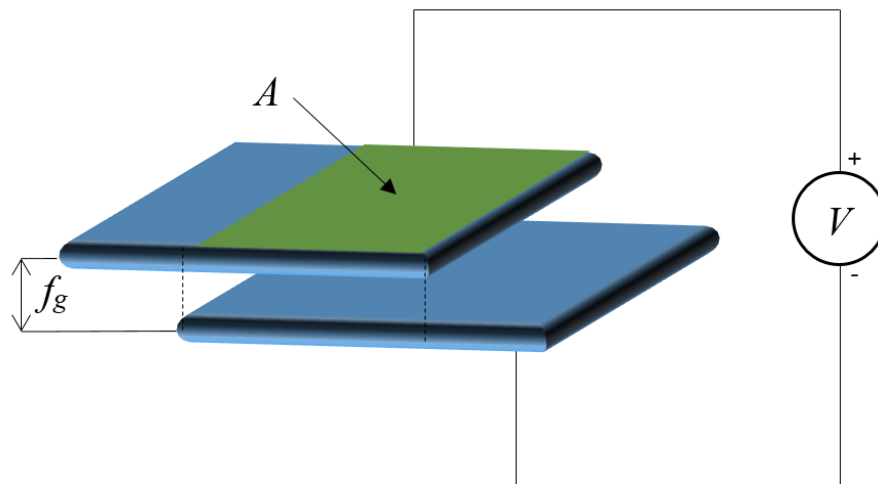
Figure 2-3: Electrostatic actuation between two oppositely charged plates

ES actuation has been the most preferred method for MEMS micro-mirrors in published literature due to fabrication compatibility with any MEMS facility without additional complex material requirements. ES actuation can be applied using either a parallel-plate or a comb configuration. The former is the typical actuation mode for bi-stable mirrors such as DMDs. However, the parallel-plate geometry restricts $\theta_{max}.D$ to small values and in fact only a few examples of resonant micro-scanners employing this actuation method have been reported [35]. Additionally, the micro-mirror displacement is limited by the electrode gap size, f_g which in turn is limited by the allowable drive voltage.

Higher scan angles can be achieved using the comb configuration which consists of two sets of interdigitated fingers, one static and one moveable as shown in **Figure 2-4**, in order to increase the overlap area density. Unlike parallel-plate actuation, where the electrode separation is variable with mirror motion, comb actuators provide a more distributed force variation over the span of electrode motion. Out-of-plane displacement of a MEMS scanner can be achieved via a vertical comb drive actuator. In order to initiate the mirror motion a disruption in the electrostatic field is required [1]. For resonant micro-mirrors (horizontal raster scanning), only a slight out-of-plane asymmetry between the moving and static electrodes is required. However for DC or quasi-static operation (vertical raster scanning), the range of motion is determined by the out-of-plane offset between both comb sets. Therefore, the fixed and moving combs of slow scanning micro-mirrors are typically fabricated from separate layers [36].

The first resonant micro-mirrors having a scanning frequency greater than 15 kHz started to emerge in the year 2000 [37]. Electrostatic actuation was considered to operate such mirrors, using either a parallel plate configuration or a vertical comb drive [37]. The vertical comb actuator consisted of two monocrystalline silicon layers, with the mirror, torsional beams and moving comb structures etched from the top 50 μm thick layer while the fixed comb structure is located in the bottom layer. With this configuration, known as Staggered Vertical Comb (SVC) drive, a voltage of 240 V_{pk-pk} is required to achieve a maximum scan angle of 6.25° for a 0.5 mm diameter mirror at a scanning frequency of 34 kHz (**Figure 2-5(a)**). Moreover, dynamic deformation measured using stroboscopic white light interferometry was found to be less than 30 nm. A number of comb structure designs have been proposed with the aim of minimizing the drive voltage while maintaining the required electrostatic torque. These range from the long SVC actuator proposed by Samsung Electronics Co. [38] or the more compact eye-

type mirror design by Ko *et al.* [39] (**Figure 2-5(b))**. The SVC actuator facilitates start-up especially at low frequency and quasi-static scanning. However, the main drawback is misalignment between the top and bottom layer patterns, which are etched using separate masks [38]. Alignment mismatch between the static and moving fingers can be overcome with angular vertical comb (AVC) drives. In AVC actuators, the static and moving frames are etched from the same layer. This considerably reduces the fabrication complexity of SVC actuators and it has been shown that for the same finger geometry, AVC actuators are more efficient [40]. Instead, electrostatic torque asymmetry for start-up is provided by an initial offset angle of the rotating fingers. A number of techniques have been proposed to achieve this offset: plastic deformation of silicon through annealing [41, 42], residual stress in a metal film coating on the SOI device layer [43] and surface-tension forces from reflow of a photoresist [40].
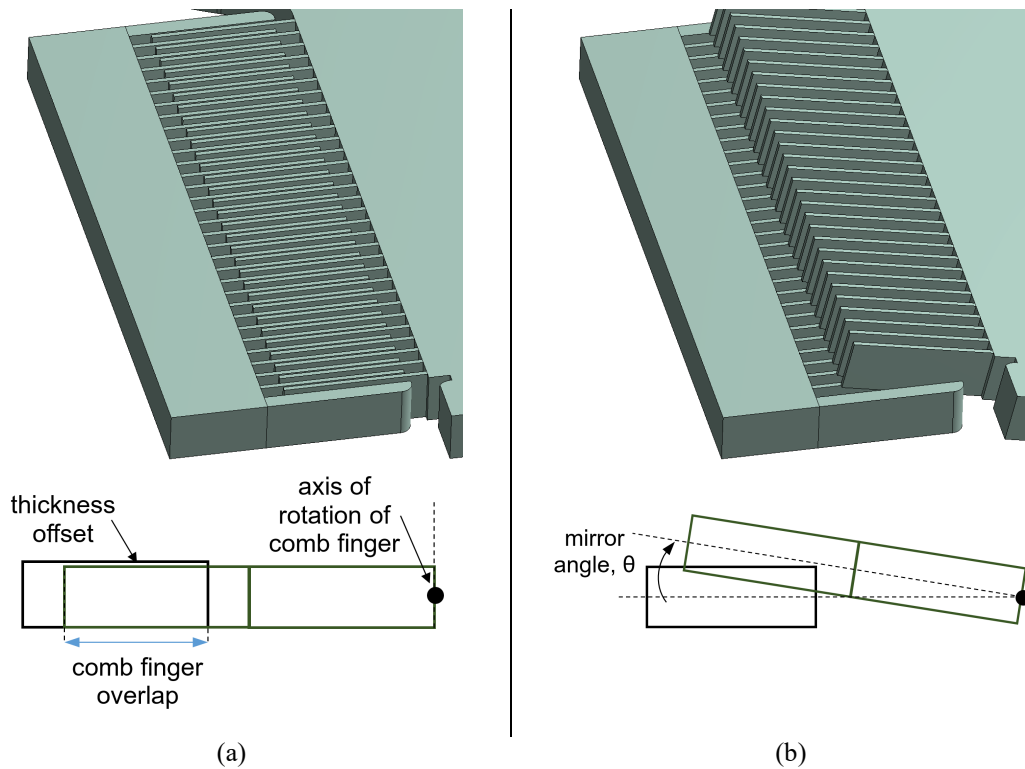
Figure 2-4: Angular vertical comb structure for electrostatic actuation of resonating micro-scanners; micro-scanner at (a) $\theta(t) = 0°$, (b) $\theta(t) \neq 0°$

On the other hand, high frequency scanning micro-mirrors with in-plane comb actuators have been developed at the Fraunhofer Institute for Photonic Microsystems (FhG-IPMS). Fabrication asymmetries which result in a slight angular deviation between the electrostatic and mechanical rest position was found to be sufficient for the micro-mirror

to start oscillating at its torsional resonance mode [2]. FhG-IPMS also presented an ES-actuated micro-mirror, shown in **Figure 2-12(d)** with a scanning frequency of 30.8 kHz and θ_{max} of 10° while adhering to the strict optical flatness requirement of $\lambda/10$ [44].

<div align="center">(a)   (b)</div>
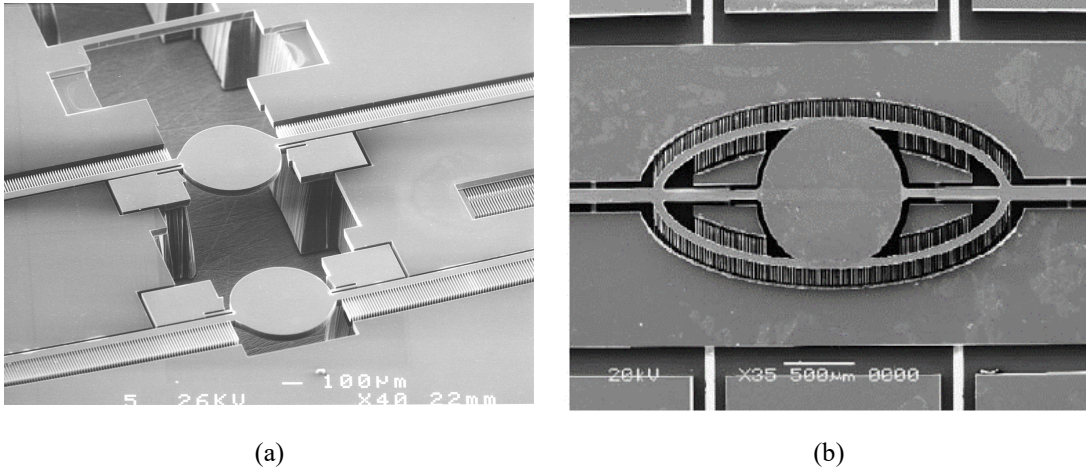
Figure 2-5: A selection of ES resonant micro-mirrors (a) [37] (b) [39]

2.2.2   **Electromagnetic Actuation**

Electromagnetic (EM) actuation can be achieved using two schemes: moving magnet or moving coil. In the former, an external coil is used while the magnet, in bulk or thin film form is deposited on the moving structure. This eliminates the need for on-chip electrical contacts leading to simplified microfabrication. In the moving coil scheme, the coil is deposited directly on the device while a static magnetic field is provided by an external magnet. In the latter configuration, a Lorentz force, F_{lor} is generated on the coil when current is applied. With reference to **Figure 2-6**, the resultant EM torque, M_{EM} can be calculated as in (2.6):

$$M_{EM} = 2\sum_{n=1}^{N} F_{lor} r_n = 2\sum_{n=1}^{N} Bil_n r_n \tag{2.6}$$

where B is the magnetic field, i is the current, l is the conductor length, N is the number of coil turns, r_n is the distance of the nth coil turn from the centre. Given that F_{lor} increases linearly with mirror width, EM becomes more efficient than ES with increasing mirror size. Apart from a linear response and a significantly lower drive voltage compared to ES, thermal dissipation in the coils limits the achievable $\theta_{max}.D$ of the micro-mirror. Furthermore, the required power consumption to sustain high conducting currents is a disadvantage for mobile devices and the external coil/magnet results in a larger package compared to other actuation methods.

Surface: Total displacement (µm)
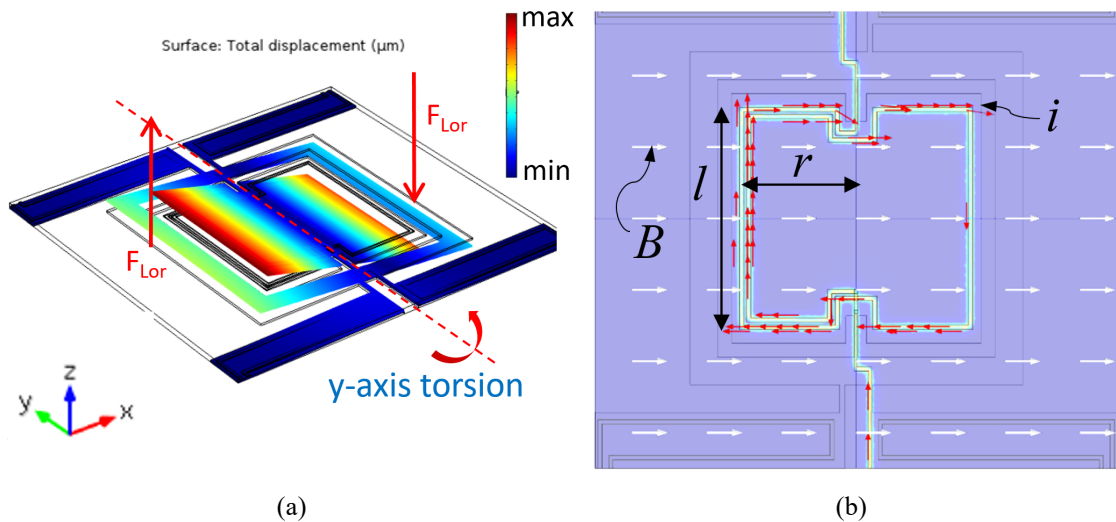
Figure 2-6: Structural-electromagnetic FE simulation of an EM micro-scanner with moving coil deposited along the perimeter of the mirror plate: (a) angular oscillations of the mirror-plate at resonance (b) top view plot of the electrical and magnetic field directions

Compared to EM actuation, ES scanning has a significant form factor advantage in one-directional scanning micro-mirrors designs and in fact, the electromagnetic moving coil principle is typically only employed in two directional scanners [45, 46]. However, several researchers have demonstrated that by locating the moving coil on a frame surrounding the mirror plate, higher scan angle and frequency can be achieved [47, 48, 49]. This is due to the mechanical amplification principle behind indirect-drive configurations which is discussed in Section 2.3.1. EM micro scanners can achieve 2-D scanning using a single coil whereby the imposed torque from Lorentz's force excitation is applied at 45° relative to the two orthogonal scan angles [47]. In order to reduce crosstalk between the relevant resonant modes, independent biaxial scanning can be achieved by introducing a separate coil for each scan direction [48].

2.2.3   Piezoelectric Actuation

Recent developments in the deposition of thin film lead zirconate titanate (PZT) improved the viability of piezoelectric (PE) actuation in resonating micro-mirrors. A potential difference applied along the thickness of a PZT thin film (z-axis) corresponds to a lateral strain (x-axis) according to the piezoelectric coefficient d_{31}. Out-of-plane displacement can be achieved through the bending of cantilever structures composed of a thin-film piezoelectric layer deposited on a silicon layer. The most common technique for piezoelectric actuation in resonant micro-mirrors consists of two Si-piezoelectric cantilevers imparting a torque on torsion bars connected to the mirror plate along its rotational axis (**Figure 2-7)** [50]. PE actuators require lower drive voltages compared to

15

vertical comb actuators and result in a more compact package compared to EM actuators. Although high forces can be generated with the same voltage, displacement or stroke length is small requiring a leverage mechanism to reach the scan angle requirements for high resolution displays. Another advantage of PE actuators is that cantilever deflection is related to the piezoelectric charge which can be estimated as an integration of the driving current. This facilitates scan angle feedback for closed-loop control without the need for any design or process modifications.

(a)

(b)
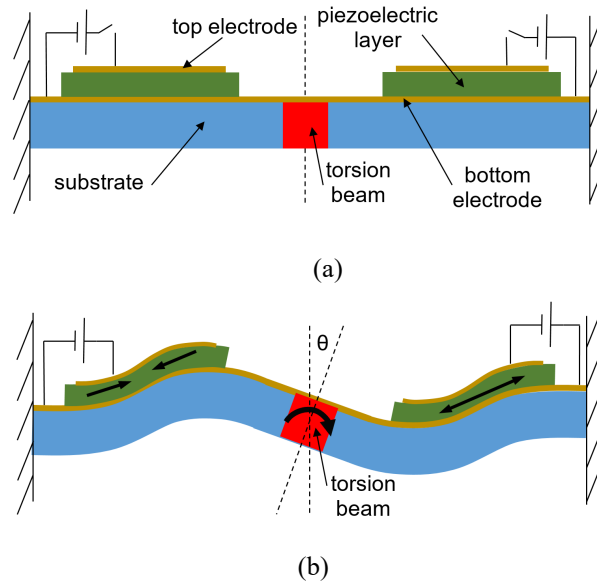
Figure 2-7: Schematics showing a technique of converting out-of-plane bending of unimorph piezoelectric-Si cantilevers into a torque at the micro-mirror torsional beams. The polarity of the voltage applied across electrodes determines the strain direction in the piezoelectric layer [19]

Apart from the method described in **Figure 2-7**, a number of actuation configurations have been proposed to translate the limited lateral deformation of the piezoelectric thin-film into mirror plate rotation. A novel actuator design was introduced by Filhol *et al.* [51] whereby a 500 μm diameter mirror is asymmetrically (50 μm off-centre of the mirror mass) connected to two torsional beams. These beams are in turn linked to fixed-fixed beam type piezoelectric bimorph actuators. As a result, the vertical displacement of the actuators is converted to rotational micro-mirror movement. This configuration has also been demonstrated with bulk PZT [52] and a thin film electro active polymer, which requires a relatively low temperature deposition process [53]. Compared to ES and EM actuation, high scanning frequencies have been demonstrated with PE actuation (see **Table 2-2**) however the available stroke length is limited, requiring long piezoelectric bimorphs to achieve a maximum scan angle over 10° [54]. In order to

overcome the displacement limitation, Baran *et al.* [55] proposed an indirect-drive design (discussed in 2.3.1) with the PZT film deposited on the outer frame to achieve a more compact design. The 1.4 mm diameter micro-mirror oscillates at a frequency of 40 kHz and reaches a maximum scan angle of 9.6° at an actuation voltage of 24 V_{pk-pk}.

2.3   State-of-the-art in Resonant Micro-Scanners

A comparison of the highest performing resonant micro-mirrors intended for laser scanning displays is presented in **Figure 2-8**. The metrics f_s and $\theta_{max}.D$ were considered in order to determine the achievable optical resolution. Details and references of the individual micro-mirrors are provided in **Table 2-2**. In general, voltage requirements for ES micro-mirrors are an order of magnitude higher than for other actuation methods. PE actuation is by far the highest performing technology for scanning frequencies greater than 30 kHz. Therefore, PE scanners with an indirect drive configuration are ideal candidates towards achieving the next generation high resolution (1080p) displays, which require horizontal scanning frequencies of around 40 kHz [19].
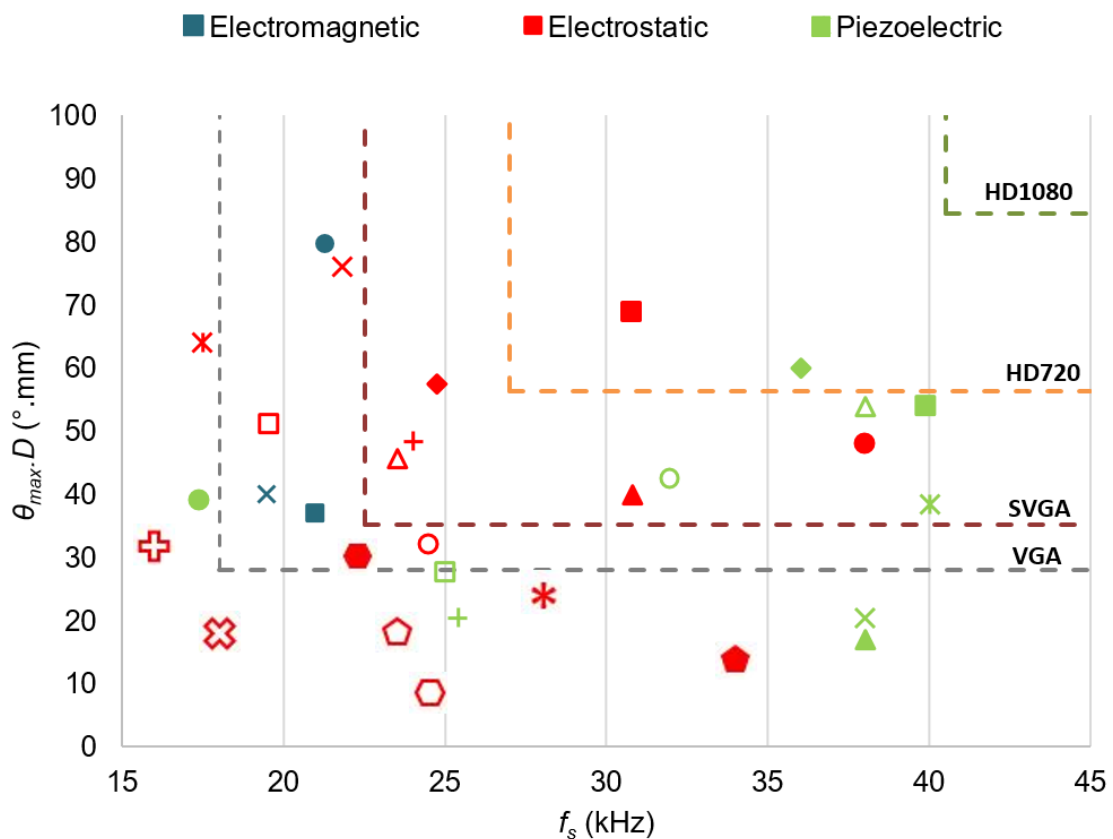
Figure 2-8: Comparison of the highest performing resonating micro-mirrors from literature. The f_s and $\theta_{max}.D$ resolution requirements are based on a 60 Hz refresh rate and bidirectional scanning. More details are provided in **Table 2-2**

Table 2-2: Data for high performance scanning micro-mirrors operating over 15 kHz

Reference	Symbol	Actuation method	Description	f_s (Hz)	θ_{max} (°)	D (mm)	$\theta_{max}.D$ (°.mm)
[49]	✕	EM	moving coil (4 V_{rms})	19.5	10	1	40
[48]	■	EM	moving coil (10 V_{pk-pk})	21	7.7	1.2	37.0
[47]	●	EM	moving coil	21.3	13.3	1.5	79.5
[56]	✚	ES	AVC (140 V_{pk-pk})	16	8	1	32
[35]	✳	ES	parallel plate (slow axis: EM)	17.5	16	1	64
[35]	✧	ES	parallel plate (slow axis: EM)	18	3.8	1.2	18.2
[57]	□	ES	SVC (100 V_{pk-pk})	19.5	8.5	1.5	51
[58]	✕	ES	AVC (196 V_{pk-pk})	21.8	19	1	76
[59]	⬡	ES	AVC (140 V_{pk-pk})	22.3	7.5	1	30
[60]	⬠	ES	SVC (100 V_{pk-pk})	23.5	4.5	1	18
[61]	△	ES	AVC (140 V_{pk-pk})	23.5	9.5	1.2	45.6
[62]	✚	ES	parallel plate (400 V_{pk-pk})	24	5.5	2.2	48.4
[63]	⬡	ES	SVC (160 V)	24.5	5.1	0.42	8.6
[39]	○	ES	SVC (100 V_{dc} + 75 V_{ac})	24.5	8	1	32
[38]	◆	ES	SVC (280 V_{pk-pk})	24.8	12	1.2	57.6
[64]	✳	ES	AVC (200 V_{pk-pk})	28	4.1	1.5	24.6
[65]	■	ES	stacked comb drive (70 V)	30.8	21.5	0.8	68.8
[44]	▲	ES	AVC	30.8	10	1	40
[37]	⬟	ES	SVC	34	6.2	0.55	13.7
[66]	●	ES	AVC (200 V_{pk-pk})	38	12	1	48
[67]	●	PE	PZT thin film (6 V_{rms})	17.4	7.5	1.3	39
[6]	□	PE	PZT thin film (10 V_{pk-pk})	25	6.9	1	27.6
[51]	✚	PE	PZT thin film (42 V_{pk-pk})	25.4	10.3	0.5	20.5
[68]	○	PE	PZT thin film (7 V_{pk-pk})	32	10.6	1	42.5
[52]	◆	PE	bulk (16 V_{pk-pk})	36	15	1	60
[69]	▲	PE	PZT thin film (6 V_{pk-pk})	38	4.3	1.2	20.4
[69]	✕	PE	ZnO thin film (25 V_{pk-pk})	38	4.3	1	17
[54]	△	PE	PZT bulk (5 V_{pk-pk})	38	13.5	1	54
[55]	✳	PE	PZT thin film (24 V_{pk})	39.9	9.6	1.4	53.9
[70]	■	PE	PZT thin film (24 V_{pk})	40	6.9	1.4	38.5

2.3.1   Indirect-Drive Concept

In the majority of high frequency micro-scanners, torque is imparted directly from the actuator to the micro-mirror. A number of researchers have presented micro-mirrors with the indirect-drive concept, whereby the mirror plate is mechanically coupled to an outer frame having a larger moment of inertia. Indirect-drive makes use of a favourable resonance mode which amplifies a small oscillation of the outer frame to a significantly larger oscillation of the mirror plate [19]. Two scanning modes are available with mechanically-coupled micro-mirrors: in-phase mode where the mirror plate and an outer frame, having a larger mass, rotate together, and the out-of-phase mode where the mirror and the outer frame oscillate in opposite directions. Typically, the amplification factor, *A*, defined as the ratio of the angular displacement of the mirror plate and the outer frame, is maximum at the out-of-phase modal frequency. The performance of ES micro-scanners with a direct drive is limited by air damping losses and actuator area limitations when the comb fingers are directly connected to the mirror plate. Damping losses can be significantly reduced by transferring the actuator fingers to a lower velocity outer frame while offering a larger comb structure area and hence higher capacitance [58] (**Figure 2-9(a)**). The advantages of the indirect-drive principle have also been demonstrated in high frequency scanners with a parallel-plate configuration [62] (**Figure 2-9(b)**). Moreover, an additional gimbal frame (moving in-phase with the mirror plate) between the mirror plate and the outer frame can also be included in order to minimize dynamic deformation [64]. Indirect drive has also been successfully demonstrated with EM [48] (**Figure 2-10(c)**) and PE [6, 70] (**Figure 2-10(d)**) actuation.

| (a) | (b) |
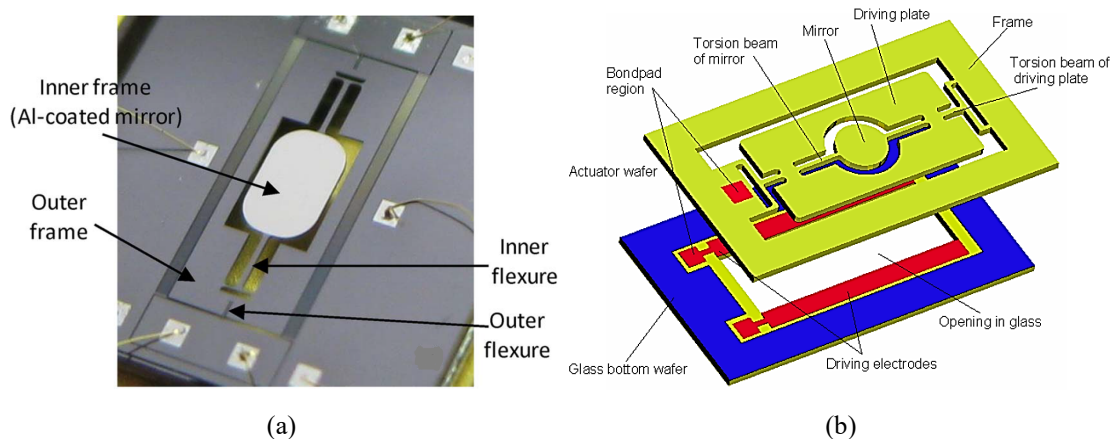
Figure 2-9: A selection of micro-scanners with the indirect-drive concept and electrostatically actuated using: (a) angular vertical comb structures [58] and (b) parallel plate configuration [62]

(a)   (b)
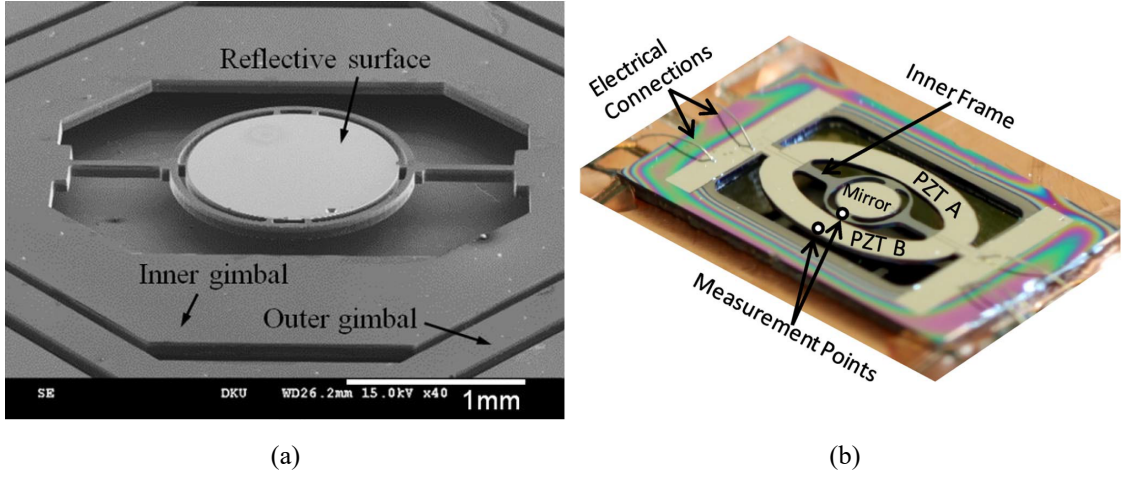
Figure 2-10: A selection of micro-scanners with the indirect-drive concept and: (a) electromagnetic moving coil actuation [48] and (b) PZT thin film actuation [70]

2.4   **Non-linear Dynamic Response**

In the majority of resonant MEMS devices, a linear relation between driving force and oscillation amplitude can be assumed with sufficient accuracy [71]. The equation of motion of a linear harmonic oscillator with angular response is given as:

$$\ddot{\theta} + \frac{\omega_0}{Q}\dot{\theta} + \omega_0^2\theta = M_0\sin\left(\omega_d t\right) \tag{2.7}$$

In (2.7), θ is the time dependent angular displacement, $\dot{\theta}$ is the angular velocity and $\ddot{\theta}$ is the angular acceleration. M_0 is the driving torque amplitude, ω_0 is the natural frequency, defined by (2.8) and ω_d is the driving torque frequency. The effective mechanical stiffness, k and the effective moment of inertia, I are a function of geometric and material properties (i.e. Young's modulus, Poisson ratio and density). The angular frequencies are related to frequencies f_0 and f_d as in (2.9).

$$\omega_0^2 = \frac{k}{I} \tag{2.8}$$

$$\omega = 2\pi f \tag{2.9}$$

The quality factor is defined as the ratio of the energy stored in the system to the energy dissipated over one cycle. The linear quality factor Q, is inversely proportional to the damping coefficient, c. In order to fulfil the optical performance requirements discussed in Section 2.1, a MEMS micro-scanner has to operate at large out-of-plane deflection angles. Additionally, the dimensions of a typical micro-mirror are in the millimetre-scale as opposed to the average MEMS devices. Consequently, the assumption of linear

behaviour may not be valid for large oscillation amplitudes. In fact, observation of a number of dynamic non-linear effects render the dynamic equation of (2.7) insufficient for the modelling of electrostatically actuated resonating micro-scanners [72, 73, 74]. In particular, the non-linear effects of elastic spring hardening, AVC electrostatic actuation and air damping have to be considered.

2.4.1   Elastic Spring Hardening

At large oscillation amplitudes, the resistance of MEMS structures to deformation increases as a result of geometric non-linearities. Mechanical spring stiffening can be modelled using the Duffing equation [75], given in (2.10), which consists of an additional non-linear cubic term:

$$I\ddot{\theta} + c\dot{\theta} + k_{s,1}\theta + k_{s,3}\theta^3 = M_0 \sin(\omega_d t) \tag{2.10}$$

From (2.10), an increase in the driving torque results in a shift in the frequency at peak response amplitude, as shown in **Figure 2-11**. Nonetheless, linearity between input force and maximum amplitude is maintained with the Duffing oscillator model.
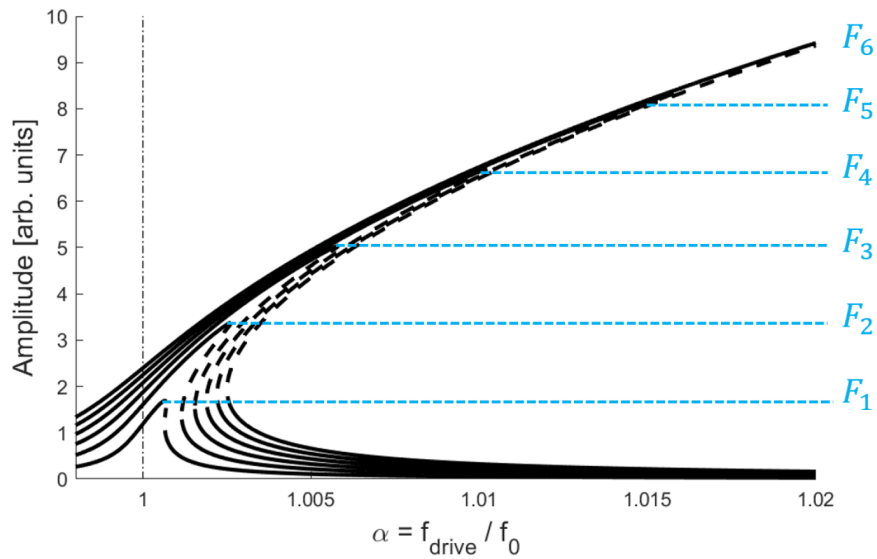
Figure 2-11: Typical amplitude response curves for a Duffing oscillator model. Solid lines denote stable solutions while dashed lines denote unstable solutions [71]

2.4.2   Electrostatic Spring Softening

Equation (2.10) can also be applied to model the effect of electrostatic spring softening in MEMS devices driven via an electrostatic parallel-plate actuators. The electrostatic force function can be approximated using the first two terms of a Taylor series expansion. If a constant bias voltage is applied, the equivalent electrostatic spring

constant for a fixed capacitive overlap area, A is given in (2.11). An increase in bias voltage is usually detected as a reduction in the resonant frequency.

$$k_e = -\frac{\varepsilon A V^2}{\theta^3} \tag{2.11}$$

2.4.3   Non-linear Damping

While (2.10) has been widely used for the modelling of resonant MEMS, it only accounts for linear damping. Measurements of MEMS micro-scanners reveal that the quality factor is amplitude-dependent. Non-linear damping, in most cases, reduces scanning efficiency and hence power consumption. The scanning efficiency is defined as the ratio of the maximum scan angle amplitude to the drive voltage amplitude. The variation of Q with amplitude is deduced from the time-dependent amplitude decay rate after the external driving torque is switched off. The addition of a non-linear damping term in (2.12) is proposed by Nabholtz et $al.$ [71] to accurately model the dynamics of a resonating micro-scanner. Equation (2.12) is based on the van-der-Pol oscillator model [76] and Q_{nl} is defined as the non-linear quality factor and is inversely proportional to the non-linear damping coefficient, c_{nl}.

$$\ddot{\theta} + \frac{\omega_0}{Q}\dot{\theta} + \frac{\omega_0}{Q_{nl}}\theta^2\dot{\theta} + \omega_0{}^2\theta = M_0 \sin\left(\omega_d t\right) \tag{2.12}$$

2.4.4   Parametric Resonance

Evidence of non-linearities due to the damping, elastic and electrostatic effects has been observed in a number of MEMS and MOEMS devices. However, in general, such devices are still governed by classic harmonic resonance whereby the electromechanical system is excited into resonance by the application of drive frequencies in the region of ω_0 (i.e. direct excitation). A system may also exhibit large response amplitudes as a result of an externally imposed periodic variation of one or more system parameters. This phenomenon is known as parametric excitation/resonance and is well understood in a number of engineering systems with classical examples such as the base excitation of a pendulum or the forced motion of a playground swing [77]. A micro-scanner driven by angular vertical comb actuators exhibits parametric resonance response near drive frequencies of $2\omega_0$. The resultant harmonic response is characterized by bifurcations depending on the direction of the drive frequency sweep [77]. Moreover, the elastic,

damping and electrostatic non-linearities strongly affect the stability characteristics of parametric resonance.

Analytical simulations of the non-linear electrostatic actuation are based on the non-linear Mathieu equation [78]. Assuming that only the torsional springs (or beams) deform elastically while the remaining elements behave as rigid bodies, the response of a micro-scanner with AVC structures in the torsional mode is given by:

$$I\ddot{\theta} + c\dot{\theta} + k_s\theta = \frac{1}{2}\frac{\partial C}{\partial \theta}V(t)^2 \tag{2.13}$$

In (2.13), C is the θ-dependent total capacitance of the AVC structures and $V(t)$ is the time-dependent applied potential across the comb finger gaps. For a sinusoidal drive voltage, (2.13) can be rewritten as:

$$I\ddot{\theta} + c\dot{\theta} + k_s\theta = \frac{1}{2}\frac{\partial C}{\partial \theta}V^2 \sin^2\left(\omega_d t\right) \tag{2.14}$$

It is worth noting that while the numerical and experimental analysis in this dissertation will be based on a sinusoidal voltage signal, better scanning efficiency has been observed using a square-wave signal with a 50% duty cycle [72]. Using trigonometric manipulation in (2.14), the forcing function becomes:

$$I\ddot{\theta} + c\dot{\theta} + k_s\theta = -\frac{1}{2}\frac{\partial C}{\partial \theta}V^2\left(1 + \cos\left(2\omega_d t\right)\right) \tag{2.15}$$

For small angles, $\partial C/\partial \theta$ can be approximated as a cubic function as shown in (2.16) [78]:

$$I\ddot{\theta} + c\dot{\theta} + k_s\theta = -(k_{e,1}\theta + k_{e,3}\theta^3)\left(1 + \cos\left(2\omega_d t\right)\right) \tag{2.16}$$

$$I\ddot{\theta} + c\dot{\theta} + \left(k_s + k_{e,1} + k_{e,1}\cos\left(2\omega_d t\right)\right)\theta + \left(k_{e,3} + k_{e,3}\cos\left(2\omega_d t\right)\right)\theta^3 = 0 \tag{2.17}$$

Equation (2.17) is a form of the generalized non-linear Mathieu equation, given in (2.18) for an arbitrary modal displacement, x [72].

$$\frac{d^2x}{dt^2} + \left(\delta + \varepsilon\cos\left(2\omega t\right)\right)x - \left(\gamma + \gamma\cos\left(2\omega t\right)\right)x^3 = 0 \tag{2.18}$$

By combining the validated analytical models of (2.12) and (2.17), a realistic representation of the non-linear dynamics exhibited by an electrostatically actuated resonant micro-scanner is the van der Pol-Mathieu-Duffing oscillator, as shown in (2.19).

$$I\ddot{\theta} + \left(c - c_{nl}\theta^2\right)\dot{\theta} + \left(k_{s,1} + k_{e,1} + k_{e,3}\cos\left(2\omega_d t\right)\right)\theta$$
$$+ \left(k_{s,3} + k_{e,1} + k_{e,3}\cos\left(2\omega_d t\right)\right)\theta^3 = 0 \qquad (2.19)$$

2.5   Air Damping

Resonating micro-mirrors are typically operated in air at atmospheric pressure in order to provide a smooth scan angle response around the resonant frequency and to prevent excessive dynamic amplification such that structural failure of the torsional springs is inhibited [79]. The three main dissipative mechanisms occurring in the resonating device are (i) viscous shear due to the relative sliding motion between the moving and static electrodes; (ii) pressure drag on the mirror-plate and comb drive structures undergoing large angle oscillations; and (iii) fluid flow interactions between the rotating micro-mirror and the underlying cavity wall.

Surface micro-machined resonating MEMS devices are typically located in close proximity to planar surfaces, forming either a fluid sliding or squeezed film viscous damper [80]. Such fluid domains can be accurately expressed by linearized analytical and numerical damping models valid for small oscillation amplitudes and fluid film gaps. The damping moment due to the angular displacement of the drive electrodes relative to the static electrodes has been derived analytically from one-dimensional Couette flow [63]. Klose et al. [81] additionally applied 1-D Poiseuille flow to model the air between adjacent rotating electrode fingers in the disengaged state of the comb structure. For specific electrostatic micro-mirror designs, fluid flow in and around the comb finger gaps is the dominant damping mechanism [82]. However, this may not always be the case and in fact significant energy dissipation due to mirror plate drag has been reported in electrostatic micro-scanners [79, 83].

The circular mirror plate begins to be affected by a nearby wall at a distance comparable to the mirror diameter [83]. Xia et al. [84] derived the squeeze film damping loss for circular micro-mirrors from the non-linear Reynolds equation and results were successfully compared to simulations in CoventorWare. Squeeze film damping, based on lubrication theory applies when the ratio of gap height to the lateral structure dimension is small [83]. Due to the large scan angle specification of micro-mirrors for projection display applications, gaps greater than 100 μm are required, rendering the aerodynamics between the mirror and cavity outside conventional lubrication theory. Moreover, the fluid velocity field surrounding the micro-mirror oscillating at high

frequency and amplitude is highly complex and three-dimensional [80]. The drag of a slow moving thin circular disc (*Re* < 1), rotating out-of-plane, has been derived from Stokes' equation [85]. Additionally, the frequency-dependent unsteadiness in the air flow surrounding the oscillating circular disc was analysed by Zhang & Stone [86]. At high oscillation frequencies, the aerodynamic torque on the disc is dominated by the inertial or added mass term, which is $\pi/2$ out-of-phase from the disc velocity and does not contribute to energy dissipation. The in-phase component consists of the Stokes drag and contributions from the Stokes and viscous boundary layers at the disc surface. Modifications to the unsteady Stokes equation were also proposed to include the effects on the fluid flow around circular discs in close proximity of an infinite plane wall [87, 88, 89]. It is important to note that the unsteady Stokes flow is valid for small amplitude oscillations. Given that high performance micro-scanners operate at a peak value of *Re* >> 1, Klose *et al.* [81] applied the semi-empirical form drag equation for laminar flow past a circular plate. This signifies that the damping torque increases quadratically with micro-mirror velocity, in contrast with the linear relationship derived from Stokes drag and squeeze-film damping.

It is evident that a deeper understanding of the airflow development in resonating micro-scanners is essential if the accuracy of the available analytical expressions is to be determined. Three-dimensional Navier-Stokes (N-S) simulations based on computational fluid dynamics (CFD) software such as ANSYS CFX, COMSOL and CFD-ACE+ have been performed to determine the micro-scanner damping torque [79, 82, 90]. The N-S equations are discretized using the finite volume method (FVM) while a dynamic meshing technique is employed to simulate the transient fluid flow profile. Separate CFD models for the comb structure and the mirror plate have been proposed due to the length scale variation present. However, a general insight on how air damping is influenced by f_s, θ_{max}, R and the micro-mirror layer thickness, t_m, is lacking. Rotational oscillating cylinders in a quiescent fluid have been extensively analysed [91], however, the wake instabilities that differentiate a fixed speed rotating circular plate from one with sinusoidal motion have not yet been fully investigated. A comprehensive CFD analysis of the wake generated by an oscillating disc in out-of-plane translation, demonstrates that different fluid flow regimes develop depending on the Reynolds number (Re), Keulegan-Carpenter number (KC) and the disc aspect ratio [92].

The accuracy of the mirror plate and comb structure CFD simulations can only be validated via measurements of the overall Q. The device layer is generally etched from monocrystalline silicon and therefore, material damping losses are negligible compared to air damping losses [93]. The non-linear electrostatic forcing and damping moments in comb structure-driven micro-scanners result in a bistable frequency response around the torsional modal frequency. Consequently, the most suitable method of deducing Q is by measuring the optical angle amplitude decay using a position sensitive detector (PSD) once the external driving signal is switched off [93]. By fitting an exponentially decaying sinusoidal function to a rolling window of the response, the variation of Q with scan angle amplitude can be deduced [94]. Nabholtz *et al.* [71] additionally suggested a method by which the real (damping) and imaginary (inertial) aerodynamic coefficients can be deduced.

2.6   Dynamic Deformation

Out-of-plane deformation resulting from periodic acceleration forces tends to be the most important limiting factor for high performance imaging and display applications [19]. In the presence of non-planarity, the main intensity peak of the reflected beam profile is reduced while the intensity of the adjacent peaks become non-negligible (see Section 2.1). This effectively results in a variation in beam spot size along the mirror scan line and a reduction in contrast between the resolvable spots, which would lead to a reduction in resolution [95]. Based on the Rayleigh criterion, in order to project an image with a resolution that is limited only by diffraction, the critical maximum out-of-plane deformation along the micro-mirror surface, δ_{crit} should be less than 1/10 of the shortest incident wavelength ($\lambda = 440$ nm: where $\delta_{crit} = 44$ nm) [96].

The simplest solution towards reducing dynamic deformation is to increase the micro-mirror stiffness by increasing its thickness. However, this will also result in an increase in torsion stiffness given that the micro-mirror structure and the torsional springs are typically etched from the same silicon layer. Other proposed designs have demonstrated that the mirror stiffness can be increased by supporting a relatively thin mirror layer on an underlying reinforcement structure either in the form of multiple rib stiffening structures (**Figure 2-12(a)**) [38], a rim along the edge [70, 97] or other more complex designs (**Figure 2-12(b, c)**) [44, 57, 60] which require additional process steps during fabrication. Instead of increasing the micro-mirror stiffness at the expense of the device unit cost, non-planarity can be reduced by optimizing the layout of the oscillating

structure, namely the micro-mirror geometry and the spring-linkage design. A significant reduction in dynamic deformation has been reported by the introduction of a gimbal-type frame connecting the torsional beams to a circular micro-mirror (**Figure 2-10(a) and Figure 2-12(d))** [52, 56, 28]. In order to achieve layout optimization, analytical equations to predict the dynamic deformation of different micro-mirror geometries have been derived from 1-D plate bending theory [97, 98]. However deformation surface profiles simulated using finite element analysis suggest limitations to the applicability of such equations [32, 57] . A comparison of the dynamic flatness achieved by a number of resonant scanners from literature is provided in **Table 2-3**. The normalised dynamic deformation, R_{def}, which will be defined in Section 6.2.2, is used to describe the effectiveness of the design layout and underlying supporting structures irrespective of mirror plate thickness, f_s, θ_{max} and D.

(a)

(b)

(c)

(d)
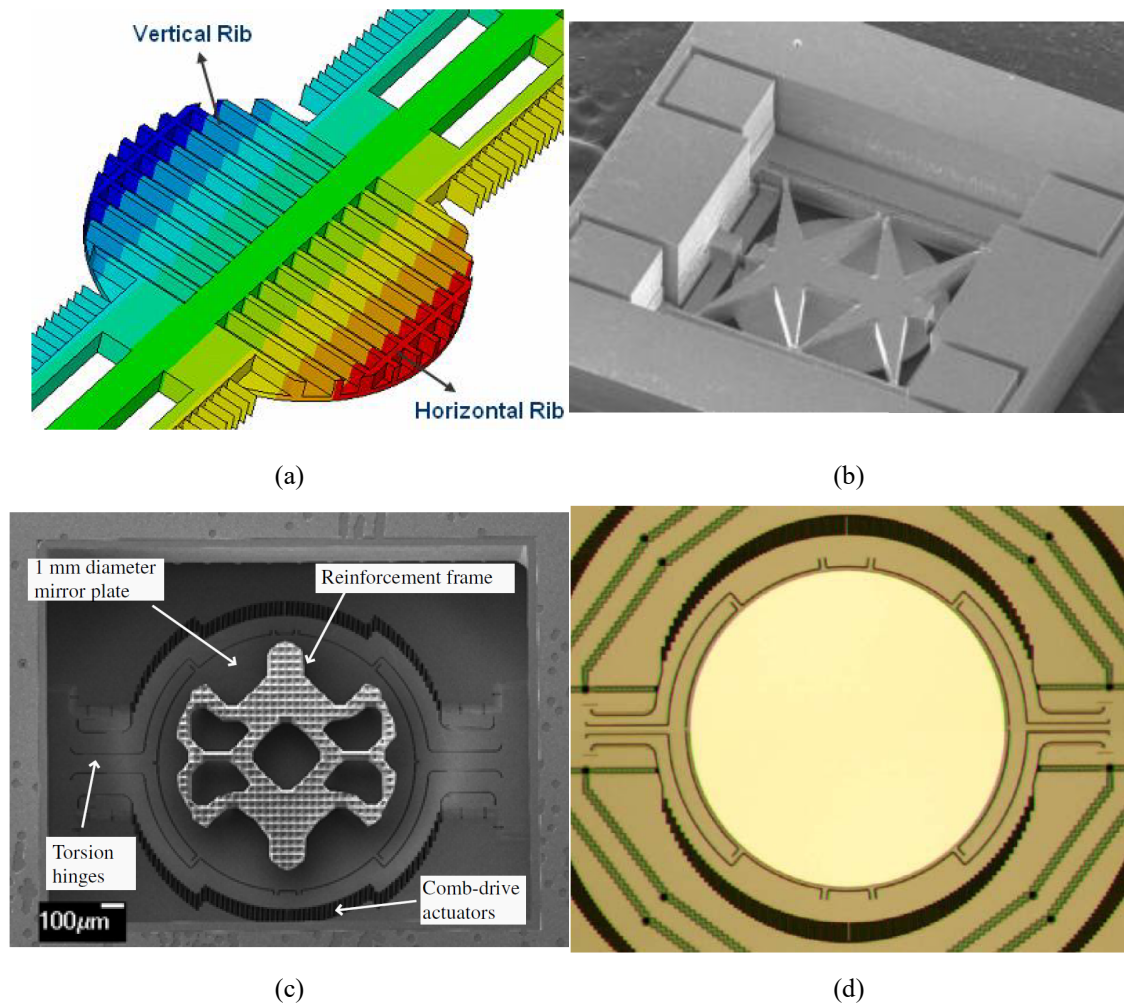
Figure 2-12: Different dynamic deformation mitigation techniques: (a) rib structure on the mirror backside [38], (b) star-shaped support back structure [60], (c) reinforcement island underneath the mirror plate [44], and (d) multiple-spring configuration with gimbal-type frame [56]

27

Table 2-3: Details of the normalized dynamic deformation for a number of high performance resonant micro-mirrors from literature presented in **Figure 2-8** and **Table 2-2**

Reference	Symbol	Actuation method	f_s (Hz)	θ_{max} (°)	D (mm)	t_m (μm)	R_{def}
[48]	◆	ES	24.75	12	1.2	30	0.008
[44]	▲	ES	30.8	10	1	30	0.027
[57]	□	ES	19.54	8.5	1.5	10	0.052
[66]	●	ES	38	12	1	75	0.082
[56]	✚	ES	16	8	1	30	0.112
[48]	■	EM	21	7.7	1.2	80	0.114
[65]	■	ES	30.8	21.5	0.8	60	0.119
[62]	✛	ES	24	5.5	2.2	280	0.135
[61]	△	ES	23.5	9.5	1.2	75	0.141
[70]	■	PE	40	6.9	1.4	125	0.201
[68]	○	PE	32	10.6	1	80	0.319
[52]	◆	PE	36	15	1	140	0.688
[37]	⬠	ES	34	6.3	0.55	50	0.707

2.7   Resonant Micro-Scanner Test Case

Prior to micro-scanner design and optimization, initial correlation tests between measurements and numerical simulations will be presented. Measurements were performed using a resonating micro-scanner designed and fabricated by ST Microelectronics (STM) for micro-display applications. In order to perform two-dimensional laser scanning, STM proposes a system that incorporates two single-axis micro-mirrors in an optical projection engine [9] as shown in **Figure 2-13**. With this method, one micro-mirror is actuated at the resonant frequency of its fundamental torsional mode in order to generate a horizontal scan, while the second micro-mirror is driven at a low frequency for vertical scanning.

The micro-mirror designed by STM for horizontal laser beam scanning is illustrated in **Figure 2-14**. It features a circular mirror plate with a radius, R of 530 μm which is driven in out-of-plane rotational oscillations at the torsional modal frequency of 21.5 kHz. The micro-scanner is electrostatically actuated via angular vertical comb (AVC) structures and all comb fingers are etched from the mirror-plate layer. The scanning micro-mirror is designed to operate at a scan angle amplitude, θ_{max} of 12° at a drive voltage amplitude

of 200 V. The definition of the dimensional parameters relevant to the analyses presented in Chapters 3, 4 and 5 is listed in **Table 2-4** and depicted in **Figure 2-15**.
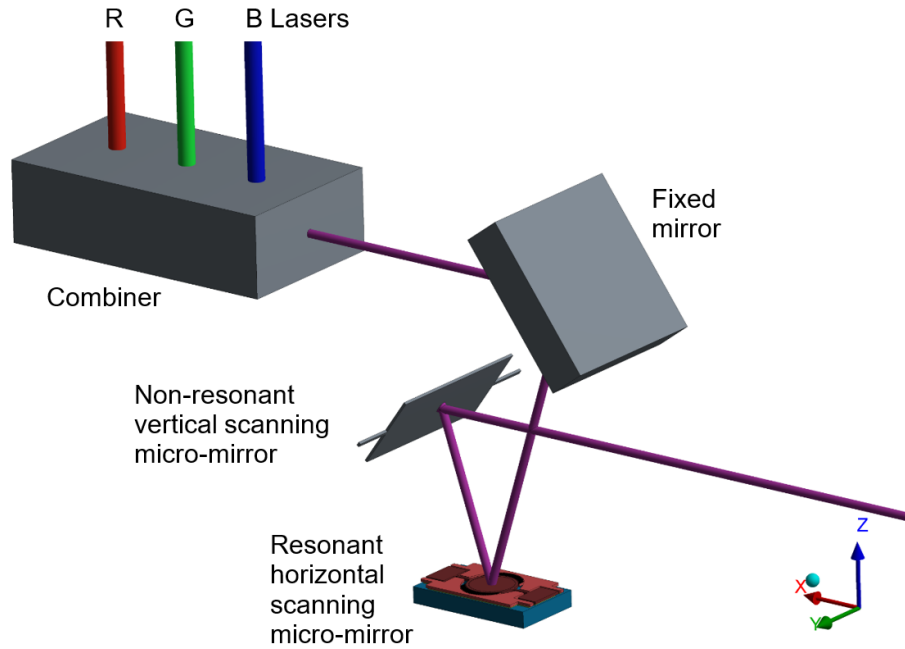
Figure 2-13: Schematic diagram of a laser scanning display system consisting of resonant and non-resonant micro-mirrors for horizontal and vertical scanning respectively
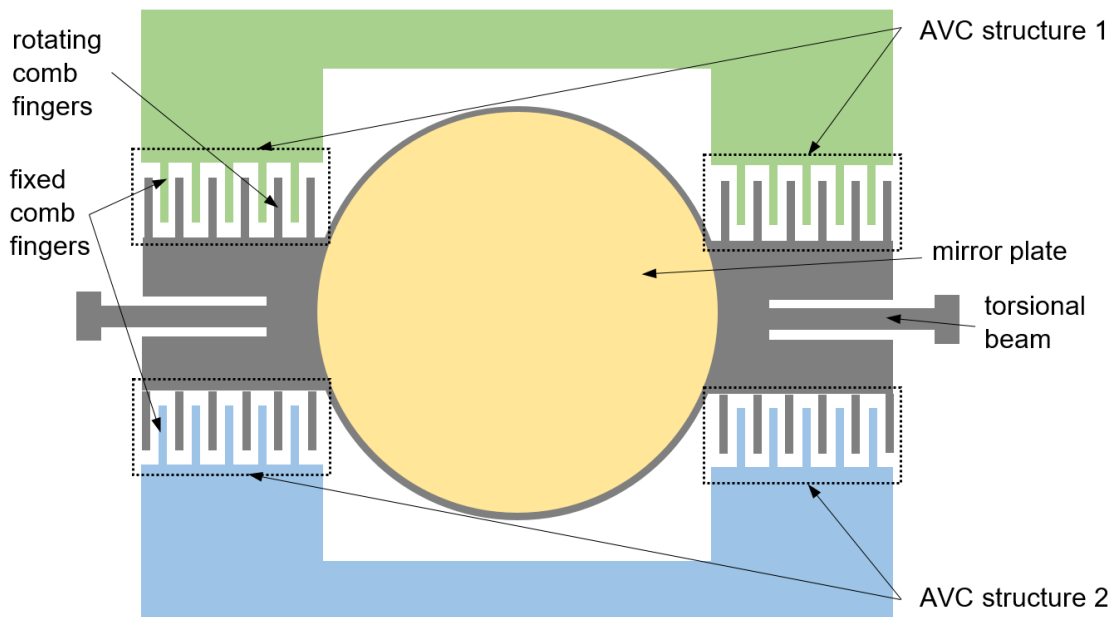
Figure 2-14: Illustration of the scanning micro-mirror designed by ST Microelectronics to operate at f_r = 21.5 kHz, θ_{max} = 12° at a drive voltage amplitude of 200 V [not to scale]

Table 2-4: Specifications and dimensions of scanning micro-mirror under test

Symbol	Description
R	mirror plate radius
t_m	mirror layout thickness
f_l	comb finger length
f_r	comb finger position relative to the rotational axis
f_o	comb finger offset
f_g	comb finger gap
N	number of comb fingers
h	cavity depth below the moving structure
l_s	torsional beam/spring length
w_s	torsional beam/spring width
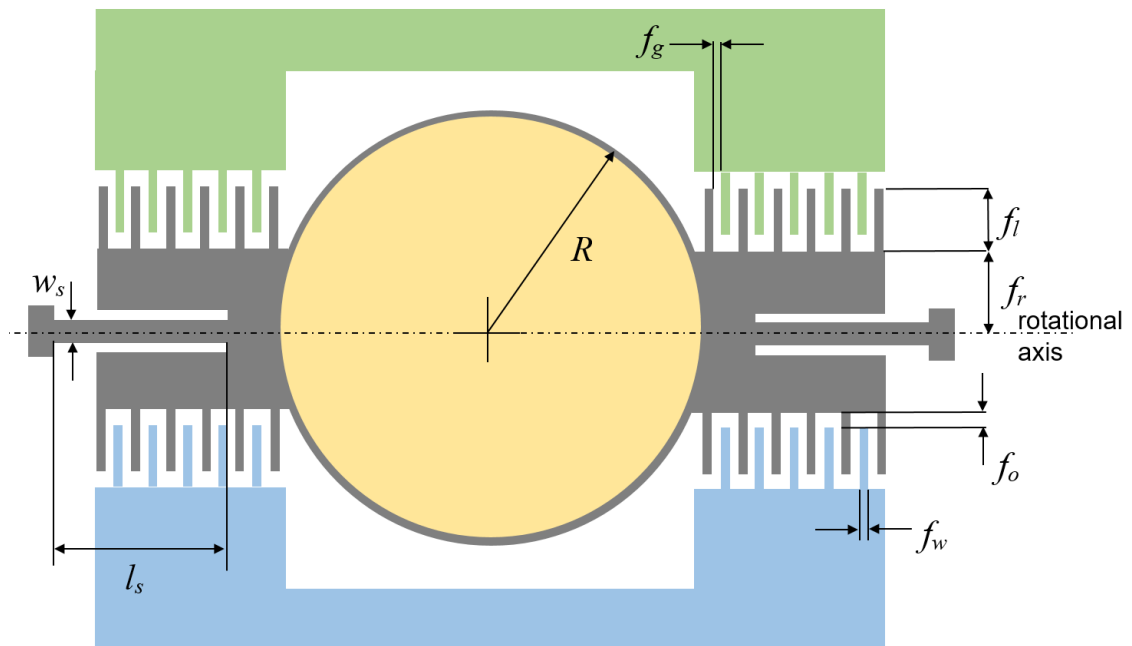
Figure 2-15: Geometrical properties of the AVC structure driving the STM resonant micro-mirror

The fabrication process consists of anodic bonding of two wafers to form a silicon-on-insulator (SOI) structure. Prior to anodic bonding, a cavity is formed via deep reactive ion etching (DRIE) from the bottom silicon wafer, which is then oxidised. After anodic bonding, the top wafer is thinned to a thickness, t_m of 65 µm and an aluminium (Al)-based layer is deposited and patterned to form the electrical contact pads and the mirror surface. A 2 µm layer is etched from fixed comb fingers of *AVC structure 1,* providing the necessary electrostatic force asymmetry to initiate out-of-plane scanning from the rest position. The suspended mirror and comb structures are then released by DRIE. A cross-sectional view demonstrating the process layers of the final micro-scanner device is shown in **Figure 2-16**.

Although the 200 nm thick Al-alloy reflective layer has a negligible effect on the dynamic mechanical performance of the micro-scanner, it induces stresses in the underlying mirror structure. Such process-related residual stresses negatively affect the static planarity of the mirror surface, especially in the case where additional dielectric coatings are added to improve the reflectivity [66]. However this process has been optimized in order to minimize the static deformation, arising from the reflective material composition, to a few tens of nanometres (for a circular micro-mirror with $R = 530$ µm) while ensuring high reflectivity [9].
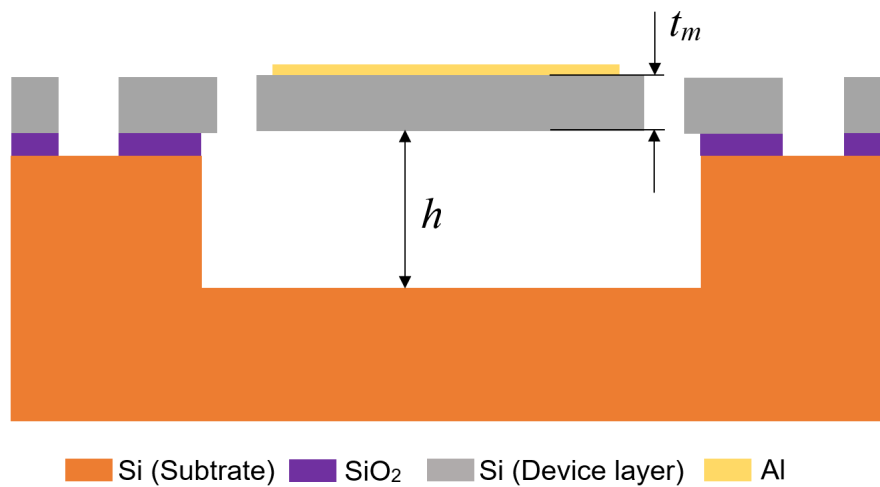
Figure 2-16: Layer cross-section of the STM resonating micro-scanner [not to scale] [9]

3   TORSION BEAM MECHANICS

Resonating micro-scanners fabricated using silicon-on-insulator (SOI) technology exploit the superior mechanical properties of monocrystalline silicon. Silicon is a brittle material exhibiting no plastic deformation at room temperature. In the absence of localised stress concentrations, which promote crack initiation, monocrystalline silicon is not prone to fatigue. In scanning micro-mirror designs, torsional springs are the most stressed components and hence, their reliability is crucial. The STM micro-scanner of **Figure 2-14** consists of straight torsion beam members with curved ends to minimize local stress peaks. The stiffness of torsion micro-beams in high-frequency resonating micro-scanners is typically assumed linear and can be deduced indirectly from dynamic measurements. However, non-linearity in the moment-angular displacement relationship of torsional silicon micro-beams has never been directly measured.

In this chapter the following research outcomes are presented:

- measurements of the linear and non-linear mechanical stiffness properties using a micro-force probing station
- comparison of measurements with analytical and finite element (FE) simulation results
- determine validity of assumptions considered in the analytical calculations
- determine the most appropriate FE model set-up for a micro-scanner design optimization set-up
- stress and failure mode analysis of the torsion beams

In Section 3.2, a theoretical evaluation of the torsional stiffness and maximum shear stress in non-circular beams is presented. Simulation results from the micro-scanner FE model are analysed in Section 3.3 followed by a discussion on the measurement set-up in Section 3.4. The analyses presented in the following sections are based on the STM resonating micro-mirror. The dimensions of the torsion beams are provided in **Table 2-4**. The structural analyses in this chapter will provide important guidelines in the design optimization process of the micro-scanner prototypes presented in Chapter 8.

3.1   **Fracture Criterion**

If we consider the 2-D material elemental plane of **Figure 3-1**, normal and shear stresses can be described in terms of principal stresses, which define the limits of the Mohr's stress circle [99]. Along the principal plane, which makes an angle ϕ with the vertical axis, the elemental shear stress is zero. The elemental maximum, minimum principal stresses (σ_1 and σ_2) together with ϕ and the elemental maximum shear stress, τ_{max} are defined in (3.1), (3.2) and (3.3) respectively. In the case of a pure torsion load, σ_1 is equivalent to τ_{max}.

$$\sigma_{1,2} = \frac{\sigma_x + \sigma_y}{2} \pm \frac{1}{2}\sqrt{\left[\left(\sigma_x - \sigma_y\right)^2 + 4\tau_{xy}^2\right]} \tag{3.1}$$

$$\tan 2\phi = \frac{2\tau_{xy}}{\sigma_x - \sigma_y} \tag{3.2}$$

$$\tau_{max} = \frac{1}{2}\left(\sigma_1 - \sigma_2\right) \tag{3.3}$$
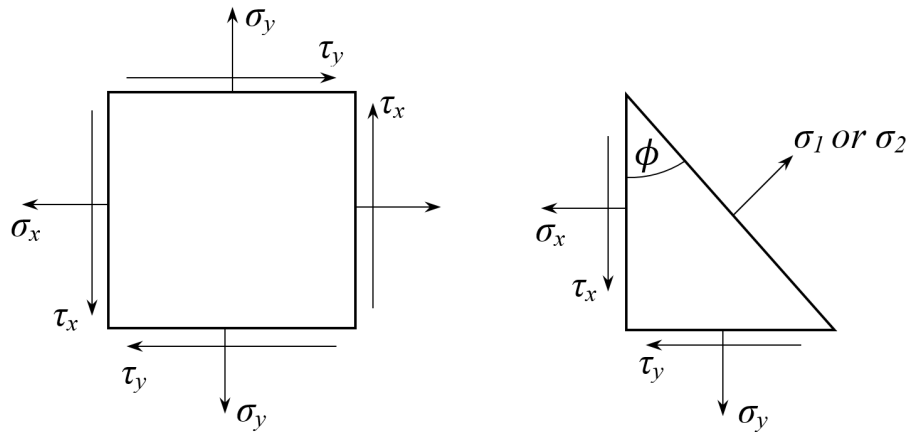
Figure 3-1: Stress components on a two-dimensional element (plane stress system)

Since mono-Si is brittle, the maximum principal stress (or Rankine) criterion can be applied which states that failure occurs at the instance when σ_1 reaches the stress at 'failure' in simple tension [100]. Failure through brittle fracture is governed by the rupture of Si-Si bonds at the tip of a micro-crack. Therefore, the probability of failure is dependent on the quantity and type of defects present in the microstructure. Consequently the tensile and shear strength in mono-Si are highly dependent on the specific technology used for microfabrication.

The standard three-point bending test has been commonly used to obtain the flexure strength of Si dies [101]. However, no standard test methods have been performed to evaluate the critical stress of Si thin films under pure torsion. Dynamic optical measurements have been published by Wolter *et al.* [102] on a micro-scanner design with simple torsion beams (no curved ends). The maximum scanning angle prior to failure is obtained by operating the micro-scanner at resonance in reducing air pressure conditions [103]. The measurements demonstrated a lower tensile strength of the Si torsion beam (1.4 GPa) compared to standard bending testing (2.2±1.2 GPa). In general, τ_{max} is the critical stress component for low rates of twist ($\theta/l_s < 0.1°/\mu m$). For higher torsional angles, the effect of torsion beam end constraints is not negligible and normal stresses at the torsion beam fixed end become predominant.

3.2   Theoretical Evaluation

Analytical evaluation of stresses and strains in the torsion beam of **Figure 3-2** can be deduced from theory of elasticity by considering the following assumptions:

1) the torsion beam is straight with a uniform cross-section;
2) the torsion beam is loaded only by equal and opposite twisting couples applied at the ends in the *y-z* plane;
3) cross-sections in the *y-z* plane rotate as a rigid body;
4) the rate of twist is constant along the beam length;
5) the torsion beam is composed of a homogenous isotropic material and is stressed below the elastic limit.
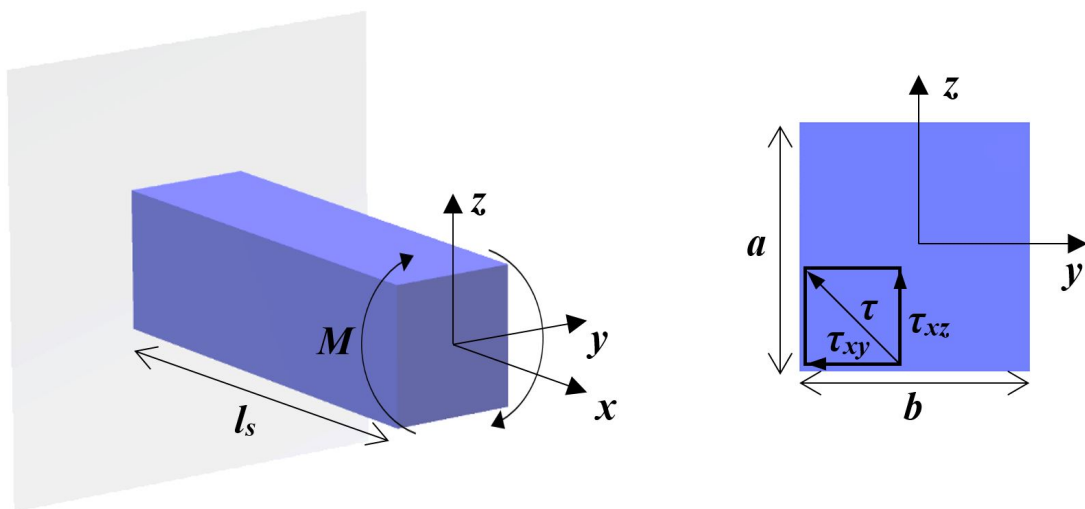
Figure 3-2: Torsion beam (orientation and relevant notations)

Torsional members with non-circular cross-section undergo twist about the x-axis with a rate of twist θ/l_s, together with deflection in the x-direction, or warp, described by the deflection function: $\varphi(y,z)$. Under the action of pure torsion the stress components can be defined as follows [104]:

$$\sigma_x = \sigma_y = \sigma_z = \tau_{yz} = 0$$

$$\tau_{xy} = \frac{G\theta}{l_s}\left(\frac{\partial\varphi(y,z)}{\partial y} - z\right) \tag{3.4}$$

$$\tau_{xz} = \frac{G\theta}{l_s}\left(\frac{\partial\varphi(y,z)}{\partial z} + y\right)$$

where G is the shear modulus and l_s is the beam length. The applied torque M, can be defined in terms of the stress tensor, τ:

$$M = \iint\left(-\tau_{xy}z + \tau_{xz}y\right)dydz \tag{3.5}$$

Equation (3.5) can be simplified to (3.6) in terms of the torsional stiffness, k_s, which is defined in (3.7):

$$M = k_s\theta \tag{3.6}$$

$$k_s = \frac{GK}{l_s} \tag{3.7}$$

For circular cross-sections, the torsion factor K is the polar moment of inertia J_s. However, in the case of non-circular sections, the assumption that cross-sections remain plane (i.e. normal to the torsional axis) during torsion is not valid, as shown in **Figure 3-3**. Warping in non-circular cross-sections is primarily caused by a non-constant angular and non-linear radial distribution of the shear stress along the section as shown in **Figure 3-4**. For rectangular cross-sections with dimensions a and b such that $a > b$, a solution for K has been derived by Timoshenko and Goodier [104], as shown in (3.8). Additionally, the maximum shear stress is given by (3.9) and occurs at the centre of the longer side of the cross-section, a. These solutions are valid for the condition that no end constraints are applied such that warping is not prevented. The inclusion of end constraints provides a degree of warping restraint and contributes to an increase in the overall torsional stiffness.

$$K = \frac{ab^3}{3}\left(1 - \frac{192b}{\pi^5 a}\sum_{n=1,3,5}^{\infty}\frac{1}{n^5}\tanh\left(\frac{\pi a}{2b}\right)\right) \tag{3.8}$$

$$\tau_{max} = \frac{4G\theta b^2}{\pi^2}\left(\sum_{n=1,3,5}^{\infty}\frac{1}{n^5}\frac{1}{\cosh\left(\frac{n\pi a}{2b}\right)}\right) \tag{3.9}$$
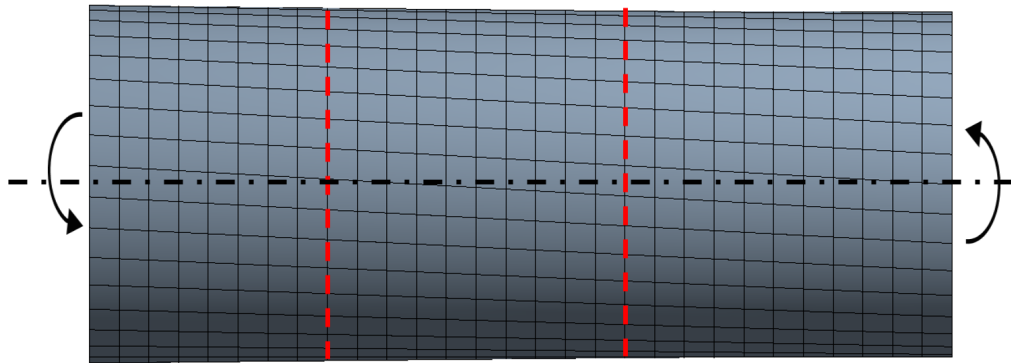
(a)
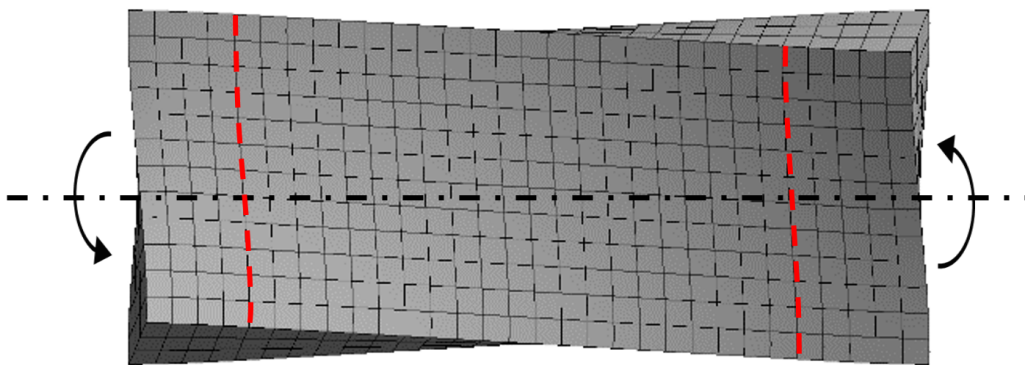
(b)

Figure 3-3: Twisting and warping in torsional members with (a) circular and (b) rectangular cross-sections
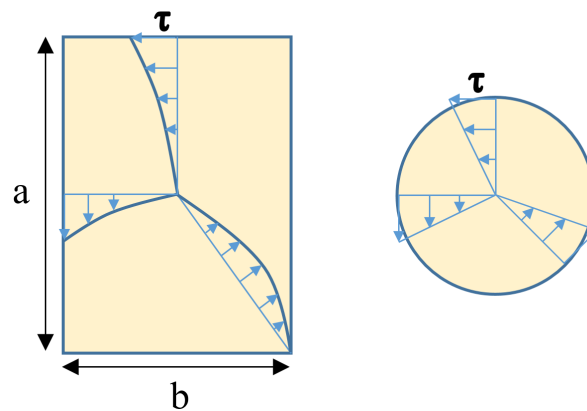
Figure 3-4: Angular and radial shear stress distribution along cross-section due to a pure torsion load

Simplified approximate forms of (3.8) and (3.9) are provided by Young and Budynas [105] ((3.10) and (3.11) respectively) with a resulting error of less than 4%.

$$K_{roark} = \frac{ab^3}{3}\left(1 - 0.63\frac{b}{a}\left(1 - \frac{b^4}{12a}\right)\right)$$ (3.10)

$$\tau_{max,roark} = \frac{3M}{2ab^2}\left[1 + 0.6095\left(\frac{b}{a}\right) + 0.8865\left(\frac{b}{a}\right)^2 + 1.8023\left(\frac{b}{a}\right)^3 + 0.91\left(\frac{b}{a}\right)^4\right]$$ (3.11)

On the other hand, values for K (3.12) and τ_{max} (3.13) in terms of constants β and α respectively are given by Ugural and Fenster [106]. The constants β and α can be obtained from a look-up table for a number of discreet cross-sectional aspect ratios.

$$K_{ugural} = \beta ab^3$$ (3.12)

$$\tau_{max,ugural} = \frac{M}{\alpha ab^2}$$ (3.13)

For the beam dimensions of **Table 2-4**, the torsional stiffness and maximum shear stress at an angle of twist of 12° are listed in **Table 3-1**.

<p align="center">**Table 3-1**: Theoretical k_s and τ_{max} for the STM resonating micro-mirror</p>

Young's Modulus, E	169 GPa
Poisson ratio, v	0.23
Shear Modulus, G	68.7 GPa
k_s (Nm/rad) - [105]	2.1319×10^{-4} Nm/rad
k_s (Nm/rad) - [106]	2.1216×10^{-4} Nm/rad
τ_{max} at θ=12° - [105]	875.9 MPa
τ_{max} at θ=12° - [106]	870.6 MPa

3.3   Numerical Analysis

A FE model was developed using ANSYS to determine the mechanical stiffness and shear stress of the 21 kHz STM micro-scanner. An evaluation of a number of modelling and simulation methods is presented in this section. For this analysis, the torsional stiffness, k_s is obtained from a least-mean-squared fit of torque-twist angle simulation data. The goodness of fit is extracted via the root mean squared error as a percentage of full-scale (*nrmse*). The latter is an indication of geometric non-linearity in the torsion beams. These results will provide key information in the development of a FE-based design optimization scheme.

3.3.1   **Finite Element Type**

3-D solid elements with mid-side nodes (SOLID186) should provide the best result in terms of accuracy and level of solution detail. However, the high computational cost associated with the 20-node elements may not be feasible for parametric analysis and design optimization. Torsion beam stiffness results obtained using solid and lower order elements is provided in **Table 3-2**. The 8-node shell element (SHELL181) is suitable for analysing thin to moderately-thick shell structures under large rotation, non-linear applications [107]. Results indicate accurate stiffness predictions relative to solid elements with less than 1% difference in k_s. When compared to solid elements, shell elements are more compliant to bending leading to a marginal increase in the simulated stiffness non-linearity. While accurate displacement results are achieved, lower maximum shear stress magnitudes are obtained using the shell elements as shown in **Figure 3-5**. In the case of the STM micro-mirror, the layer thickness, t_m is larger than the width of the torsion beam, w_s, such that maximum shear stress is expected to occur at the mid-plane of the torsion beam thickness. This is confirmed in the maximum shear stress contour plot of **Figure 3-6** obtained using solid elements. The shear stress contour plot of **Figure 3-7**, obtained using shell elements is not in agreement with the solid element results. While shell elements are not appropriate for the torsion beam aspect ratio considered, **Figure 3-8** shows that 8-node solid-shell elements (SOLSH190) offer a feasible alternative towards achieving accurate and computationally efficient structural predictions of the micro-scanner.

Table 3-2: Comparison of torsion beam stiffness results obtained from three finite element types (ANSYS mechanical)

Element type	Torsion beam angle range for linear fit	k_s (Nm/rad)	% difference in k_s relative to solid elements	k_s non-linearity (% *nrmse*)
8-node shell (SHELL281)	$0 < \theta < 20°$	2.3628×10^{-4}	0.542	1.684
	$0 < \theta < 12°$	2.2531×10^{-4}	0.344	0.534
8-node solid-shell (SOLSH190)	$0 < \theta < 20°$	2.3730×10^{-4}	0.977	0.751
	$0 < \theta < 12°$	2.2779×10^{-4}	1.450	0.263
20-node solid (SOLID186)	$0 < \theta < 20°$	2.3500×10^{-4}	/	0.810
	$0 < \theta < 12°$	2.2453×10^{-4}	/	0.284
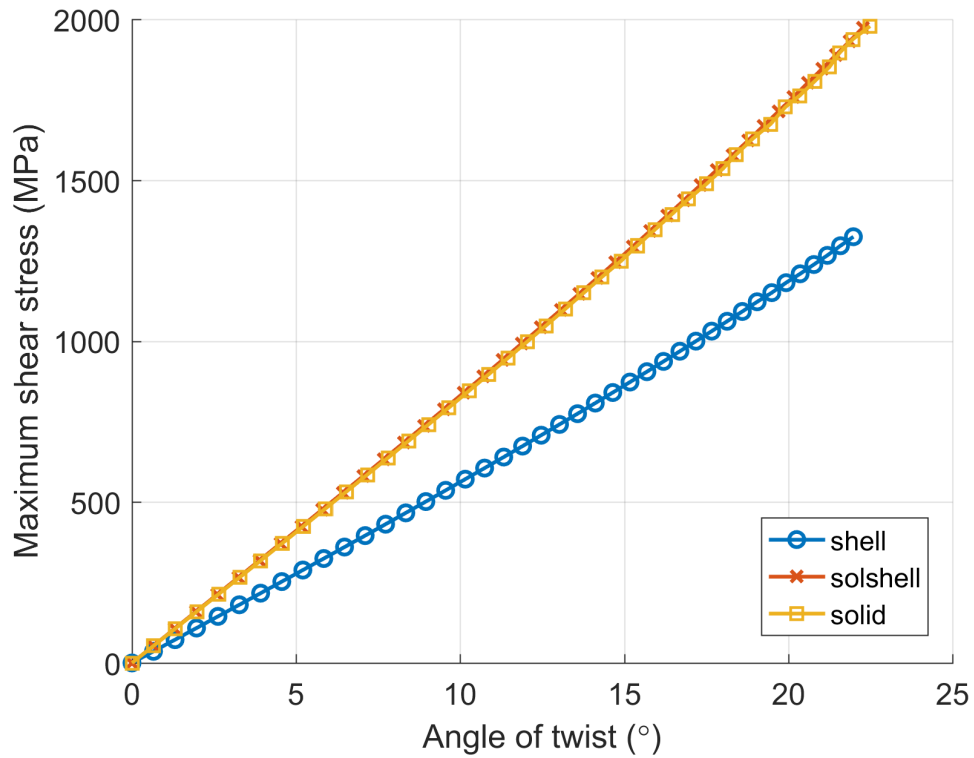
Figure 3-5: Maximum τ_{max} magnitude versus angle of twist of the torsion beam: comparison of FE simulation results obtained using SOLID186, SHELL281, SOLSH190 finite elements
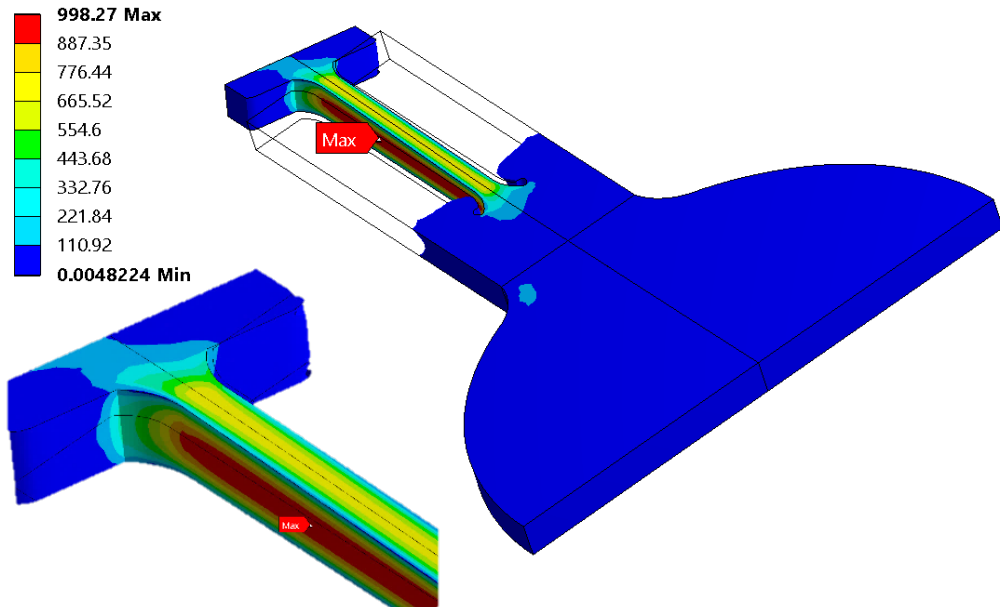
Figure 3-6: τ_{max} distribution at the outer surface of the torsion beam
(ANSYS SOLID186 elements, θ_{max}=12°) [units in MPa]

39
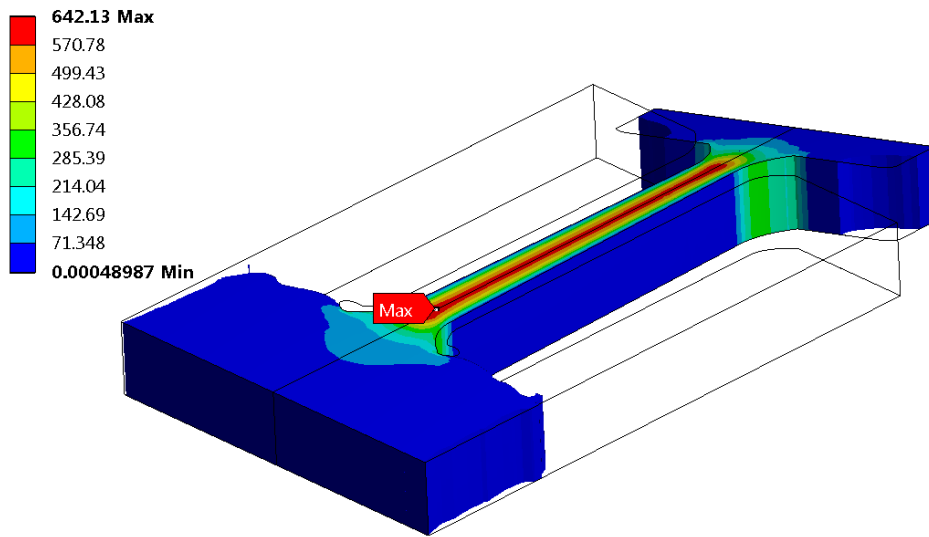
Figure 3-7: τ_{max} distribution at the outer surface of the torsion beam
(ANSYS SHELL281 elements, θ_{max}=12°) [units in MPa]
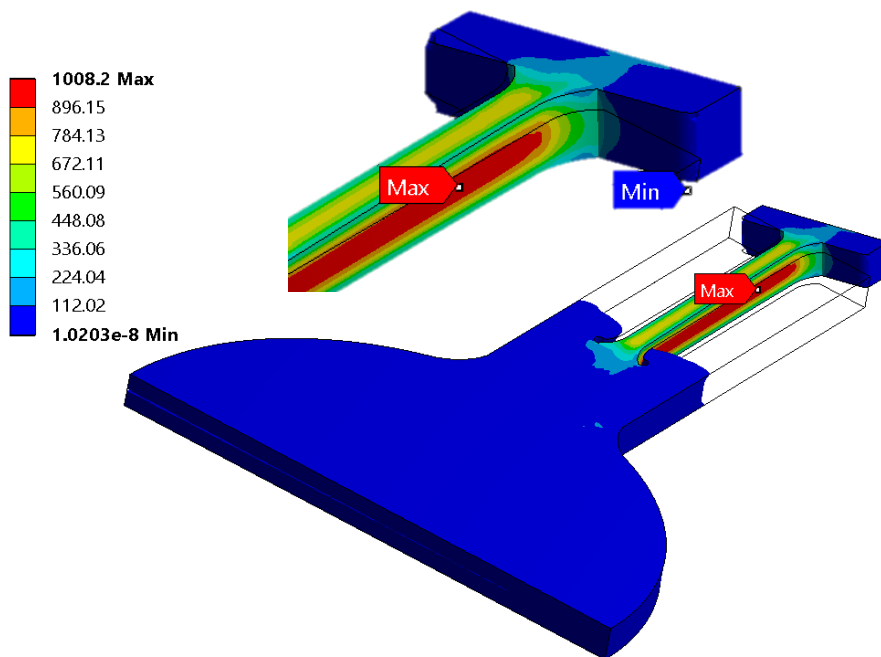
Figure 3-8: τ_{max} distribution at the outer surface of the torsion beam
(ANSYS SOLSH190 elements, θ_{max}=12°) [units in MPa]

3.3.2 Material Properties

The theoretical calculations for the torsion beam stiffness, presented in Section 3.2 are based on the isotropic material properties defined in **Table 3-1**. However mono-crystalline silicon has orthotropic elastic behaviour as shown in **Table 3-3**. The wafer orientation is such that the rotational axis of the micro-scanner is parallel to the plane of maximum elastic modulus. Simulation results of **Table 3-4** demonstrate a negligible difference in torsion beam stiffness between applied isotropic and orthotropic Si material properties.

Table 3-3: Orthotropic elastic properties of (100) silicon wafer in the [110] frame of reference [108]

E_x	E_y	E_z	v_{yz}	v_{zx}	v_{xy}	G_{yz}	G_{zx}	G_{xy}
169 GPa	169 GPa	130 GPa	0.36	0.28	0.064	79.6 GPa	79.6 GPa	50.9 GPa

Table 3-4: Effect of the elastic property definition in FE simulations on the torsion beam stiffness results (ANSYS mechanical)

Silicon elastic properties	k_s (Nm/rad)	% Δk_s	k_s non-linearity (%$nrmse$)
Isotropic	2.2613×10^{-4}	0.585	0.488
Orthotropic	2.2482×10^{-4}		0.496

3.3.3 Geometric Non-Linearity

The effect of geometric non-linearity on the torsion beam stiffness is taken into account in ANSYS by activating the large strain analysis which, takes into account changes to the element shape and orientation due to loading. **Table 3-5** indicates that the mirror displacement is over predicted when non-linear geometric effects are not considered in the FE simulation. Torsion beam warp discussed in Section 3.2 is significant for angular displacements higher than 12° leading to an increase in magnitude and non-linearity in the torsion beam stiffness. This implies that stress stiffening as a result of geometrical non-linearities have to be considered in subsequent structural FE simulations.

Table 3-5: Effect of geometric non-linearities on the torsion beam stiffness

Geometric non-linearities	$0 < \theta < 20°$			$0 < \theta < 12°$		
	k_s (Nm/rad)	% Δk_s	k_s non-linearity (% $nrmse$)	k_s (Nm/rad)	% Δk_s	k_s non-linearity (% $nrmse$)
included	2.3628×10^{-4}	7.006	1.684	2.2531×10^{-4}	2.183	0.534
not included	2.1972×10^{-4}		0.100	2.2039×10^{-4}		0.034

3.3.4   Load Application Method

Under pure torsional loading, the magnitude and location of the highest σ_1 and τ_{max} are expected to be equivalent barring slight deviations due to the effect of end constraints and geometric non-linearity. This can be observed in **Figure 3-9**, where a moment is generated by two equal forces acting in opposite directions and applied at opposite ends of the mirror plate. However, a single point force can be applied with the microforce probing measurement method, discussed in Section 3.4. The combined torsion and bending resulting from the unbalanced loading method (see **Figure 3-14**) introduces a normal stress (σ_x) to the torsion beam. For the same applied moment, elevated stresses can be observed in **Figure 3-10** compared to the balanced loading method. Moreover, the location of peak σ_1 does not coincide with that of peak τ_{max}. This implies that although the torsion beam stiffness can be measured using the micro-force probing experiment (see **Table 3-6**), this experimental technique will not yield an accurate indication of the maximum shear stress at failure and fracture mode which occur during dynamic loading conditions.

Table 3-6: Effect of the loading method in FE simulations on the torsion beam stiffness results

Load application method	k_s (Nm/rad)	% Δk_s
balanced points forces	2.2482×10^{-4}	0.217
unbalanced point forces	2.2531×10^{-4}	

(a)

(b)
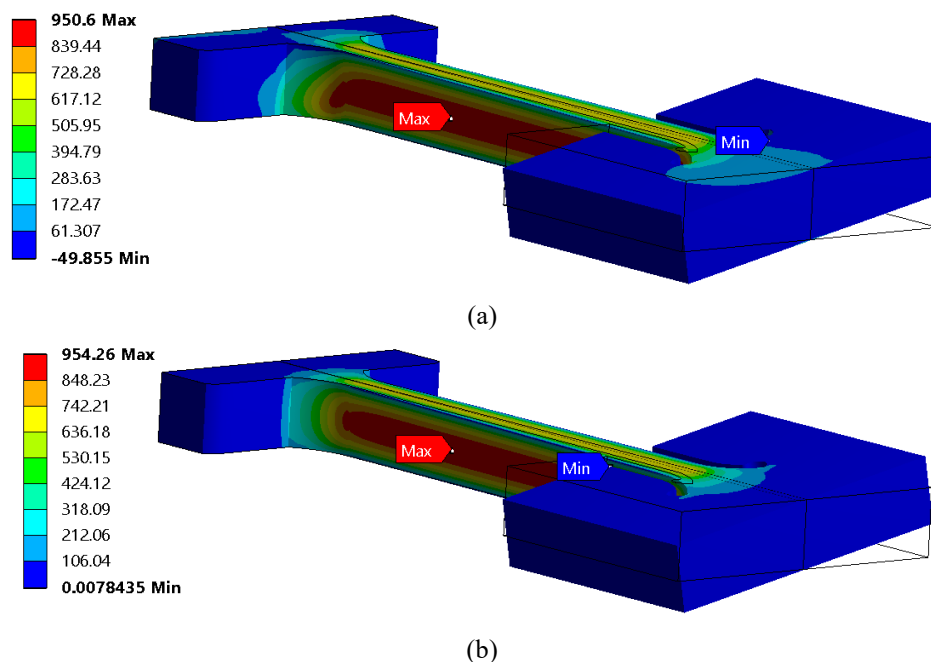
Figure 3-9: Stress on the micro-scanner torsion beam at a $\theta = 12°$ from FE model with solid elements and balanced force loading: (a) σ_1 and (b) τ_{max} [units in MPa]

(a)

(b)
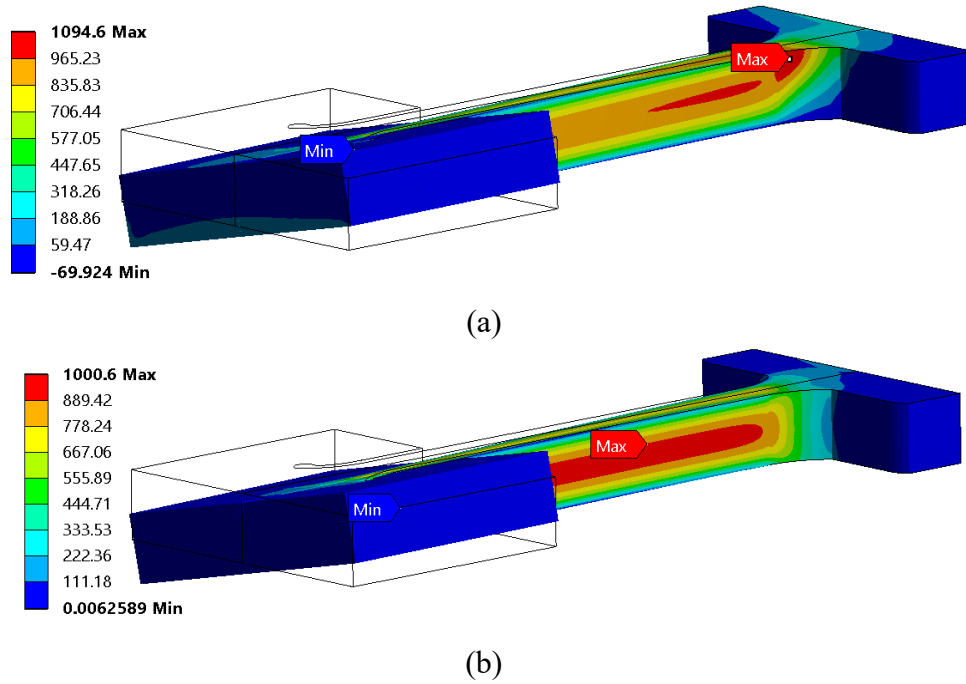
Figure 3-10: Stress on the micro-scanner torsion beam at a $\theta = 12°$ from FE model with solid elements and unbalanced force loading: (a) σ_1 and (b) τ_{max} [units in MPa]

3.4   Micro-Force Probing Measurements

Force-position measurements were performed using the FemtoTools micromechanical probing system, detailed in **Table 3-7**, in order to deduce the torsion beam stiffness of the STM micro-scanner of **Figure 2-14**. The FT-RS 1002 microrobotic system (**Figure 3-11**) consists of a piezoelectric manipulation unit with integrated optical encoders allowing for displacement and position sensing of the force probe along three axes. The force applied by the moving robotic arm is acquired from an electrostatic comb driven MEMS structure, which forms part of the FT-S100000 micro-force sensing probe (**Figure 3-12**).

Table 3-7: Micromechanical Probing system specifications [109]

FT-RS 1002 Microrobotic System	
Actuation principle	Piezoelectric stepping
Actuation range	26 mm x 26 mm x 26 mm
Minimum motion increment	50 nm
Maximum velocity	5mm/s
Optical encoder resolution	1 nm
FT-S100000 Microforce Sensing Probe	
Sensing principle	Electrostatic comb drive
Force Range	± 0.1 N
Resolution	5 µN
Contact area	50 x 50 µm
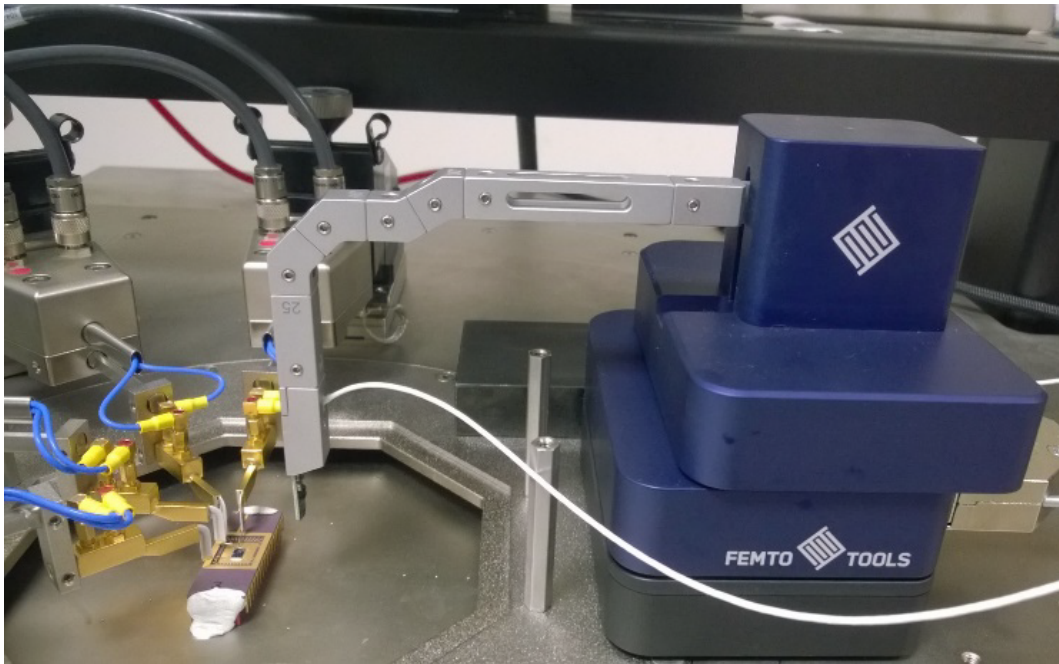
Figure 3-11: FemtoTools MicroMechanical Testing Station installed
on the Cascade MicroProbing Station
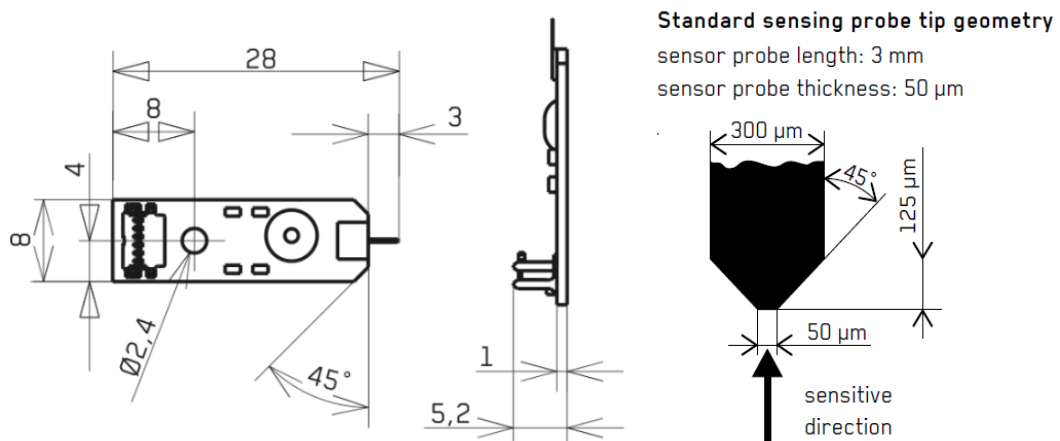
Figure 3-12: MicroForce Probe (FT-S100000) dimensions; (Force range ±100000μN; Resolution: 5μN)
(Dimensions in mm unless otherwise specified)

The micromechanical probing system was installed on a Cascade Microscope station (**Figure 3-11**) in order to determine the location of contact between the force-sensing probe and the mirror surface. The contact point was positioned as close as practically possible to the edge of the reflective mirror surface, as shown in **Figure 3-13**, in order to achieve micro-mirror rotation with minimal out-of-plane torsion beam bending and without exceeding the allowable force probe range (0.1 N). The micro-mirror was assumed rigid such that the angle of twist along the mirror rotation axis is constant and equal to the maximum angle of twist of the torsion beam.
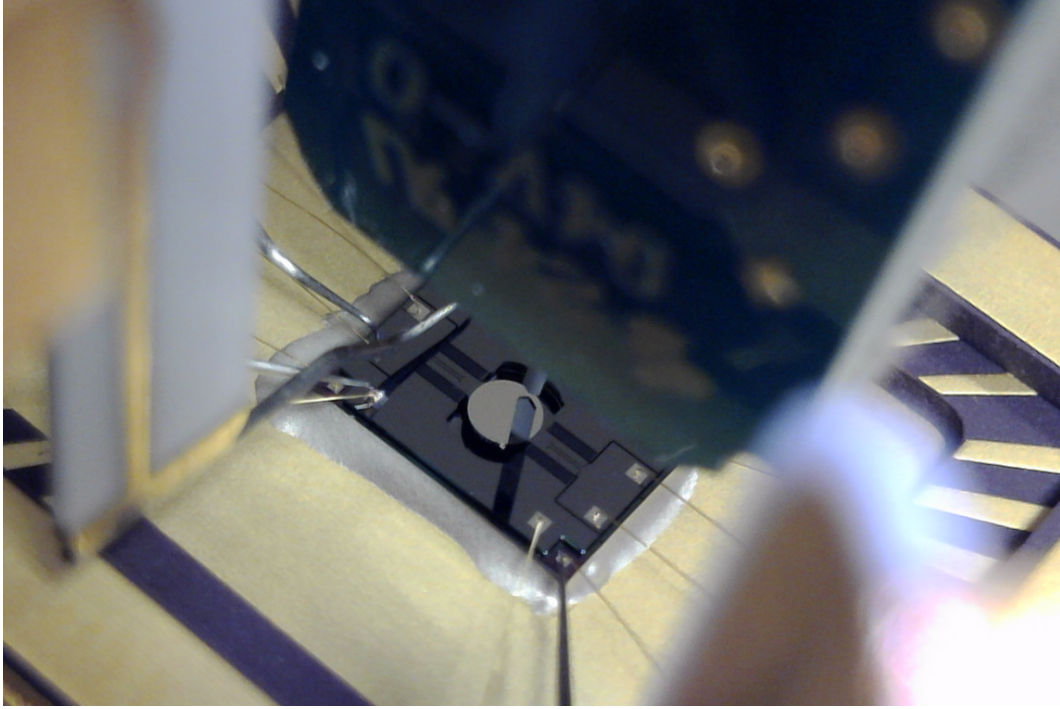
Figure 3-13: MicroForce Probe (FT-S100000) point of contact on micro-mirror surface

The single vertical load, *F*, applied by the micro-force probe imparts a combination of torsion and bending to the beam members. In order to quantify the degree of beam bending, the vertical deflection at the centre of the mirror surface, δ_0 (**Figure 3-14**), was measured using the optical microscope having a high precision z-scale (1 μm resolution). The angle of mirror rotation about the x-axis was deduced from the difference between the force probe vertical displacement, δ_1 and δ_0. The torsional stiffness, k_s was deduced from a linear fit of equation (3.14).

$$Fx = k_s \sin^{-1}\left(\frac{\delta_1 - \delta_0}{x}\right)$$

(3.14)
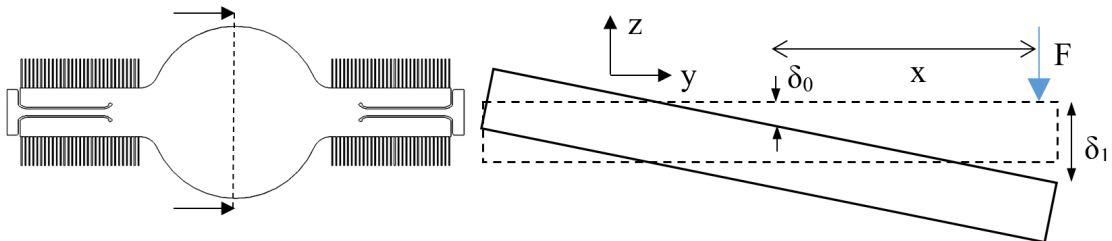
Figure 3-14: Measured force, F and displacements, δ_0 and δ_1

The results from micromechanical probing measurements are listed in **Table 3-8.** Bi-directional displacement sweeps were performed with 0.1 μm increments and a speed of 0.1 μm/s. Due to the highly polished aluminium mirror surface, lateral slip of the force probe was observed during the initial measurement run. However, the surface scratches introduced by the contacting force probe provide enough friction to eliminate lateral probe bending during successive measurement runs. The torsional stiffness results are repeatable with slightly higher values observed in the downward displacement direction. **Figure 3-15** shows a predominant linear k_s up to a mirror rotational angle of 9.5°. A non-zero angle of twist at the end of the displacement sweep (see **Figure 3-16**) does not suggest a permanent deformation of the torsion beam but is an indication of: (i) initial force readings due to small mirror vibrations prior to actual probe contact and (ii) weak stiction forces upon release of the force probe from the mirror surface. The degree of stiffness non-linearity as a percentage of the maximum measured torque is plotted in **Figure 3-17**.

Table 3-8: Torsion beam stiffness measurement results

measurement run	maximum measured force (μN)	displacement sweep direction	k_s (Nm/rad)	k_s non-linearity (%*nrmse*)
Run 1	25941.11	down	2.1259×10^{-4}	1.109
		up	2.0962×10^{-4}	2.138
Run 2	61472.54	down	2.0684×10^{-4}	0.699
		up	2.0000×10^{-4}	1.076
Run 3	79104.43	down	2.0380×10^{-4}	0.427
		up	2.0000×10^{-4}	1.893
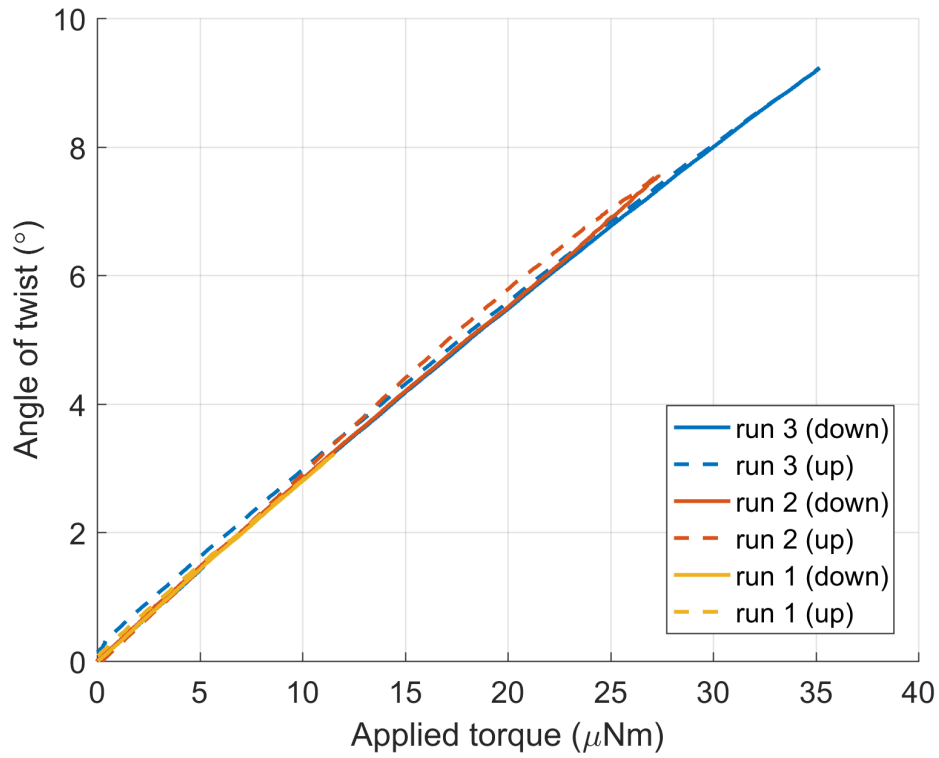
Figure 3-15: Measured angle of twist versus applied torque
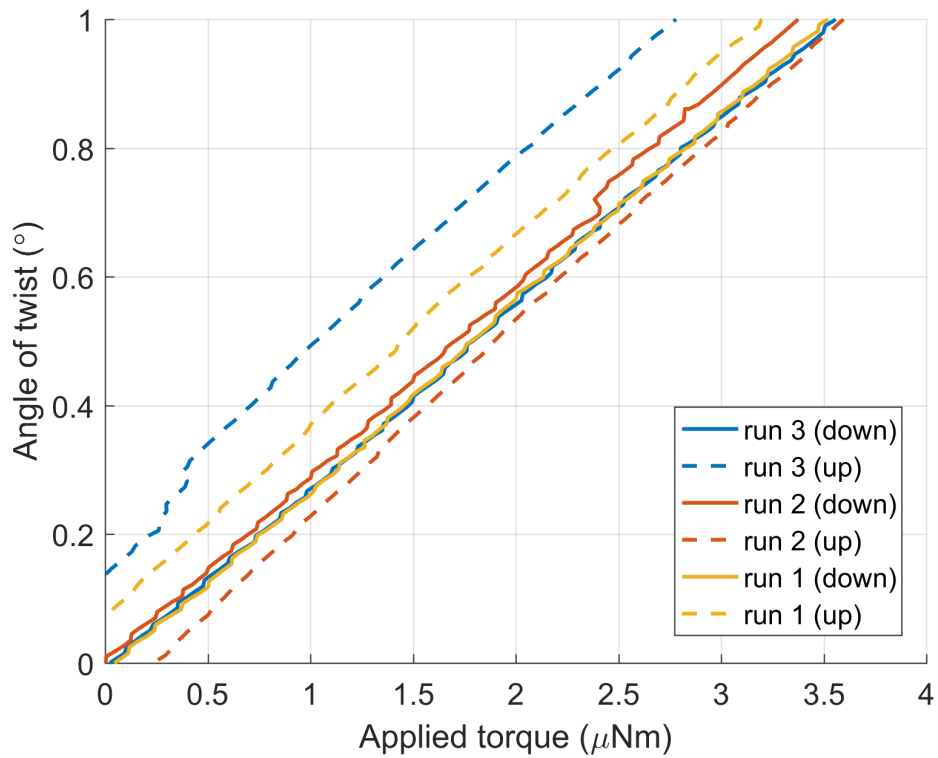
Figure 3-16: Measured angle of twist versus applied torque (small angles)
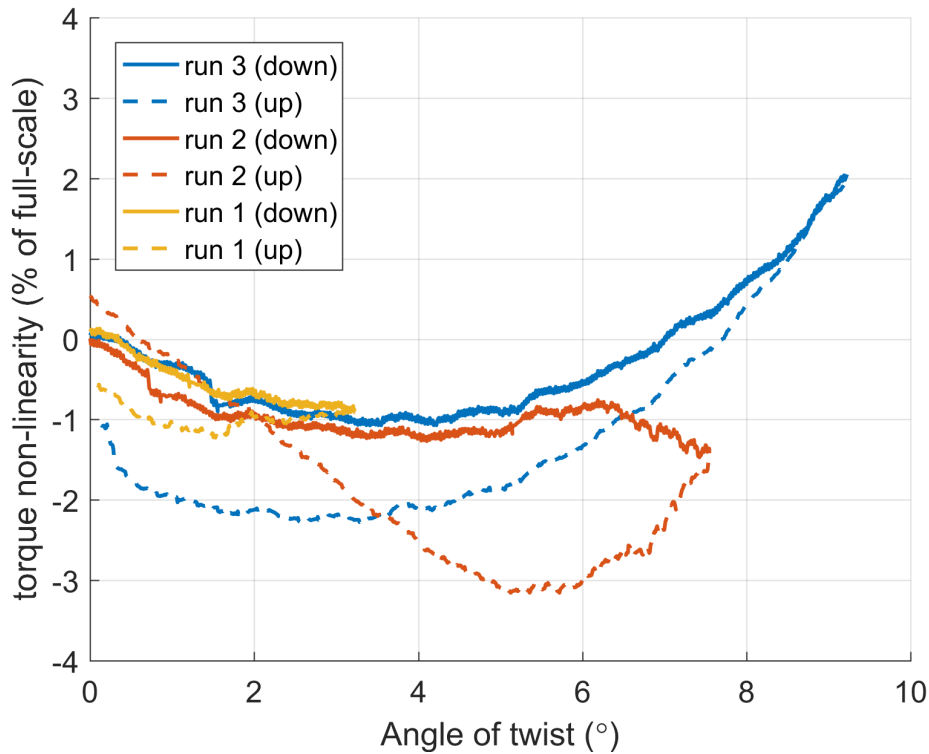
Figure 3-17: Measured variation of torque non-linearity with angle of twist

3.5   Results Comparison

A summary of results for the magnitude and non-linearity of the micro-scanner stiffness is presented in **Table 3-9** and **Figure 3-18**. The analytical and numerical predictions are within 10% of the measurement results. FE simulation results indicate that the effect of bending due to the unbalanced loading method employed in the experimental procedure has a negligible impact on the torsion stiffness evaluation. The fillet radii at the ends of the torsion beam are not considered in the analytical calculations and is potentially the cause leading to a lower k_s compared to the numerical simulations. Measurement and simulation results demonstrate the stiffness non-linearity of the torsional beam is less than 2% of the maximum θ. **Figure 3-19** indicates that FE simulations under predict the stiffness non-linearity, however lateral bending of the microforce probe or a degree of non-linearity in the electromechanical sensor transduction may accentuate the measured stiffness non-linearity.

Table 3-9: Torsion beam stiffness: result comparison

Method	k_s (Nm/rad)	k_s non-linearity (%*nrmse*)
Analytical	2.1319×10^{-4}	/
Measurements	2.0380×10^{-4}	1.893
FE Simulations	2.2531×10^{-4}	0.534
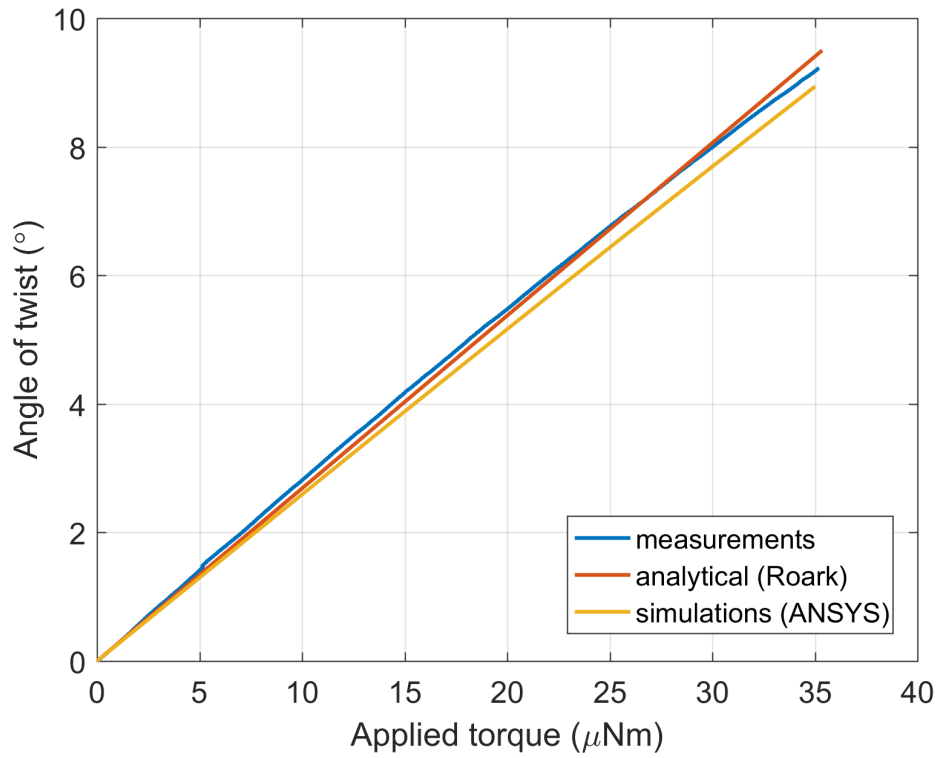
Figure 3-18: STM micro-scanner: Moment-angular displacement profile
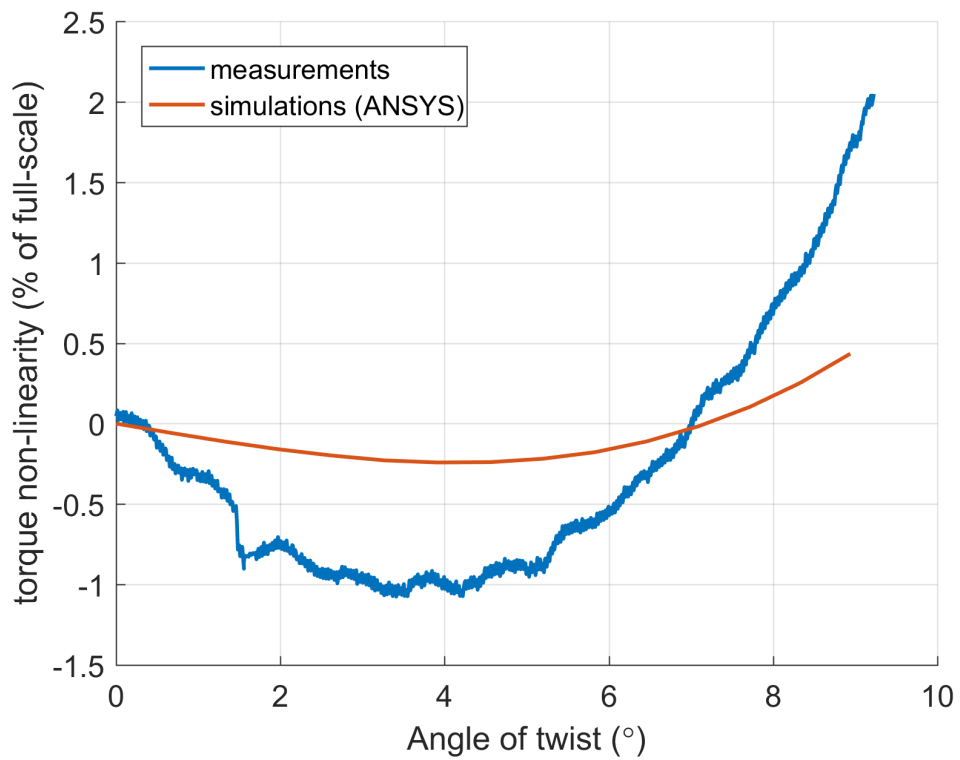
Figure 3-19: STM micro-scanner: Angular variation of the torque non-linearity

49

The stiffness non-linearity translates into a non-linear shear stress increase with angular displacement. The non-constant deviation between numerical and analytical τ_{max} predictions is shown in **Figure 3-20**. The allowable shear stress beyond which torsional beam failure may occur, i.e. τ_{crit} is 1.4GPa [102]. The FE model constructed using SOLID186 elements predicts that τ_{crit} is reached at a mirror-scanner angle of 16.5°. On the other hand, the critical angle deduced from the analytical equation of (3.13) is 19.3°.
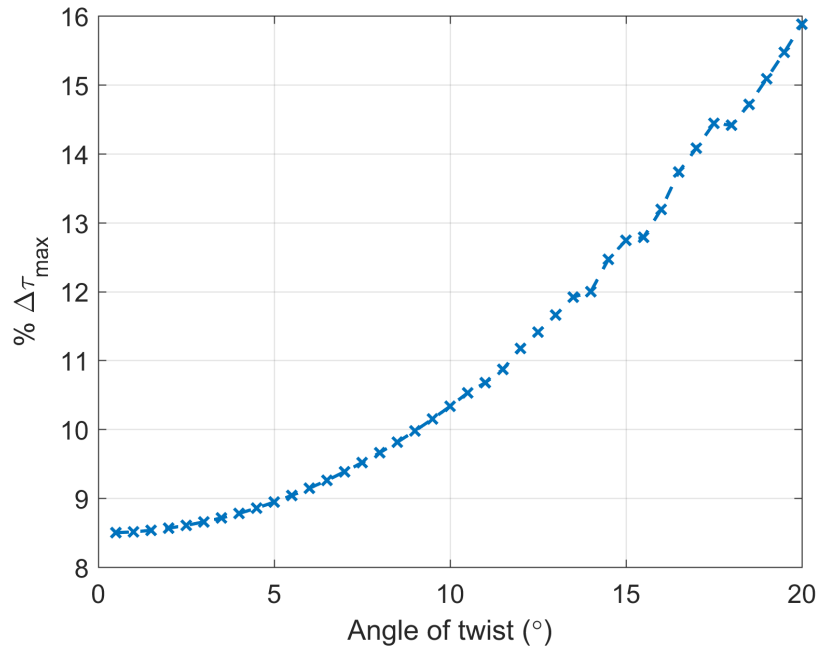
Figure 3-20: Percentage difference in the peak τ_{max} between FE simulations and the analytical formulation of (3.13)

3.6   **Conclusions**

The suitability of shell elements in the numerical stress analysis of resonant micro-scanners depends on the aspect ratio of the cross-section of the torsion members. Measurements and simulations demonstrate that the stiffness of the resonant micro-scanner test case is predominantly linear within the expected region of operation: $0 < \theta_{max} < 12°$. However, the impact of geometric non-linearities on k_s is not negligible, therefore large strain computations which account for element shape changes, should be considered in subsequent FE modal and structural simulations. It has been demonstrated that direct measurements of the mechanical stiffness of a resonating micro-scanner can be achieved using a high precision micro-force probing system. The measurement of the stiffness non-linearity is also achieved however further investigations on the effect of lateral probe bending on the results' accuracy is necessary. Moreover, the force-

displacement experiment can be considerably improved by implementing small changes to the layout of the device under test. For example, an area on the mirror plate can be left uncoated (with the reflective layer) which corresponds to the probe's contact area and location. This will not only act as marker for the precise alignment of the probe but will also minimize the possibility of slip between the probe tip and the mirror surface.

4   ANGULAR VERTICAL COMB STRUCTURE

The electrostatic forcing function of (2.13) is proportional to the rate of change of capacitance with angular displacement. Therefore, evaluation of the angular-dependent $dC/d\theta$ of an oscillating AVC structure, depicted in **Figure 2-4**, is essential in order to predict the scanning efficiency of the resonating micro-scanner. In this chapter, analytical and numerical solutions of the AVC structure capacitance will be validated against capacitance measurement techniques. This analysis is based on the STM micro-scanner described in Section 2.7 with AVC structure dimensions listed in **Table 2-4** and depicted in **Figure 2-15**. The micro-mirror is operated at a high resonant frequency (21.5 kHz) and actuation voltage (maximum 200 V_{pk}) while the change in capacitance is in the order of a few pico-farads [110]. This may limit the suitability of conventional measurement techniques for the acquisition of the AVC structure capacitance. In this chapter, a novel capacitance measurement technique is proposed in order to overcome the low signal-to-noise ratio encountered in the dynamic measurement technique. Moreover, the electrostatic numerical model presented will be implemented in Chapters 5, 7 and 8 for the estimation of the scanning efficiency of resonating micro-mirrors. Parts of the work presented in this chapter has been published in [111].

4.1   Analytical and Numerical Simulations

Figure 2-4 shows the cross-section of the mirror actuator at zero deflection angle and at maximum deflection. The capacitance variation with tilt angle, θ of the AVC structure can be described analytically via a piecewise continuous function [112] [113] [114]. Three distinct regions of interaction between the rotating and fixed comb fingers can be observed in **Figure 4-1**:

-   Region A: at small angles comb fingers are engaged leading to a constant $dC/d\theta$;
-   Region B: transition region occurs where $dC/d\theta$ decreases quadratically;
-   Region C: comb fingers are completely disengaged resulting in zero $dC/d\theta$.

The limits of each region are dependent on the finger length, finger width, initial finger overlap length and finger offset from the rotational axis. It has to be noted that fringing effects at the comb finger edges are neglected in the analytical formulations.
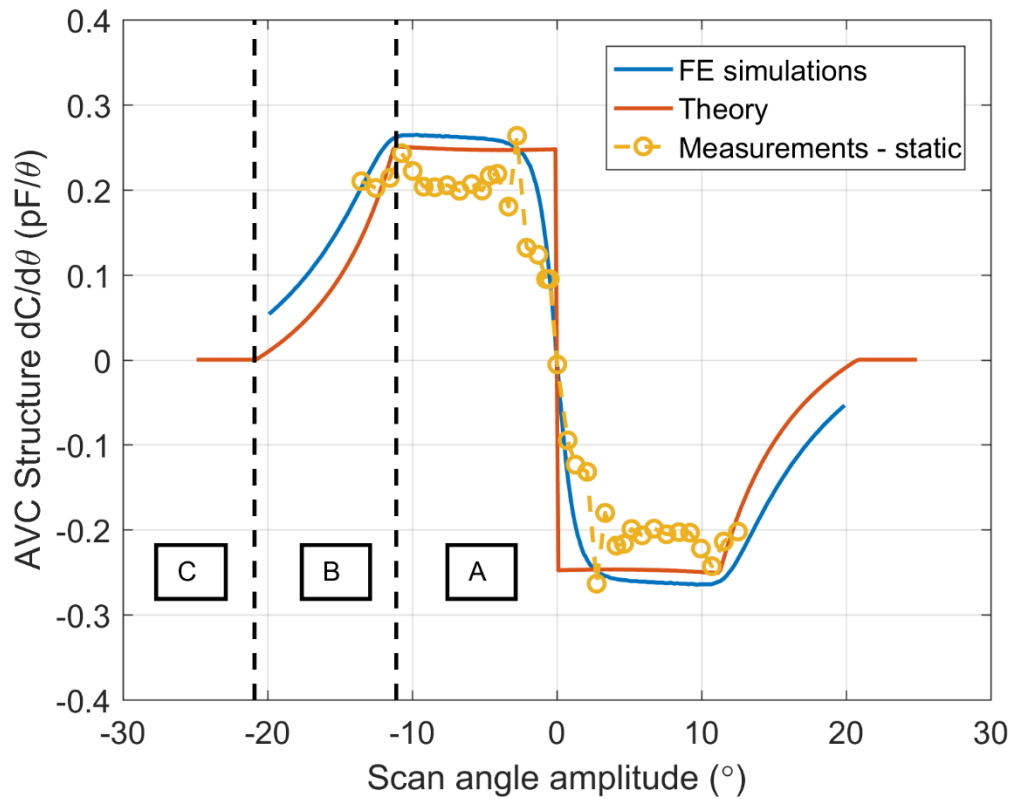
Figure 4-1: STM micro-scanner: Angular dependence of total AVC structure *dC/dθ*

The analytical solution was then compared to steady-state electrostatic simulations using ANSYS Mechanical. The FE model of **Figure 4-2** was developed to compute the capacitance between the rotating and static finger boundaries at discrete scan angles of the rotating comb finger. The air volume separating the electrode boundaries is meshed using charge-based electric elements (10-node SOLID123 tetrahedra). Only the unit cell of the comb structure pattern of **Figure 2-14** is modelled. This enables higher FE densities, which in turn, minimizes the mesh dependence of the resultant capacitance-θ relationship.

Good agreement in *dC/dθ* (see **Figure 4-1**) is achieved between the analytical and numerical solutions up to scan angle of 15°. However, the numerical capacitance profile of **Figure 4-3** has a vertical offset of 15% relative to the analytical profile. This offset demonstrates that fringing effects in AVC structures are not negligible. Nonetheless, fringing effects have a small influence on *dC/dθ* and hence the electrostatic forcing function in the region -12° < θ < 12°.

(a)

(b)   (c)
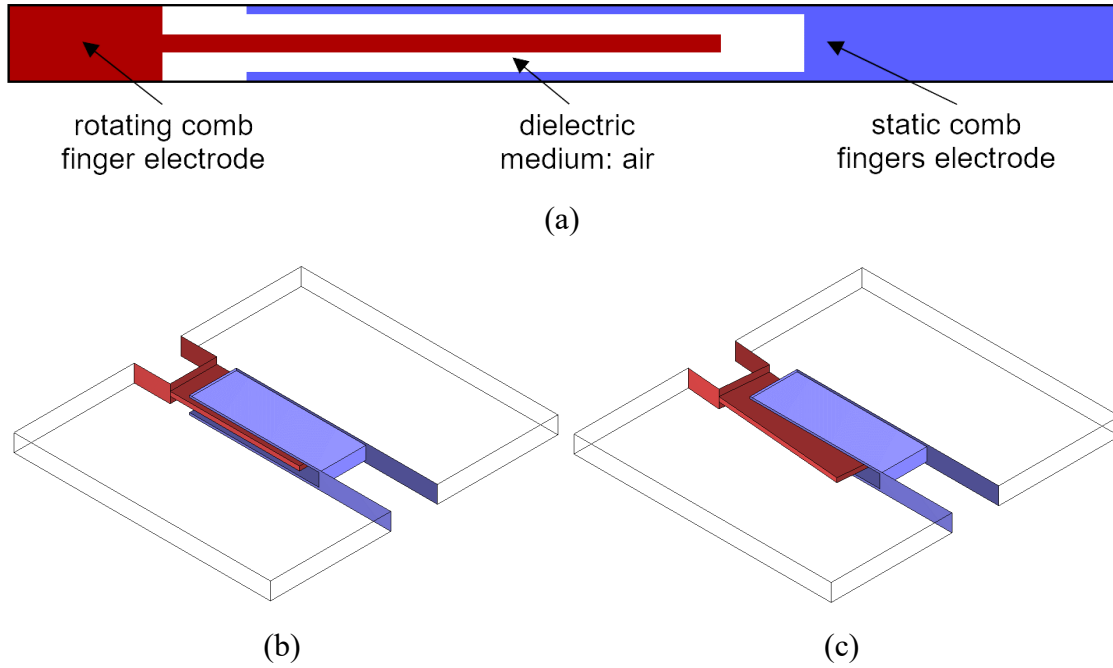
Figure 4-2: Electrostatic FE model to deduce the capacitance variation with θ of a rotating AVC finger
(a) top view (b) isometric view at $\theta = 0°$ (c) isometric view at $\theta = 5°$
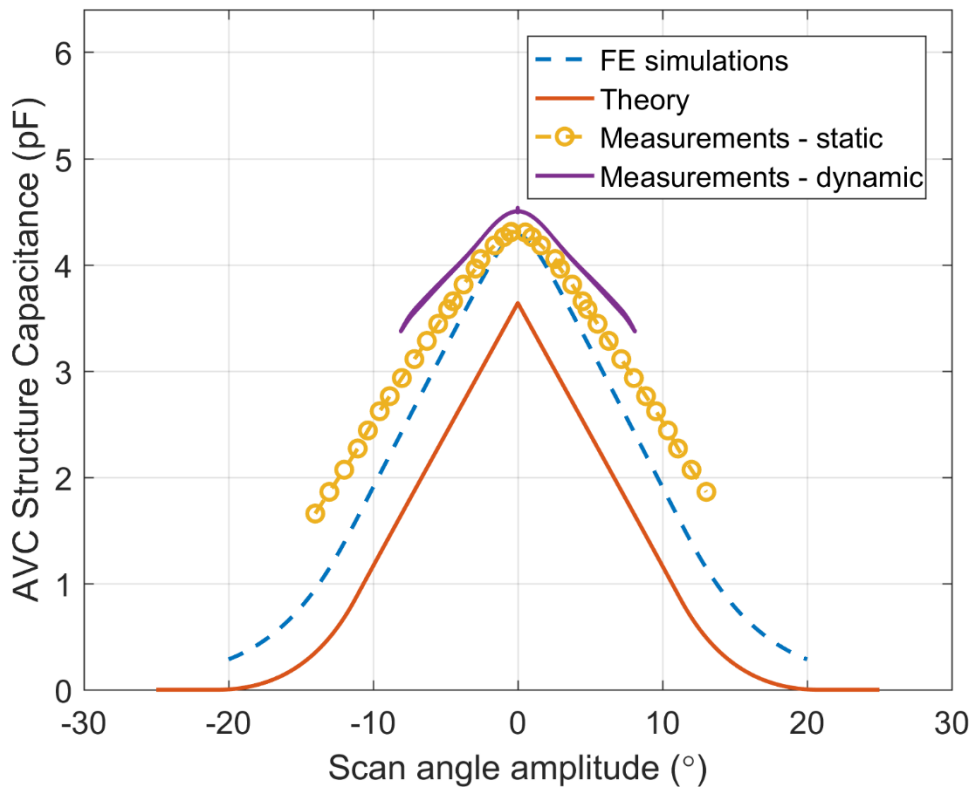
Figure 4-3: STM micro-scanner: Angular dependence of total AVC structure capacitance

4.2   Capacitance Measurements

4.2.1   Dynamic Method

In the first measurement technique, capacitance measurements are acquired from the instantaneous voltage and current in the comb structure using the electrical set-up of **Figure 4-4** and a custom-built optical test bench. The following experimental set-up is developed to drive the micro-scanner and acquire the scanning angle and sense.
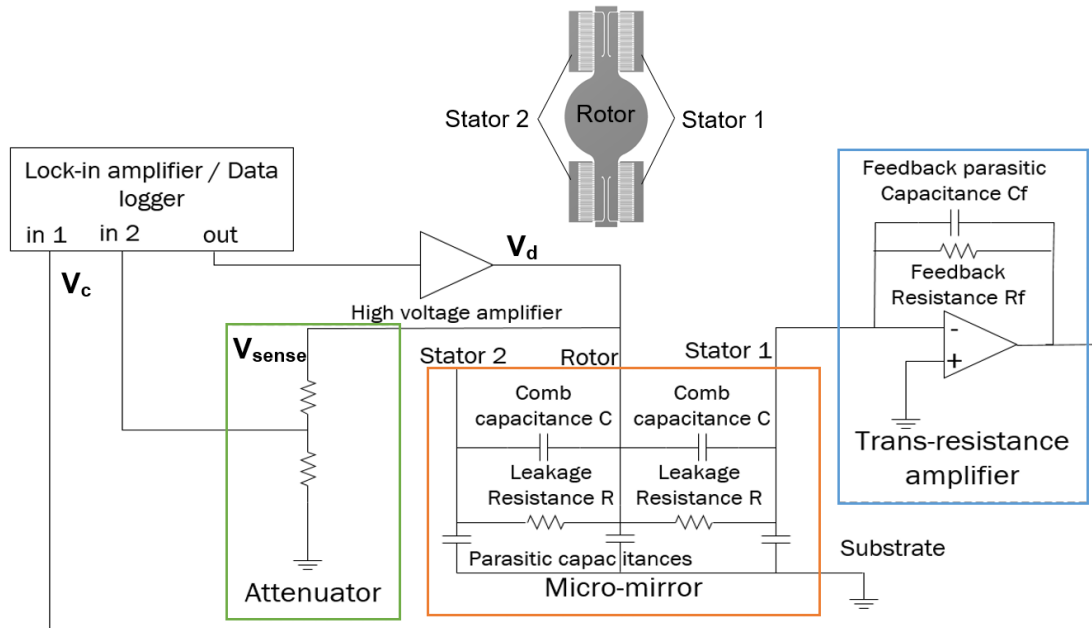
Figure 4-4: Electrical setup for driving the resonant micro-scanner and simultaneously acquiring the AVC structure capacitance (dynamic capacitance measurement method) [111]

A lock-in amplifier (Zurich Instruments HF2LI) is used to generate a sinusoidal voltage signal at a frequency corresponding to the resonant frequency of the micro-scanner. The internal reference oscillator of the lock-in amplifier allows for precise and stable control of the frequency (resolution of 0.001 Hz) and phase of the output signal. The output signal is than amplified using a high voltage amplifier (Trek PZD350A) in order to generate a sinusoidal signal of up to 200 V_{pk} to drive the micro-mirror at resonance. The drive voltage signal is applied to the packaged (ceramic DIP-32) micro-scanner via a custom-designed printed circuit board (PCB). The drive voltage, V_d is applied to the rotating comb fingers while the static fingers and substrate are grounded. The actual voltage signal supplied to the rotating comb fingers (V_{sense}) is recorded by an oscilloscope (Picoscope 5000) via an attenuator. A trans-resistance amplifier is implemented in order to convert the comb structure electrical current into a voltage signal (V_c). In the case of a variable

capacitor, the measured AVC structure current, *i(t)* is dependent on both the instantaneous capacitance and rate of change of capacitance, as shown in (4.1). However, the $V_d = dC/dt$ term in (4.1) is positive when the mirror is rotating in one direction and negative when the mirror is rotating in the opposite direction. This means that by averaging the current measured during opposite mirror movement directions, this term can be cancelled out. Therefore, the capacitance at discrete mirror scan angles was deduced by averaging 3600 samples of the *i(t)* and *dV$_d$(t)/dt* readings at a particular phase angle of the mirror oscillation. Parasitic capacitances resulting from the experimental setup were estimated by operating the setup with the packaged mirror removed. By assuming that the parasitic capacitances from the setup are in parallel with the micro-scanner capacitance, this offset can be subtracted from the data collected. However, the parasitic capacitances resulting from the micro-scanner packaging (ceramic DIP-32) are unaccounted for with this measurement technique.

$$i(t) = V_d(t)\frac{dC(t)}{dt} + C(t)\frac{dV_d(t)}{dt} \qquad (4.1)$$

Simultaneous measurement of the dynamic mirror scan angle was performed using the optical test bench set-up depicted in **Figure 4-5(a)**. A HeNe laser source (632.8nm, 0.8mW) is directed towards the oscillating mirror surface, which in turn, projects a line image onto a two-dimensional position sensitive detector (Hamamatsu C10446-04). The laser beam intensity was limited by a neutral density filter to obtain an acceptable voltage signal from the PSD without any saturation. In order to maximize the detectable scan angle amplitude, the optical path between the micro-mirror and the PSD was reduced by introducing a beam splitter cube. A correction factor, K_r, defined in (4.2) was applied to the measured optical angle to account for the glass cube's refraction as shown in **Figure 4-5(b)**.

$$K_c = \frac{x'}{x} = \frac{l_a \tan(2\theta) + l_g \tan\left(2\theta/1.517\right)}{(l_a + l_g)\tan(2\theta)} \qquad (4.2)$$
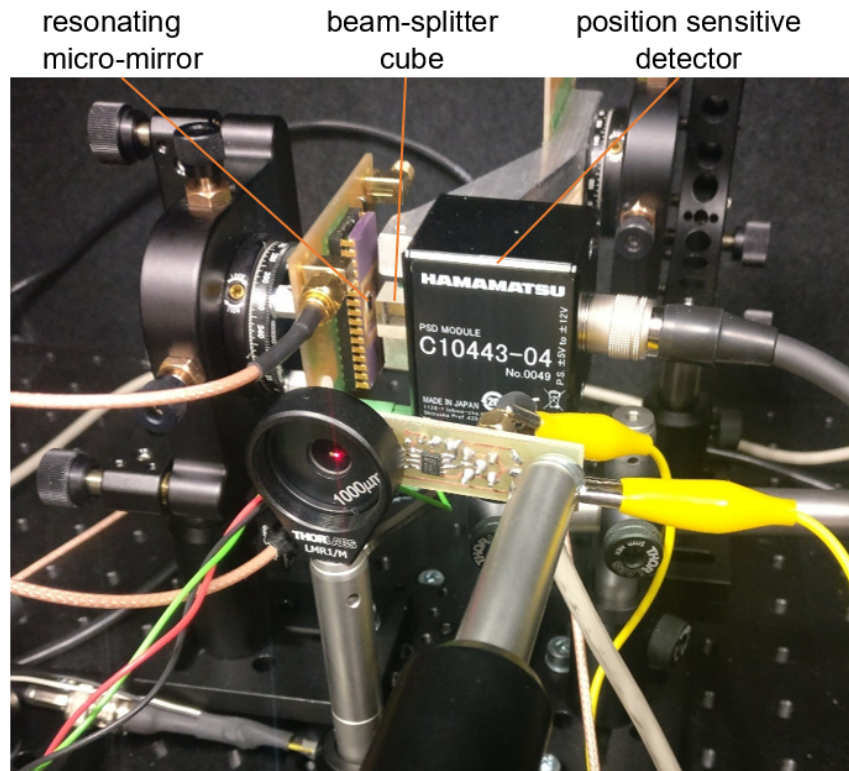
(a)
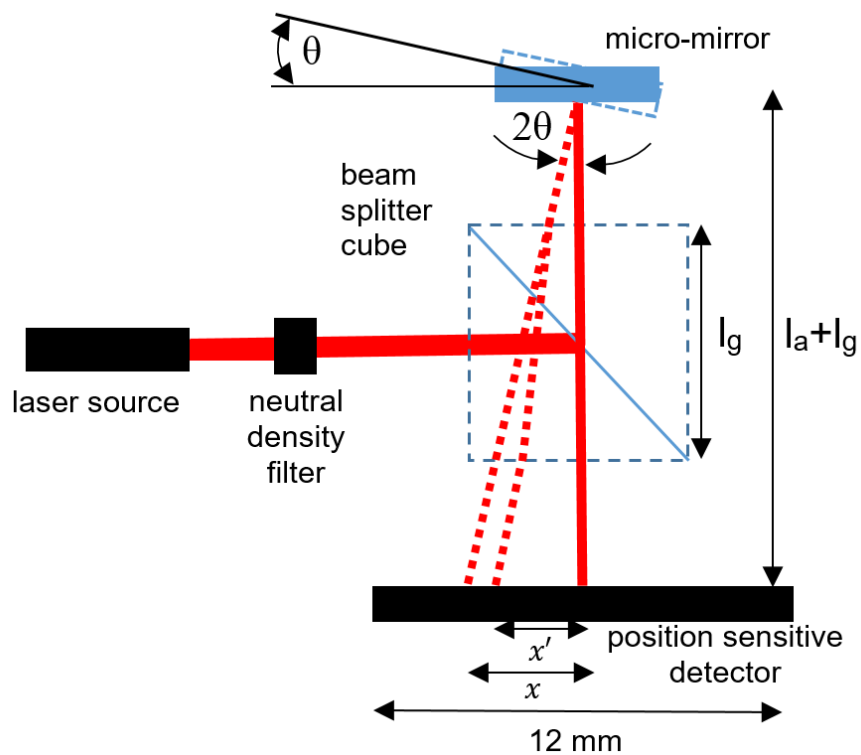
(b)

Figure 4-5: (a) PSD-based high frequency scan angle measurement system (b) optical path showing refraction correction factor *x'/x*

57

4.2.2   Static Method

In the second measurement technique, the capacitance variation with scan angle is obtained by mechanically tilting the micro-scanner using a microprobe. The displacement of the micro probe is precisely controlled and recorded by the FemtoTools FT-MTA02 microrobotic station (see **Figure 3-11**). This allows for static capacitance measurements at discrete mirror deflection angles using an Agilent E4980A high precision LCR meter.

The out-of-plane displacement and hence the angular displacement of the mirror plate were manually determined using an optical microscope with a high precision z-scale. It is assumed that the micro-mirror and AVC structures behave rigidly and their angular displacements are equal. The capacitance was directly measured from the micro-scanner die using Kelvin-connected electrical probes shown in **Figure 4-6**. The electrical and mechanical probes together with the micro-scanner substrate are grounded in order to minimize parasitic capacitance effects.
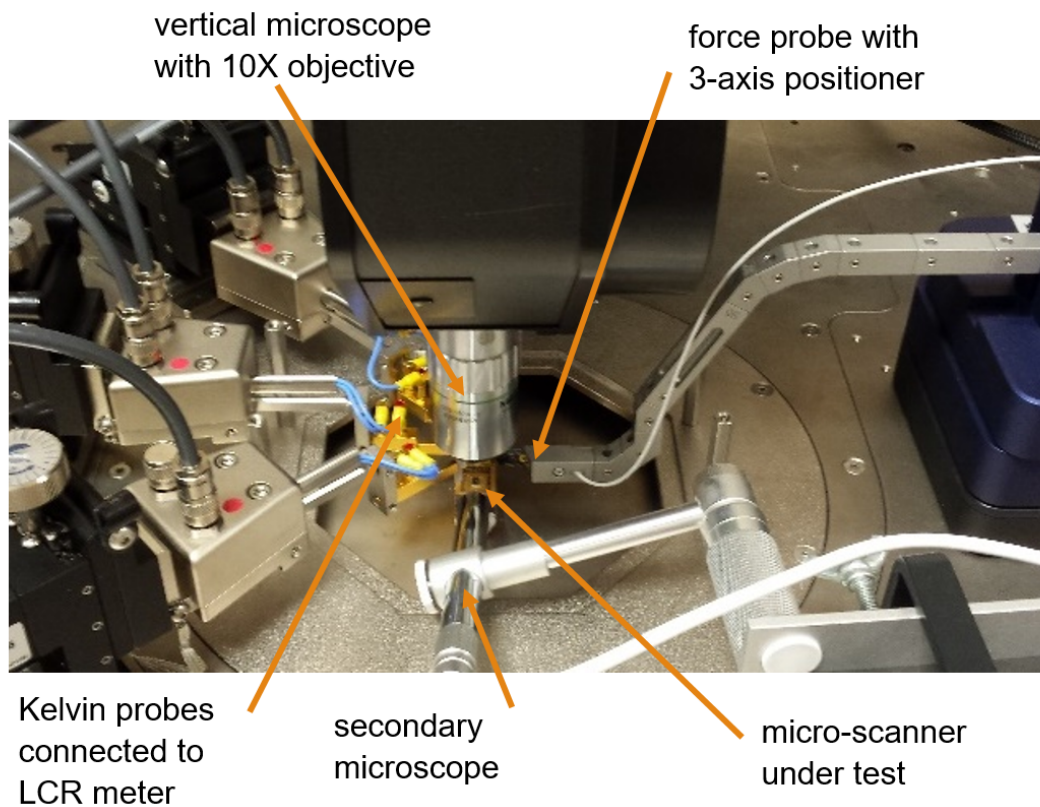
Figure 4-6: Microscope setup for measuring capacitance at different micro-scanner out-of-plane angle (static method)

The micro-scanner is not electrostatically actuated with the static measurement technique and capacitance measurements with improved accuracy and reduced noise can be obtained with the high precision LCR meter. Nonetheless, the unbalanced loading method applied to tilt the mirror plate introduces a non-negligible out-of-plane bending in the torsion beams (as previously discussed in Section 3.4). FE electrostatic simulations were performed to quantify the effect of bending on $dC/d\theta$ and apply a correction factor to the measurements results obtained using the static method.

4.3   Discussion and Conclusions

The results of **Figure 4-3** show a slight vertical offset in $C(\theta)$ between the dynamic and static measurement methods. A major contributor to this offset is the parasitic capacitance originating from the device packaging. In the static technique, the parasitic capacitances are reduced since the capacitance is probed directly on-chip using the Kelvin-connected setup. A second major drawback with the dynamic method is the low signal-to-noise ratio observed in spite of the implementation of sample averaging and the introduction of low pass filter to the current signal.

The dynamic measurement method can be applied during micro-scanner operation to monitor and control the mirror response. In fact, the voltage read-out from the trans-resistance amplifier can be used for mirror scan position/direction feedback as part of a phase-locked loop (PLL) [115]. However, experimental validation of the simulated electrostatic performance of the AVC structures requires capacitance measurements with a higher accuracy and angular resolution. This can be obtained via the mechanical probing (static) method proposed in this chapter. Overall, the results of **Figure 4-1** show good agreement between the experimental and numerical simulation results. The electrostatic FE model of **Figure 4-2**, developed for estimation of the AVC structure capacitance, will be implemented in the numerical micro-scanner design procedures presented in Chapters 7 and 8.

5   AIR DAMPING

At resonance, the maximum scan angle amplitude is determined by the capacitance-θ variation of the comb drive actuators and the air damping losses [82]. Therefore, accurate evaluation of the air damping characteristics at the design stage is essential in order to determine the viability of a scanning micro-mirror prototype [80].

In this study, the complex fluid-structure interactions in resonating micro-mirrors with electrostatic actuation will be discussed. Moreover, computationally efficient Navier-Stokes CFD models capable of simulating large scan angles will be proposed and compared to results from simplified analytical and numerical models. The motivation behind this study is to answer the following research questions.

i.   Are the Couette and steady Stokes flow models accurate in predicting the damping energy loss of angular comb structures?
ii.   What is the wake of a micro-mirror plate undergoing out-of-plane rotational oscillations?
iii.   Are the squeeze thin film and unsteady Stokes models applicable to high performance micro-mirror plate damping predictions?
iv.   What is the effect of scan angle amplitude on the comb-structure and micro-mirror plate damping?
v.   What is the effect of the micro-mirror cavity on the micro-mirror drag damping?

Using a resonating micro-mirror fabricated by STM as a test case (**Figure 2-13**), the numerical results were validated using a PSD (position sensitive detector)-based measuring system. Parts of the work presented in this chapter has been published in [116, 117, 118].

5.1   Air Damping Theory

The pressure, p and the velocity field, **u** of the fluid flow past an oscillating micro-mirror can be described by the Navier-Stokes and continuity equations [119] for unsteady, incompressible flow (Mach number, $M < 0.3$), where ρ is the fluid density and μ is the fluid viscosity:

$$\rho\left(\frac{\partial \mathbf{u}}{\partial t}\right) + \rho\left(\mathbf{u}.\nabla\right)\mathbf{u} = -\nabla p + \mu\nabla^2\mathbf{u} \tag{5.1}$$

$$\nabla \cdot \mathbf{u} = 0 \tag{5.2}$$

Resonating MEMS structures are typically separated from the fixed substrate by a thin air gap and are driven to relatively small oscillation amplitudes. Gas damping is

consequently, predominantly viscous, allowing for the inertial terms on the left-hand side of (5.1) to be neglected. The ratio of inertial to viscous forces acting on a moving object in a quiescent fluid is defined by the Reynolds number, Re as shown in (5.3). The Re is proportional to the maximum velocity of the moving body, U_{max} and the characteristic flow dimension, L. In the case of the micro-scanner motion, $\underline{U_{max}}$ is taken as the velocity amplitude of the maximum radial dimension of the oscillating mass from the rotational axis.

$$Re = \frac{\rho U_{max} L}{\mu} \tag{5.3}$$

Therefore, in the limit $Re \ll 1$, the thin gas films form either a Couette or squeeze-film viscous damper. Energy dissipation due to air damping in resonant micro-mirrors is derived from two main sources described below.

5.1.1   Angular Vertical Comb Structure

Slide film damping refers to the energy dissipated by the viscous fluid flow between two closely spaced surfaces that move tangentially relative to each other. At low frequencies, slide film damping is governed by Couette flow, which assumes that the velocity gradient along the fluid gap is constant. In AVC actuators, the viscous resistance due to the relative out-of-plane motion of adjacent fingers separated by a small air gap of width, f_g, can be estimated by the Couette flow model [120]. It can be assumed that Couette flow occurs within the angular region where the rotating and fixed comb fingers are predominantly engaged (Region A of **Figure 4-1**). By selecting f_g as the characteristic flow dimension, the Reynolds number [63], Re_c of the flow in the AVC structure is (refer to **Figure 2-15**):

$$Re_c = \frac{2\pi\rho f_s \theta_{max} \left(f_r + f_l \right) f_g}{\mu} \tag{5.4}$$

According to the Couette flow model, the damping moment, M_d acting on the AVC structure is proportional and in phase with respect to the angular velocity of the rotating comb fingers. For $Re_c \ll 1$, M_d of N number of comb fingers is given by (5.5) [63]:

$$M_d(t) = -\frac{2N\mu_{eff}t_m\dot{\theta}(t)}{3f_g}\left[\left(f_r + f_l\right)^3 - f_r^{\,3}\right] \tag{5.5}$$

61

where $\dot{\theta}(t) = 2\pi f_s \theta_{max} \cos(2\pi f_s t)$. For small values of f_g, the assumption of zero flow velocity at the rotating comb structure boundary may not be valid. To account for slip flow in (5.2) a modification to the gas viscosity, μ_{eff} is applied, which is a function of the Knudsen number, Kn as shown in (5.6) [121]. Kn is defined as the ratio of the gas mean free path length of air to the finger gap width.

$$\mu_{eff} = \frac{\mu}{1 + 9.658 Kn^{1.159}} \tag{5.6}$$

5.1.2 Micro-Mirror Plate

Damping due to the rotational oscillations of the cavity-bound micro-mirror plate has been estimated using the squeeze-film damping model. Based on lubrication theory, the model is valid for $h/R \ll 1$, where h is the cavity depth. The damping moment of a circular micro-mirror at $\theta = 0°$ has been derived from the non-linear Reynolds equation [84]:

$$M_{d(\theta=0°)} = \frac{\mu\pi^2 f_s R^6 \theta_{max}}{4h^3} \tag{5.7}$$

The cavity depth of resonating micro-mirrors for pico-projection applications is typically greater than 100 μm in order to accommodate large scan angles. This implies that the viscous thin film squeeze effect may be minimal compared to drag forces acting on the lower and upper micro-mirror surfaces. Consequently, the characteristic length used to define the Reynolds number of a circular plate oscillating in out-of-plane rotation (Re_m in (5.8)) is the plate radius R [86].

$$Re_m = \frac{2\pi\rho f_s \theta_{max} R^2}{\mu} \tag{5.8}$$

At sufficiently low f_s and θ_{max} the surrounding air around the mirror plate is governed by Stokes flow where the damping torque for an unbounded thin disc with a fixed angular velocity is given by (5.9) [85]:

$$M_d = \frac{32\mu R^3 \dot{\theta}}{3} \tag{5.9}$$

Kim *et al.* [89] provide a modification to (5.9) to include the effect of the proximity of cavity wall on the plate damping moment. Although Re_m can be low, (5.9) does not account for the flow instabilities propagated by the mirror's periodic change in angular

direction. By retaining the temporal acceleration term in (5.1), the aerodynamic resistance of a circular disk undergoing small amplitude oscillations can be derived from the unsteady Stokes equation [86]:

$$\rho\left(\frac{\partial \mathbf{u}}{\partial t}\right) = -\nabla p + \mu \nabla^2 \mathbf{u} \tag{5.10}$$

By reducing (5.10) to dual integral equations, the high frequency dependence of the damping moment of an oscillating disc in out-of-plane rotation is given by (5.11) [86]:

$$M_d = \frac{32\mu R^3 \dot{\theta}}{3}\left(0.43\lambda \cos\left(0.27\pi\right)\right) \tag{5.11}$$

where $\lambda^2 = 2\pi\rho f_s R^2 / \mu$ is a dimensionless frequency parameter characterizing the time scale for vorticity diffusion into the surrounding fluid relative to the oscillation time scale [86]. Additionally, the aerodynamic moment acting on the oscillating disc consists of an added-mass term, which is $\pi/2$ out-of-phase with the angular velocity and does not contribute to energy dissipation.

While Stokes drag varies linearly with velocity, in the laminar flow regime (for $Re_m > 1$), M_d is expected to be a quadratic function of the angular velocity. The overall aerodynamic moment, M_{plate} about the rotational axis can be deduced from Morison's equation intended for the hydrodynamic analysis of offshore floating structures [92]. The damping and inertial components of M_{plate} (given in (5.12)) are a function of the average damping coefficient, C_d and the added mass coefficient, C_a typically obtained via empirical methods.

$$M_{plate} = M_d + M_i = -\frac{4}{15}C_d\rho R^5 \dot{\theta}\left|\dot{\theta}\right| - \frac{\pi}{4}C_a\rho t_m R^4 \ddot{\theta} \tag{5.12}$$

The energy dissipation via air damping, E_{loss} over one period of oscillation is defined in (5.13). Considering the form drag moment equation of (5.12), E_{loss} can derived as in (5.14). The quality factor, Q is given by (5.15), where I is the mass moment of inertia of the micro-mirror.

$$E_{loss} = \int_0^T M_d(t)\dot{\theta}(t)dt; \ T = \frac{1}{f_s} \tag{5.13}$$

$$E_{loss} = \frac{16}{15}C_d\pi^3\rho f_s^2\theta_{max}^3 R^5 \tag{5.14}$$

63

$$Q = \frac{4\pi^3 I f_s^2 \theta_{max}^2}{E_{loss}}$$

(5.15)

5.2 Numerical Damping Analysis

The suitability of the analytical calculations discussed in the previous section in predicted air damping losses of electrostatically-actuated resonating micro-mirrors is assessed through numerical simulations. Due to the presence of significant length scale variation, separate numerical models were developed for damping analysis of the oscillating AVC structure and circular mirror plate. The results, presented in Sections 5.2.1 and 5.2.2, are based on the dimensions and scanning characteristics of the STM micro-mirror test case listed in **Table 2-4**.

5.2.1 Angular Vertical Comb Structure

Accurate representation of the complex airflow surrounding the rotating comb fingers necessitates three-dimensional numerical modelling. Given the large number of comb fingers required to drive the resonant micro-mirror, only a comb finger or finger gap cell is considered to enable suitable grid discretization for acceptable solution accuracy. For a θ_{max} of 12°, the Re_c of the simulated comb structure design is 3.83 at maximum angular velocity and radial position. Moreover, given that Kn is between 10^{-3} and 0.1, the non-slip flow assumption at the comb structure-fluid boundary is not valid.

Air damping due to the oscillating AVC structure was analysed using (a) the steady-state Stokes flow solver in CoventorWare and (b) the transient Navier-Stokes (N-S) solver for incompressible, laminar flow in ANSYS Fluent. In CoventorWare, the moving boundary viscous forces are solved using the boundary element method (BEM) requiring the solid body surfaces to be numerically discretized. In contrast, the finite volume method (FVM) in ANSYS Fluent requires the air volume surrounding the solid bodies to be meshed. In order to simplify the fluid-structural coupling, the micro-mirror structure was assumed to be rigid.

5.2.1.1 Steady-state Stokes flow simulations using a boundary element model

The comb finger cell shown in **Figure 5-1(a)** consists of a single rotatable comb finger between two fixed comb fingers. The solid surfaces were meshed using mapped quadrilateral elements. Rarefaction effects are included in the computation by modifying the air viscosity as in (5.6). The Stokes flow solver is only capable of simulating steady flow. Therefore, the damping coefficient, c_d was obtained for a number of discrete out-

plane angular displacements of the rotating comb finger. The temporal damping moment profile was deduced from: $M_d(t) = c_d(\theta).\dot{\theta}(t)$. **Figure 5-1(b)** shows the shear stress distribution on the moving surfaces at $\theta = 12°$.

fixed
comb
fingers

rotating
comb
finger

(a)

Force Density Z: -3.5E-04   -2.4E-04   -1.3E-04   -2.4E-05   8.4E-05

uN/um^2

COVENTOR

(b)
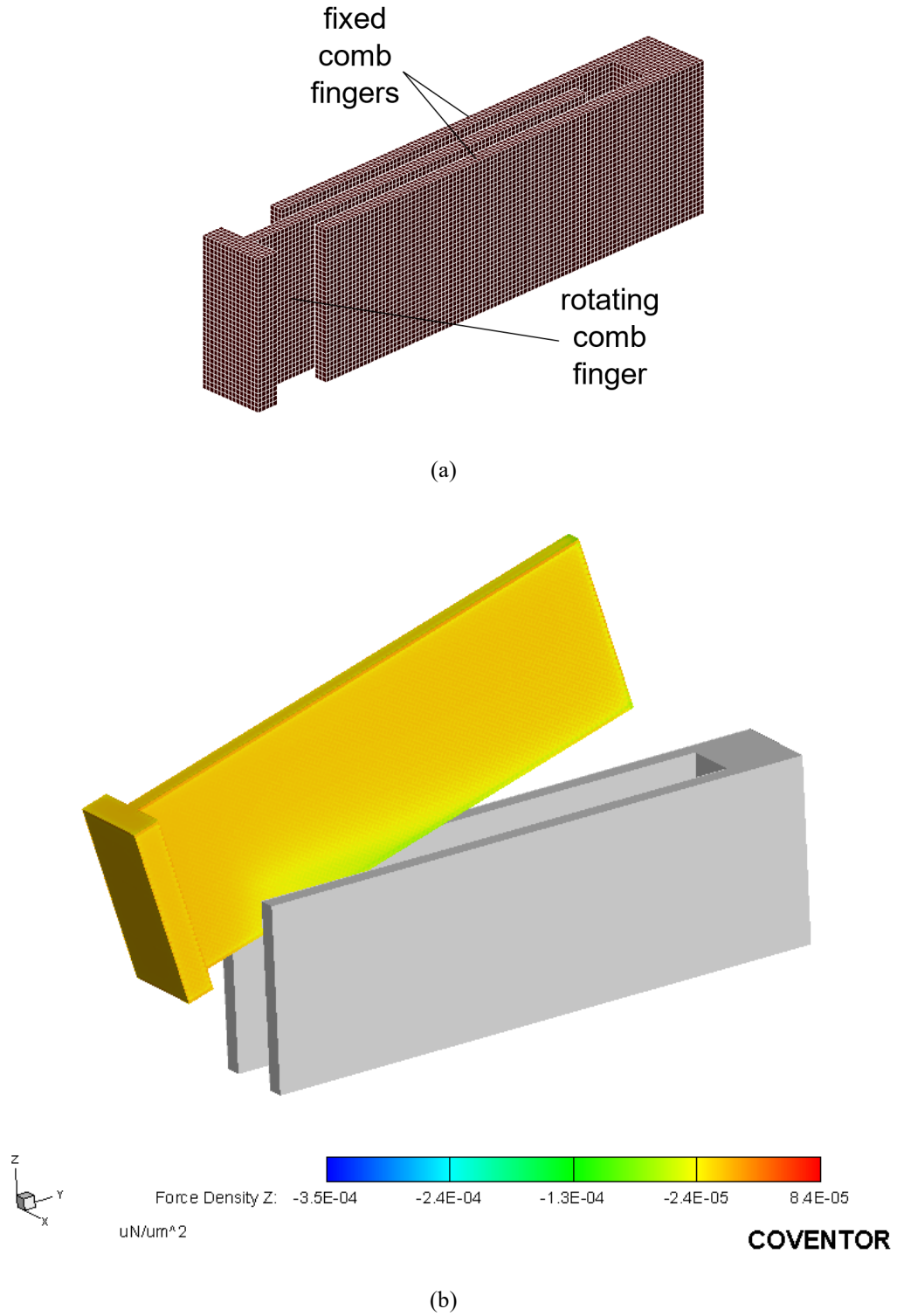
Figure 5-1: Stokes flow solver in CoventorWare: (a) AVC structure cell mesh (b) Shear stress distribution at the rotating comb finger boundary at $\theta = 12°$

5.2.1.2   Transient Navier-Stokes simulations using a finite volume model

The boundaries of the comb structure N-S model are shown in **Figure 5-2(a)**. The model consists of a single finger gap on either side of the rotational axis to facilitate the simulation of rotor finger rotation. In order to simulate the relative movement between the rotating and fixed comb fingers in the N-S model, the *sliding mesh* technique available in ANSYS Fluent was applied [122]. Given that the flow is time-periodic and the solution is not a function of mesh motion, the *sliding mesh* is more efficient in modelling fluid boundary motion compared to the *dynamic mesh* which involves mesh cell deformation. The numerical domain was split in two zones as shown in **Figure 5-2(b)**. The inner cylindrical volumetric zone (*A*) consists of the rotating finger surface boundaries (*R1* and *R2*). The element nodes of zone (*A*) are allowed to rotate and slide relative to the outer volumetric zone (*B*), which includes the static finger surface boundaries (*S1* and *S2*). Fluid motion is allowed to occur through the non-conformal interfaces between both zones, which are dynamically updated after every time step. Both fluid zones were discretized using hexahedral elements and following a grid discretization study, six elements along the finger gap were prescribed. Moreover, the low-pressure boundary slip option is activated in order to model rarefaction effects using Maxwell's velocity slip formulation [123].

(a)   (b)
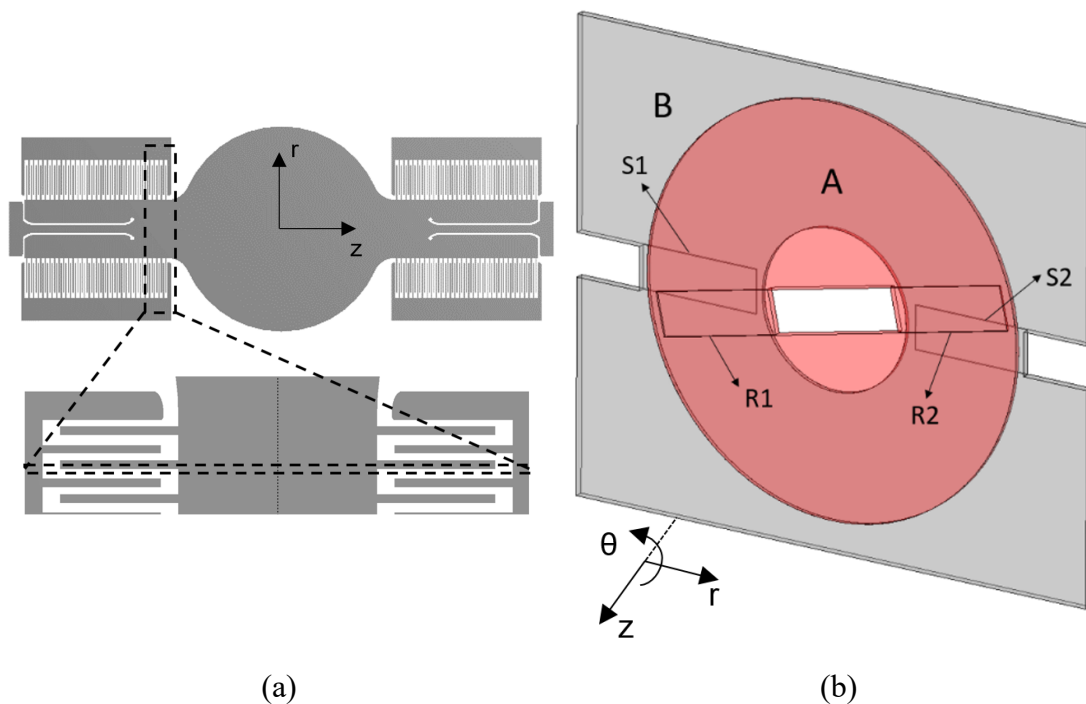
Figure 5-2: N-S model of the AVC structure in ANSYS Fluent: (a) boundaries of the comb finger cell (b) rotating mesh zone A (red) including drive finger boundary surfaces (R1, R2) and stationary mesh zone B (grey) including static finger boundary surfaces (S1, S2)

The magnitude of the total aerodynamic moment, M acting on the oscillating body is composed of the viscous shear and pressure drag moment components, M_{visc} and M_{press} respectively. M is obtained from (5.16) where $M = \vec{\tau}.\hat{z}$, with $\vec{\tau}$ being the aerodynamic torque vector and $\vec{r}$ the radial position vector component with respect to the rotational axis [79]. The viscous shear force, $\vec{\tau}_v$ is proportional to μ, and the velocity gradient at the fluid-structure interface, $\partial\vec{u}/\partial\vec{n}$: where $\vec{u}$ is the velocity field adjacent to the rotating surface area, A and $\vec{n}$ is the unit vector normal to A. On the other hand, the pressure drag force is proportional to the local fluid pressure, p normal to the moving boundary area.

$$\vec{\tau} = \int_A (\vec{r} \times \vec{\tau}_v)\, dA + \int_A (\vec{r} \times p\vec{n})\, dA \tag{5.16}$$

A sinusoidal time-varying angular velocity profile was prescribed via a user-defined function (UDF) in ANSYS Fluent to enable oscillatory motion of the mesh zone A about the z-axis. Transient simulations were performed for a duration of 3 oscillation cycles and 100 time steps per cycle while 30 iterations were performed during every time step to ensure solution convergence and stability. A second UDF was developed to extract the elemental viscous shear stresses and static pressures acting on the rotating surface boundary. The UDF is activated at the end of each time step in order to compute the temporal aerodynamic moment using (5.16).

A verification study of the *sliding mesh* CFD model was performed by considering a similar comb structure design simulated by Mirzazadeh *et al.* [79] using the *dynamic mesh* method in ANSYS CFX. With the *sliding mesh* method (ANSYS Fluent) and the *dynamic mesh* method (ANSYS CFX) the quality factor was found to be 1066 and 1074 respectively. The resulting fluid flow velocity distribution at the finger gap mid-plane together with the shear stress distribution on the partially-disengaged rotating finger surfaces are displayed in **Figure 5-3**.
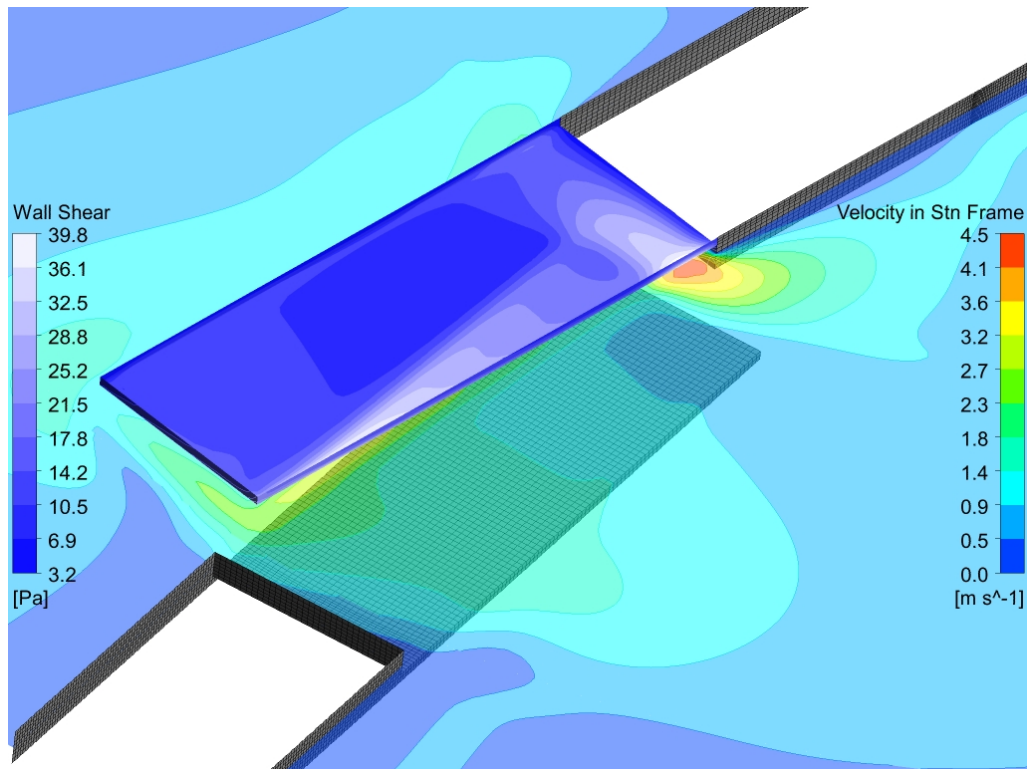
Figure 5-3: Contour plots showing shear stress distribution on the rotating comb finger surface and air velocity contours at the finger gap mid-plane at the instant when $\theta = 12°$ ($\theta_{max} = 12°$) (ANSYS Fluent)

5.2.1.3   Results and discussion

The N-S CFD results of **Figure 5-4** demonstrate that the damping moment acting on the rotating comb finger is predominantly viscous. This may suggest that slide film damping is the major source of energy loss in out-of-plane comb structures. The simulated flow velocity gradient along the comb finger gap is plotted in **Figure 5-5**. A slight deviation from the linear Couette flow velocity gradient is observed. This follows on from the suggestion that Stokes flow is more suitable than Couette flow in predicting slide film damping at high oscillation frequencies [124].

In contrast to the 1-D Couette flow model, the 3-D steady Stokes flow solver also computes the viscous drag present at the rotating comb finger edges and the faces orthogonal to the flow direction. Moreover, the flow interactions with the static comb finger as the rotating finger transitions from an engaged to disengaged state are considered in the steady Stokes simulations. However, pressure-induced drag is not simulated by the Stokes solver. Pressure drag acting on the finger surfaces, which lie normal to the flow direction, is not negligible as seen in **Figure 5-4** and its relative

contribution to damping increases with scan angle amplitude. In fact the fraction of the total energy loss resulting from pressure drag increases from 15.5% at $\theta_{max} = 2°$ to 25.8% at $\theta_{max} = 20°$.
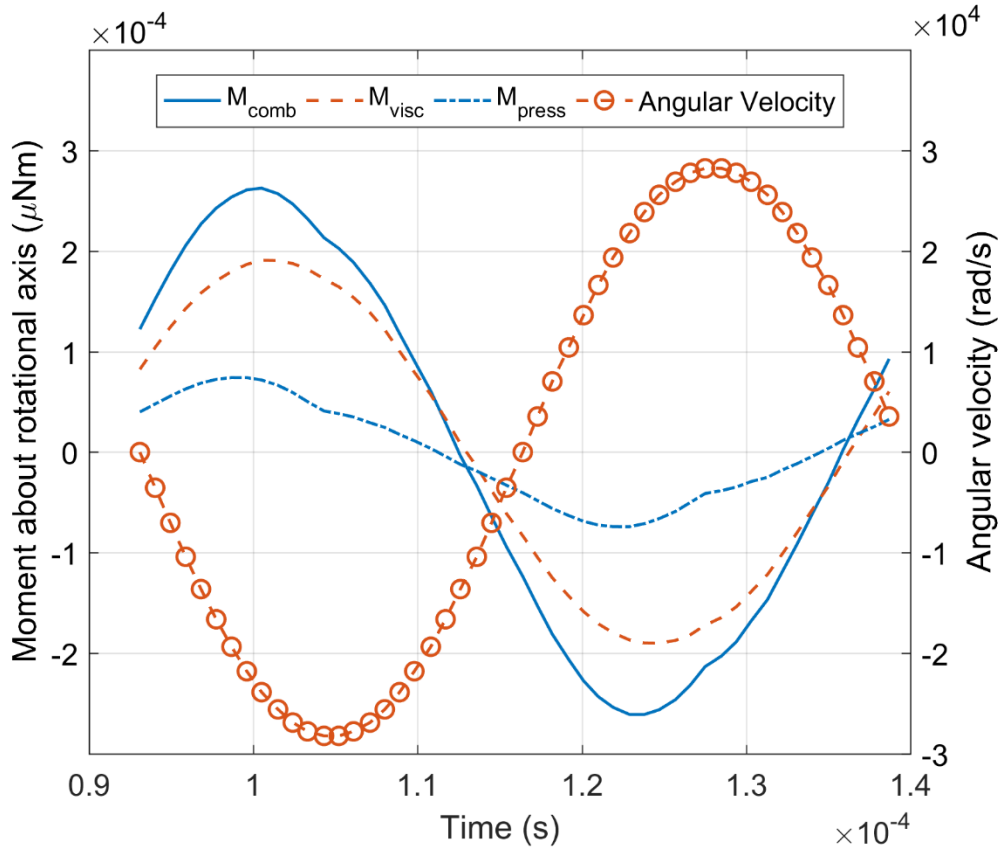
Figure 5-4: Aerodynamic moment acting on the moving comb structure resulting from pressure and viscous stresses ($f_s = 21.5$ kHz; $\theta_{max} = 12°$) (From transient N-S simulations in ANSYS Fluent)
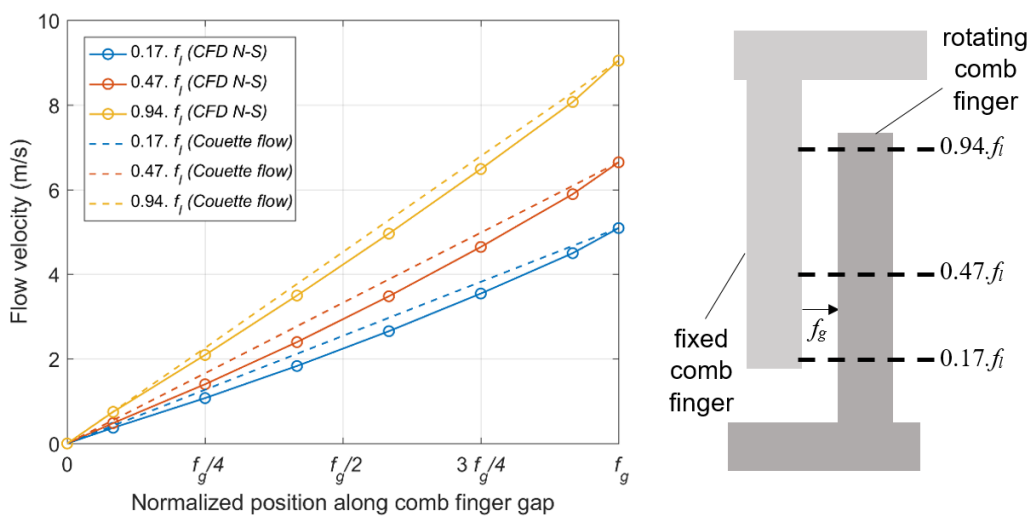
Figure 5-5: Flow velocity along the finger gap at different radial positions along the comb structure gap at $\theta(t) = 0°$ ($\theta_{max} = 12°$)

69

The 1-D Couette model leads to an underestimated E_{loss}, ranging from 44.8% ($\theta_{max} = 12°$) to 62.8% ($\theta_{max} = 2°$) of the value predicted from the N-S model. It can also be observed in **Figure 5-4** that for $\theta_{max} = 12°$, the overall aerodynamic moment, M_{comb} is 29.1° out-of-phase from the angular velocity. This implies that inertia effects, although not significant, need to be considered at high f_s and θ_{max}. With a maximum Re_c greater than 1, the flow development at both ends of the rotating comb finger (see **Figure 5-3**) renders a more complex shear stress distribution compared to that predicted by the Stokes flow solver (see **Figure 5-1(b)**).

The CFD simulation results of **Figure 5-6** demonstrate that the damping coefficient, c_D, defined in (5.17), of the angular comb structure increases with scan angle amplitude. This highlights the principle limitation of the linearized Couette flow model intended for small oscillation amplitudes. It can also be noted that the deviation of c_D between the steady Stokes and N-S models increases with θ_{max}. While Stokes flow analysis is valid for small angle amplitudes, the flow instabilities linked with higher angular velocity and acceleration oscillations can only be accurately assessed via transient Navier-Stokes simulations.

$$c_D = f_s \int_0^{1/f_s} \frac{M_d(t)}{\dot{\theta}(t)} dt \tag{5.17}$$
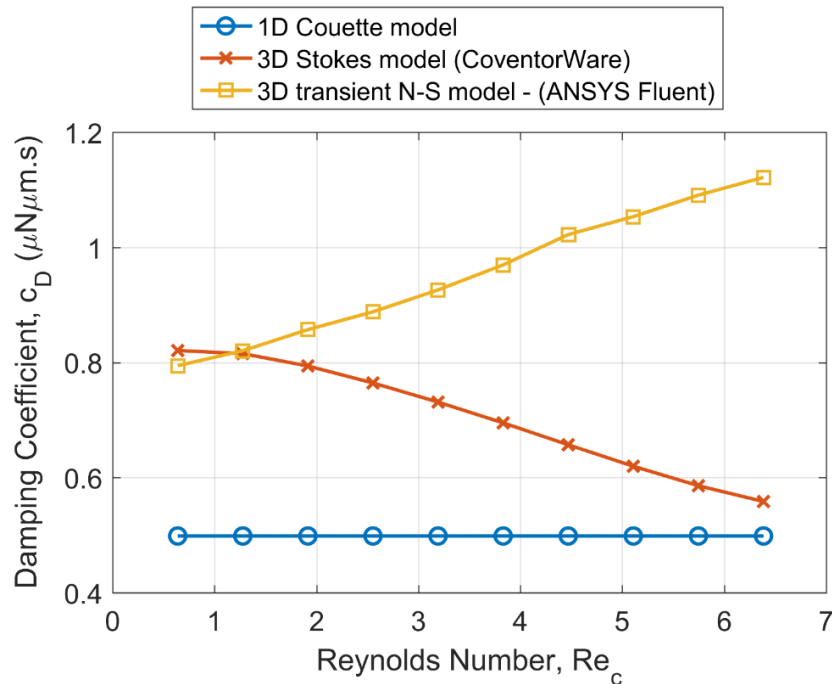
Figure 5-6: Variation of the damping coefficient of the AVC structure with Re_c
($f_s = 21.5$ kHz; $2 < \theta_{max}$ (°) <20)

5.2.2   **Micro-Mirror Plate**

In this section, a 3-D N-S finite volume model of the STM micro-mirror plate will be presented in order to determine: (1) the amplitude dependence of the temporal wake development of the oscillating structure; (2) the applicability of the available analytical models; (3) the effect of micro-mirror cavity on the damping moment; and (4) the relative influence of drag damping on the overall Q.

For a θ_{max} of 12°, the Reynolds number based on micro-mirror motion, Re_m is 543.5 at maximum angular velocity. Therefore, the airflow surrounding the micro-mirror structure is expected to be laminar since the maximum Re_m is significantly below the critical Re of 2300 beyond which the flow is considered turbulent. Apart from Re_m, the flow unsteadiness surrounding the oscillating circular mirror plate can be described in terms of the dimensionless frequency parameter, λ^2 mentioned in Section 5.1.2 ($\lambda^2 = 2566.4$ when $f_s = 21.5$ kHz).

5.2.2.1   *Transient Navier-Stokes simulations using a finite volume model*

A hemispherical computational fluid domain is used to simulate the flow around the oscillating micro-mirror, as shown in **Figure 5-7** using ANSYS Fluent. The micro-mirror plate wall boundary includes a simplified version of the support structures to which the comb actuators are attached. The cavity wall boundaries are also included and define the lower section of the fluid domain. The origin of the computational domain coincides with that of the surface wall boundaries of the circular mirror plate. The micro-mirror oscillates in out-of-plane rotation about the z-axis. A no-slip velocity boundary condition is imposed on the rotating surface while the pressure is set to zero at the outer hemispherical boundary. Tetrahedral elements are used to discretize the entire computational domain and the grid resolution is gradually increased towards the solid surface boundaries to resolve the high velocity gradients present in the adjacent region.

In order to realize the oscillatory motion of the micro-mirror plate, the *dynamic mesh* method is applied. Unlike the rigid element motion of the *sliding mesh* method (see Section 5.2.1.2), the grid deforms to accommodate the imposed angular displacement of the rigid plate boundary. In spite of grid deformation, the topology of the mesh is retained from the initial time step and the mesh quality is preserved by applying a grid smoothing method. However, given that large boundary displacement occurs, local re-meshing is activated when the element face skewness exceeds a pre-defined value.
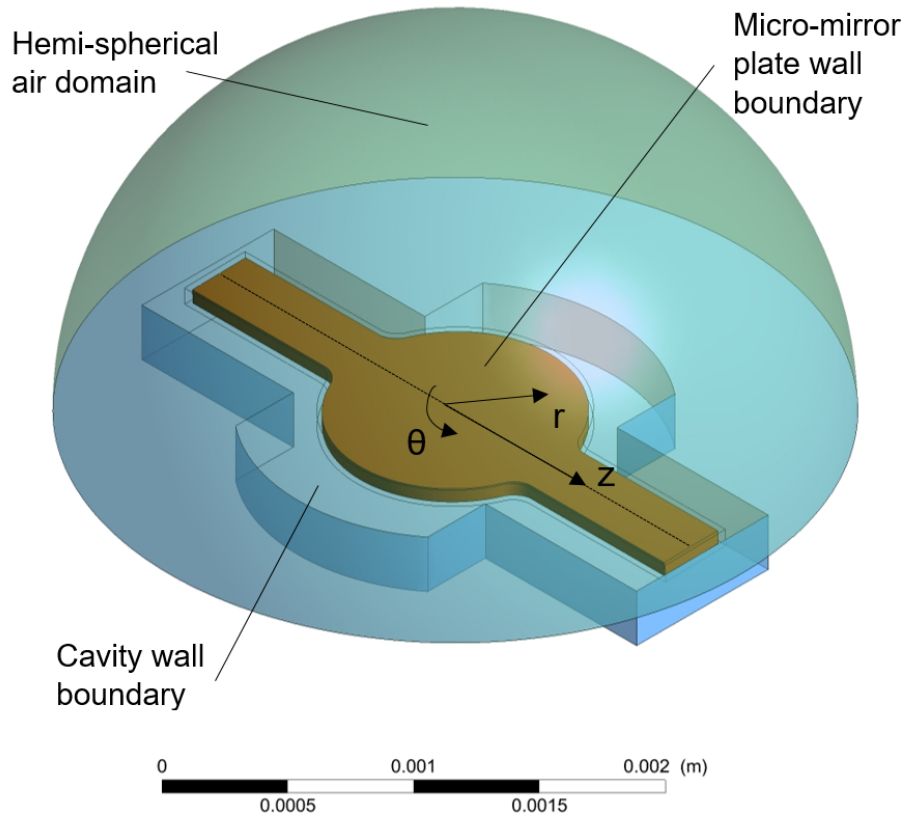
Figure 5-7: Navier-Stokes model of micro-mirror structure and cavity in ANSYS Fluent

An assessment of the temporal and spatial resolution influences on the numerical solution was performed at the target micro-mirror operation (f_s = 21.5 kHz; θ_{max} = 12°). For all subsequent runs, 3 oscillation cycles and 100 time steps per cycle were simulated while 50 iterations were performed during every time step to ensure solution convergence and stability. Post processing of results was performed using the methodology described in Section 5.2.1.2 in order to deduce the aerodynamic moment acting on the rotating structure after the end of each time steps. The resulting fluid flow velocity streamlines along the micro-mirror mid-plane together with the static pressure distribution along the mirror surface are shown in **Figure 5-8**, **Figure 5-9** and **Figure 5-10**.

(a)

(b)
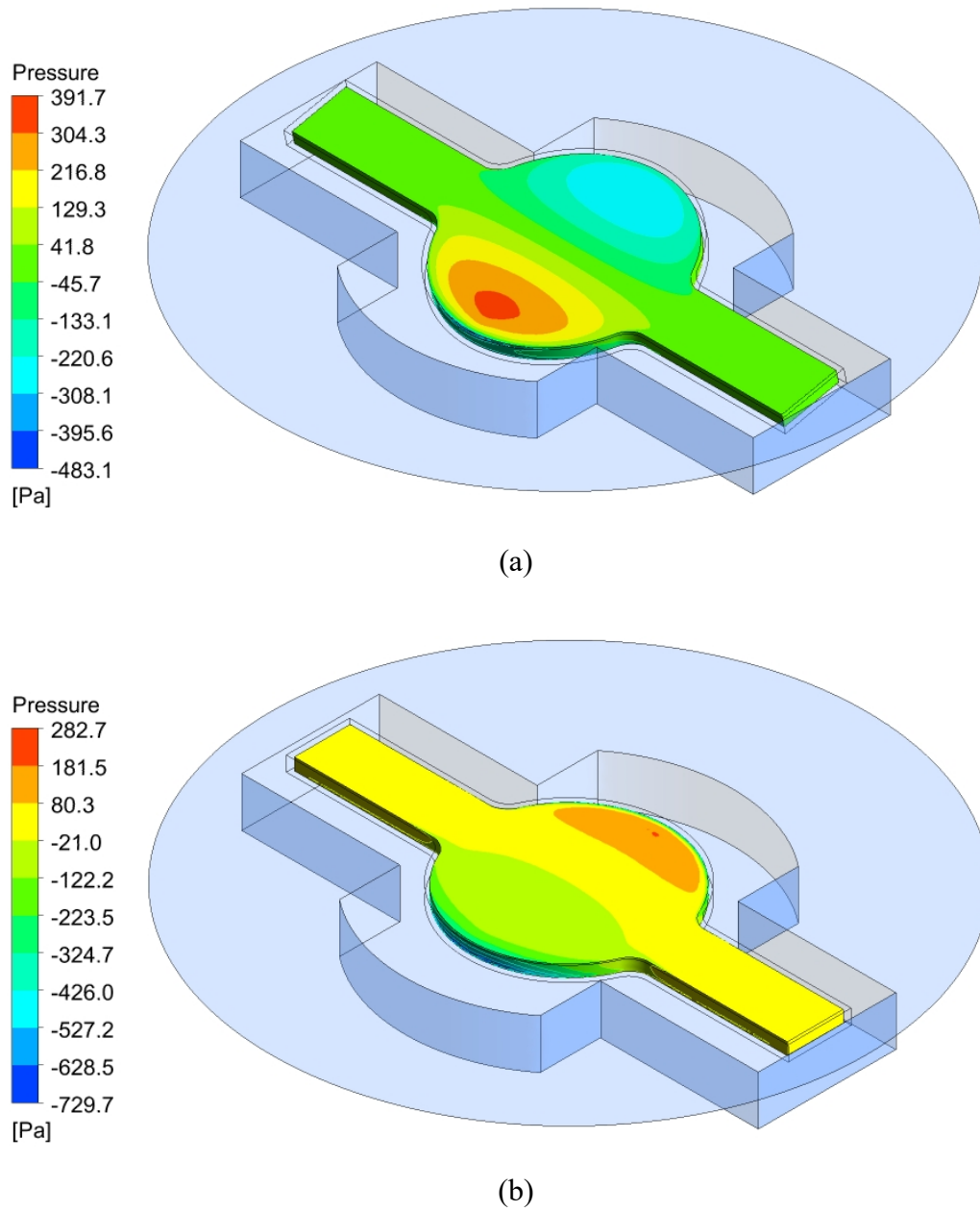
Figure 5-8: Contour plots showing the static pressure distribution on mirror plate surface at the instant when (a) $\theta(t) = 12°$ (b) $\theta(t) = 0°$ with a scanning amplitude, θ_{max} of 12°

73
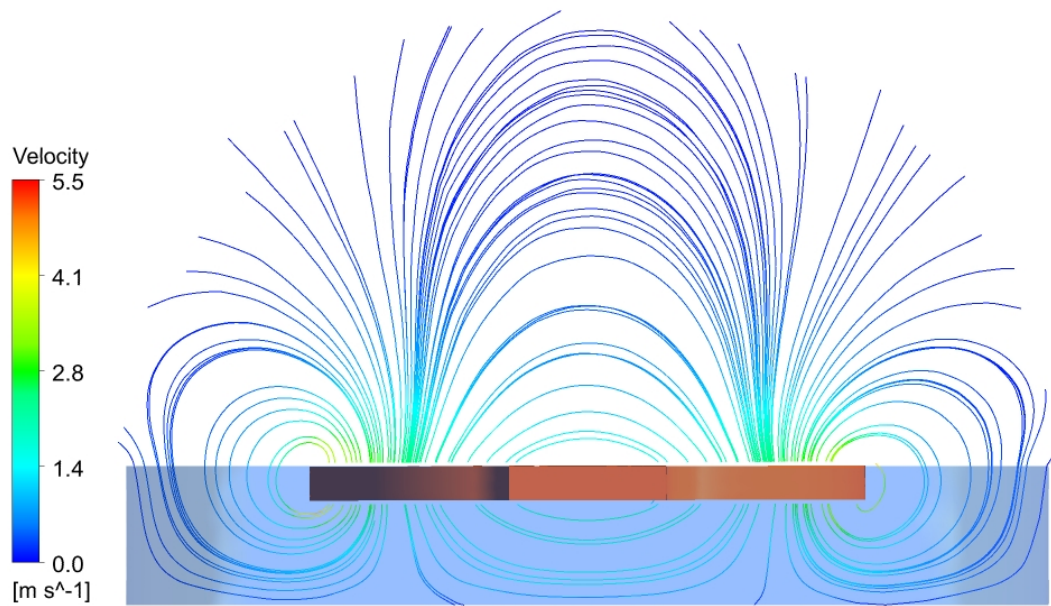
(a)
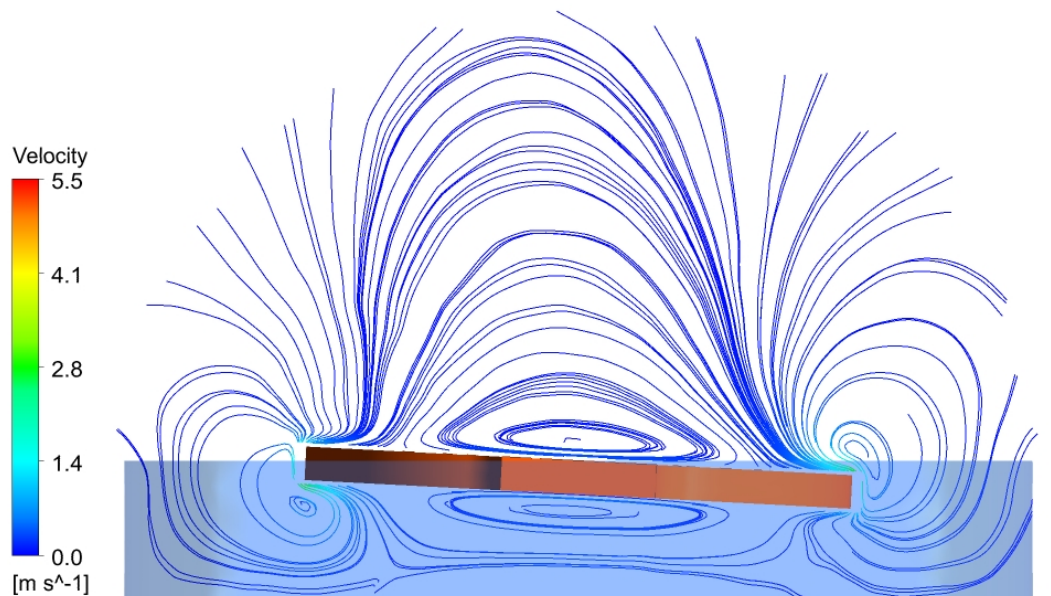
(b)

Figure 5-9: 2-D flow velocity streamline plots in the micro-mirror mid-plane
at the instant (a) $\theta(t) = 0°$; (b) $\theta(t) = 3°$ with a scanning amplitude, θ_{max} of $3°$

(a)

(b)
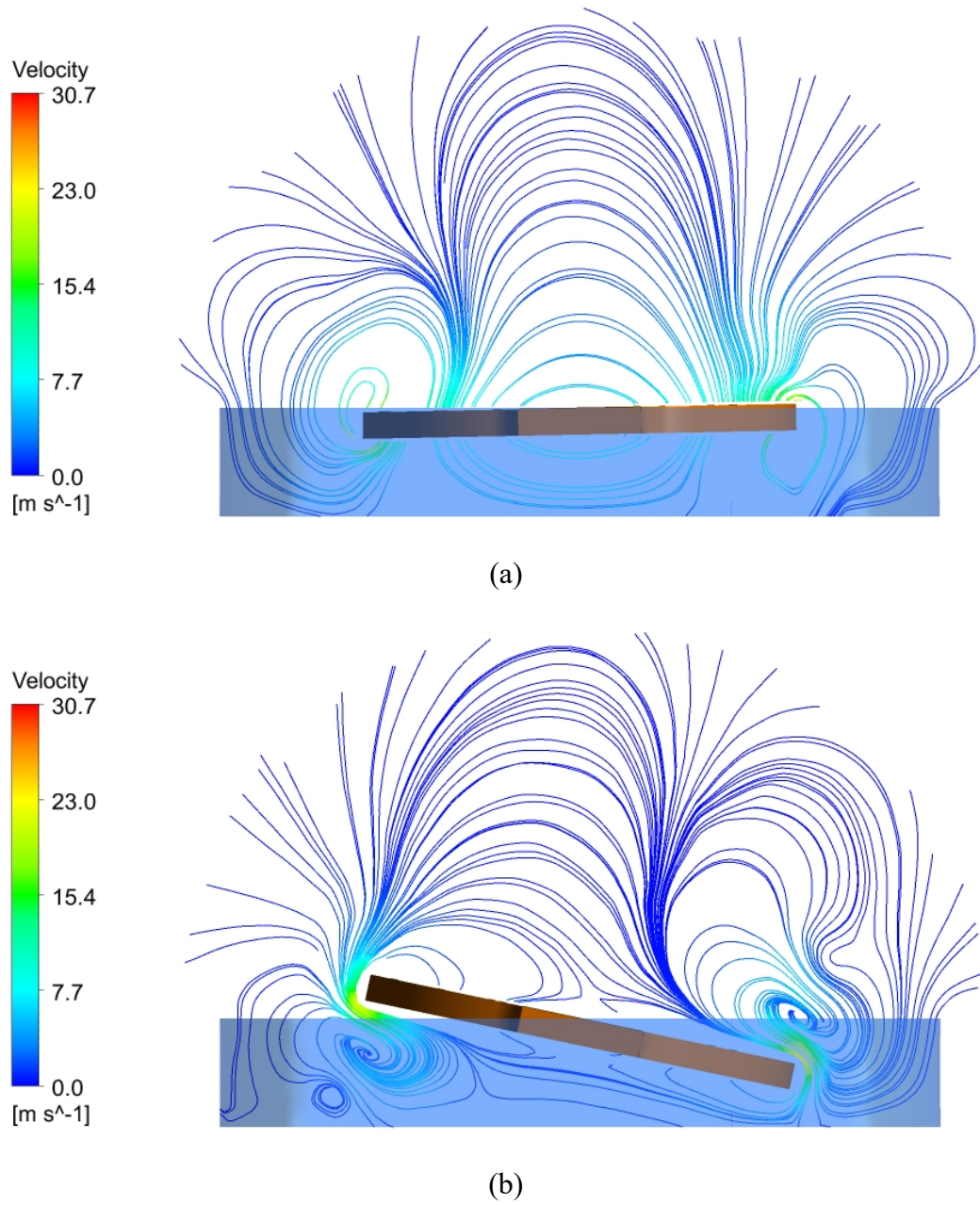
Figure 5-10: 2-D flow velocity streamline plots in the micro-mirror mid-plane
at the instant (a) $\theta(t) = 0°$; (b) $\theta(t) = 12°$ with a scanning amplitude, θ_{max} of 12°

75

5.2.2.2   Results and discussion

At the operating frequency, the mirror wake behaves in an inviscid manner and in fact, the viscous moment component, M_{visc} is very small compared to the pressure component, M_{press} as shown in **Figure 5-11**. Moreover, M_{plate} is 73.5° out-of-phase from the angular velocity for θ_{max} = 12° and so unlike the angular comb structure flow domain, $M_i > M_d$. This is in accordance with equations for high frequency oscillatory flow derived by Zhang & Stone [86], where the out-of-plane added mass component is predominant compared to the in-phase damping moment. **Figure 5-9** and **Figure 5-10** provide better insight on the different flow regimes developing at low and high θ_{max}. In the case of θ_{max} = 12°, flow separation occurs leading to vortical diffusion towards the surrounding fluid. Vortex-to-vortex interactions between vortices diffused from successive cycles can also be noted, which is analogous to the formation of vortex rings behind an oscillating disc in out-of-plane translation [92].

The aerodynamic moment is sinusoidal in time as shown in **Figure 5-11** and provides the possibility for the damping moment amplitude, $|M_d|$, to be calculated from the real part of M_{plate} (in-phase with $\dot{\theta}$). The variation of the simulated $|M_d|$ with θ_{max} is compared to the theoretical estimations from (5.7), (5.9) and (5.11) presented in Section 5.1.2. The quadratic relationship between M_d and θ_{max} for $Re_m \gg 1$ is in agreement with the form drag equation for laminar flow, as shown in **Figure 5-12**. Squeeze film damping based on lubrication theory is not applicable to high performance resonant micro-mirrors. Additionally, for a 1 mm micro-mirror oscillating above 20 kHz, the unsteady Stokes model is only valid for $\theta_{max} < 2°$ due to the pressure-driven flow instabilities at high angular velocities.

For an object with oscillatory motion, the instantaneous drag coefficient, C_d defined in (5.12) is not constant but varies periodically according to the mirror's scan angle. An averaged drag coefficient over one cycle can be deduced from N-S simulation results by comparing the E_{loss} equations: (5.13) and (5.14) as shown in (5.18). The average drag coefficient of the STM micro-mirror is 4.08.

$$C_d = \frac{\int_0^{1/f} M_{plate}(t).\dot{\theta}(t)dt}{16/15 \, \rho \pi^3 f^2 R^5 \theta_{max}{}^3} \tag{5.18}$$

N-S simulations were also performed on an unbounded, simplified version of the STM micro-mirror model consisting only of a circular plate in a spherical domain. C_d of the oscillating circular plate under out-of-plane rotation is 2.42, in contrast with $C_d = 1.11$ for a fixed disc in steady axial flow. By deducing C_d at each simulated θ_{max}, **Figure 5-13** demonstrates that the assumption of a constant C_d is valid for $Re_m > 350$. In reality, C_d is dependent on Re_m and the asymptotic relationship deduced from the N-S simulations is in agreement with published damping measurement results [80]. From a MEMS design perspective, the damping coefficient, c_D is required for system-level modelling. **Figure 5-14** demonstrates that the predicted damping coefficient from the N-S model is not constant, however the linear approximation, derived from (5.12), is sufficiently accurate within the operating window of the micro-mirror under test.
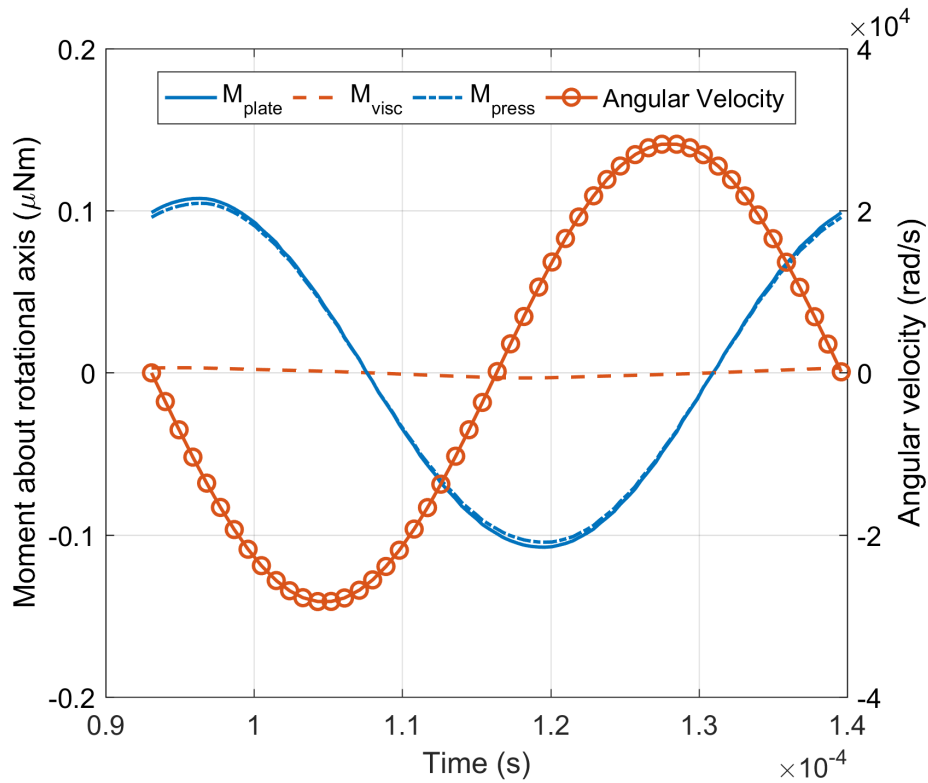
Figure 5-11: The total aerodynamic moment together with the pressure and viscous components acting on the mirror plate ($\theta_{max} = 12°$)
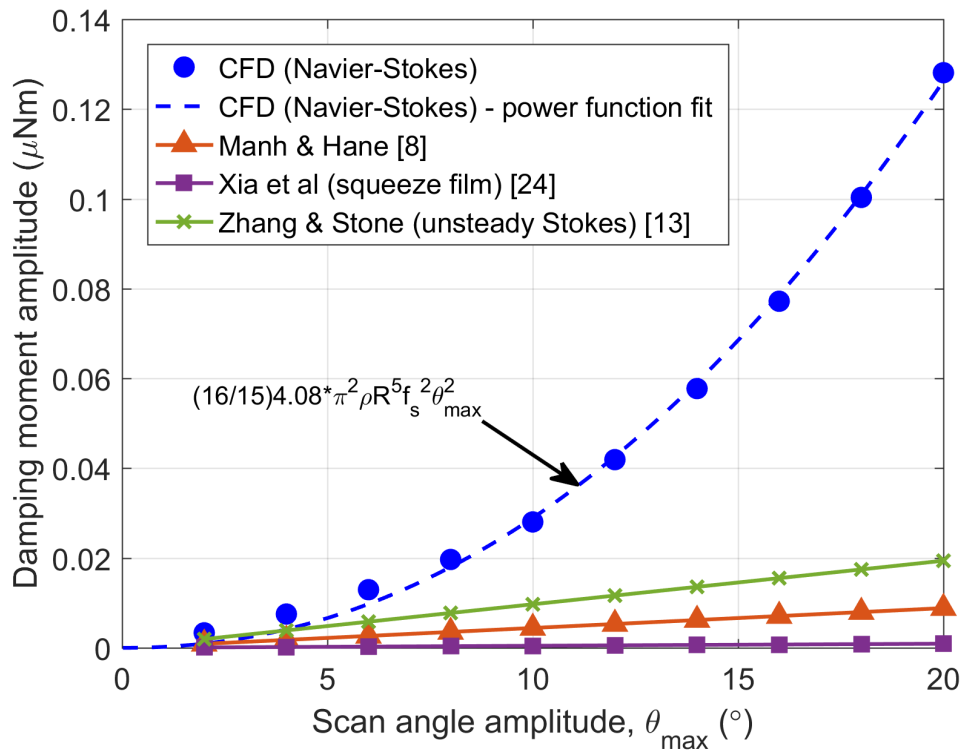
Figure 5-12: Mirror plate damping moment, M_d amplitude versus scan angle amplitude as predicted from numerical and analytical models
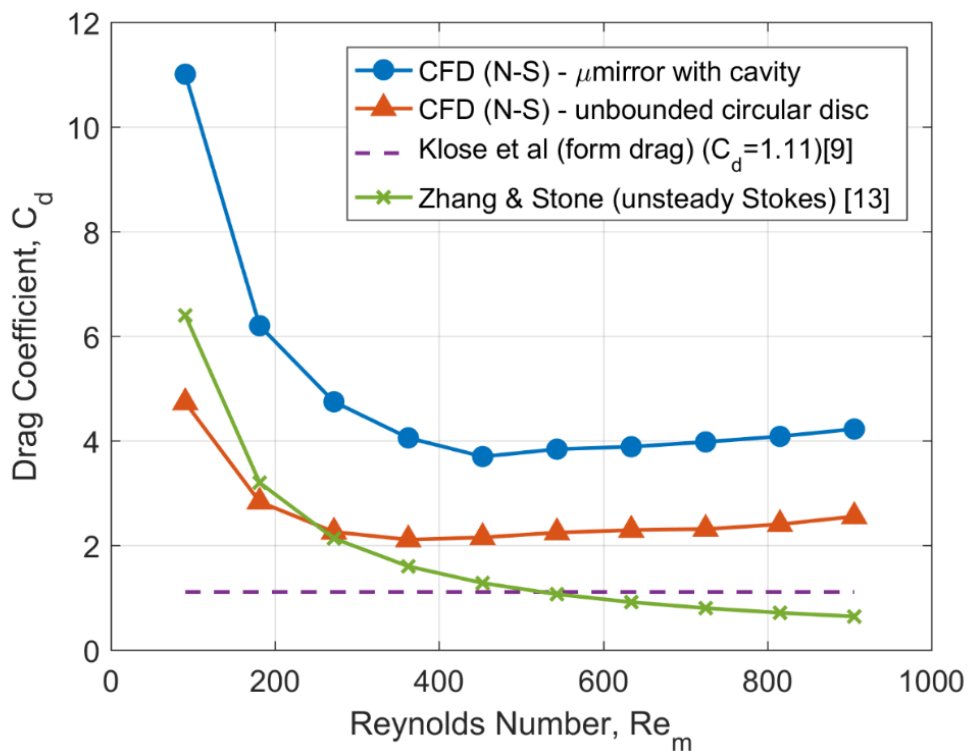
Figure 5-13: The effect of Re on the drag coefficient of the torsional micro-mirror plate
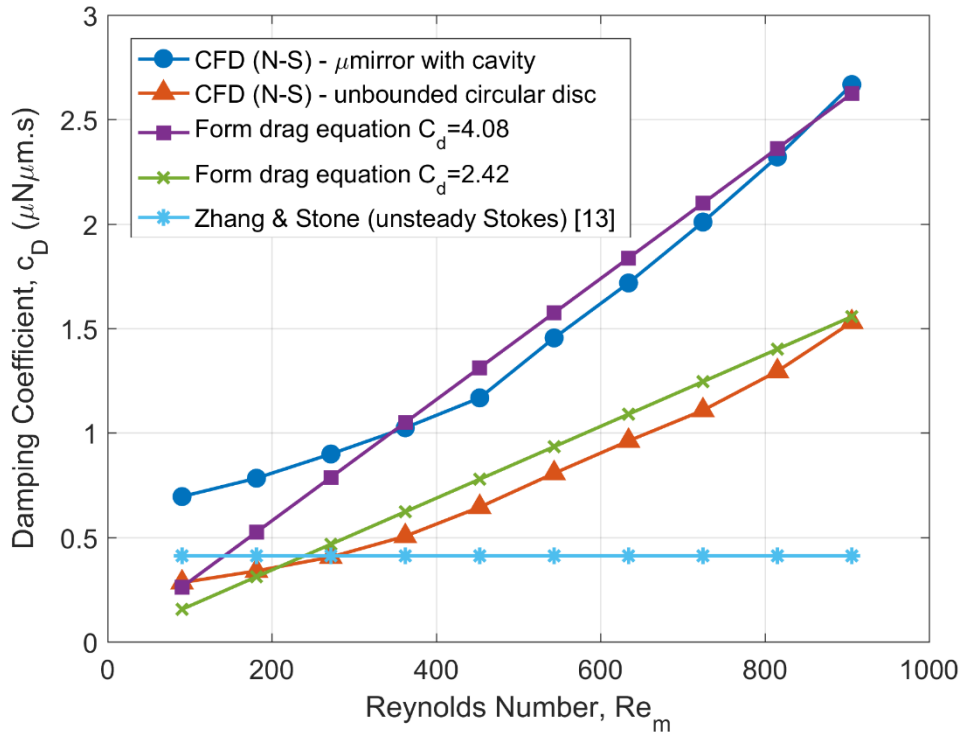
Figure 5-14: The effect of Re on the damping coefficient of the torsional micro-mirror plate

A comparison between Q obtained from the comb structure and mirror plate N-S models is presented in **Figure 5-15**. The damping loss due to mirror plate drag overcomes the comb structure loss above a θ_{max} of 5°, indicating that air drag forces are predominant at high velocities while comb structure viscous flow has a greater effect on the overall Q at lower velocities. However, the relative damping contributions from both sources depend on the design of comb structure-driven micro-mirrors. Moreover, if micro-mirror drag is predominant at the target f_s and θ_{max}, the number of comb fingers can be increased without significantly reducing the overall Q, thus allowing for a lower drive voltage requirement. **Figure 5-15** also shows that mirror-cavity flow interactions further reduce the mirror plate Q especially at high oscillation amplitudes.
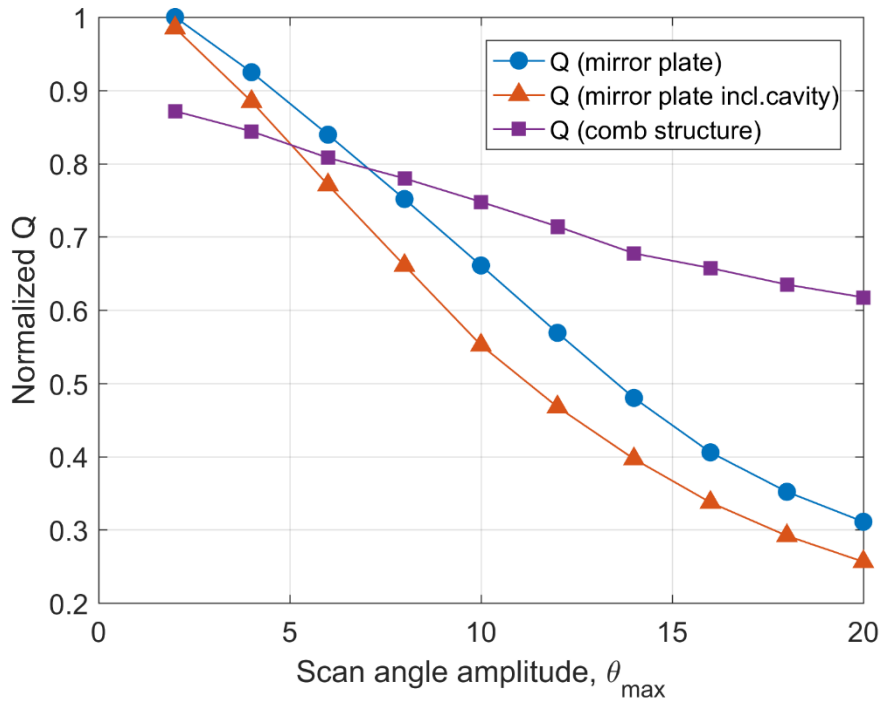
Figure 5-15: Variation of the quality factor with scan angle amplitude from the main air damping micro-mirror sources

5.3   Quality Factor Measurements

To validate the CFD damping results the PSD-based measurement system described in Section 4.2.1 was set-up in order to deduce Q from the decay rate of the damped free oscillations of the resonating micro-mirror. Given that Q is dependent on scan angle, the non-constant optical angle decay rate was deduced by fitting a decaying exponential function to a rolling window (**Figure 5-16**) using the least squares method. The Q-θ_{max} results from the micro-mirror under test (**Figure 5-17**) were obtained using a 50 cycle rolling window with a 10-cycle increment. The decay rate of the measured Q with scan angle amplitude is in agreement with the simulation results. Repeated readings were taken and multiple samples were characterized. However, it has to be noted that results below $\theta_{max} = 2°$ are affected by a low signal-to-noise ratio.
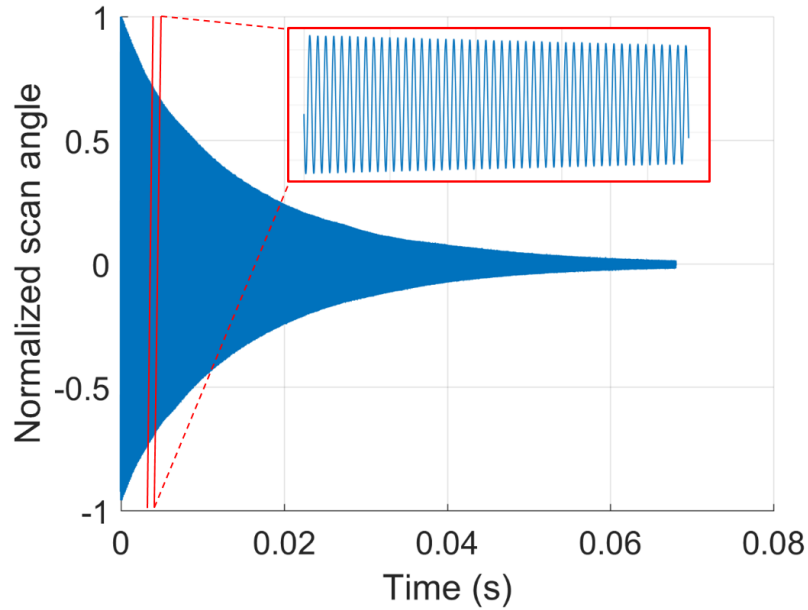
Figure 5-16: Measured damped free oscillations of the scanning micro-mirror
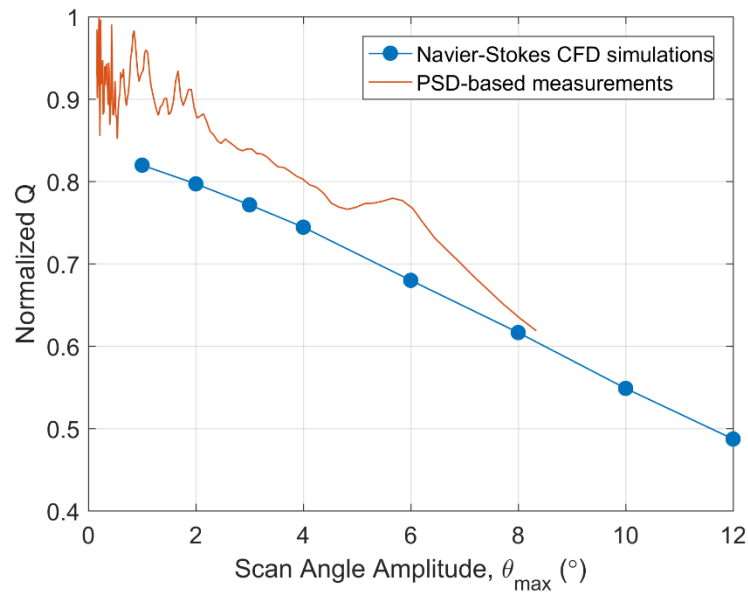
Figure 5-17: Q variation with θ_{max} from Navier-Stokes simulations using ANSYS Fluent and PSD-based measurements

5.4   Electrostatic–Fluidic Analysis

The results obtained from the CFD simulations can be used to determine the achievable θ_{max} for a given drive voltage, $V(t)$. At maximum torsional mode amplification, the induced electrostatic energy, E_{el} is balanced by the energy lost due to air damping over one oscillation cycle. The electrostatic moment generated by the vertical comb drive structure is dependent on the variation of the capacitance, C with scan angle [111]. Finite

element simulations were performed to obtain the relationship between C and θ as shown in **Figure 4-3** in order to derive E_{el} as in (5.19).

$$E_{el} = \int_{0}^{T} \left[\frac{dC(t)}{dt} V(t)^2 + \frac{dV(t)}{dt} C(t).V(t) \right] dt \qquad (5.19)$$

A phase angle of 45° between $V(t)$ and $\theta(t)$ was applied to the E_{el} calculations, which was deduced from peak θ_{max} measurements at different sinusoidal drive voltage amplitudes. A drive frequency down sweep was performed to search for the maximum optical angle response of the 21.5 kHz STM micro-mirror. An increase in the resonant frequency of less than 20 Hz, resulting from the non-linear electrostatic drive torque, was observed when the drive voltage is varied from 60V$_{pk}$ to 160V$_{pk}$. This shift in micro-mirror frequency has a negligible influence on E_{el} and E_{loss} derived from simulations. Good agreement in the V_{pk}-θ_{max} relationship is achieved between the measurement and simulation results as shown in **Figure 5-18**. It has to noted that the accuracy of the damping and electrostatic results are compromised by possible laboratory environment deviations from the standard air pressure, temperature and viscosity considered in the CFD simulations. Furthermore, the results are conditioned by the alignment and measured distance between the components of **Figure 4-5**.
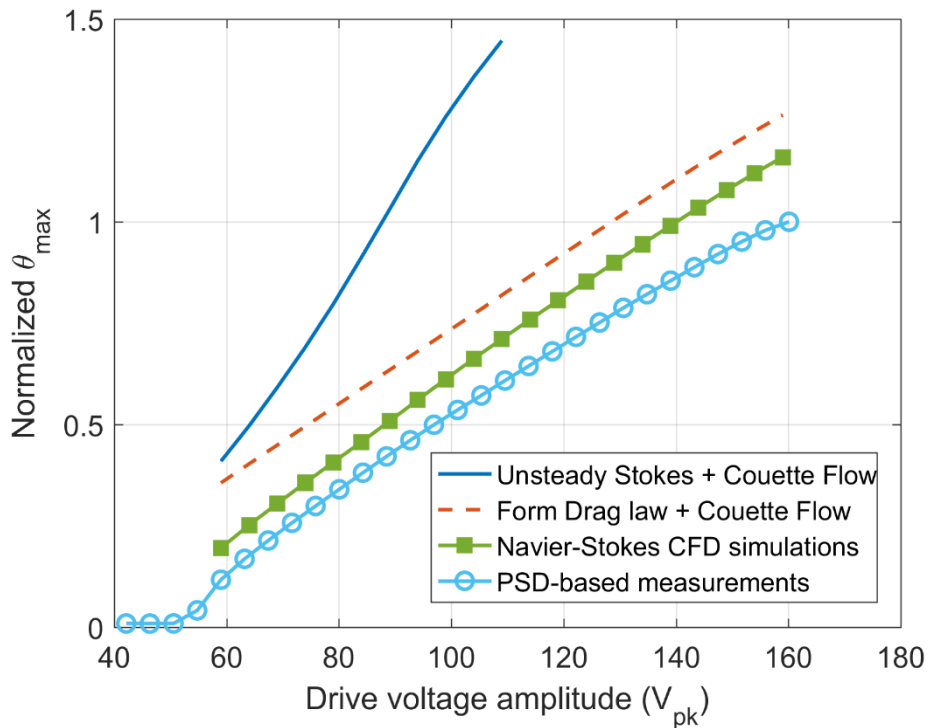
Figure 5-18: Normalized maximum scan angle amplitude versus drive voltage amplitude

5.5   Further Analysis on Micro-Scanner Aerodynamics

In general, the drag coefficient C_d, of steady moving objects is not constant in the laminar flow regime ($1 < Re < 2300$), which coincides with the operating region of resonating micro-scanners. The experimental-evaluation of C_d for a scanning micro-mirror plate is often hindered by additional damping effects resulting from the oscillating actuator structures [80].

In the absence of an empirical expression for C_d of circular micro-plates oscillating in out-of-plane rotation, the micro-scanner damping characteristics can be analysed in detail using computational fluid dynamic (CFD) simulation methods. A comprehensive CFD study was recently performed to evaluate the drag coefficient and flow regimes of a circular plate undergoing translational out-of-plane oscillations having Re values in the range 100 [92]. On the other hand, the physical processes leading to non-linear damping observed in millimetre-scale micro-mirrors with large amplitude oscillations are not yet fully understood [71]. The aim of this study is to investigate the fundamental flow characteristics of a circular plate oscillating in out-of-plane rotation and to deduce the parametric dependence of the drag coefficient of a circular-shaped resonating micro-scanner using three-dimensional transient CFD analysis. The flow characteristics of the oscillating circular plate will be analysed in terms of Re_m as previously defined in (5.8).

5.5.1   Description of the CFD Model

The numerical simulations presented in this section are based on the CFD modelling techniques of Section 5.2.2, which have been experimentally validated using a 21 kHz electrostatically actuated resonating micro-mirror. A spherical computational fluid domain is developed for the simulation of the flow around an oscillating disk as shown in **Figure 5-19**. Navier-Stokes simulations are performed in ANSYS Fluent using the PISO pressure-velocity coupling scheme for transient analysis. The origin of the computational domain coincides with that of the surface wall boundaries of the circular disk. The disk oscillates in out-of-plane rotation about the x-axis. A no-slip velocity boundary condition is imposed on the disk surface while the pressure is set zero at the outer spherical boundary. Hexahedral elements are used to discretize the entire computational domain and the grid resolution is gradually increased towards the disk surface to resolve the high velocity gradients present in this region.

In order to realize the oscillatory motion of the unbounded disk, the deforming mesh method is applied. The grid is allowed to deform in order to accommodate the imposed angular displacement of the rigid disk surface boundary. In spite of grid deformation, the topology of the mesh is retained from the initial time step (i.e. no re-meshing takes place between time steps). The mesh quality and validity is preserved by applying a grid smoothing method.
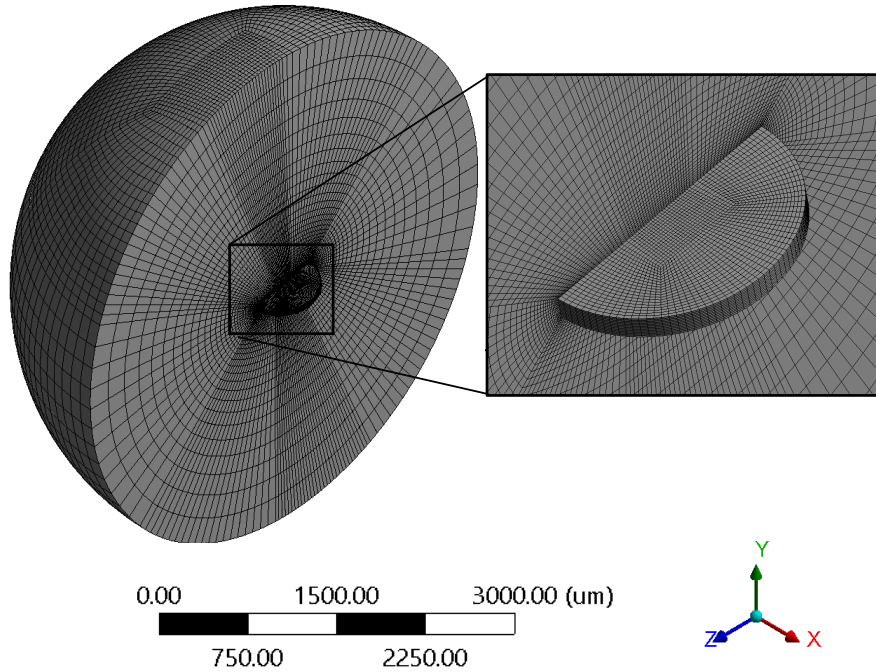
Figure 5-19: A cross-section of *Mesh_1*: the computational fluid domain surrounding the unbounded circular plate surface - ($R = 500\mu m$; $t_m = 65\mu m$; domain radius = 3.75mm; number of elements: 268000)

A sinusoidal time-varying angular velocity profile was prescribed via a user-defined function to enable disk motion. At each time step, the elemental viscous shear stress and pressure components acting normal to the rotating surface boundary are combined, as in (5.16), to obtain the temporal aerodynamic moment, M_{plate} acting on the scanning circular plate. The real part of M_{plate} is defined as M_d, which is in phase with the disk's angular velocity.

An assessment of the temporal and spatial resolution influences on the numerical solution is performed at the reference micro-scanner operating point ($f_s = 20$ kHz; $\theta_{max} = 12°$). The convergence of C_d was analysed with respect to domain size, number of grid elements and number of time steps per cycle. The radius of spherical fluid domain is set to $7.5R$

and the element height adjacent to the rotating boundary surface varies is less than 2 μm. For the parametric evaluation detailed in **Table 5-1**, 3 oscillation cycles and 500 time steps per cycle were simulated while 50 iterations were performed during every time step to ensure solution convergence and stability based on the aerodynamic moment amplitude and phase.

5.5.2   Results and Discussion

Two underlying characteristics are observed within the design parameter and operating ranges listed in **Table 5-1**: (i) M_{plate} is mainly composed of the pressure force component indicating a predominantly inviscid behaviour of the surrounding fluid; (ii) M_d is a small fraction of the non-dissipative inertial moment component, which is out-of-phase relative to the plate motion. These flow characteristics are typical for oscillatory motion involving mass displacement of fluid whereby the far-field (potential flow region) does not instantaneously adjust to the disk oscillations.

Table 5-1: Input parameters for the resonant micro-scanner CFD models

Parameter	Description	Range	Step Size
θ_{max} (°)	scan angle amplitude	2-20	2
f_s (kHz)	scan frequency	2-36	5
R (μm)	circular plate radius	250-950	125
t_m (μm)	circular plate thickness	20-80	15
h (μm)	micro-mirror cavity depth	200-600	200

The velocity field obtained at low oscillation amplitude ($\theta_{max} = 2°$), shown in **Figure 5-20(a)**, is in agreement with velocity streamline patterns obtained from unsteady Stokes flow solutions [86]. On the other hand, vortex shedding from the plate edges can in fact be observed in **Figure 5-20(b)** for $\theta_{max} = 12°$ while the cycle of nucleation, growth and disappearance of the viscous eddies is depicted in **Figure 5-21**. The spatial definition of the vortices in ANSYS Fluent is determined using the three-dimensional vortex Q-criterion [125]. The simulation results demonstrate that within the plate operating range considered, the surrounding fluid transitions from Stokes to inviscid flow behaviour.

For $50 < Re_m < 1000$, a quadratic relationship between M_d and θ_{max} is deduced from the simulation results, in agreement with the form drag equation of (5.12). Given the periodic variation of C_d, cycle-averaged coefficient values were derived from (5.18) for each simulation run.

(a)

(b)
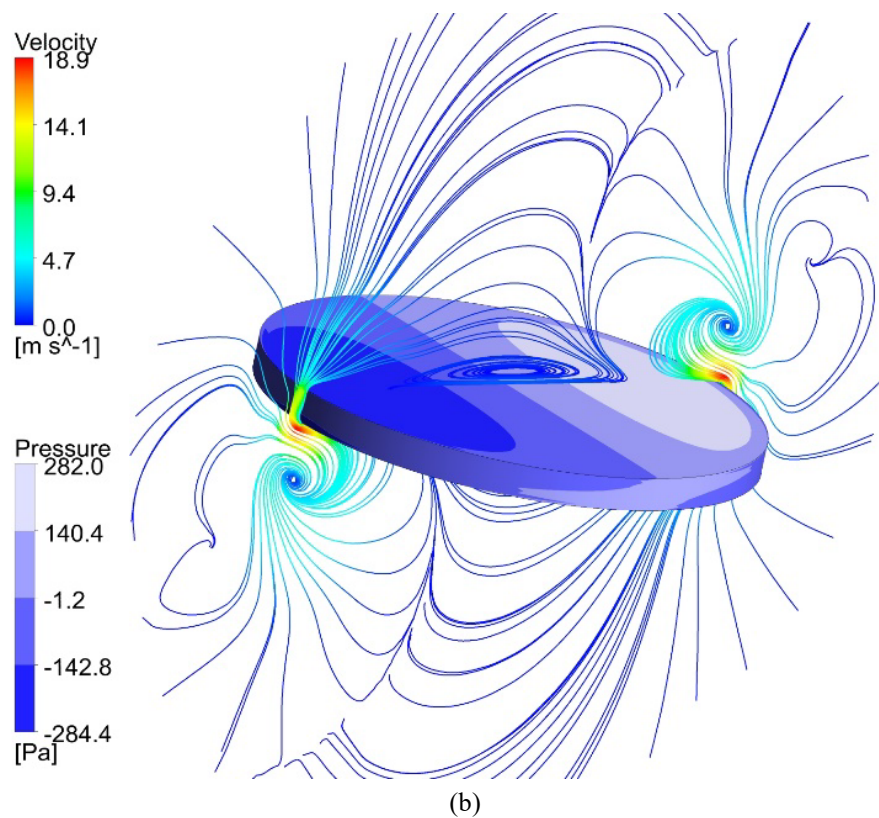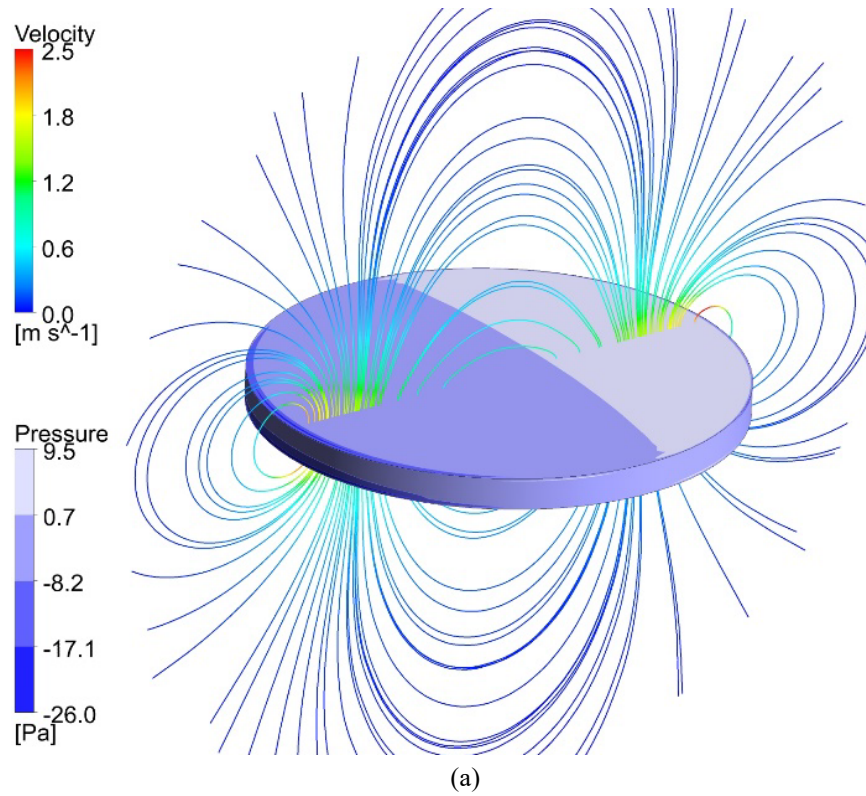
Figure 5-20: Air pressure distribution on the oscillating plate surface and air velocity streamlines along the mid-plane at f_s = 20 kHz, $\theta(t) = \theta_{max}$ for (a) θ_{max} = 2° (b) θ_{max} = 12° *[obtained using Mesh_1]*

86

oscillating 1 mm
circular plate

attached
vortex
core
region

$\theta(t) = 0$

separated
vortex
core
region

$\theta(t) = \theta_{max}$
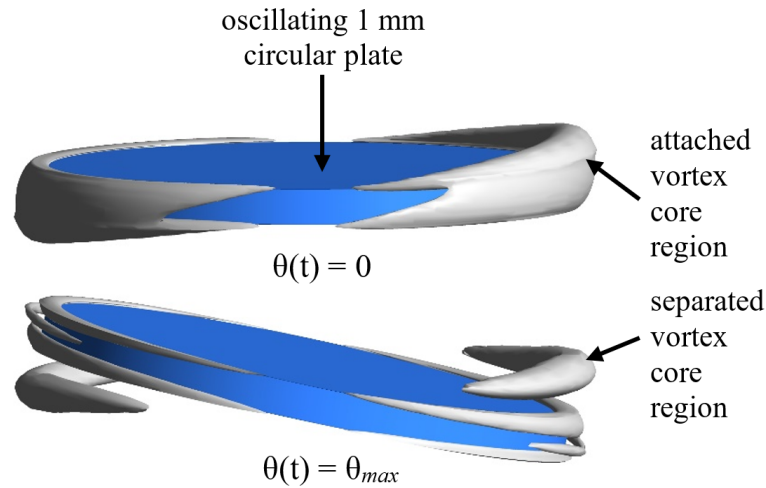
Figure 5-21: Vortical structures identified on the basis of the *Q-criterion* (defined as the second invariant of the velocity gradient tensor) during a quarter oscillation cycle (Re_m =448) *[obtained using Mesh_1]*

An evaluation of the parametric dependence of the drag coefficient was performed using the unbounded disk CFD model (*Mesh_1*). The influence of f_s and θ_{max} at a fixed R (500 μm) and t_m (65 μm) is demonstrated in **Figure 5-22**. It can be seen that C_d can only be assumed constant at relatively high Re_m. Therefore, in the typical region of operation of high performance micro-scanners C_d is an asymptotic function of Re_m.
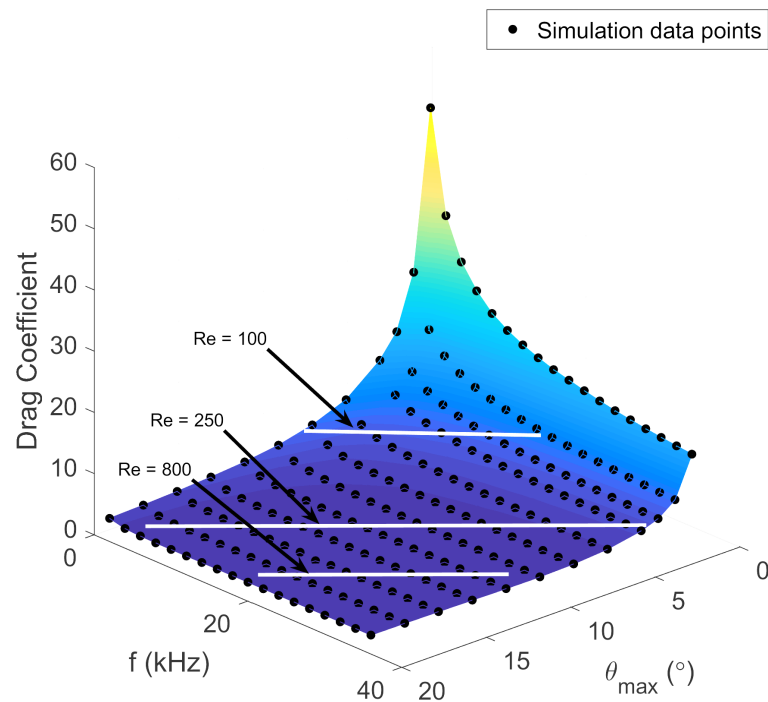
Figure 5-22: Scan frequency and scan angle amplitude dependence of the drag coefficient of a circular plate oscillating in out-of-plane rotation ($R = 500$ μm; $t_m = 65$ μm) *[obtained from Mesh_1]*

87

A general expression for C_d in terms of Re_m is deduced in order to evaluate the damping losses of the circular plate oscillating within the transition region of between the Stokes flow regime and the form drag flow regime. A total of 306 N-S simulation runs were performed using the *Mesh_1* CFD model whereby f_s, θ_{max} and R were varied within the parameter ranges defined in **Table 5-1**. The numerically-deduced C_d results are plotted in **Figure 5-23** for a range of $3 < Re_m < 3000$. It is observed that C_d is an asymptotic function of $Re_m.\theta_{max}$ and (5.20) is deduced by applying a least squares fit to the simulation data points:

$$C_d = \frac{10.9123}{\left(\mathrm{Re}_m .\theta_{max} \right)^{0.5645}} + 2.4073 \qquad (5.20)$$
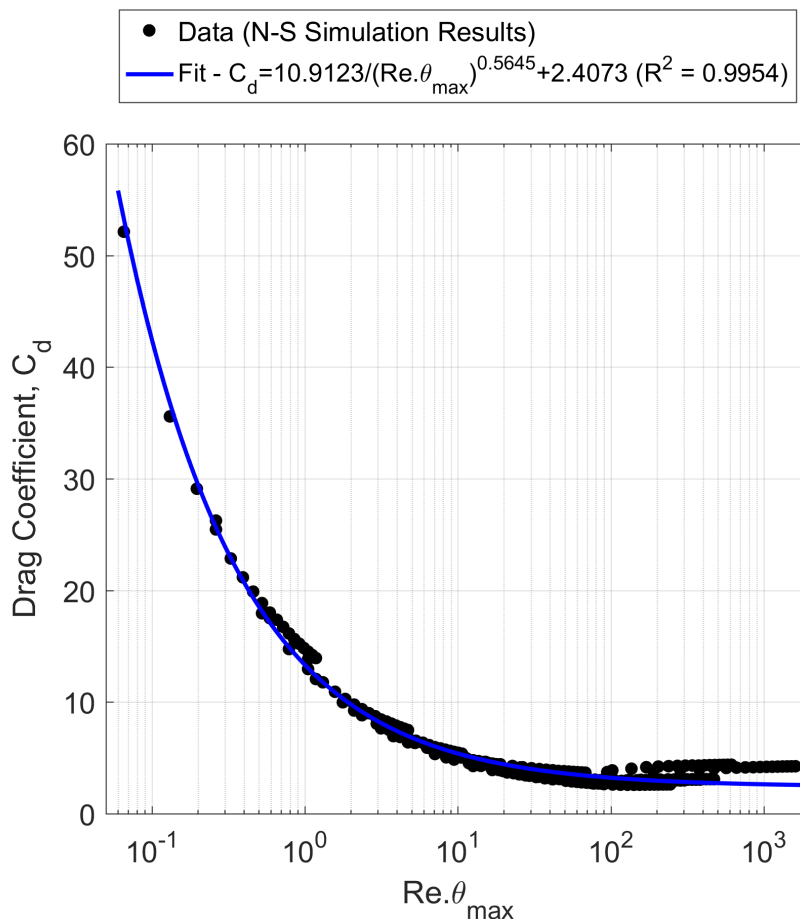
Figure 5-23: Dependence of the drag coefficient of a circular plate oscillating in out-of-plane rotation on the Reynolds number, Re_m; obtained from N-S simulation results using *Mesh_1* ($t_m = 65$ μm)

The variation of Q with scanning frequency and amplitude can be observed from the N-S simulation results plotted in **Figure 5-24(c)**. At low scan angle amplitude, the variation of Q with f_s is governed by the unsteady Stokes flow relation evident from a comparison between **Figure 5-24(a)** and **(c)**. In fact for $\theta_{max} < 1°$, an expression for Q can be deduced from the damping moment equation of (5.11). Equation (5.21) demonstrates that at low θ_{max}, Q is constant with response amplitude variations and is a function of the scanning frequency and the air viscosity.

$$\theta_{max} < 1° : Q = \frac{\rho_{Si} t_m \left(3R^2 + t_m^{\,2}\right)}{4.6232 R^2} \sqrt{\frac{f_s}{\mu \rho}} \tag{5.21}$$

On the other hand, by comparing **Figure 5-24(b)** and **(c)** at high scan angle amplitude, the variation of Q with θ_{max} is governed by form drag. A general equation for the estimation of the quality factor of circular micro-mirrors can be deduced from the drag coefficient expression of (5.20), which is valid for the flow regime: $3 < Re < 3000$. The moment of inertia of a circular plate rotating about an in-plane axis is: $I = \pi \rho_{Si} R^2 t_m \left(3R^2 + t_m^{\,2}\right)/12$. Therefore, provided that mirror plate drag is the predominant damping source, the quality factor of resonating circular micro-mirrors can be derived by substituting (5.20) into (5.14). Equation (5.22) can be also applicable to one directional circular micro-scanner designs which employ piezoelectric and electromagnetic modes of actuation.

$$Q = \frac{5\pi \rho_{Si} t_m \left(3R^2 + t_m^{\,2}\right)}{16 \rho C_d R^3 \theta_{max}} \tag{5.22}$$
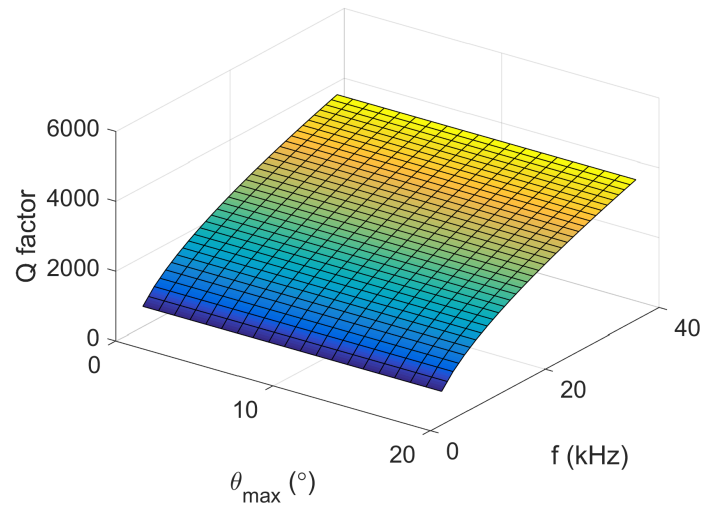
(a) Unsteady stokes flow: $M_d(f^3 R^4 \theta)$
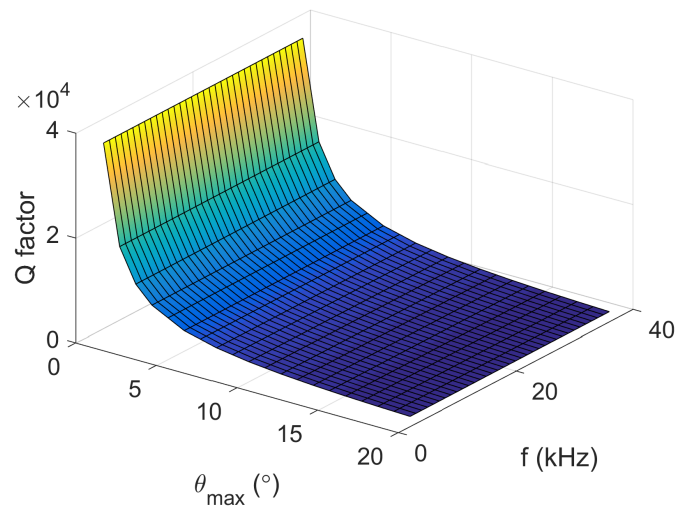
(b) Form drag: $M_d(f^2 R^5 \theta^2)$
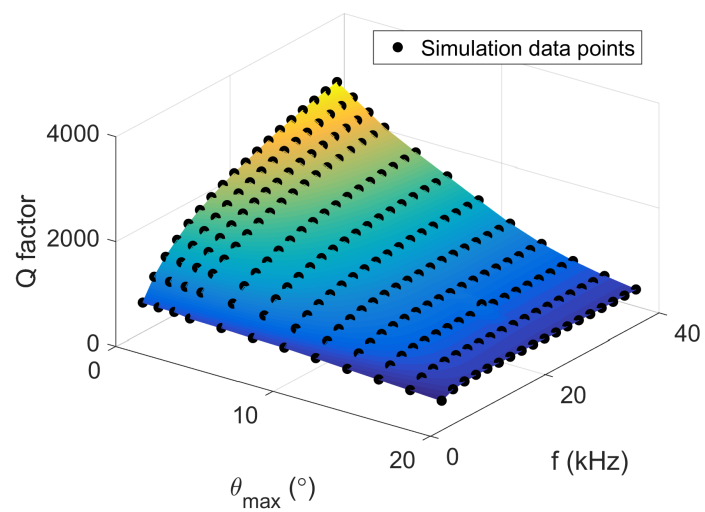
(c) CFD simulations

Figure 5-24: Variation of Q with oscillation frequency and amplitude for a circular plate oscillating in out-of-plane rotation (a) obtained from unsteady Stokes flow (b) form drag equation (c) transient N-S CFD simulations [$t_m = 65$ µm; $R = 500$ µm]

The drag coefficient expression of (5.20) has been deduced for a micro-mirror plate thickness of 65 µm. The plate thickness, t_m is not considered as a characteristic length for the definition of Re_m while the analytical damping moment equations of (5.7), (5.9) and (5.11) are independent of t_m. The dependence of the drag coefficient on the plate dimensions is displayed in **Figure 5-25**. A 51.2% increase in C_d is observed when t_m is reduced from 80 to 20 µm at $\theta_{max} = 12°$, $f_s = 20$ kHz and $R = 500$ µm. Therefore, simulation results demonstrate that plate thickness has non-negligible effect on the air damping losses in resonating micro-scanners. Analysis of the periodic flow development surrounding mirror plate indicates that the onset of flow separation (described in **Figure 5-21**) is facilitated with a thinner plate edge. Consequently, the effect of air damping on the quality factor of micro-scanners can be reduced by increasing the thickness of the device layer.
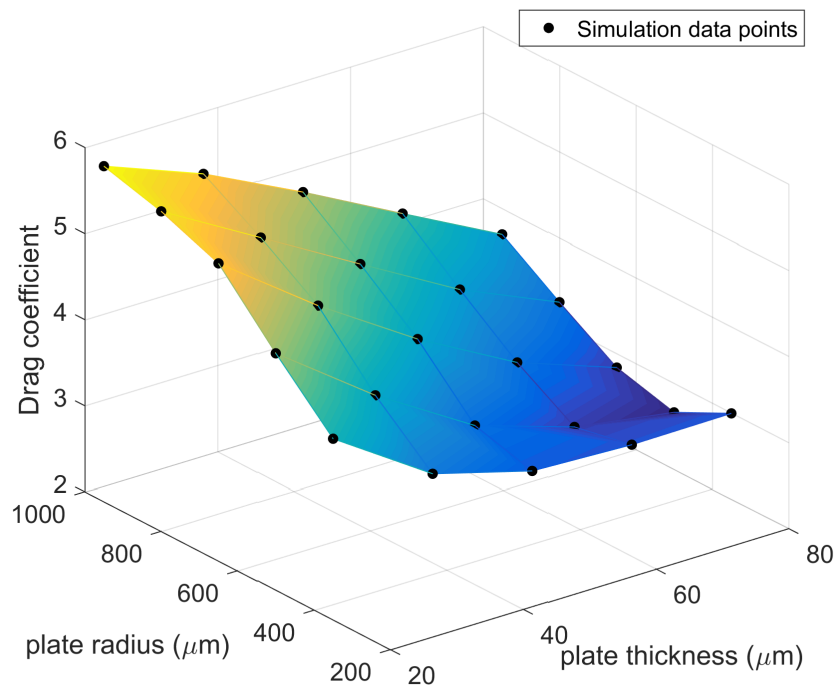
Figure 5-25: Radius and thickness dependence of the drag coefficient of a circular plate oscillating in out-of-plane rotation ($f_s = 20$ kHz; $\theta_{max} = 12°$) *[obtained from Mesh_1]*

Changes to the flow velocity field displayed in **Figure 5-20** are expected in micro-scanners due to the presence of the underlying cavity bottom surface. Resonating micro-scanner cavities are typically a few hundred microns deep to accommodate the high oscillation amplitudes of the mirror plate. Both factors render the assumption of

Poiseuille-type flow within the air cavity as inaccurate. The CFD model described in the previous section was modified as shown in **Figure 5-26** by including a wall boundary in order to emulate the underlying cavity of a micro-scanner. **Figure 5-27** indicates that the proximity of the cavity surface negatively impacts the quality factor for $\theta_{max}.R/h$ ratios higher than $\pi/12$.
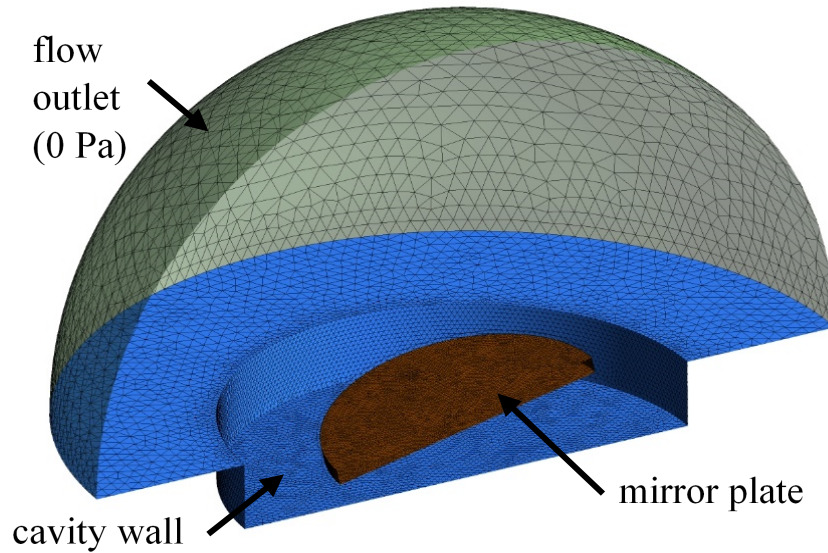
Figure 5-26: A slice of the computational domain with the cavity wall boundary included (Mesh_2)
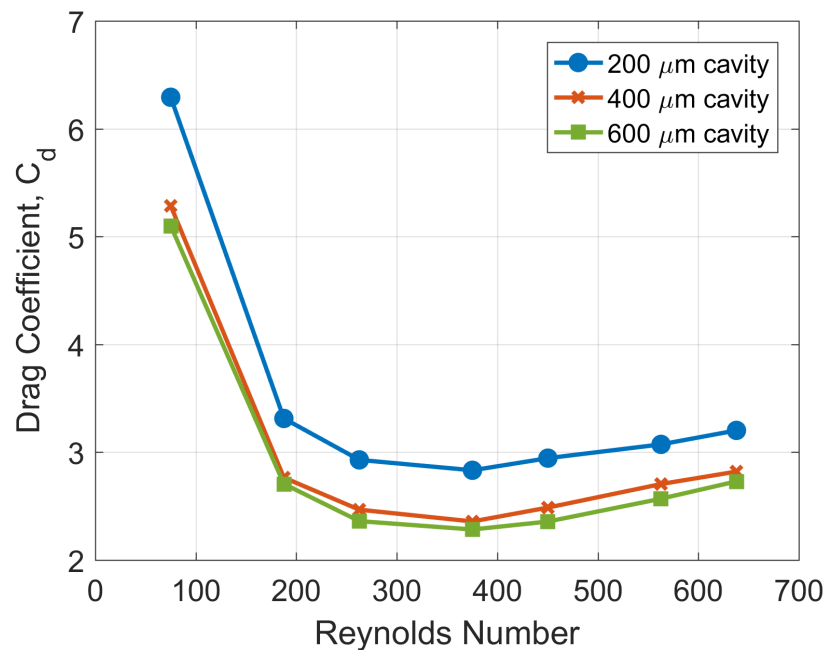
Figure 5-27: C_d variation with Re_m for different micro-scanner cavity depths, h ($f_s = 20$ kHz; R = 500 μm; $t_m = 65$ μm) [obtained from Mesh_2]

5.6   Conclusions

An in-depth analysis on the fluid-structure interactions of an electrostatic micro-mirror resonating at high frequency is presented. Transient Navier-Stokes simulations were performed on CFD models of an angular vertical comb actuator and a circular micro-mirror plate. The application of the *sliding mesh* technique for transient damping analysis of AVC structures is proposed. Results demonstrate that the overall Q decays with scan angle amplitude and the rate of decay is in agreement with optical measurements. This underlines the limitations of the Couette, Stokes and squeeze-film damping models at high oscillation amplitudes and Re. It has been demonstrated that pressure-driven flow separation and complex vortex-to-vortex interactions occur adjacent to the mirror plate at high scan angle amplitudes.   Simulation results verify that for high frequency resonant micro-mirrors, the mirror drag damping moment varies quadratically with scan angle amplitude. This demonstrates that non-linear damping is present in micro-scanners intended for micro-projection display applications irrespective of the actuation method. The predicted damping moment of high performance micro-scanners, obtained from transient N-S simulations, is generally underestimated by the analytical damping models. For this reason, expressions for the drag coefficient and the quality factor are proposed in order to quantify the air damping losses of a circular mirror plate oscillating in out-of-plane rotation and operating within the flow regime of $3 < Re > 3000$. The effect of mirror plate thickness on the air drag damping losses was found to be non-negligible and in general, an increase in damping moment occurs with the reduction of t_m. Moreover, evidence of the effect of mirror-cavity flow interactions on the mirror plate damping moment was also demonstrated in spite of the fact that squeeze-film damping based on lubrication theory was found to be negligible.

6   DYNAMIC DEFORMATION

Currently the drive towards consumer miniaturized display systems offering high optical resolution has resulted in large demands on f_s, θ_{max} and size of one-directional resonant micro-mirrors. An increase in the three main scanning performance characteristics is limited by power consumption, overall device footprint and non-planarity of the micro-mirror surface. Out-of-plane deformation resulting from dynamic acceleration forces tends to be the most important limiting factor for high performance imaging and display applications [1].

Analytical formulas to predict the dynamic deformation of different micro-mirror geometries have been derived from one-dimensional plate bending theory [98, 97]. However deformation surface profiles simulated using finite element analysis suggest limitations to the applicability of such equations [32, 57]. In this chapter, the following research questions will be addressed.

i.   Can micro-scanner dynamic deformation be accurately predicted from one-dimensional plate bending theory?

ii.   Can dynamic deformation be reduced by optimizing the mirror layout and without modifying the fabrication process?

The derivation of the dynamic deformation of rectangular-shaped micro-scanner is presented in Section 6.1. In Section 6.2, the influence of micro-mirror plate geometry on the dynamic deformation is investigated using FE simulations. Modifications to the plate bending calculations are proposed in Section 6.3 and the gimbal-type support structure is introduced and evaluated in Section 6.4. Parts of the work presented in this chapter has been published in [126, 127].

6.1   Classical Plate Theoretical Analysis

The most basic design of a resonating micro-scanner consists of a mirror plate suspended by two beams acting as torsional springs as shown in **Figure 6-1**. Micro-scanner dynamic deformation, δ, is defined as the deviation from mirror planarity resulting from dynamic inertial loading (see **Figure 6-2**).
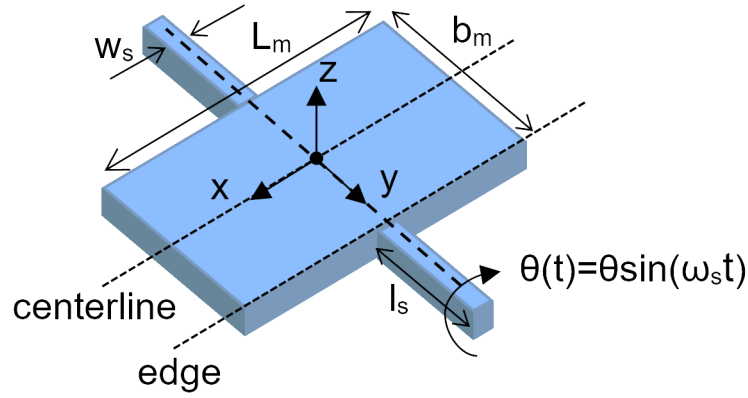
Figure 6-1: Dimensional notations for a rectangular micro-mirror directly suspended by torsional springs along $x = 0$
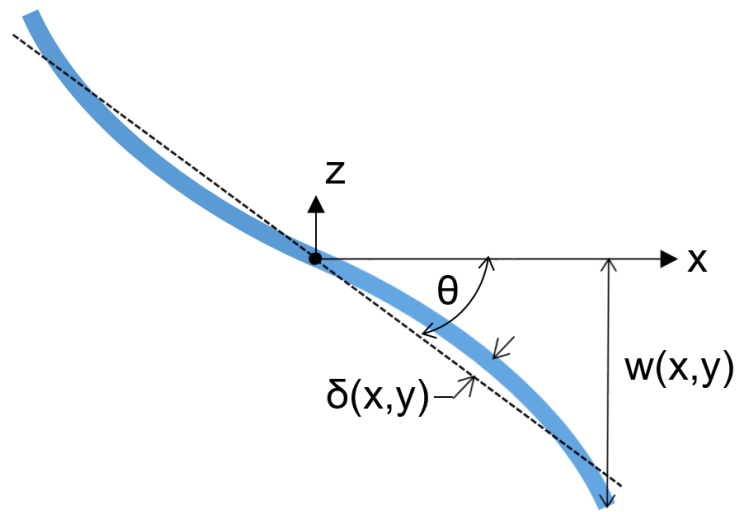
Figure 6-2: Cross-section view of micro-mirror showing the bending deflection w and the dynamic deformation, δ profiles due to inertia loading; $\delta(x,y)$ is defined as the deviation from the best line fitted to $w(x,y)$ using the least squares method

The governing equation describing the two-dimensional elastic deformation $w(x,y)$ in plates subject to a distributed transverse load $q(x,y)$ is based on classical thin plate theory [128]:

$$\frac{\partial^4 w}{\partial x^4} + 2\frac{\partial^4 w}{\partial x^2 \partial y^2} + \frac{\partial^4 w}{\partial y^4} = -\frac{q(x,y)}{D} \tag{6.1}$$

where $D = Et_m^3/12(1-v^2)$ is the plate flexural rigidity while E, v and t_m are the elastic modulus, Poisson ratio and plate thickness respectively. Additionally by computing equilibrium of moments, the plate curvature due to bending: $\partial^2 w/\partial x^2$, $\partial^2 w/\partial y^2$ and twist: $\partial^2 w/\partial x \partial y$ can be described in terms of the resultant internal bending moments M_x, M_y

and twisting moment, M_{xy} as in (6.2) [128]. It is important to note that all moment resultants are defined per unit plate length in the direction of the applied moment.

$$
\begin{pmatrix}
\dfrac{\partial^2 w}{\partial x^2} \\[2mm]
\dfrac{\partial^2 w}{\partial y^2} \\[2mm]
\dfrac{\partial^2 w}{\partial x \partial y}
\end{pmatrix}
= \frac{12}{E t_m{}^3}
\begin{pmatrix}
1 & -v & 0 \\
-v & 1 & 0 \\
0 & 0 & (1+v)
\end{pmatrix}
\begin{pmatrix}
M_x \\
M_y \\
M_{xy}
\end{pmatrix}
\tag{6.2}
$$

For the purpose of this theoretical evaluation, isotropic elastic properties are prescribed to the Si mirror plate while in-plane residual stresses are not considered. An analytical equation for the dynamic deformation of a rectangular mirror plate oscillating about its torsional in-plane axis was first deduced by Brosens [98] from classical plate theory. As the micro-mirror oscillates about the torsional axis with an angular frequency, ω_s, it is subject to an inertial sinusoidal angular acceleration $\ddot{\theta}(t) = \omega_s{}^2 . \theta(t)$. This corresponds to a torsional load, $T(t) = I.\ddot{\theta}(t)$ on the micro-mirror where I is the polar mass moment of inertia about the rotational axis.

Maximum dynamic deformation, δ_{max} occurs at the point of maximum angular acceleration and is defined as the peak-to-valley dynamic deformation, $\delta(x,y)$ at the instance when $\theta(t) = \theta_{max}$. The inertial loading distribution per unit length, $F'(x)$ along the mirror plane can be calculated as:

$$
F'(x) = \rho b_m t_m \alpha x
\tag{6.3}
$$

By integrating twice, the inertial moment $M(x)$ for a rectangular-shaped mirror can be deduced as:

$$
M(x) = -\frac{(\rho b_m t_m \alpha)}{8} \left(-\frac{x L_m{}^2}{2} + \frac{x^3}{6} + \frac{L_m{}^3}{3} \right)
\tag{6.4}
$$

In this case it is assumed that $M(x)$ results in a pure bending internal moment ($M_x = M(x)/b_m$) about the rotational axis (y-axis) which is constant along mirror width b_m. Thus plate theory can be reduced to beam theory as shown in (6.5):

$$
\frac{d^2 w}{dx^2} = \frac{12 M(x)}{E t^3 b_m}
\tag{6.5}
$$

Using (6.4) and (6.5) the deflection w can be derived by considering the boundary conditions of $w = 0$ and $dw/dx = 0$ at $x = 0$. The resultant deflection profile (refer to **Figure 6-2**) due to inertial loading for a rectangular-shaped mirror is given by (6.6):

$$w(u) = -\frac{\rho \alpha L_m{}^5}{320 E t_m{}^2}\left(u^5 - 10u^3 + 20u^2\right) \tag{6.6}$$

where $u = 2x/L_m$. The dynamic deformation, δ, depicted in **Figure 6-2**, can be defined as the deviation from the best fit line deduced using the least-squares method. In this case, the normalized gradient of the best fit line was found to be 9.6388 and therefore the dynamic deformation is given by (6.7):

$$\delta(u) = \frac{L_m{}^5 \rho \omega_s{}^2 \theta}{320 E t_m{}^2}(u^5 - 10u^3 + 20u^2 - 9.6388u) \tag{6.7}$$

where the theoretical maximum δ occurs at $u = \pm 1$. Equation (6.7) shows that δ is proportional to $L_m{}^5$. The optical resolution that can be obtained from a laser scanning micro-mirror is directly proportional to the mirror plate length, as in (2.3). Therefore, any attempt in improving optical performance by increasing L_m is limited by beam divergence problems resulting from a corresponding increase in dynamic deformation. Given that altering the fabrication process to introduce underlying mirror stiffening structures is generally unfeasible, non-rectangular micro-mirror profiles can be considered for the reduction in dynamic deformation. For instance, for the same L_m, circular and diamond-shaped mirror profiles are characterised by a lower mass towards the micro-mirror tip compared to rectangular profiles. The dynamic deformation of non-rectangular mirror profiles can be evaluated analytically, by modifying (6.4) such that the micro-mirror width, b_m is some function of u. For a diamond-shape mirror plate with $b_m(u) = L_m/2(1-u)$, the out-of-plane bending deflection is given by (6.8). For a circular mirror with $b_m(u) = L_m/2(1-u^2)^{1/2}$, the out-of-plane bending deflection is given by (6.9).

$$w(u) = \frac{L_m{}^5 \rho \omega_s{}^2 \theta}{192 E t_m{}^2}\left\{\frac{3u^5}{10} - \frac{u^4}{2} - u^3 + 3u^2\right\} \tag{6.8}$$

$$w(u) = \frac{L_m{}^5 \rho \omega_s{}^2 \theta}{128 E t_m{}^2}\left\{\frac{u^5}{5} - \frac{5u^3}{3} + 3u\left(-\left(\sin^{-1}u\right)^2 + \pi \sin^{-1}(u) + 2\right) \right.$$
$$\left. + 3\sqrt{1-u^2}\left(\pi - 2\sin^{-1}(u)\right) - 3\pi\right\} \tag{6.9}$$

6.2   Finite Element Analysis

Dynamic deformation of rectangular-shaped micro-mirror plates are evaluated using static structural finite element (FE) analysis in ANSYS Mechanical. Initially, displacement boundary conditions are applied in order to verify the dynamic deformation calculations deduced from classical plate theory – *Method 1*. Subsequently, displacement boundary conditions are altered to reflect a micro-mirror plate supported by two torsion beams – *Method 2*. Simulation results performed using *Method 2* boundary conditions will be used to validate the applicability of 1-D plate bending theory in micro-scanner dynamic deformation predictions.

6.2.1   Displacement Boundary Conditions: *Method 1*

The 3-D FE model of **Figure 6-3** consists of a square-shaped micro-mirror plate without the torsional beams. The micro-mirror plate dimensions is defined in terms of length L_m along the *x*-axis and width, b_m along the *y*-axis. Elastic properties of Si (E = 169 GPa; v = 0.23) and a micro-mirror plate thickness of 65 µm were prescribed to all subsequent FE simulations. Furthermore, the FE mesh was generated using 20-node structural solid elements. A fixed support boundary condition was applied to the nodes lying on the *y-z* plane as shown in **Figure 6-4**. The distributed inertial load acting on the mirror-plate at $\theta(t) = \theta_{max}$ is applied to compute the δ_{max}. The static-equivalent inertia load can be indirectly applied using the ANSYS APDL command DOMEGA. The latter specifies a rotational acceleration of the structure about a particular Cartesian axis, therefore δ_{max} is expected when $\ddot{\theta} = \omega_s^2 \theta_{max}$.
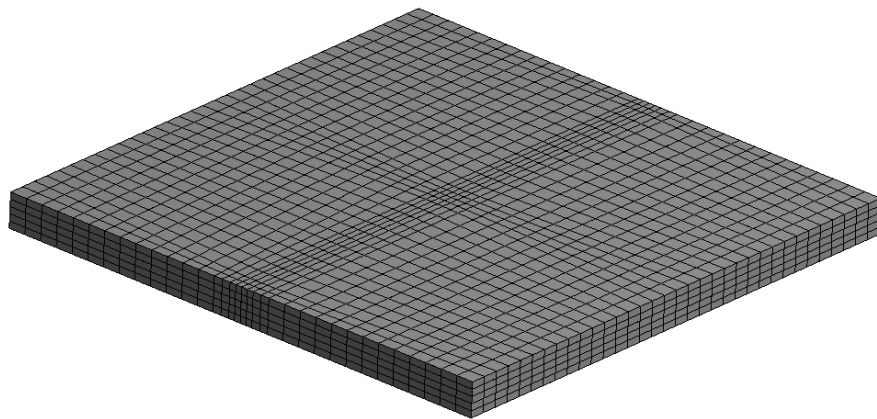
Figure 6-3: FE model of rectangular micro-mirror plate
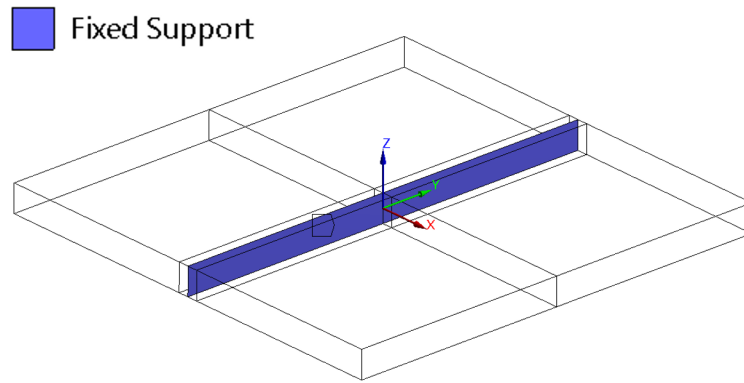
Figure 6-4: Displacement boundary conditions for FE simulations (*Method 1*)

Considering the requirements for SVGA resolution: $L_m = b_m = 1$ mm; $f_s = 25$ kHz and $\theta_{max} = 12°$ [19], a peak-to-peak dynamic deformation, δ_{max} of 163 nm is predicted from (6.4). The resultant mirror plate deflection and deformation surface profiles are presented in **Figure 6-5** and **Figure 6-6** respectively. The discrepancy between the analytical solution and the FE result, in terms of δ_{max}, is 1.1%. A difference in dynamic deformation between the edge ($y = b_m$) and centreline ($y = 0$) of the micro-mirror plate is observed in the FE simulation results of **Figure 6-6(a)**. This is due to the anticlastic behaviour of a two-dimensional plate with non-zero Poisson ratio, demonstrated from a comparison with **Figure 6-6(b)**. The resultant curvature about the x-axis is unaccounted for in (6.7) .
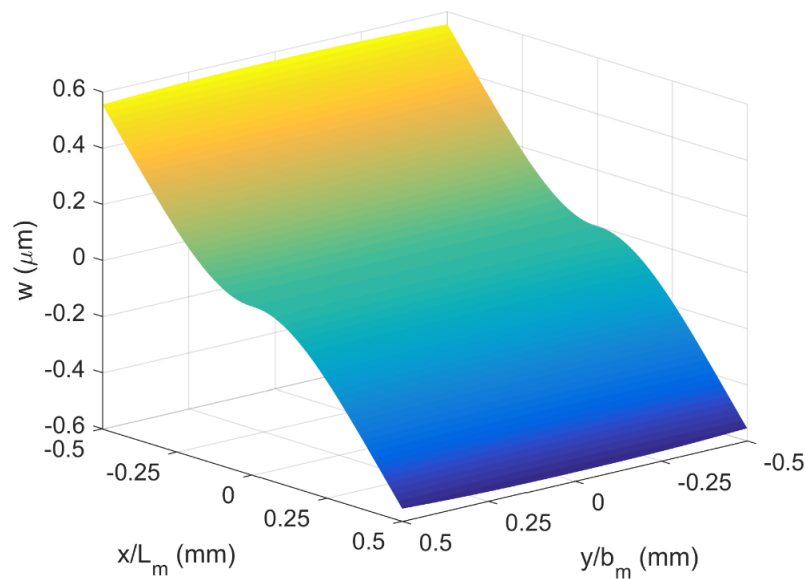
Figure 6-5: Out-of-plane deflection of a square-shaped mirror plate relative to torsional beams at $\theta(t) = \theta_{max}$ ($f_s = 25$ kHz; $\theta_{max} = 12°$, $L_m = b_m = 0.5$ mm) - FE simulations (Method 1)
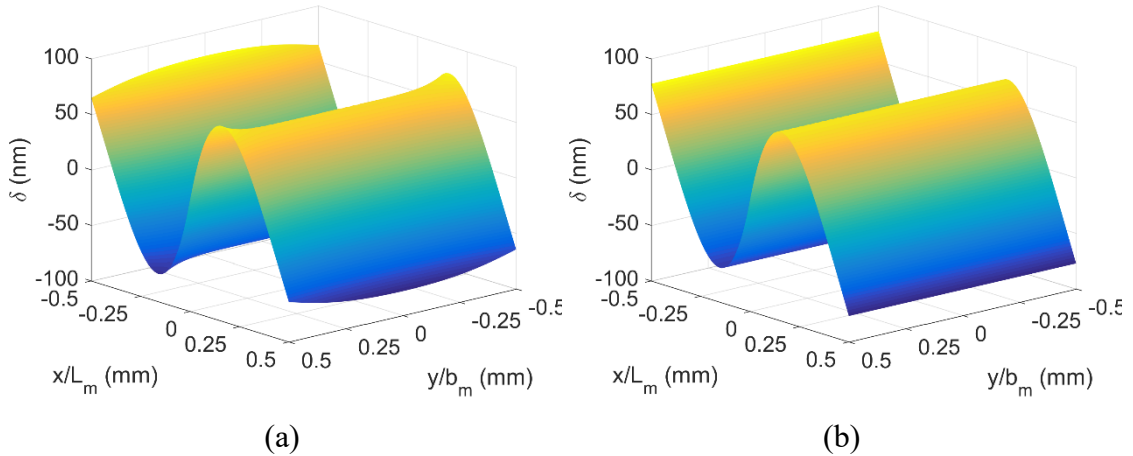
Figure 6-6: Dynamic deformation profile of square-shaped mirror plate at $\theta(t) = \theta_{max}$ (a) $\nu = 0.23$ (b) $\nu = 0$ ($f_s = 25$ kHz; $\theta_{max} = 12°$, $L_m = b_m = 0.5$ mm) - FE simulations (*Method 1*)

Simulations based on the boundary conditions of **Figure 6-4** were also performed on circular and diamond-shaped mirror layouts as shown in **Table 6-1**. Increased displacement discrepancy between FE and analytical results is observed in **Table 6-2** for non-rectangular mirror plates. This is partly due to the Poisson ratio effect on the anticlastic curvature. However, results indicate the possibility that the non-constant bending moment variation along the length of non-rectangular micro-mirrors may result in a more pronounced 2-D variation of the mirror plate deformation. By considering an equal L_m, b_m for the mirror geometries of **Table 6-1**, improvements in plate flatness with non-rectangular layouts is demonstrated in **Table 6-3**.

Table 6-1: Micro-mirror designs (spring-linkage effects are not considered)
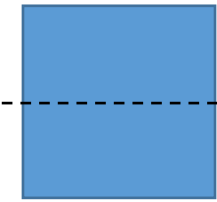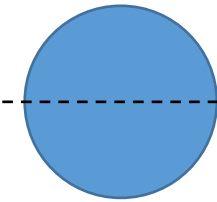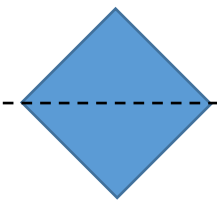
| (a) square | (b) circular | (c) diamond |

Table 6-2: Maximum micro-mirror deflection with *Method 1* boundary conditions including the percentage deviation between FE simulation and analytical results

Mirror plate shape	$w(u = 1)$ in [μm]		
	1-D plate bending theory	FE simulations (*Method 1*)	
		v = 0	v = 0.23
(a)	1.567	1.570 (0.2%)	1.594 (1.72%)
(b)	0.894	0.968 (8.3%)	1.007 (12.64%)
(c)	0.427	0.505 (18.3%)	0.542 (26.9%)

Table 6-3: Analytical and FE results for the dynamic deformation for different micro-mirror designs when *Method 1* displacement boundary conditions

Mirror plate shape	Relative dynamic deformation: $\dfrac{\delta_{rms}}{\delta_{rms,square}}$	
	1-D plate bending	FE simulations (*Method 1*)
(a)	1	1
(b)	0.330	0.335
(c)	0.561	0.613

6.2.2   Displacement Boundary Conditions: *Method 2*

In the above numerical and analytical analysis, the actuator and linkage effects are not included in the dynamic deformation calculations. The method by which the micro-mirror is structurally constrained will have an effect on the distribution of the inertial stresses. Consequently, displacement boundary conditions are applied, as shown in **Figure 6-7**, emulating the connection of the mirror plate to torsional beams of width $w_s = 50$ μm and thickness, $t_m = 65$ μm. Static structural simulations using the DOMEGA command were compared to transient structural simulations. The latter were carried out in two solution steps: (1) an initial static vertical displacement corresponding to the target θ was applied, (2) initial displacement was removed and time integration was activated at the same time step allowing the micro-mirror to oscillate at ω_s without any decaying oscillation amplitude in the absence of damping. The results showed good agreement between static and transient simulations for a number of different mirror profiles in term of the dynamic deformation profile (square: $\Delta\delta_{max}(static\text{-}transient) <$ 2%). Furthermore, simulations showed that non-linearities such as warping of the non-circular torsional spring cross-section had negligible effects on the results.

The out-of-plane deflection and dynamic deformation profiles of a square-shaped micro-mirror, are shown in **Figure 6-8** and **Figure 6-9** respectively. Compared to **Figure 6-6(a)**, a substantial variation in the deformation profile is observed when the displacement boundary conditions of **Figure 6-7** are applied. For $L_m = b_m = 1$ mm, the predicted peak-to-peak dynamic deformation from 1-D plate bending theory is 74% lower than that obtained from the numerical simulations. The simulation results are consistent with similar results by Ji *et al* [57]. The validity of (6.4) was further investigated by varying the mirror width as shown in **Figure 6-10**. It can be seen that when $b_m < 0.2L_m$, δ_{max} is approximately independent of micro-mirror width and is in agreement with the theoretical δ_{max}. However δ_{max} increases significantly with mirror width, b_m. This demonstrates that dynamic deformation is dependent on the micro-mirror width and the 1-D bending approximation of (6.7) is only valid for $b_m < 0.2L_m$.
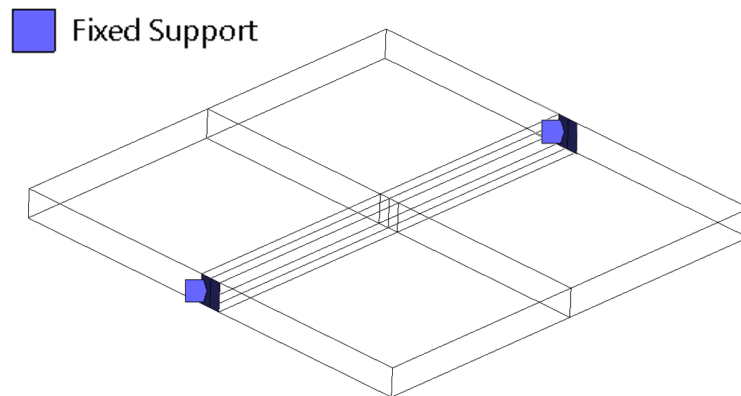
Figure 6-7: Displacement boundary conditions for FE simulations (Method 2)
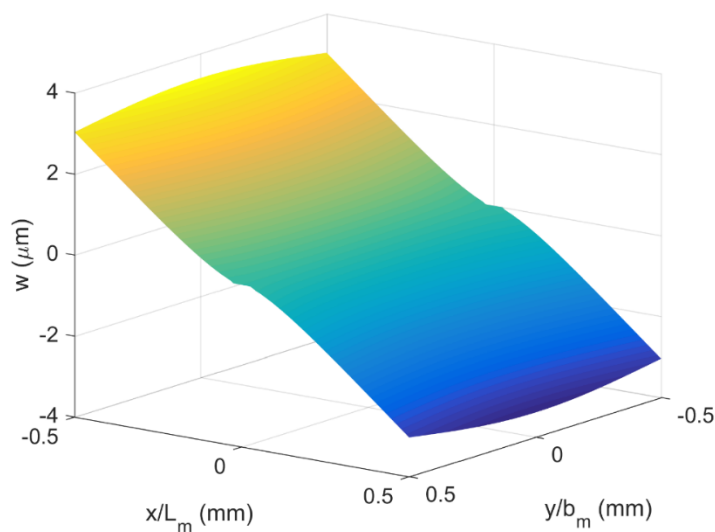
Figure 6-8: Out-of-plane deflection of a square-shaped mirror plate relative to torsional beams at $\theta(t) = \theta_{max}$ ($f_s = 25$ kHz; $\theta_{max} = 12°$, $L_m = b_m = 0.5$ mm) - FE simulations (*Method 2*)

102
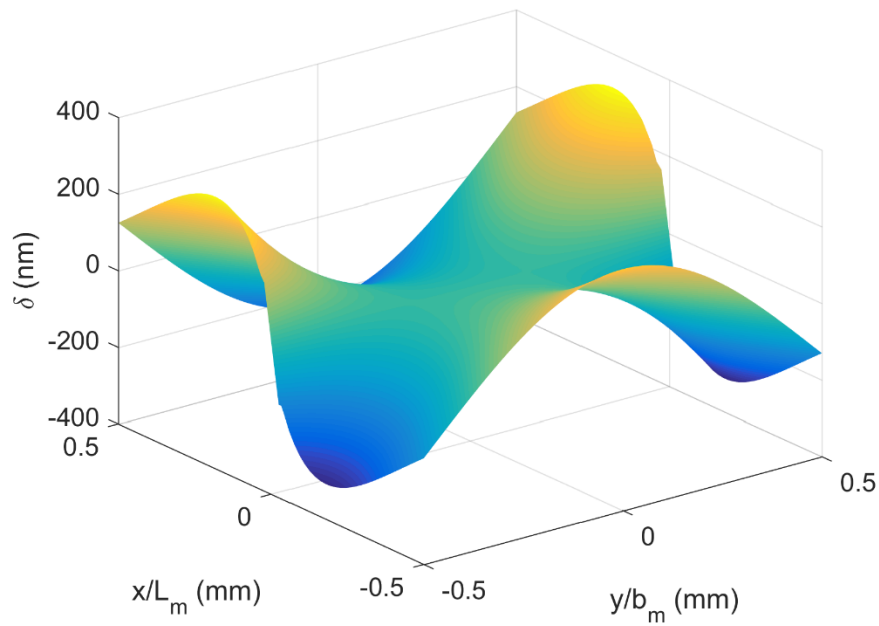
Figure 6-9: Dynamic deformation profile of square-shaped mirror plate at $\theta(t) = \theta_{max}$
($f_s = 25$ kHz; $\theta_{max} = 12°$, $L_m = b_m = 0.5$ mm) - FE simulations (*Method 2*)
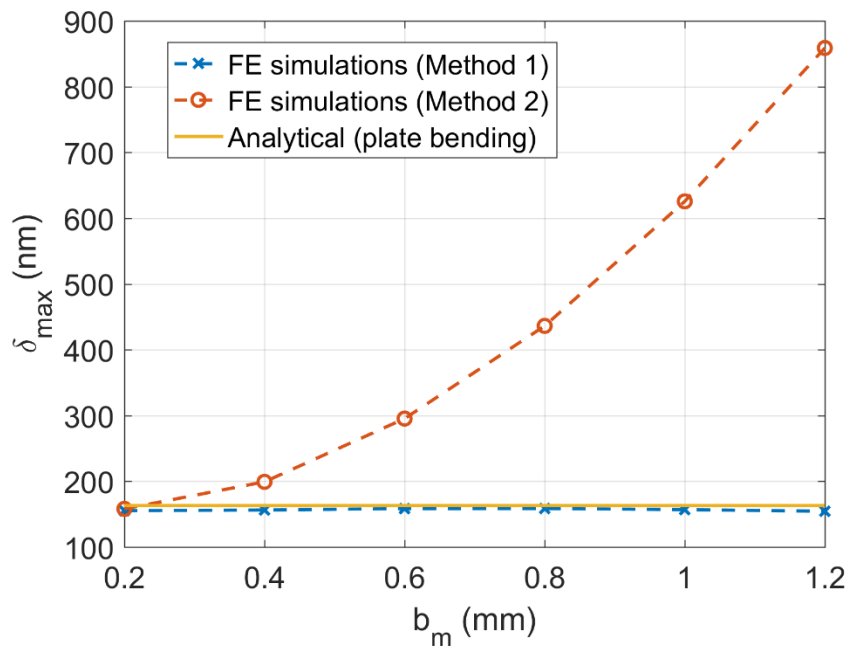
Figure 6-10: Variation of δ_{max} with micro-mirror width: comparison between FE simulation results and
1-D plate bending theory ($L_m = 1$ mm; $\theta_{max} = 12°$; $f_s = 25$ kHz)

The dynamic deformation variation along the micro-mirror width is mainly attributed to
the mirror-spring linkage configuration. The mirror plate is connected to torsional beams
along the axis of rotation. Therefore, the location of the fixed supports is such that the

103

prescribed inertial loading given by (6.3) results in added twisting moment about the x-axis. Given that the torsional stiffness is inversely proportional to the distance from the fixed supports, the angle of twist of the micro-mirror plate at $y = 0$ is greater than that at $y = \pm b_m/2$. In contrast, the micro-mirror bending deflection equation of (6.6) is deduced by assuming a constant dw/dx along $x = 0$. The variation of $d\delta/dx$ along $x = 0$, observed in **Figure 6-9** signifies that the dynamic twisting effect on the reflective surface is not negligible and the mirror plate support configuration needs to be included in dynamic deformation FE simulations.

Reducing the angle of twist variation at the micro-mirror tip is one method which can be applied for the reduction of bending and twisting contributions to dynamic deformation. This can be attained by reducing the micro-mirror width at $x = \pm L_m/2$, thus altering the mirror shape. A number of plate geometries, as shown in **Table 6-4**, were consequently simulated to analyse how the in-plane dimensions can be optimized with the intention of reducing the maximum dynamic deformation. FE simulations were performed by applying the displacement boundary conditions of **Figure 6-7**. The structure thickness, elastic properties, torsion beam width, the maximum mirror length and the distance between supports were kept constant for all geometries. Moreover, the angular acceleration at $f_s = 25$ kHz and $\theta_{max} = 12°$ is applied in all simulations.
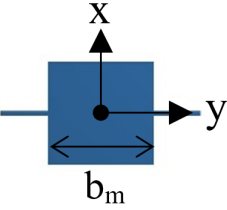
In order to enable a direct comparison among different micro-mirror layouts, the normalized maximum dynamic deformation, R_{def}, given by (6.10) is introduced. The dimensionless parameter R_{def} will be used in this dissertation to classify the effectiveness of a micro-mirror layout design in reducing dynamic deformation irrespective of the mirror plate thickness, material properties and scanning performance. R_{def} is defined in terms of δ_{rms} which is the root-mean-square of the simulated $\delta(x,y)$ at θ_{max}. Normalization of δ_{rms} is performed with respect to the parametric dependencies of δ given in (6.7).

$$R_{def} = \frac{\delta_{rms} E t_m^{\ 2}}{\rho \omega_s^{\ 2} \theta (L_m/2)^5} \qquad (6.10)$$

The relative R_{def} results of **Table 6-4** are calculated by considering the best plane fit of $w(x,y)$ over the entire plate area. Compared to the square-shaped mirror plate, a reduction in R_{def} is achieved through octagonal (30%), hexagonal (23%), circular (43%), and diamond-shaped (73%) geometries. This demonstrates that a direct correlation exists between dynamic deformation and the width of the micro-mirror tip (i.e. $x = \pm L_m/2$).

Additionally, a reduction in R_{def} corresponds to a lower micro-mirror moment of inertia. A reduction in the mirror moment of inertia enables a faster scanning response and lower stress in the torsional springs. However, it has to be noted that, with reference to (2.1), an improvement in the optical resolution by altering the micro-mirror geometry are limited by the aperture shape factor, a (a = 1: square; a = 1.27: circle; a = 2: diamond). The introduction of a radial fillet at the intersection between the micro-mirror and the spring (as in mirror profiles (b) and (d)) was also evaluated with the aim of improving the dynamic deformation distribution along $y = \pm b_m/2$. However, results indicate no reduction in dynamic deformation compared to mirror profiles (a) and (c) due to the added moment of inertia contribution.

Table 6-4: FE results for the maximum dynamic deformation from different micro-mirror designs when the spring-linkage effects are considered ($b_m = L_m = 1$mm; $f_s = 25$ kHz; $\theta_{max} = 12°$; $t_m = 65$ μm)

Mirror plate geometry		δ_{max} (nm)	δ_{rms} (nm)	R_{def}	$\dfrac{R_{def}}{R_{def,square}}$
(a)		625.67	114.37	0.229	1.000
(b)		639.83	116.53	0.233	1.019
(c)		421.67	65.50	0.131	0.573
(d)		463.25	76.06	0.152	0.665
(e)		540.45	79.60	0.159	0.696
(f)		555.77	87.84	0.176	0.768
(g)		185.23	30.40	0.061	0.266

6.3   Inclusion of Twist in Micro-Mirror Plate Theory

The above study has shown that for typical micro-mirror geometries, the boundary condition: $\partial w/\partial x = 0$ is not a suitable assumption in the derivation of the $w(u)$ in (6.6) and plate twist about the y-axis should also be considered. Given that the inertial moment $M(x)$ is evenly distributed along the y-axis, the resultant twisting moment per unit width for a rectangular micro-mirror varies linearly in the form of $M_{xy} = M(x)(y/L_m b_m)$. Therefore, from (6.2) and (6.4) the curvature and the mirror plate deformation due to the twisting moment can be deduced as in (6.11) and (6.12):

$$\frac{\partial^2 w}{\partial x \partial y} = \frac{-12(1+v)\rho\alpha}{Et_m^2 L_m}\left(-\frac{xL_m^2}{2} + \frac{x^3}{6} + \frac{L_m^3}{3}\right)y \qquad (6.11)$$

$$\delta(u,\gamma) = -\frac{(1+v)\rho\alpha L_m^3 b_m^2}{128 Et_m^2}\left(-6u^2 + u^4 + 8u\right)\gamma^2 \qquad (6.12)$$

where $u = 2x/L_m$ and $\gamma = 2y/b_m$. From (6.12), it can be seen that for a rectangular micro-mirror, the resultant deformation is 0 along the centreline ($y = 0$) and maximum along micro-mirror edges ($y = \pm b_m$). In order to assess the accuracy of plate bending and twist formulations relative to FE simulations, the root-mean square dynamic deformation, δ_{rms} is evaluated for an array of plate length and width combinations as shown in **Figure 6-11**. From plate twist calculations the δ_{rms} varies quadratically with b_m in agreement with the numerical results. The limits of applicability of both plate twist and bending equations can be deduced from **Figure 6-12**. Dynamic deformation is governed by plate bending and plate twist at low and high mirror width respectively. By combining the plate bending and twist equations of (6.7) and (6.12), a general analytical formulation is achieved for the accurate prediction of inertia-driven dynamic deformation of a rectangular-shaped micro-scanner.

(a) FE simulations

(b) Plate bending theory

(c) Plate torsion theory

(d) Combined plate bending + torsion theory
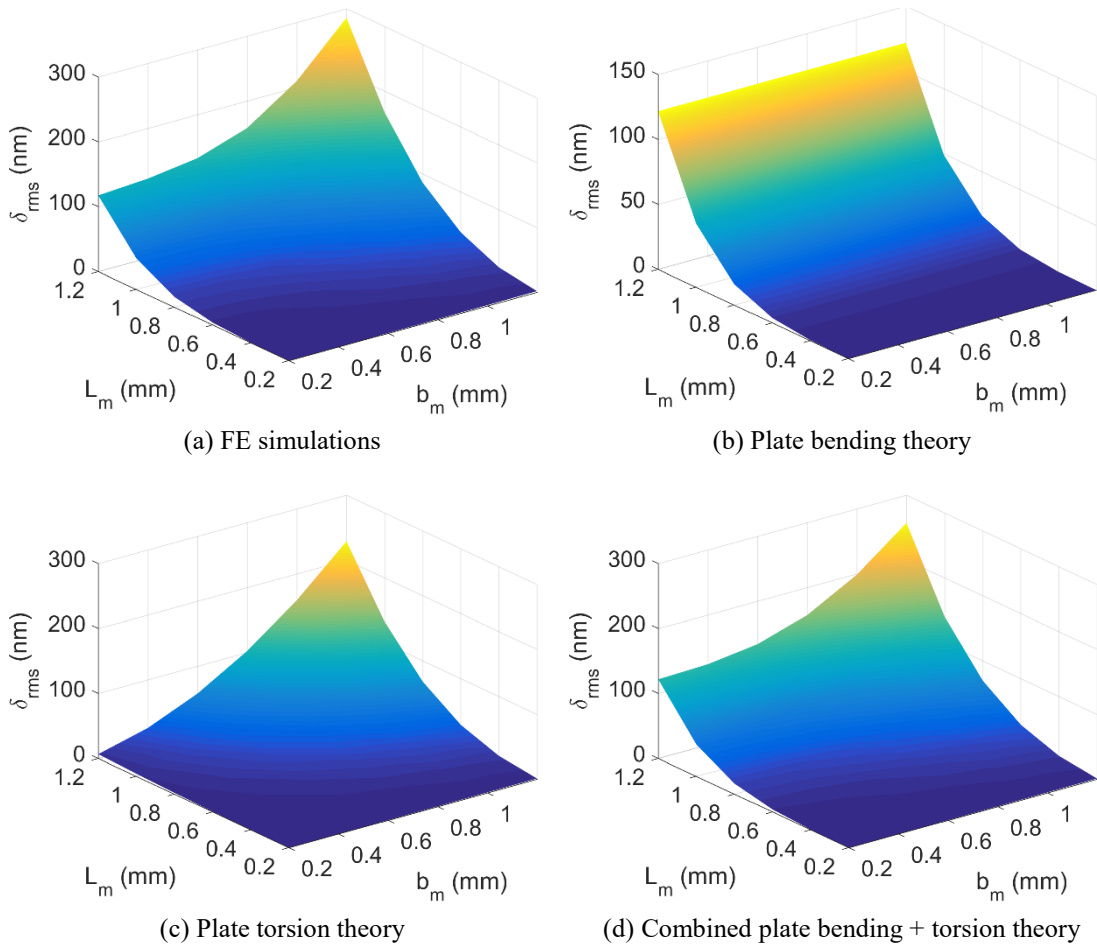
Figure 6-11: Variation of rms dynamic deformation with rectangular mirror plate dimensions
(f_s = 25 kHz, θ_{max} = 12°, t_m = 65 µm)
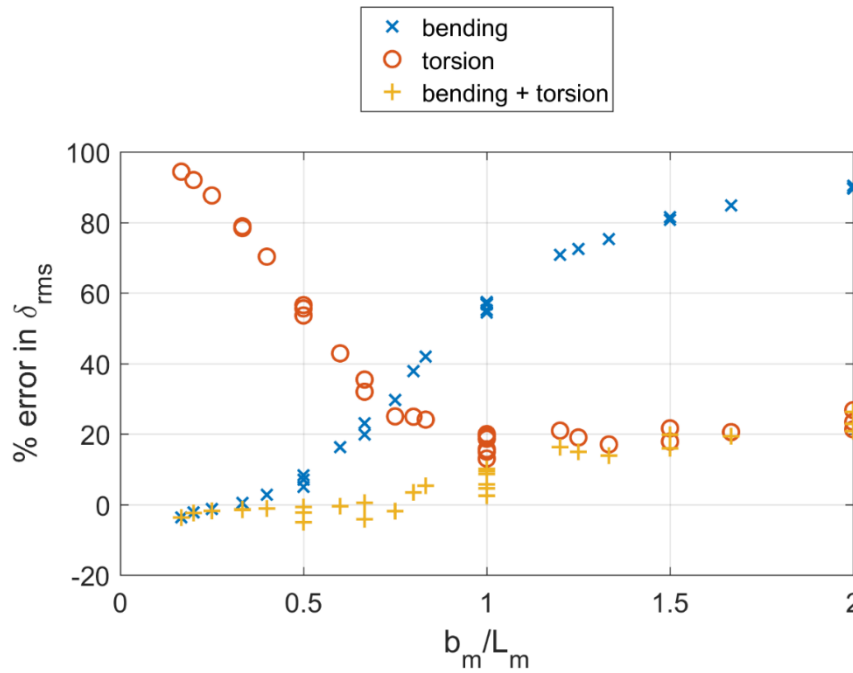
Figure 6-12: Percentage error in δ_{rms} obtained from different analytical methods (based on classical plate theory) when compared to FE simulation results (for the rectangular-shaped mirror plate of **Figure 6-1** at θ_{max} = 12°; f_s = 25 kHz)

107

6.4   Gimbal-Frame Micro-Mirror Design

For all mirror in-plane geometries considered in **Table 6-4**, $\delta_{max} > \delta_{crit}$ at the target scanning frequency and amplitude ($f_s = 25$ kHz, $\theta_{max} = 12°$). Modifications to the micro-mirror layout provide limited improvement towards dynamic flatness. This is due to the variation in angle of twist along the micro-mirror width inherent to designs in which the mirror plate is directly suspended from torsional springs along its axis of rotation. In order to obtain a scan angle which is independent of the mirror width, the position of the link connecting the mirror to the springs should not lie along the axis of rotation [56]. This can be achieved by introducing a gimbal structure between the micro-mirror and the springs as shown in **Figure 6-13** [48]. In this design, the springs and the gimbal frame will twist as a result of the inertial moment and rotation of the circular mirror is achieved by an equal and opposite displacement applied through the gimbal-mirror links.
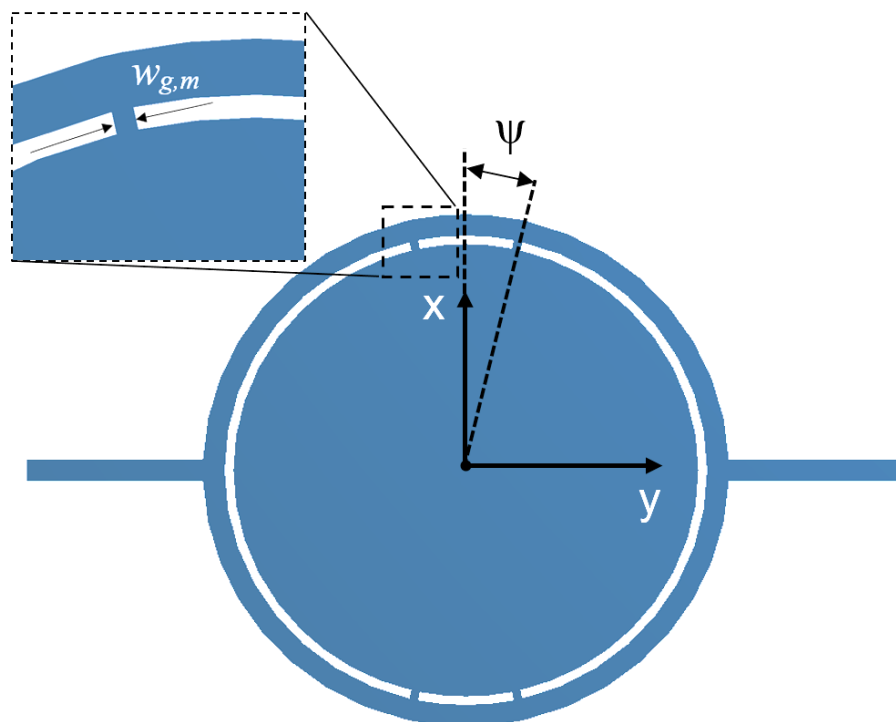
Figure 6-13: Circular micro-mirror connected to a gimbal frame through four links having width $w_{g,m}$ and positioned symmetrically at angle ψ from the x-axis

The number of links between the gimbal frame and mirror is an important parameter in such a design. Four links were introduced in the design instead of two links in order to suppress the mirror torsional mode. Increasing the number of links may also improve

the resultant force distribution on the mirror plate. However a high number of links would increase the stiffness of the gimbal structure and therefore cancelling out any improvements pertaining to this design. The length of the gimbal-mirror link was set to 20 μm. A parametric study was subsequently carried to determine the optimal geometry and position of the gimbal-mirror links. The effect of angle, ψ, of the four gimbal-mirror links on the normalised dynamic deformation is plotted in **Figure 6-14**. Although the general trend is that lower dynamic deformation is achieved when the gimbal-mirror links are placed further away from the rotational axis, R_{def} increases with ψ for small angles. In fact from FE simulations, the optimal value for ψ was found to be 10 - 15°. The effect of the link width between the gimbal and the mirror, $w_{g,m}$ on the dynamic deformation was also analysed as shown in **Figure 6-15**. The von-Mises stress at the link was also examined and was found to be less than 20% of the yield stress of Si for the lowest $w_{g,m}$ considered.

The dynamic deformation profiles of the circular micro-mirror with and without the gimbal frame are shown in **Figure 6-16**. It can be seen that the gradient $d\delta/dx$ of the gimbal frame micro-mirror is constant along the rotational axis ($x = 0$) in contrast with the micro-mirror which is directly linked to the springs. For the operating target conditions, without the gimbal frame, a δ_{rms} of 65.4 nm is obtained. In contrast, the inclusion of a gimbal frame with four links at $\psi = 12.5°$ and $w_{g,m}$ of 25 μm results in a δ_{rms} of 12.7 nm which lies within the range of the $\lambda/10$ Rayleigh diffraction criteria.
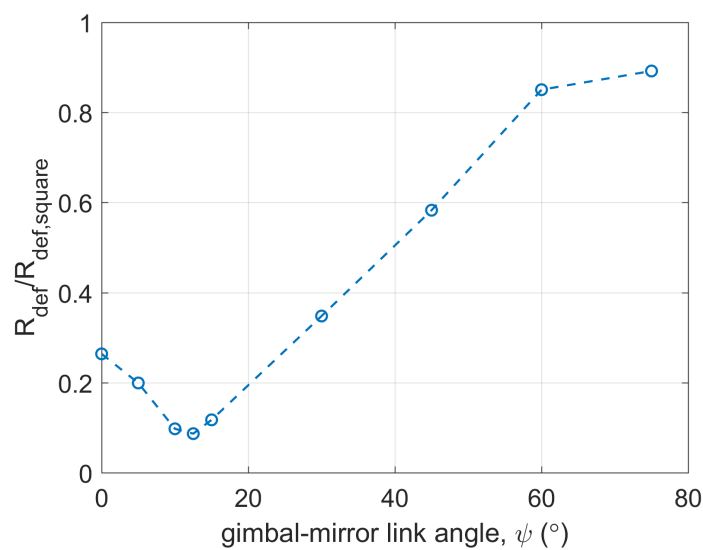
Figure 6-14: Plot showing the variation of the normalized dynamic deformation with gimbal-mirror link angle, ψ (°) obtained using FE analysis ($E = 169$ GPa; $v = 0.23$; $t_m = 65$ μm; $w_{g,m} = 25$ μm)
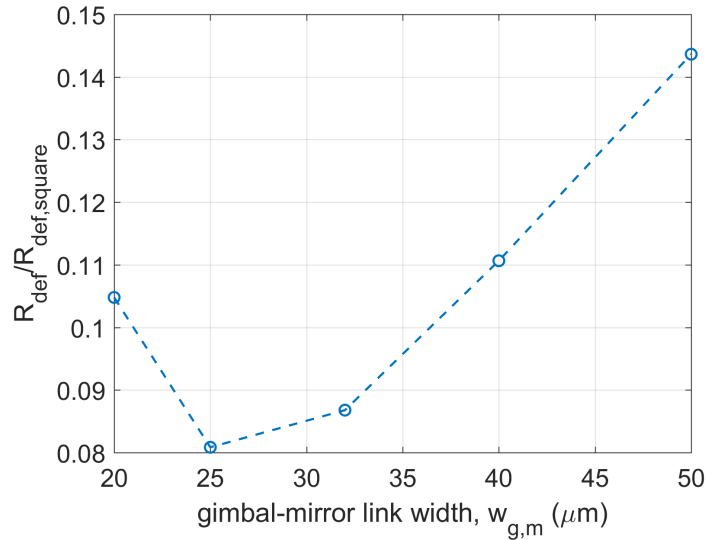
Figure 6-15: Plot showing the variation of the normalized dynamic deformation with gimbal-mirror link width, $w_{g,m}$ (μm) obtained using FE analysis (E = 169 GPa; ν = 0.23; t_m = 65 μm; ψ = 12.5°)

(a) circular mirror without gimbal-type frame

(b) circular mirror with gimbal-type frame
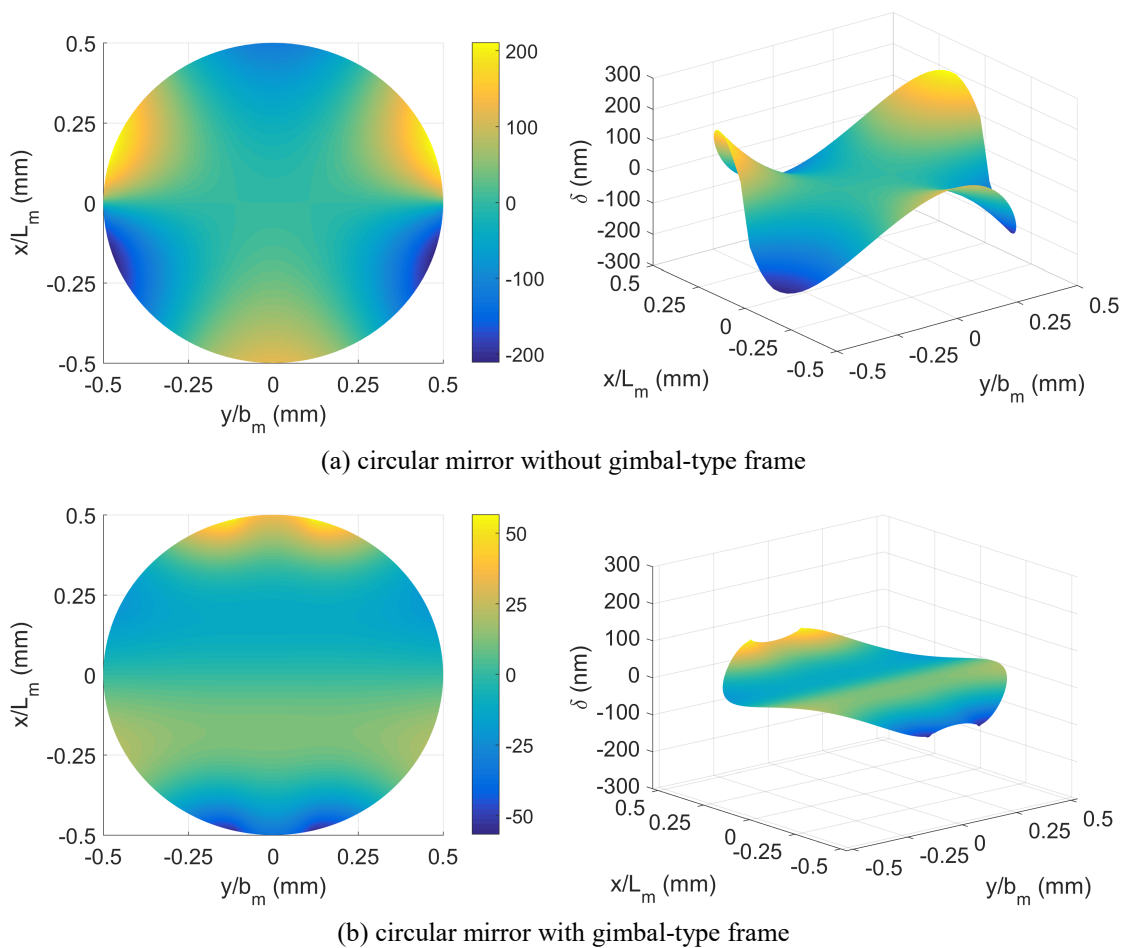
Figure 6-16: Surface plot of the dynamic deformation profile for a circular micro-mirror with (a) a direct connection to the springs (gimbal-less) and (b) gimbal frame connected to the springs (E = 169 GPa; ν = 0.23; t_m = 65 μm; ψ = 12.5°, $w_{g,m}$ = 25 μm)

110

6.5   Conclusion

Dynamic deformation is a crucial characteristic limiting the implementation of resonating micro-mirrors in high definition display applications. Finite element results demonstrated the limited use of 1-D plate bending calculations for dynamic deformation predictions. It has been shown that a complex 2-D dynamic deformation profile occurs that is a result of combined mirror plate bending and twisting mode contributions at the operating spring torsional frequency. By considering the two-dimensional plate curvature due to a combined bending and twisting moment, better agreement with the FE dynamic deformation simulation results is achieved. The effect of the micro-mirror layout and the mirror-spring linkage design on the dynamic deformation was also investigated. A reduction in dynamic deformation was achieved through circular and diamond-shaped micro-mirrors compared to rectangular-shaped micro-mirrors. It has also been shown that the linkage design between the torsional springs and the micro-mirror considerably affects the dynamic deformation profile. Compared to the direct mirror-spring linkage design, a significant reduction in dynamic deformation was in fact achieved by incorporating a gimbal-frame structure between the torsional springs and the micro-mirror. This latter result was obtained following a parametric analysis whereby the optimum position and dimensions on the gimbal-mirror links was achieved.

7   MICRO-SCANNER DESIGN OPTIMISATION

This chapter presents a multi-criteria design optimization scheme to determine the optimal geometric configuration, with respect to dynamic fluid-mechanical characteristics, of a high frequency resonating micro-scanner. One of the main aims of this design optimisation is to minimize mirror dynamic deformation. In Chapter 6 it has been demonstrated that dynamic deformation of a circular micro-mirror may be reduced by approximately 70% with the introduction of gimbal-type support structure. However, the optimal configuration of the gimbal-frame has not yet been identified. Moreover, dynamic deformation is not normally included as an output parameter in performance-based or reliability-based design optimization techniques for scanning micro-mirrors [56, 129, 130].

The conventional approach towards the optimization of MEMS devices typically relies on single-physics mathematical or FE models that optimize a single output response using genetic algorithms or artificial neural networks [131]. In direct optimization methods, the actual simulation results are used to determine the next design point in an iterative process until the design goal is met. A direct design optimization process for a 2-D resonant micro-mirror using a MATLAB optimization algorithm has been presented by Shock *et al* [129]. These optimization techniques are limited and may not be particularly efficient for the analysis of multiple output responses, complex device geometries and the coupled multi-physics interactions present in MEMS micro-mirrors [130]. A number of authors have proposed the implementation of simulation based Design of Experiments (DOE) technique and a Response Surface Methodology (RSM) to enable multiple response design optimization of MEMS micro-mirrors [130] [132]. DOE and RSM techniques enable a computationally efficient method to investigate the design space in detail and to analyse the effect of multiple input parameters on the output responses.

The multiphysics interaction prevailing in the operation of MEMS devices with electrostatic parallel-plate type actuators requires specific elements such as TRANS126 in ANSYS to model and possibly establish an optimized design solution [132] [133]. The drawback of these elements is that they are not able to model the fringing effects predominant in out-of-plane electrostatic comb-drives. FE models, which independently solve the mechanical and electrostatic domains can be employed, but are computationally intensive within a design optimization process. On the other hand

performing a fully coupled structural-electrostatic-fluidic model transient analysis for resonating micro-mirrors with bistable behaviour, is currently not viable. A possible alternative for optimization of comb-driven resonating micro-mirrors is a system-level model based on the principle of conservation of energy at the resonance frequency. In this case, capacitance-scan angle and damping coefficient-frequency look-up tables are constructed from FE electrostatic and simplified 2-D CFD simulations [129]. In Chapter 5 it has been demonstrated that in order to accurately model air damping, the complex 3-D flow structure around the rotating comb-fingers together with drag damping effects of the oscillating mirror plate have to be considered.

The optimization scheme presented in this chapter is based on 3-D CFD models for air damping analysis and a 3-D FE solid model for modal, stress and dynamic flatness evaluation. The implementation of DOE and RSM meta-modelling techniques in a three-stage design optimization process is proposed, with the aim of seeking a balance between predictive modelling accuracy and computation efficiency. Parts of the work presented in this chapter has been published in [134, 135]

7.1   Design Overview

The design of the micro-scanner consists of a circular mirror plate connected to torsional beams (springs) lying along the axis of rotation (x-axis), as shown in **Figure 7-1**. The micro-mirror is electrostatically actuated via a vertical comb drive structure, where the interdigitated movable fingers are attached to the gimbal frame. The device is intended for fabrication using the resonant micro-mirror process developed by ST Microelectronics described in Section 2.7 [9]. The aluminium mirror reflective layer was not included in the FE model discussed in Section 7.2.3. Additionally no residual stresses were considered and the initial mirror curvature was assumed to be insignificant.
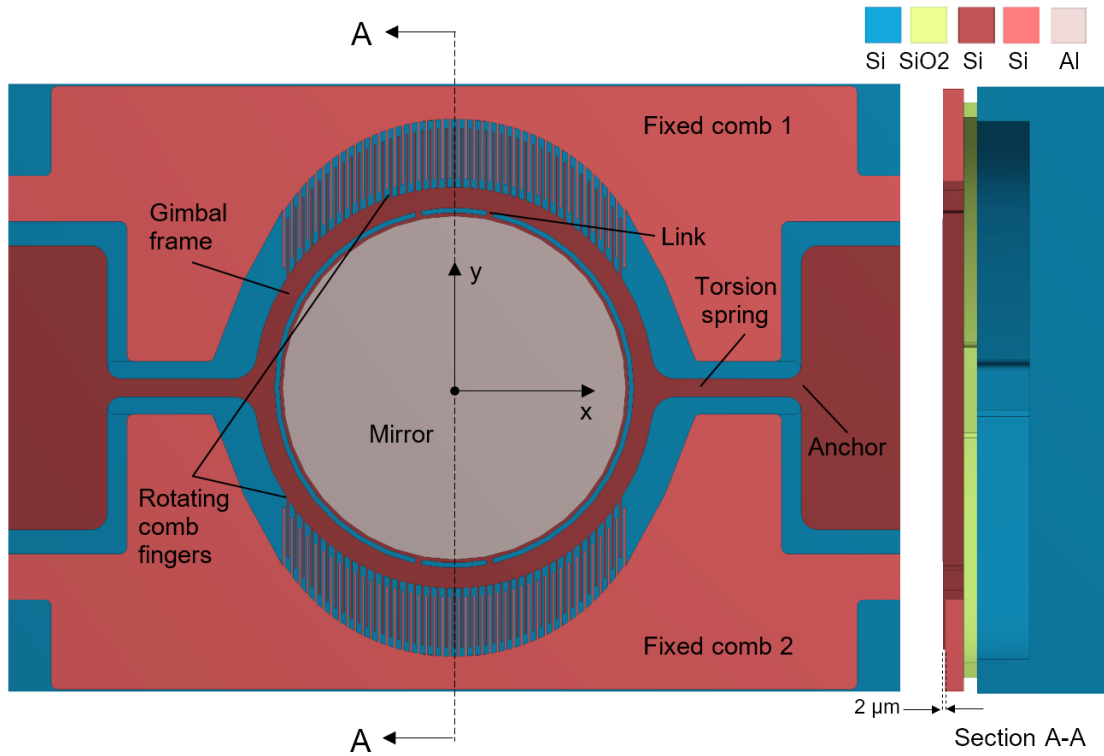
Figure 7-1: Simplified design layout of the gimbal-frame resonant micro-mirror (not to scale)

7.2   Design Optimization Scheme

The scheme presented in this section and summarised in **Figure 7-2**, is adapted from a design optimization procedure developed to assess the effect of geometric and material uncertainty on the performance and reliability of MEMS devices [132]. Given that the device's sensitivity to process-related uncertainties is not included in this study, the multi-criteria objective function *F(s)*, given in (7.1), can be defined in terms of *n* number of partial objectives, *Fi(s)*, having an equal weighting factor:

$$F(s) = \sum_{i=1}^{n} F_i(s) \qquad (7.1)$$

where vector *s* refers to the design input parameters s_j ($j = 1, 2…m$ where *m* refers to the number of design parameters). A total of five partial objectives (see Section 7.2.1) and 14 design parameters (see Section 7.2.2) were identified for design optimization. Instead of solving for all optimal design parameter values simultaneously, a three-step DOE and RSM-based optimization process is proposed. During each optimization step, one or more partial objectives together with the related input parameters were selected to define the objective function *F(s)* as described in Section 7.2.6.

114
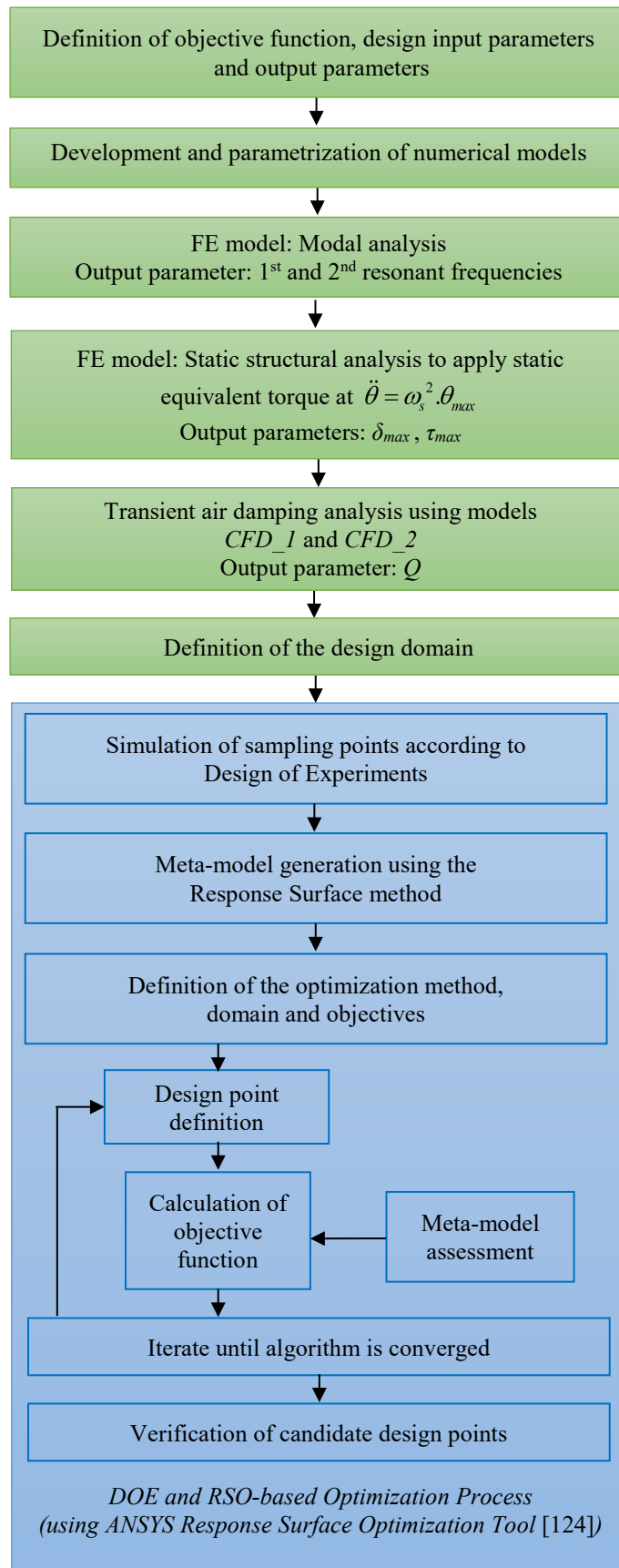
Figure 7-2: Flowchart of the design optimization scheme

7.2.1   **Objective Function**

The partial objectives considered to define the objective function are listed in **Table 7-1**. One of the partial objectives of this study is to minimize the dynamic deformation of a micro-mirror designed for laser projection with SVGA optical resolution (see **Table 2-1**). The number of resolvable pixels in the horizontal scanning direction, N_h is proportional to θ_{max} and mirror plate radius, R as shown in (2.3). The horizontal scanning frequency determines the vertical resolution, N_v for a single laser beam and bidirectional horizontal projection as shown in (2.4) [32].

Table 7-1: Output parameters and related partial objectives

Output Parameter	Description	Related Partial Objective	ANSYS RSO tool [136] implementation	Comments
δ_{max}	peak-to-peak dynamic deformation	$F_1(s_1,s_2,s_3,s_4, s_5,s_6,s_7,s_8.s_9)$	Minimize	F_1 increases when δ_{max} is minimized
f_s	torsional modal frequency	$F_2(s_5,s_6,s_7,s_8.s_9)$	Seek Target (=25 kHz)	F_2 increases when f_s approaches 25 kHz
$\|f_s\text{-}f_p\|$	difference between torsional and piston modal frequencies	$F_3(s_5,s_6,s_7,s_8.s_9)$	Maximize	F_3 increases when $\|f_s\text{-}f_p\|$ is maximized
τ_{max}	maximum shear stress	$F_4(s_5,s_6,s_7,s_8.s_9)$	Minimize	F_4 increases when τ_{max} is minimized
Q	quality factor	$F_5(s_{10},s_{11},s_{12},s_{13},s_{14})$	Maximize	F_5 increases when Q is maximized

The mirror diameter and θ_{max} were thus set to 1 mm and 12° respectively while a scanning frequency of 25 kHz, being considered as another partial objective, was sought. Maximizing the separation gap between f_s and the adjacent piston-mode frequency (see **Figure 7-5(b)**) was also considered as partial objective. A limiting factor hindering improvements in the optical resolution through higher scan angles, is torsional beam failure. The most probable mode of failure is in shear [103]. It has to be ensured that the springs can be twisted to the target θ_{max} without exceeding the critical shear stress, τ_{crit}. The critical shear stress for a monocrystalline silicon (100) wafer under static load is greater than 3 GPa [137]. However, experiments carried out on similar scanning micro-mirrors with straight beam-type torsional beams oriented in the [110] direction demonstrated that under dynamic loading, τ_{crit} = 1.4 GPa [102]. Minimization of the

maximum shear stress, which should be below the latter value of τ_{crit}, is therefore also considered as a partial objective.

One of the limitations in electrostatically-actuated resonant micro-mirror design is the high actuation voltage, V, required to achieve the desired θ_{max}. By carrying out electrostatic and air damping analysis, the required V at the resonant frequency can be deduced from (3). Optimization of the comb structure is required to minimize V, and hence the damping loss, in order to achieve the target optical requirements (θ_{max}, f_s). In this optimization scheme, only air damping analysis is presented using numerical models discussed in Section 7.2.4. The energy dissipation via air damping, E_{loss} over one period of oscillation is given by (5.13) and therefore, maximising the quality factor, Q given by (5.15), is set as a partial objective.

7.2.2   **Input and Output Parameters**

Following the definition of the objective function, the output parameters 1 to 5, given in **Table 7-1**, were selected for the optimization task. A sensitivity analysis was subsequently performed to determine which design parameters mostly influence the scanning frequency and dynamic deformation of the micro-mirror surface. The results were used to identify the input parameters considered for the optimization task shown in **Figure 7-3** and listed in **Table 7-2**. Variations in input parameters 1 to 5 influence δ_{max} while f_s is strongly determined by input parameters 6 to 9.

The damping analysis of Chapter 5 demonstrated that the energy dissipation of the oscillating micro-scanner results from AVC structure and mirror-plate drag damping. Therefore optimization of the Q requires separate CFD models for the simulation of the damping moment acting on both the AVC and the mirror plate structures. This also implies that the range of design parameters which impact the overall damping losses is substantial. A detailed parameter sensitivity analysis of the overall quality factor is presented in Section 7.2.5. In this study only the design parameters pertaining to the comb structure (input parameters 10 to 14) were considered for the optimization of Q given that minimizing the dynamic deformation is the main objective.

117

Table 7-2: Nominal values and range of variation for the input design parameters

Design Parameter, s_j	Symbol	Description	Nominal Value	Range of Variation
s_1	n_l	number of links	4	2,4..12
s_2	ψ	link angle	15°	± 10°
s_3	$w_{g,m}$	link width	15 μm	±10 μm
s_4	$l_{g,m}$	link length	10 μm	± 5 μm
s_5	w_g	gimbal frame width	50 μm	± 30 μm
s_6	w_s	torsional beam width	50 μm	± 5 μm
s_7	l_s	torsional beam length	42 μm	± 10 μm
s_8	$r_{s,1}$	support-spring fillet radius	60 μm	± 40 μm
s_9	$r_{s,2}$	spring-gimbal fillet radius	60 μm	± 40 μm
s_{10}	f_o	comb finger offset	27 μm	± 5 μm
s_{11}	f_l	comb finger length	180 μm	± 20 μm
s_{12}	f_g	comb finger gap	8 μm	± 2 μm
s_{13}	f_w	comb finger width	8 μm	± 2 μm
s_{14}	N	number of comb fingers	43	± 10
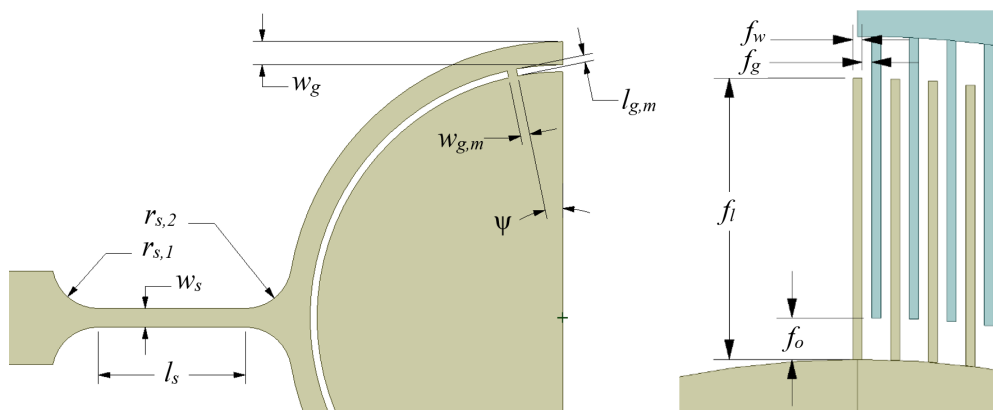
Figure 7-3: Input parameters (s_j) for the resonant micro-mirror FE and CFD models

7.2.3   Micro-Scanner FE Model

The FE model was developed in ANSYS using 20-node hexahedral elements (SOLID186) as shown in **Figure 7-4**. The geometrical model of the rotating micro-mirror was parametrized such that the inputs of **Table 7-2** can be varied within the stipulated range. The maximum element aspect ratio was closely monitored for all simulated parameter variations such that no significant mesh distortion is developed throughout the different DOE models. The numerical accuracy of the models was thus ensured. Silicon was modelled with orthotropic elastic properties for the (100) wafer

reference frame [108]. For all simulations, geometric non-linearity was considered and fixed support boundary conditions were applied at the ends of the torsional beams.

Modal analysis was carried out in order to determine the first two resonant frequencies of the micro-scanner structure. These frequencies refer to the torsion mode, f_s: rotational oscillations about the x-axis (**Figure 7-5(a)**) and the piston mode, f_p: linear oscillation in the z-axis (**Figure 7-5(b)**). By analysing the modal displacement at the centre point of the mirror, a condition statement was used to discriminate between the torsion and piston modes. The torsional resonant frequency, f_s was then used as an input parameter in a static structural simulation. The latter simulation was performed to analyse the dynamic deformation at the mirror surface together with the maximum shear stress at the point where the mirror is at its maximum scan angle ($\theta_{max} = 12°$). Instead of performing a transient analysis, a static-equivalent inertial torque, $M_I = (2\pi f_s)^2$. θ_{max} is applied using the DOMEGA command [127]. The half peak-to-peak dynamic deformation, δ_{max} was obtained using the *FlatnessDefect* ACT Extension tool in ANSYS [138].
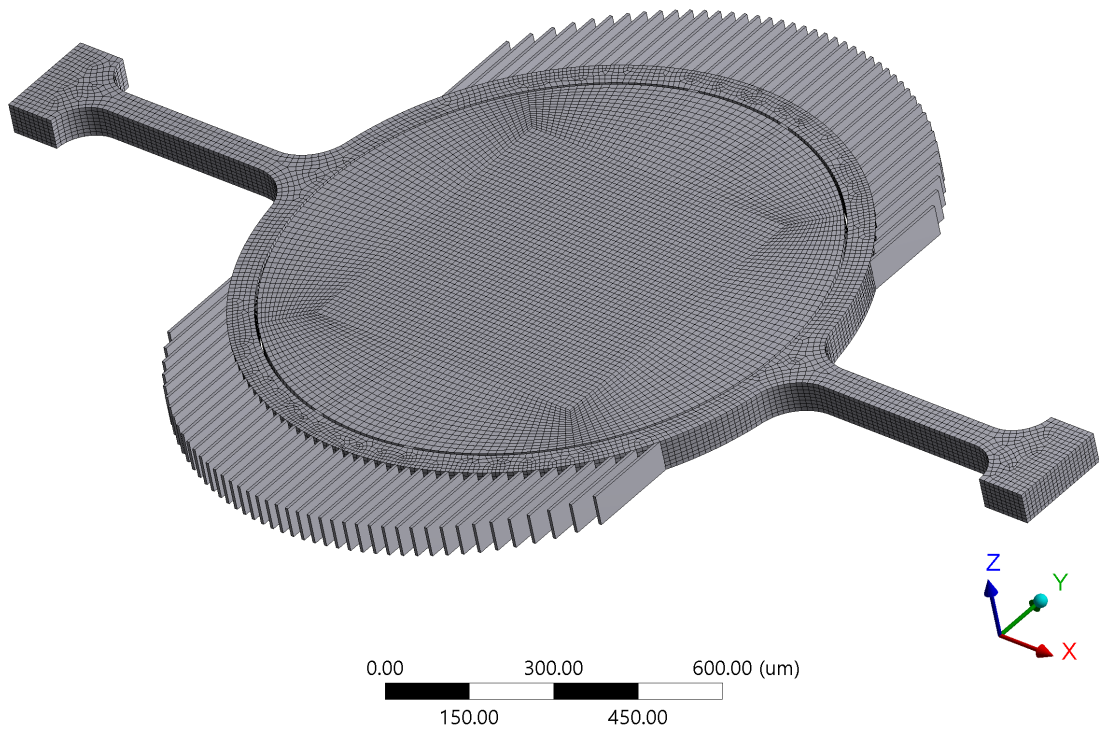
Figure 7-4: FE model of the gimbal-frame resonant micro-mirror (ANSYS)

119

<div align="center">(a)   (b)</div>
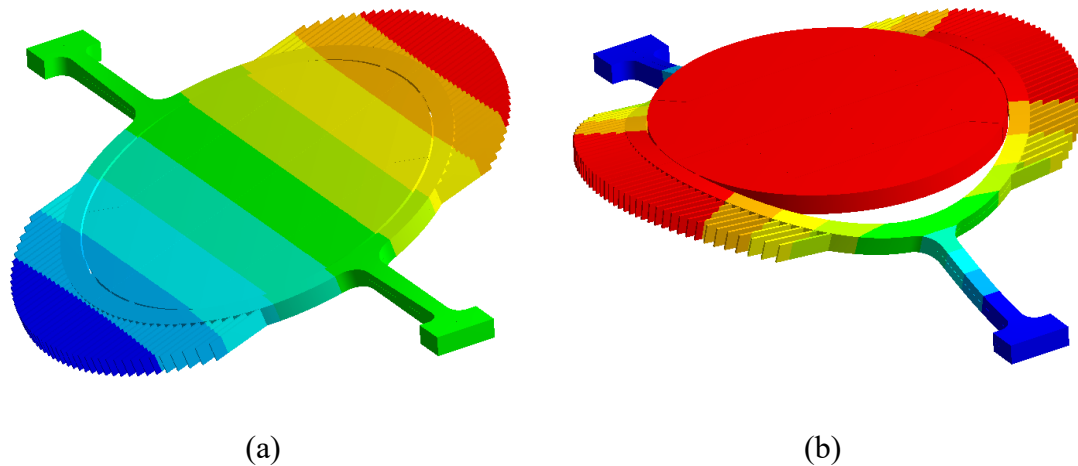
Figure 7-5: (a) Torsion mode at f_s and (b) piston mode at f_p of the gimbal-frame resonant micro-mirror
(blue to red: minimum to maximum modal displacement)

7.2.4   Micro-Scanner CFD Models

Navier-Stokes simulations, based on the methodologies discussed in Chapter 5 were performed to analyse the air damping of the resonating micro-mirror as part of *Step 3* in the design optimization scheme. Separate CFD models were developed for the comb structure and mirror plate based on the methodologies described in Sections 5.2.1.2 and 5.2.2. The boundaries of the comb structure fluid model (*CFD_1*) are shown in **Figure 7-6(a)**. The model consists of a single finger gap on either side of the rotational axis in order to facilitate the simulation of rotor finger rotation. The *sliding mesh* technique in ANSYS Fluent was applied in order to simulate the relative movement between the rotating and fixed comb fingers as previously described in Section 5.2.1.2 . The mirror structure fluid model (*CFD_2*) consists of half the mirror plate and gimbal frame while the comb structure was not included, as shown in **Figure 7-7**. In this optimization exercise, the underlying mirror cavity wall boundary is not included. In the case where the presence of the cavity wall has a negligible impact on the damping coefficient of the micro-mirror, the computationally-intensive *dynamic mesh* method described in Section 5.2.2.1 can be replaced by the *sliding mesh* method in ANSYS Fluent. In the absence of the non-moving cavity wall boundary, the transient flow around the oscillating mirror can be modelled as a single fluid mesh domain oscillating about the micro-scanner's rotational axis. A cylindrical fluid domain was considered to facilitate mesh motion. Both models were simulated under transient flow conditions to account for any phase shift between the damping moment and the angular velocity of the micro-mirror resulting from fluid flow inertia [79].

<div align="center">120</div>

(a)   (b)
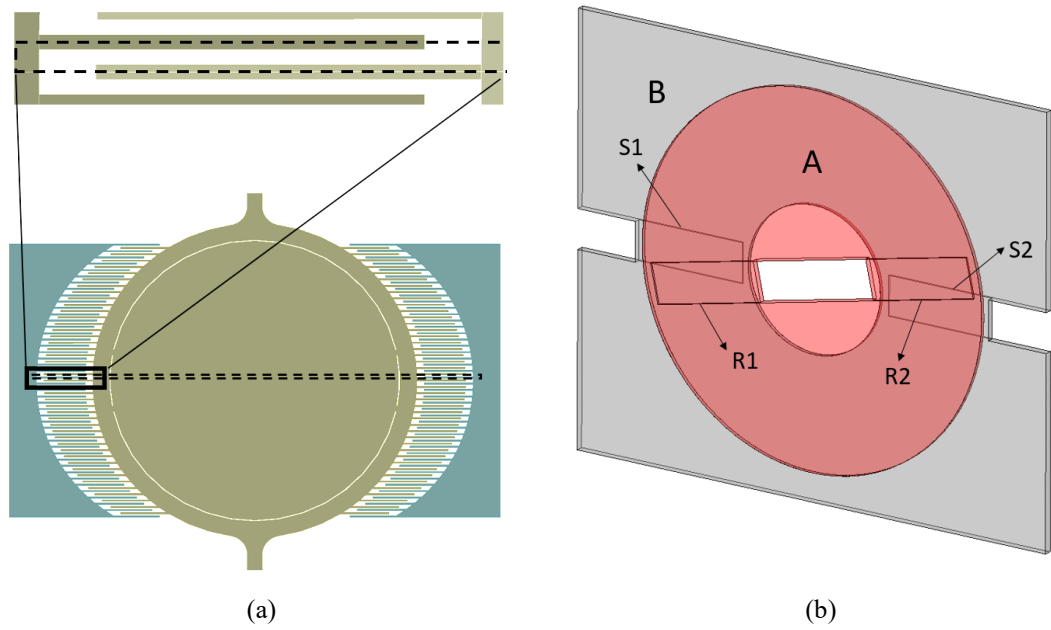
Figure 7-6: CFD model of the AVC structure cell (*CFD_1*): (a) boundaries of the comb finger cell
(b) rotating mesh zone A (red) including rotating finger boundary surfaces (R1, R2) and stationary mesh
zone B (grey) including static finger boundary surfaces (S1, S2)
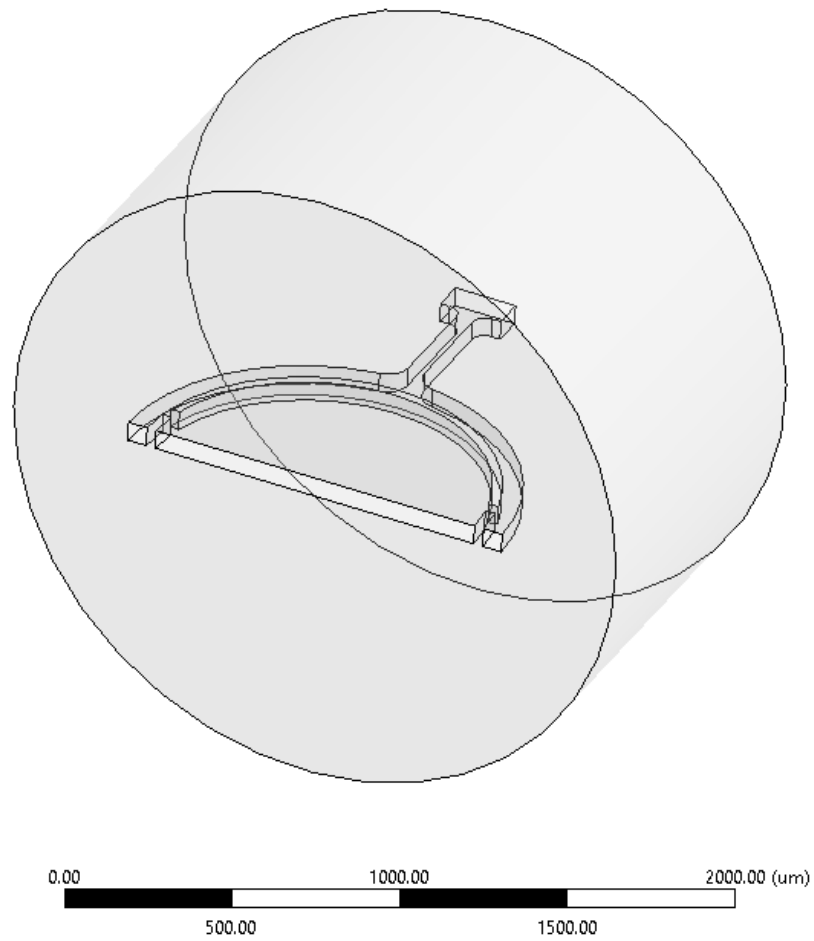
Figure 7-7: CFD model of a cylindrical volume of air surrounding the micro-mirror structure (*CFD_2*)

121

The models *CFD_1* and *CFD_2* were parametrized and it was ensured that no significant mesh distortion occurs within the stipulated ranges of parameter variation listed in **Table 7-2**. The sinusoidal time-varying angular velocity profile was prescribed via a user-defined function, to enable mesh motion. For all runs, 3 cycles and 50 time steps per cycle were simulated, while 20 iterations were performed during every time step to ensure solution convergence. The total damping moment due to pressure drag and viscous shear forces on the rotating boundaries was calculated using (5.19) and stored at each time step via a user-defined function compiled in ANSYS Fluent. Due to the different length scales involved and fluid flow complexity, a comprehensive mesh independence study was performed by analysing the total damping magnitude and profile shape. Additionally, the CFD models were validated by comparing the total Q with that obtained from numerical and experimental results for a similar micro-mirror design [79].

7.2.5   **Parameter Sensitivity of the Quality Factor**

As part of the electrostatic-fluidic optimization, the influence of a number of design parameters on the air damping characteristics of the gimbal-frame micro-scanner is analysed. The sensitivity analysis is based on output damping parameters E_{loss} and Q. The energy dissipation over one cycle, E_{loss} is equated to the electrostatic energy input, E_{el} in order to deduce the scanning efficiency at resonance. On the other hand, Q is a dimensionless parameter describing the qualitative dynamic behaviour of the damped resonating micro-scanner. The parameter sensitivity of E_{loss} may not correspond to that of Q given that the latter is a function of the micro-scanner's moment of inertia (see (5.15)). All relevant design parameters for the CFD models of the comb actuator cell (*CFD_1* of **Figure 7-6**) and the mirror plate (*CFD_2* of **Figure 7-7**) are listed in **Table 7-3** and **Table 7-4** respectively.

Table 7-3: Input parameters for *CFD_1* numerical model

Symbol	Description	Nominal value	Range of variation
t_m	thickness	65 μm	±17 μm
f_l	comb finger length	180 μm	±40 μm
f_o	comb finger offset	27 μm	±5 μm
f_w	comb finger width	6 μm	±4 μm
f_r	comb finger position from rotational axis	450 μm	±150 μm
f_g	comb finger gap	6 μm	±3 μm

Table 7-4: Input parameters for *CFD_2* numerical model

Symbol	Description	Nominal value	Range of variation
t_m	thickness	65 µm	±17 µm
R	mirror plate radius	500 µm	±140 µm
ψ	gimbal-mirror link angle	23°	±8°
$l_{g,w}$	gimbal-mirror link length	20 µm	±10 µm
$w_{g,m}$	gimbal-mirror link width	40 µm	±20 µm
w_g	gimbal width	60 µm	±8 µm

The sensitivity, *sens$_{fcd}$* of Q and E_{loss} as a result of the above design parameter variations is calculated using the finite central difference method as in (7.2) where x is the nominal value and h is the range of variation. The sensitivity of each design parameter is calculated by performing simulations at the respective minimum and maximum values defined in **Table 7-3** and **Table 2-4** while the remaining parameters are set at their nominal values.

$$sens_{fcd} = \frac{f\left(x+\frac{h}{2}\right)-f\left(x-\frac{h}{2}\right)}{\left(x+\frac{h}{2}\right)-\left(x-\frac{h}{2}\right)} \qquad (7.2)$$

Initially, parameter sensitivity of damping loss is investigated for each individual CFD model. The sensitivity of the $E_{loss,comb}$ and Q_{comb} to the design parameters listed in **Table 7-3** are plotted in **Figure 7-8(a)** and **Figure 7-9(a)**. The sensitivity results are also presented as a Pareto chart as shown in **Figure 7-8(b)** and **Figure 7-9(b)** whereby the first 95% of the cumulative distribution is displayed. It can be seen that the position of the rotating comb finger with respect to the mirror rotational axis predominantly determines the AVC structure damping losses. A greater t_m sensitivity of Q_{comb} compared to $E_{loss,comb}$ can be observed as a result of the dependence of the mirror's moment of inertia on t_m.
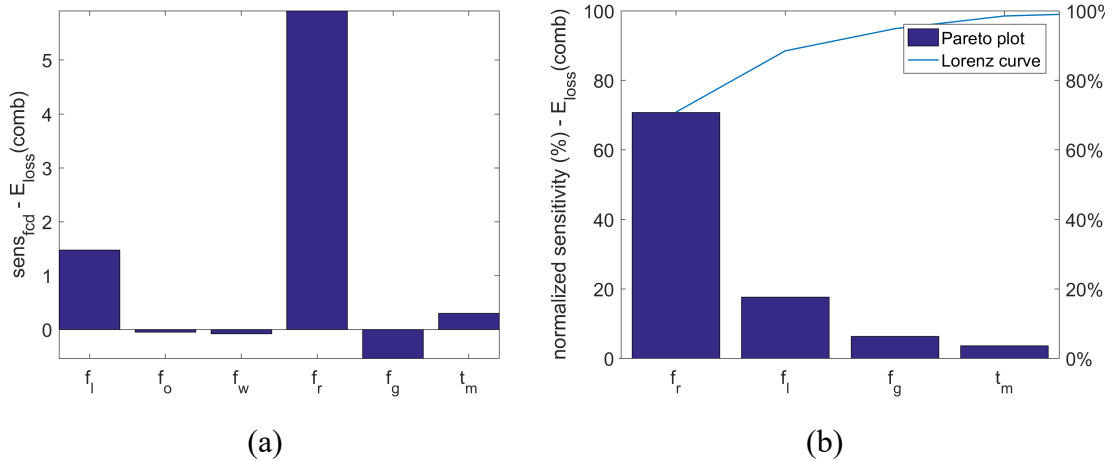
Figure 7-8: E_{loss} from air damping simulations of an AVC structure (*CFD_1*): (a) parameter sensitivity (b) Pareto plot and Lorenz curve for the normalized sensitivities
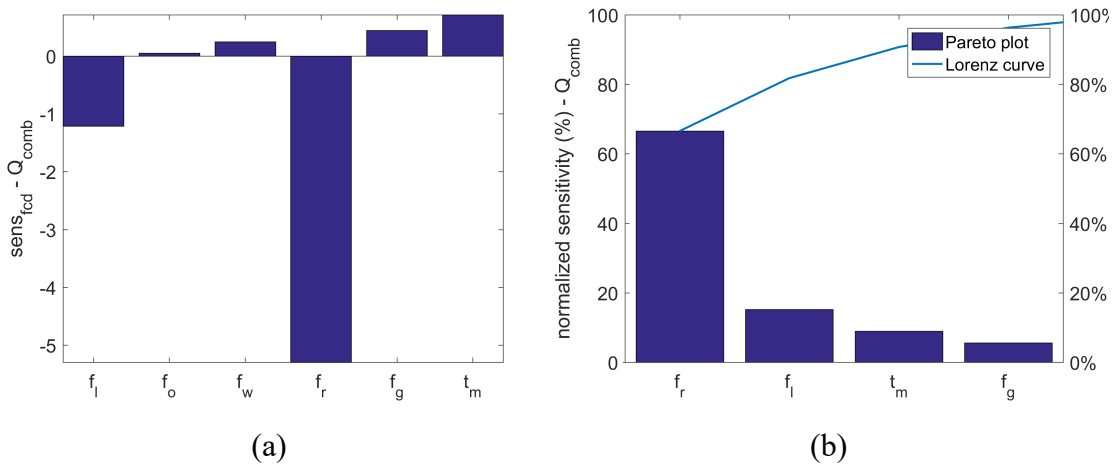
Figure 7-9: Q due to air damping simulations of an AVC structure (*CFD_1*): (a) parameter sensitivity (b) Pareto plot and Lorenz curve for the normalized sensitivities

Results from sensitivity analysis based on the mirror plate CFD model are displayed in **Figure 7-10** and **Figure 7-11**. As expected, the mirror plate radius and the gimbal frame width predominantly effect $E_{loss,plate}$ and Q_{plate} in line with damping theory for a circular plate oscillating in out-of-plane rotation. However, the effect of thickness on the damping losses is not negligible and these results provide further evidence that Q of resonant micro-scanners can be significantly improved by increasing t_m.
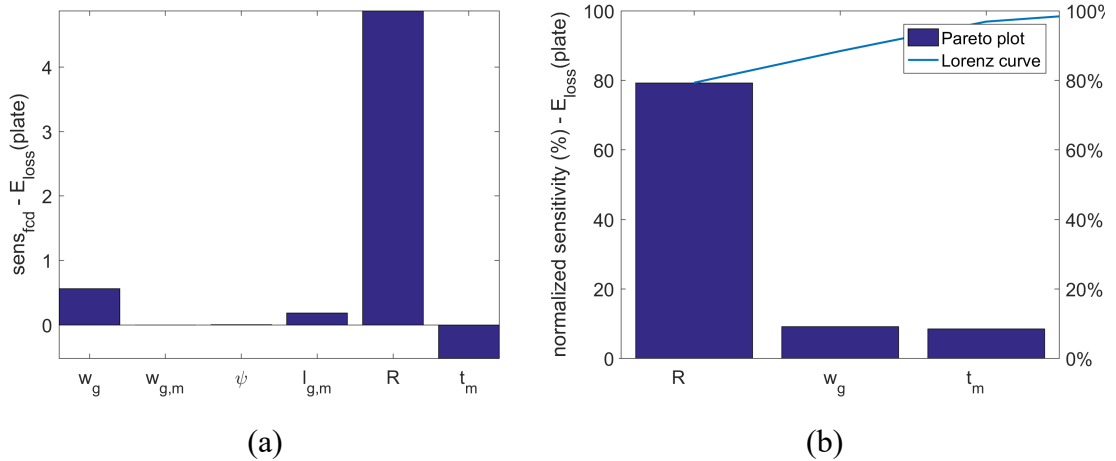
Figure 7-10: E_{loss} from air damping simulations of a gimbal-framed micro-mirror (*CFD_2*): (a) parameter sensitivity (b) Pareto plot and Lorenz curve for the normalized sensitivities
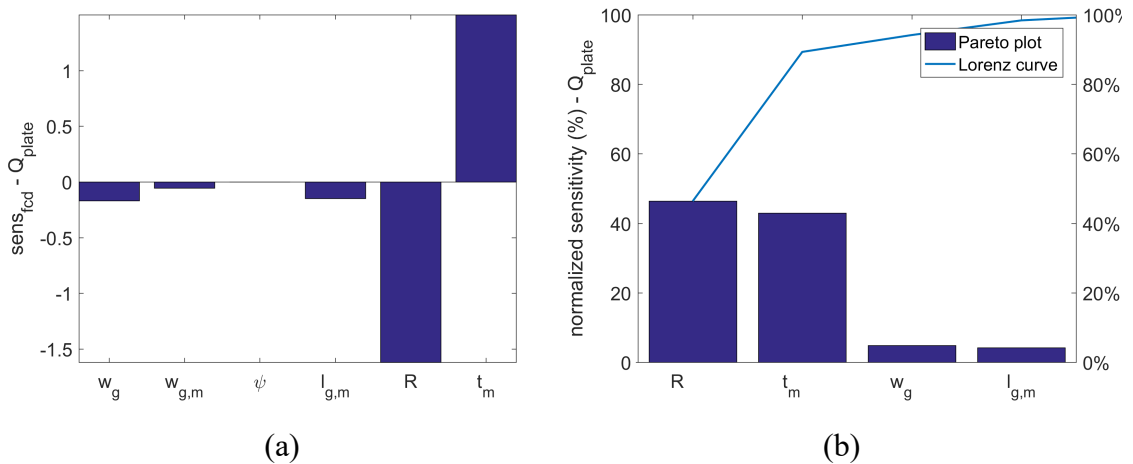
Figure 7-11: Q from air damping simulations of a gimbal-framed micro-mirror (*CFD_2*): (a) parameter sensitivity (b) Pareto plot and Lorenz curve for the normalized sensitivities

By combining the transient damping moment responses obtained from the N-S models *CFD_1* and *CFD_2*, the overall Q and E_{loss} of the gimbal-framed micro-scanner of **Figure 7-1** can be deduced. A sensitivity analysis is performed by considering the design parameters from both **Table 7-3** and **Table 7-4**. It has to be noted that the AVC structure of **Figure 7-1** lies on a curved path such that f_r is not constant. Consequently the design parameter f_r is replaced by the total number of comb fingers, N. The position of each comb finger from the rotational axis is factored into the calculation of the N sensitivity. A variation in N of 30 ± 10 is considered and sensitivity of the overall E_{loss} and Q are displayed in **Figure 7-10** and **Figure 7-11** .

Results demonstrate that E_{loss} is highly dependent on the mirror diameter, an indication that mirror plate drag is the predominant damping mechanism. On the other hand, mirror thickness and the AVC structure characteristics predominantly determine the overall Q. The increase in energy dissipation with R is offset by a corresponding increase in the energy stored by the oscillating structure. Given that the layout thickness is dictated by the selected fabrication process, the AVC structure parameters f_l, f_g, N, and f_w can be considered as the input parameters for the partial objective F_5.
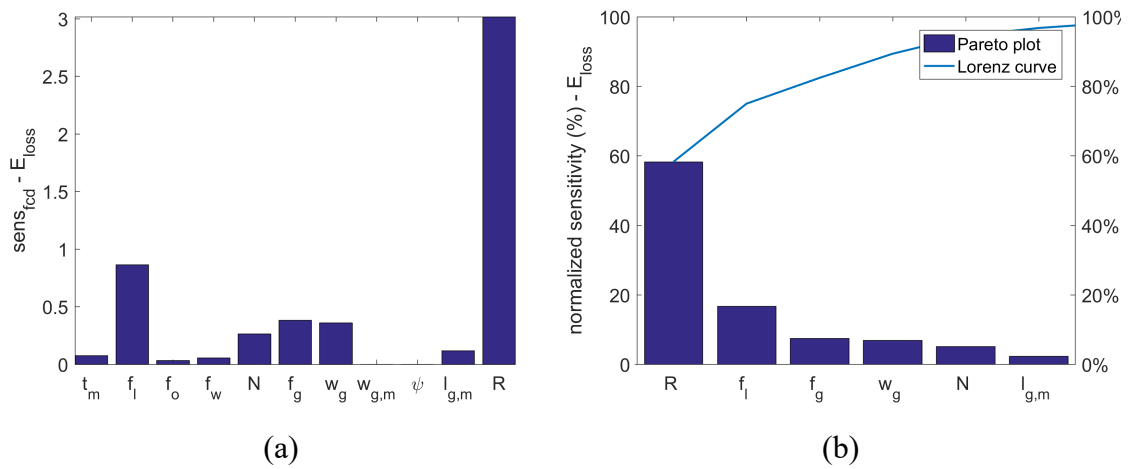
Figure 7-12: Total E_{loss} of a gimbal-framed micro-scanner actuated by an AVC structure with a circular edge (a) parameter sensitivity (b) Pareto plot and Lorenz curve for the normalized sensitivities
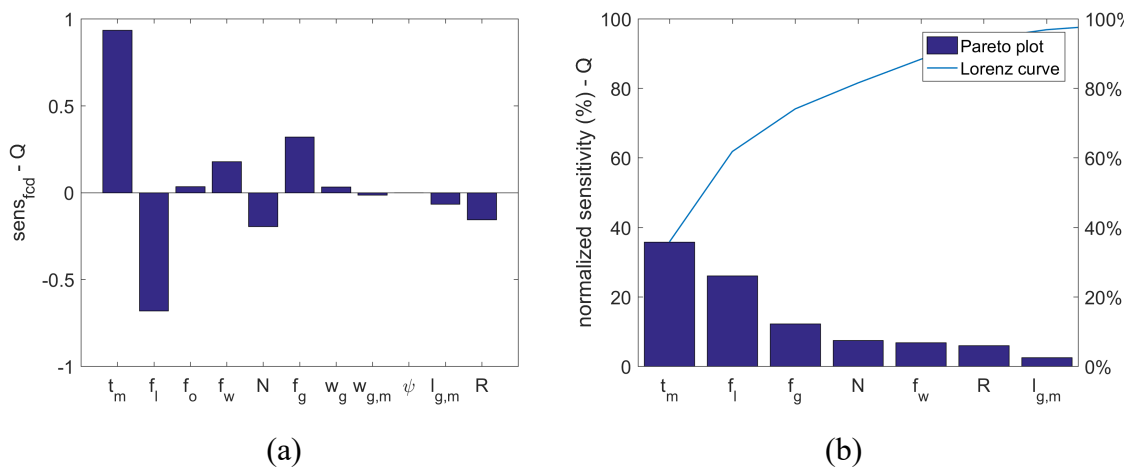
Figure 7-13: Overall Q of a gimbal-framed micro-scanner actuated by an AVC structure with a circular edge (a) parameter sensitivity (b) Pareto plot and Lorenz curve for the normalized sensitivities

7.2.6   Meta-Modelling and Optimization Methods

The determination of input parameters and numerical model parametrization defining the design domain is followed by a selection of the allowed ranges of design variations: $s_j \in [s_{j,min}, s_{j,max}]$, listed in **Table 7-2**. Following the sensitivity analysis performed to determine the input parameters, the optimization task was subdivided in three steps:

Step 1:   Minimization of the dynamic deformation was achieved by performing the static structural simulation at a fixed angular acceleration (constant $f_s = 25$ kHz) such that for the computation of the objective function $F_1(s)$, s_1 - s_4 are varied while $s_5 - s_9$ kept constant at their respective nominal value.

Step 2:   In the second step, both modal and static simulations are performed as described in Section 7.2.3 such that the multiple-criteria objective function in (7.1) is defined by $n = 4$. In this case, for the computation of the partial objective functions $F_{1-4}(s)$, s_5-s_9 are varied while s_1-s_4 are kept constant at the values previously determined in *Step 1*.

Step 3:   Finally, transient CFD models described in Section 7.2.4 are simulated at a fixed $f_s = 25$ kHz and $\theta_{max} = 12°$ such that for the computation of the objective function F_5, s_{10}-s_{14} are varied while s_1-s_9 are kept constant at the values previously determined in *Steps 1* and *2*.

For each step, the optimization task was implemented using the ANSYS Response Surface Optimization Tool [136]. Instead of solving the FE model for each sample iteration during the optimization process, the computational time can be significantly reduced if the sample points are predetermined within the design domain using a Design of Experiments (DOE) method [133]. A meta-model of the design is then constructed by fitting a response surface function to the DOE points. The Central Composite Design with a Standard Face-Centred type was selected as the DOE method after ensuring an acceptable response surface goodness of fit. For instance, 25 equally distributed sampling points are generated for the four input parameters considered in *Step 1*.

The response surfaces are then fitted to the DOE points using the Genetic Aggregation method where a number of response surface types are simultaneously solved in order to generate the best-suited response surface for each output parameter [136]. The accuracy of each generated response surface fit was evaluated using the adjusted coefficient of multiple determination R^2, which was found to be greater than 0.97 (best value is 1).

Finally, the optimization task was performed using the Multi-Objective Genetic Algorithm (MOGA), which supports the multiple objectives evaluated in *Step 2* and is suitable for searching for global optima [136]. A convergence stability of 2%, based on the mean and standard deviation of the output parameter, is set as the convergence criterion. One hundred sample points per iteration were generated from the meta-models and the number of iterations was limited to 20. For each optimization run, the meta-model results obtained from the optimized input parameters were then verified by directly solving the FE model.

7.3   Results

7.3.1   Design Optimization Step 1: Dynamic Deformation

The DOE points used for the optimization task of minimizing the dynamic deformation were generated using the design variation ranges for input parameters 1 to 4, while the input parameters 5 to 9 were fixed using the nominal values defined in **Table 7-2**. The optimal link dimensions and angle, ψ, for different link quantities are listed in **Table 7-5**. It can be seen that dynamic deformation is lowest with four links. The response surface for δ_{max} with respect to $w_{g,m}$ and ψ is plotted in **Figure 7-14**.

Table 7-5: Summary of the optimal design parameters s_2, s_3 and s_4 for different values of s_1
(f_s = 25 kHz; θ_{max} = 12°)

s_1 - n_l	s_2 - ψ [°]	s_3 - $w_{g,m}$ [µm]	s_4 - $l_{g,m}$ [µm]	δ_{max} [nm]
2	-	200	13	106.0
4	*23.2*	*20*	*5*	*95.1*
6	7.7	34	5	105.3
8	5.8	24	5	105.7
10	4.1	20	5	105.7
12	3.9	10	5	106.0
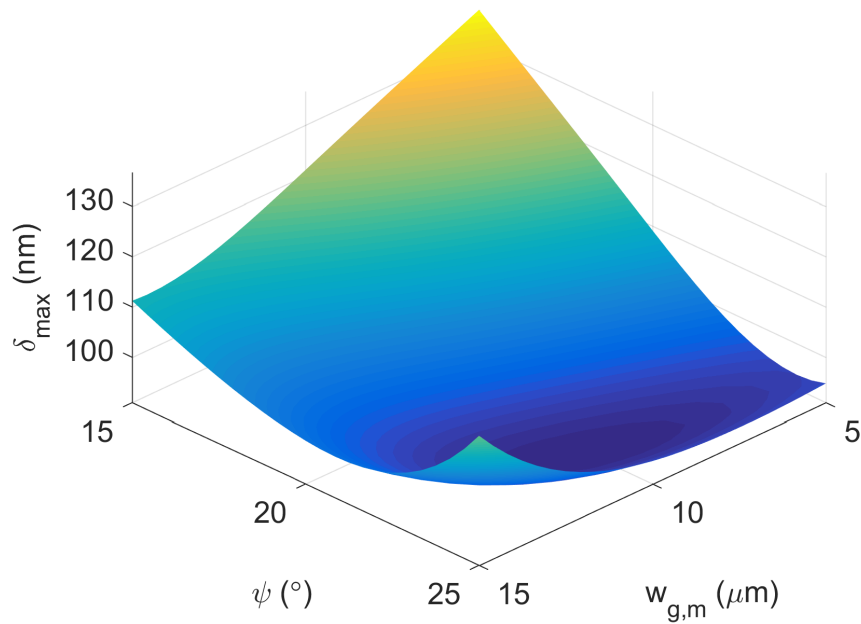
Figure 7-14: Response surface plot of δ_{max} against gimbal link angle (ψ) and width ($w_{g,m}$) for $n_l = 4$ ($f_s = 25$ kHz; $\theta_{max} = 12°$)

7.3.2   Design Optimization Step 2: Performance and Reliability

For the second optimization task, the four partial objectives of **Table 7-1** were considered while the design domain was defined from the variation ranges for input parameters s_5 to s_9, given in **Table 7-2**. On the other hand, the optimal values deduced from *Step 1* were used to set the input parameters s_1 to s_4. The best design configuration, verified using the FE model, was found to be:

- $s_5 = 51.9$ µm; $s_6 = 51.4$ µm; $s_7 = 408.8$ µm; $s_8 = 56.1$ µm; $s_9 = 57.3$ µm

The simulated characteristics of the resonant micro-mirror with the optimal design configuration deduced from the optimization tasks discussed above were found to be:

- $f_s = 25093$ Hz; $\left| f_s\text{-}f_p \right| = 3652$ Hz; $\delta_{max} = 96.7$ nm; $\tau_{max} = 1299.3$ MPa

It can be seen that the simulated τ_{max} is less than the critical shear stress for the torsional beams. Moreover, **Figure 7-15** depicts a surface plot of the dynamic deformation obtained by solving the FE model using the optimal design configuration. The resultant δ_{rms} is 10.7 nm and therefore below the critical out-of-plane deformation, δ_{crit} (44 nm) defined by the Rayleigh diffraction limit. These results successfully demonstrate that,

by incorporating an optimized gimbal structure design, an optically-flat resonating micro-mirror designed for LBS micro-displays with SVGA resolution is achieved.
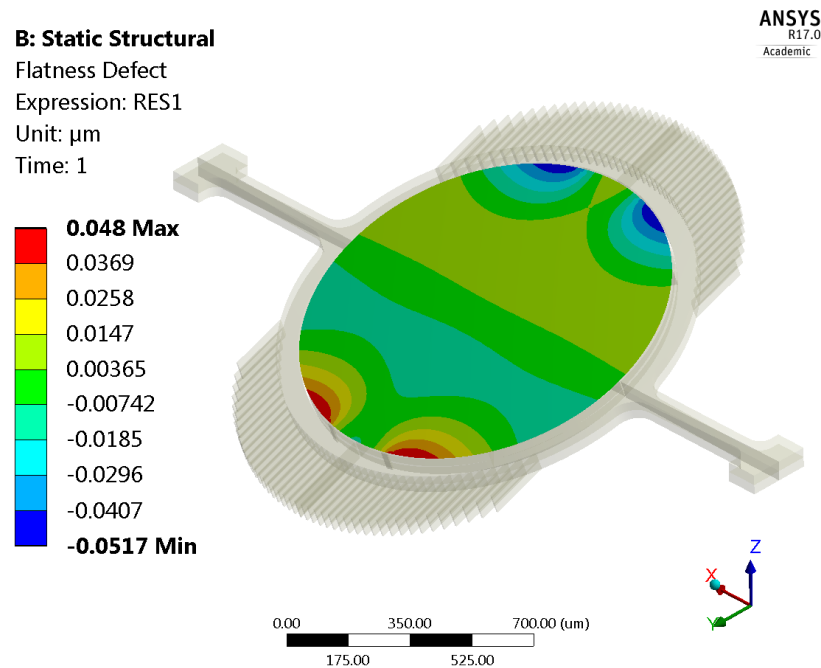
Figure 7-15: Surface plot of the dynamic deformation, δ for the optimal design configuration obtained using static structural FE analysis (f_s = 25.1 kHz; θ_{max} = 12°).

7.3.3   Design Optimization Step 3: Quality Factor

In order to evaluate Q, the damping moment, M_d due to pressure drag and viscous shear forces was deduced from the comb structure and mirror plate models: *CFD_1* and *CFD_2*. The resulting fluid flow velocity around the comb finger cell together with the shear stress distribution on the rotating finger surfaces is depicted in **Figure 7-16**. The variable position of each finger from the rotational axis was factored into the summation of E_{loss} for the entire comb structure, in order to deduce energy dissipation due to N rotating comb fingers. The fluid flow velocity at the mid-plane of the micro-mirror together with the static pressure distribution along mirror surface are shown in **Figure 7-17**.

130
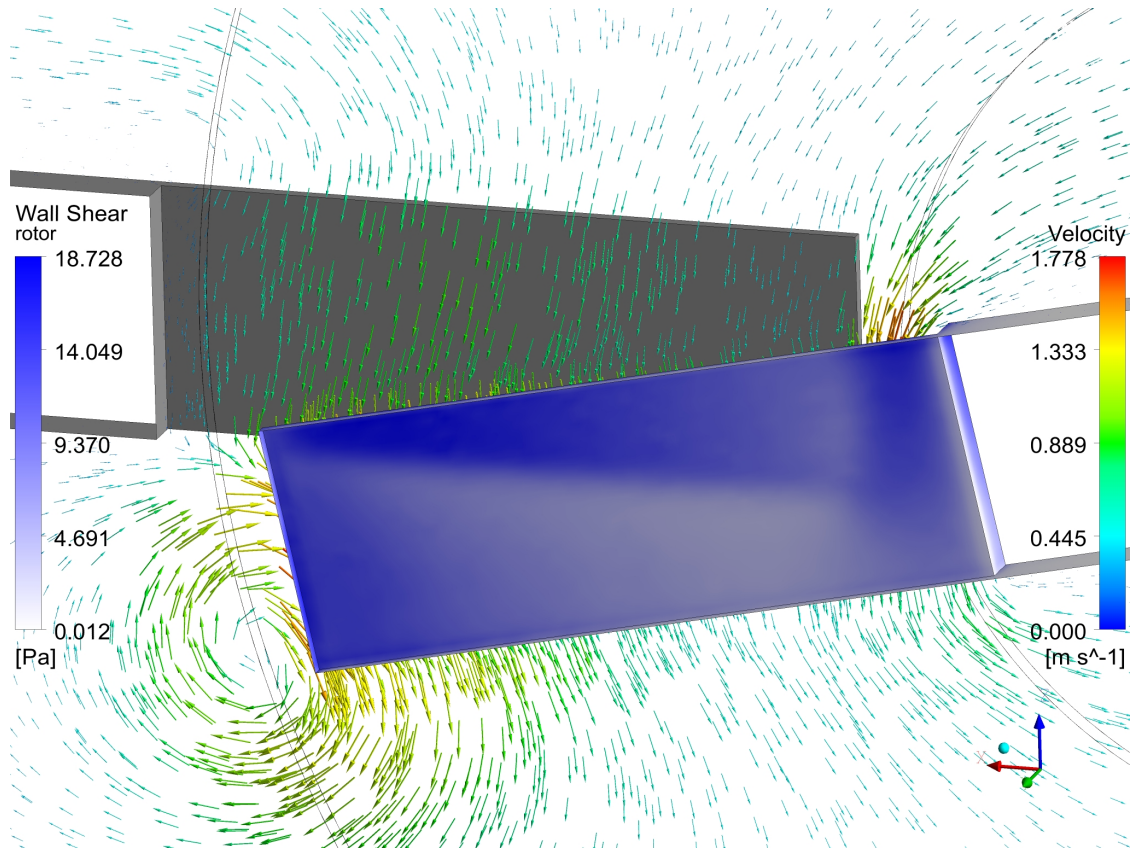
Figure 7-16: Contour plot showing shear stress distribution on rotating comb finger and vector plot showing flow velocity field ($f_s = 25$ kHz; $\theta_{max} = 12°$)
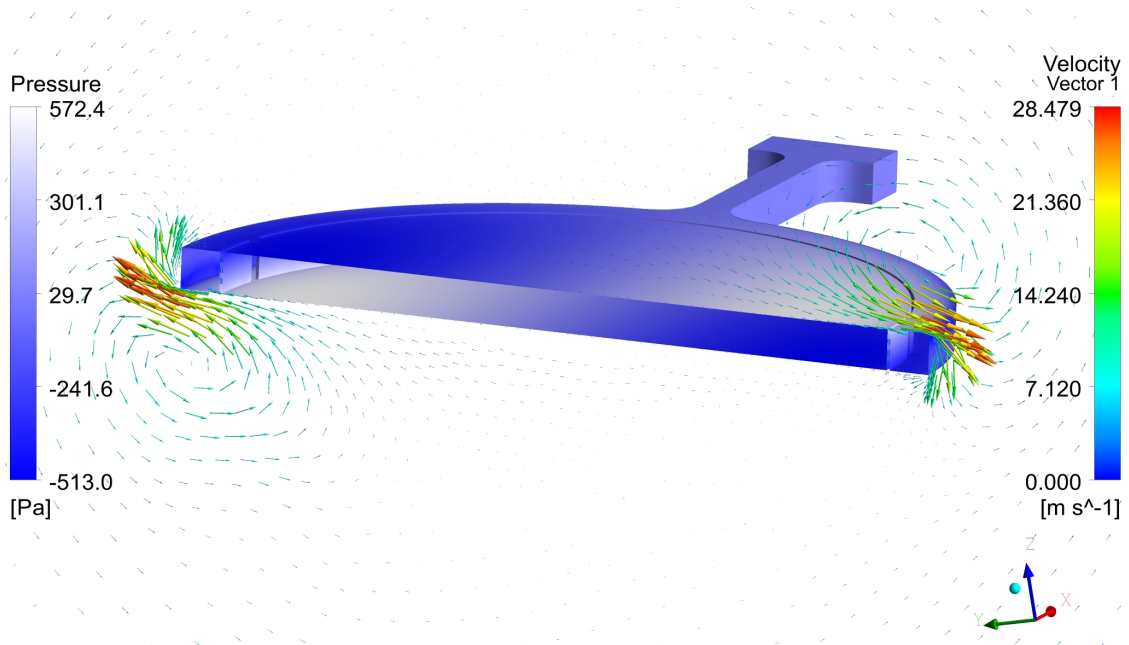
Figure 7-17: Contour plot showing static pressure distribution on mirror plate and vector plot showing flow velocity field at the mid-plane at time step where M_d is maximum ($f_s = 25$ kHz; $\theta_{max} = 12°$)

131

Figure 7-18 shows the response surface plot of Q with respect to f_l and N for the micro-mirror with optimized design parameters deduced from *Step 1* and *Step 2*. The variation of Q with N was found to be non-linear due to the position of the rotating comb fingers that is dependent on the curvature of the gimbal frame. The results obtained from the CFD simulations can be coupled with electrostatic analysis from which the variation of comb structure capacitance with θ, and hence the electrostatic torque, M_{el}, can be deduced. This completes the optimization process by minimizing the required actuation voltage in order to achieve the target micro-mirror performance objectives. Coupled electrostatic-fluidic optimization will be presented in Section 7.3.3 as part of the SOIMUMPs direct-drive micro-scanner design process.
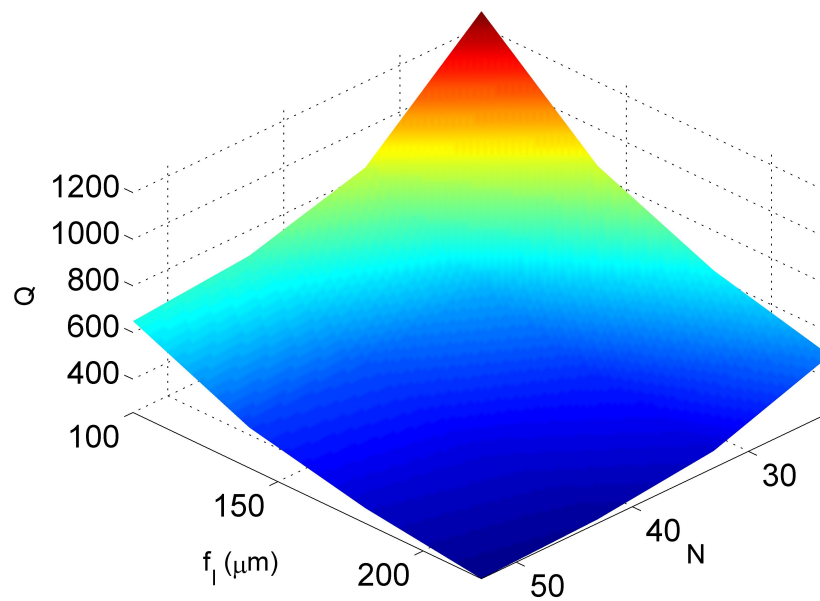
Figure 7-18: Response surface plot of Q against finger length (f_l) and number of fingers (N)
(f_s = 25 kHz; θ_{max} = 12°; f_g = 6 μm; f_w = 6 μm)

7.4   Conclusions

A design optimization scheme targeting the fluid and mechanical characteristics of resonating micro-mirrors driven by electrostatic comb structures is presented. Dynamic deformation, resonant frequency, modal separation gap, maximum shear stress at the torsional beams and Q are the output parameters considered in the novel three-stage multi-objective optimization process. DOE and RSM techniques are invoked to reduce

the computational time for optimization and provide a detailed analysis of the design space.

Micro-mirror surface non-planarity is a critical limitation in the development of high-resolution laser scanning displays. An efficient optimization process for micro-mirrors designed to achieve low dynamic deformation is demonstrated. This is achieved by the implementation of accurate dynamic deformation FE simulations in a multi-stage optimization scheme based on meta-modelling. Results show that an optimal configuration of the micro-mirror gimbal-type frame ($n_l = 4$; $\psi = 23.2°$; $w_{g,m} = 20$ μm; $l_{g,m} = 5$ μm) is effective in reducing dynamic deformation to below δ_{crit} at the target f_s and θ_{max} for XGA optical resolution.

Meta-model generation for the evaluation of the fluid damping characteristics of the high frequency scanning micro-mirror is also demonstrated. 3-D transient CFD models are developed in order to assess, in detail, the effect of the comb structure and gimbal-framed mirror geometries on Q. Electrostatic FE simulations can be integrated to the CFD air damping results in the design optimization scheme to achieve the optimal comb structure configuration in order to minimize the required drive voltage.

8   PROTOTYPE FABRICATION AND MEASUREMENTS

In this section, the design and fabrication of a high performance resonating micro-scanner for pico-projection applications is presented. The main objectives behind this work is to demonstrate that a high frequency scanning of 1mm-diameter micro-mirror can be achieved while maintaining high energy-transduction efficiency and dynamic flatness. The design optimisation scheme proposed in Chapter 7 is applied in order to achieve the target specifications listed in **Table 8-1**.

Table 8-1: Target performance specifications for resonant micro-scanners

Specification	Value
Scanning frequency, f_s	25 kHz
Scan angle amplitude, θ_{max}	12 °C
Maximum drive voltage amplitude	200 V
Maximum dynamic deformation, δ_{rms}	44 nm
Maximum principal stress at θ_{max}	1.4 GPa

8.1   Process Selection

SOIMUMPs, offered by MEMSCAP, is a bulk silicon-on-insulator (SOI) micromachining process available for multi-project wafer (MPW) runs. Bulk micromachining refers to the removal of a relatively thick silicon layer using liquid or plasma based chemistries [139]. Through its affiliation with the EUROPRACTICE programme, the University of Malta has access to the SOIMUMPs MPW runs which take place every 3 months. No other SOI microfabrication process was made accessible for the fabrication of the resonating micro-scanner design. A cross-sectional view showing all layers of the SOIMUMPs process is depicted in **Figure 8-1**.

Silicon	Substrate
Oxide	Metal
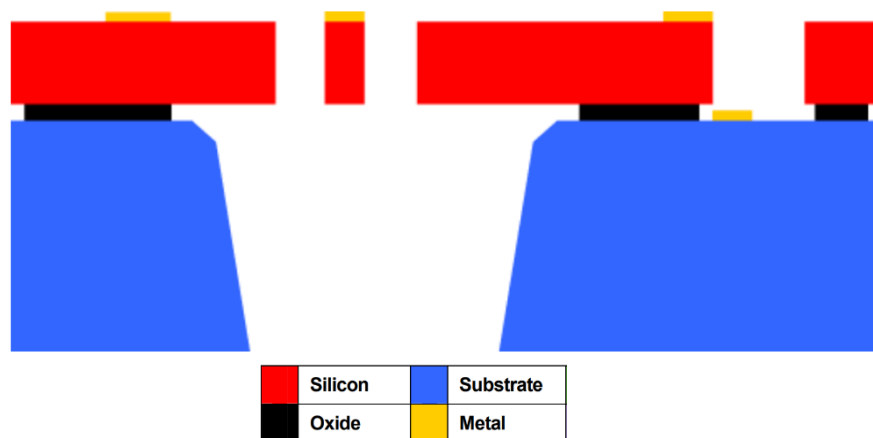
Figure 8-1: Cross-section view of the SOIMUMPs process layers [140]

8.1.1   **Process Definition**

The process utilizes a 150mm diameter n-type double-side polished SOI wafer [140]. The SOI wafer consists of a (1 0 0) single crystal silicon (SCS) wafer (referred to as *Substrate*), a thermal grown SiO₂ insulation layer (referred to as *Oxide*) and a mechanically thinned SCS layer (referred to as *Silicon*) which is used to create moving structures [139]. The *Silicon* layer, which is used to create movable structures, can be either 10 or 25 μm thick. Doping in the *Silicon* layer is achieved by depositing a layer of phosphosilicate glass on the top surface followed a process of annealing. The SOI patterning and etching steps are described as follows:

1) A metal stack consisting of 20 nm of Cr and 500 nm of gold (referred to as *PadMetal*) is deposited and patterned, using the *PADMETAL* mask layer through a *liftoff* process [141]. This metal layer is not suitable for optical mirror applications due to the relatively high surface roughness resulting from the exposure to high temperature during the subsequent deep reactive ion etching (DRIE) process.

2) The *Silicon* layer is patterned via lithography with the second mask level (*SOI*) and etching is performed using DRIE, which allows for the creation of near-vertical walls along the Si thickness.

3) After the application of a front-side protection material to the *Silicon* layer's top surface, the wafer is then reversed to pattern the *Substrate* layer from the bottom side using the third mask level (*TRENCH*). The pattern is etched into the *Substrate* and *Oxide* layers through DRIE and a wet-oxide etching respectively. The mechanical structures in the Silicon layer, located over through-holes in the *Substrate* layer are released once the front-side protection material is removed. The exposed regions in the *Oxide* layer are then removed using a vapour hydrofluoric (HF) acid process to allow for electrical contact to the *Substrate* layer.

4) A shadow masking technique is applied to deposit and pattern a metal stack comprising 600 nm of Au over 50 nm of Cr (referred to as *BlanketMetal*). The shadow mask is prepared from a separate Si wafer which is placed over the SOI wafer. Standoffs are included in the shadow mask to allow for temporary bonding between the two wafers without contacting the patterned features. The shadow mask is then patterned using the fourth mask level (*BLANKETMETAL*) followed by DRIE to create through-hole structures. After alignment and bonding of the shadow mask and SOI

wafers, the metal is evaporated (electron beam) and deposited on the top surface of the Si layer.

The maximum *Silicon* layer thickness available with the SOIMUMPs process is 25 μm or 62% less than the Si layer thickness available in the STM process for the fabrication of movable structures (see Section 2.7). The reduced thickness entails important limitations towards achieving the above mentioned design objectives. Static and dynamic flatness of the micro-scanner's reflective surface are proportional to the Si thickness. In order to quantify dynamic deformation improvements achieved by the design irrespective of the fabrication process, results in this section are presented in normalized form: R_{def} (defined in (6.10)). Other limitations brought about by a low micro-scanner thickness are: (i) reduced electrostatic energy given the lower angular range during which the AVC structures are engaged (ii) lower quality factors due to mirror plate drag as previously discussed in Section 5.5.2.

Table 8-2: SOIMUMPs process details [140]

Layer Name	Thickness (μm)	Lithography Level Name	Material
PadMetal	0.52	*PADMETAL*	20 nm Cr + 500 nm Au
Silicon	25	*SOI*	monocrystalline n-type doped Si
Oxide	2	*TRENCH*	SiO$_2$
Substrate	400		monocrystalline Si
BlanketMetal	0.65	*BLANKETMETAL*	50 nm Cr + 600 nm Au

The *Silicon* layer is oriented such that the <100> crystallographic axes are aligned parallel to the coordinate system of the user-defined mask set [139]. Therefore, the orthotropic elastic properties listed in **Table 3-3** were considered for modal and structural numerical analysis. The in-plane residual stress values of the laminated composite wafer were not directly available from the vendor, however data from published sources are listed in **Table 8-3**. The in-plane residual stress in the *Silicon* layer is calculated from in-plane strain measurements of pointer micro-structures. It has to be noted that the doping process in the *Silicon* layer additionally introduces a strain gradient along the material thickness resulting in the out-of-plane curvature of released metal-free silicon structures. The through-thickness strain gradient in the *Silicon* layer is

calculated from the curvature of micro-cantilever structures in the as-released condition by Miller *et al.* [139].

Significant out-of-plane curvature is expected after the deposition of a thin metallization layer. This is primarily due to the coefficient of thermal expansion (CTE) mismatch between Au and Si and the fact that the metallization layer is deposited at elevated temperatures. The *BlanketMetal* residual stress has been deduced from a comparison between the simulated and measured radius of curvature of a micro-scanner fabricated using the SOIMUMPs process. The material stress data published by Zuo *et al.* [43] are applied to the micro-scanner structural FE models presented in this chapter.

The thickness variation of the *Silicon* layer is ±1 μm. The top surface and sidewall of the *Silicon* layer has a peak-to-valley roughness of 3.6 nm and 82.6 nm respectively, measured using AFM scans [139]. Tensile fracture strength is highly dependent on the sidewall surface topography, which may vary from die to die. Strength values ranging from 1.47 to 1.97 GPa were measured for the SOIMUMPs process.

Table 8-3: Available in-plane residual stress data of SOIMUMPs

Layer/s	Measurand	Measurement Technique	Value	Source
Silicon	in-plane residual stress	in-plane displacement measurements of pointer micro-structures	-1.9 ± 2.4 MPa	[128]
Silicon	in-plane through thickness stress gradient	curvature measurements of micro-cantilever structures	0.42 MPa/μm	
Silicon + PadMetal	combined effect of in-plane residual stress and through thickness stress gradient	curvature measurements of micro-cantilever structures	207.6 MPa	
BlanketMetal	in-plane residual stress	curvature measurements of a micro-scanner	360 MPa	[35]

8.2   Micro-Scanner Designs

Three designs concepts were evaluated in order to maximize the scanning efficiency of the micro-mirror during high frequency operation. The principle differentiating factor among the three concepts is the method with which the electrostatic moment is transferred from the AVC structures to the reflective mirror surface. The resonating micro-scanners devices fabricated using the SOIMUMPs process are listed in **Table 8-4**.

Design *D1* consists of a single torsion beam centred along the rotational axis, on either of the mirror plate. The AVC structures are rigidly connected to the mirror plate such

that the angular displacement of both components at resonance is equal in both magnitude and phase (i.e. direct drive). In the second direct drive concept (*D2*), micro-mirror rotation is achieved by combined torsion and out-of-plane bending of three parallel beams on either side of the mirror plate. The third design, *D3* is based on the indirect drive configuration (discussed in Section 2.3.1) whereby the AVC structures are connected to an outer frame while an inner frame consists of the mirror plate. The motion of the outer frame is coupled to the mirror plate in such a way that the angular displacement and phase of both components may not be equal.

All design prototypes include the gimbal-type structure, which was identified through the FE simulations of Section 6.4 as an effective method of reducing the impact of dynamic deformation in high frequency micro-scanners. In order to verify the simulation results, a copy of each design is fabricated without the reflective mirror coating (*BlanketMetal* layer). Given that the mirror surface curvature is expected to be substantial due to the high temperature deposition of the metallization layer, this would aid in differentiating between the measured static and dynamic deformation.

Table 8-4: Resonating micro-scanner designs submitted for fabrication using SOIMUMPs

Device Name	Drive Configuration	Design Type	*BlanketMetal* layer included	AVC comb finger length (μm)
D1-C-100	Direct	D1	Yes	100
D1-C-150	Direct	D1	Yes	150
D1-NC-150	Direct	D1	No	150
D2-C-150	Direct	D2	Yes	150
D2-NC-150	Direct	D2	No	150
D3-C-150	Indirect	D3	Yes	150
D3-NC-150	Indirect	D3	No	150

8.2.1   Electrostatic Design Considerations

All the fabricated micro-scanners are operated electrostatically via angular vertical comb structures. Minimizing the comb finger gap is essential in order to maximize the applied input energy into the system. Although comb finger widths and gaps of 2 μm can be fabricated using the SOIMUMPs process, minimum values of 3 μm are recommended especially for non-orthogonal features. In addition, gaps in the *Silicon* layer are typically oversized by 0.18±0.14 μm from the as-designed dimensions. Line features are similarly undersized by the same amount. Apart from process limitations, the design has to ensure that the comb fingers do not move in-plane under the application of the drive signal to the extent that electrical breakdown occurs. The mechanical stiffness of the torsional

beams and comb-fingers is designed such that in-plane motion between rotating and static AVC structures is restricted under mirror operation. In addition, the comb finger end is rounded to reduce the electric field concentration that is expected at acute features. Electrical breakdown may also occur through the medium (air) between two rigid conducting surfaces. Corner filleting is also included at the comb finger anchor point to reduce the probability of cracking during the application of the front-side protective layer prior to the Trench etch. Design rules also recommend a maximum length of 100 μm for features anchored from one end having a width less than 6 μm. This limitation ensures that the out-of-plane curvature due to residual stresses is minimal.

In all micro-scanner designs, the AVC structures are characterized by (i) a finger length of 150 μm, (ii) finger width of 6 μm and (iii) finger gap of 3 μm. A variant of design *D1* micro-scanner was fabricated with a finger length of 100 μm (D1-C-100 in Table 8-4).

8.2.2 Stress Concentrations

The torsional beam is expected to be the most stressed component of the scanning micro-mirror. However, the fracture strength of the Si moving structure is determined by the presence of features such as acute corner that promote crack propagation. For this reason, all micro-scanner designs incorporate certain details at critical locations with the aim of reducing the development of stress concentrations during the fabrication process or micro-scanner operation. These design details include:

(a) corner filleting at the torsional beam ends;

(b) corner filleting at the comb finger ends;

(c) increased radius of curvature at the edges of the gimbal-spring links.

8.3 Direct-Drive Designs

The design optimization process was divided in two subsequent stages. In the first stage, a parametrized FE model was developed in order to obtain output parameters δ_{pk}, f_s, $(f_s - f_p)$ and τ_{max} that define the partial objectives F_1, F_2, F_3, and F_4 (**Table 7-1**). In the second stage, electrostatic and fluidic simulations were performed to optimize the scanning efficiency of the micro-mirror.

8.3.1 Opto-Mechanical Optimization

The design optimization scheme proposed in Chapter 7 was modified in order to account for characteristics inherent to the SOIMUMPs process, which are not present in the STM

process. The reduced Si thickness and the high residual stresses resulting from the reflective layer deposition (*BlanketMetal*) lead to:

    (i)   a non-negligible out-of-plane curvature of the released micro-mirror which has an impact on the dynamic micro-mirror flatness and the torsional modal frequency;

    (ii)   a lower moment of inertia which requires significantly shorter springs for additional stiffness to achieve the target scanning frequency.

Three FE simulations were performed using ANSYS Mechanical to obtain the output parameters listed in **Table 7-1**:

1) Static structural analysis: the mirror plate curvature resulting from the process-derived residual stresses was simulated. Biaxial residual stress data for the *Silicon* and *BlanketMetal* layers was applied using the initial stress state command (INISTATE).

2) Pre-stressed modal analysis: the resultant stress distribution from the previous simulation was inserted as the initial condition in a modal analysis. This allows for the consideration of pre-stress effects on the micro-scanner's natural frequencies. The torsion and piston resonating modes were deduced from the first two modal frequencies using the method discussed in Section 7.2.3. From this analysis, output parameters F_2 and F_3 were derived.

3) Static structural analysis: the torsional resonant frequency obtained from the previous modal simulation was used to define a static-equivalent inertial torque, M_I. The in-plane residual stress and M_I were applied in a static structural analysis to obtain the overall static and dynamic mirror plate curvature together with the maximum shear stress in the torsional beam during the scanner operation at a $\theta_{max} = 12°$. From this analysis, output parameters F_1 and F_4 were deduced.

8.3.1.1   Finite Element Model

The lower Si layer thickness, which leads to torsional beam aspect ratios, w_s/t_m much larger than 1, renders shell elements suitable for stress analysis (see Chapter 3). Shell elements offer a number of advantages over solid elements: (i) more computationally efficient parametric analysis (ii) easier implementation of composite structures with in-

plane stresses and (iii) improved mesh quality generation for non-orthogonal features. Additionally, more than one solid element through the thickness is recommended in order to accurately model out-of-plane bending. The finite element model was developed in ANSYS using quadrilateral shell elements (SHELL181). The shell elements forming part of the mirror surface are defined with two layers: 25 µm *Silicon* and 0.65 µm *BlanketMetal*. The solution accuracy of the shell FE models was verified against results obtained from solid FE models. It was ensured that the difference in the maximum principal stress at the torsional spring between solid and shell elements is less than 1%.

8.3.1.2 *Single spring micro-scanner design (D1)*

As part of the optimization process, the selected input design parameters are listed in **Table 8-5**. The link length, $l_{g,m}$ is set to 6 µm, n_l is set to 2 and $r_{s,1}$, $r_{s,2}$ are set to half the torsional beam length, l_s. Optimal values for s_{1-5} together with the related output parameter values are listed in **Table 8-6**. It has to be noted that subsequent amendments to the mirror design were included at a later stage following the opto-mechanical optimization process. The AVC structures were extended along wing-shaped features protruding from the gimbal-frame in order to maximize the mirror scanner efficiency. The optimal configuration of the AVC structures was deduced from the electrostatic-fluidic optimization process to be presented in Section 8.4.2. Moreover, filleting was introduced at the gimbal-mirror links to minimize the development of stress concentrations in the fabricated prototypes. The final layout of design *D1* is shown in **Figure 8-2**.

Table 8-5: Nominal values and range of variation for the input parameters considered in the design optimization process of micro-scanner *D1*

Design Parameter, s_j	Symbol	Description	Nominal Value	Range of Variation
s_1	ψ	link angle	12°	± 5°
s_2	$w_{g,m}$	link width	50 µm	± 20 µm
s_3	w_g	gimbal frame width	80 µm	± 20 µm
s_4	w_s	torsional beam width	130 µm	± 50 µm
s_5	l_s	torsional beam length	110 µm	± 70 µm

Table 8-6: Opto-mechanical optimization results for design *D1*

Design Parameter	Value		Output Parameter	Value
s_1	9.0°		F_1	0.817 µm
s_2	56.2 µm		F_2	24985 Hz
s_3	89.7 µm		F_3	4746.5 Hz
s_4	115.3 µm		F_4	1.451 GPa
s_5	153.6 µm			
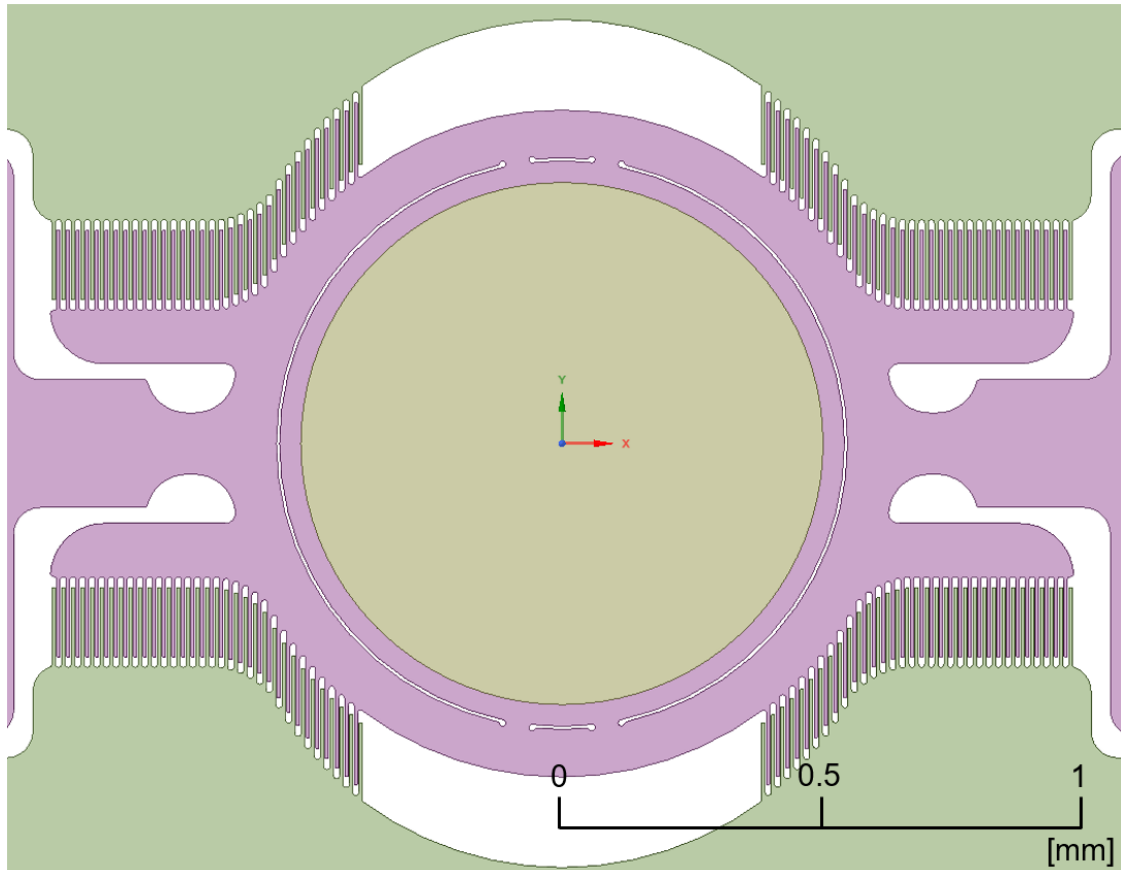
Figure 8-2: Final layout of micro-scanner design *D1* based on the direct-drive concept and consisting of a single set of torsional beams

8.3.1.3   *Multi-spring micro-scanner design (D2)*

Parametric analysis presented in Section 7.3.1, indicated that the lowest dynamic deformation is achieved with a total of four links between the gimbal frame and the mirror plate. A second direct-drive micro-scanner layout is developed based on the design proposed by Wolter *et al.* [56]. The design of **Figure 8-3** consists of a multi-spring configuration with eight links to the mirror plate. An increase in the number of links supporting the mirror plate should lead to an improved elastic strain distribution

and hence lower dynamic deformation. The inner spring is connected to the nearest mirror links and exhibits pure torsion during out-of-plane mirror rotation. The outer springs are connected to the farthest mirror links and exhibit combined torsion and bending as the mirror rotates out-of-plane. While maintaining the same design objectives listed in **Table 7-1**, the relevant input design parameters for design *D2* are given in **Table 8-7**. The design and corresponding output parameter values obtained from optimization are listed in **Table 8-8**. It can be seen that compared to design *D1* (see **Table 8-6**), slightly lower dynamic deformation is predicted. However, the maximum shear stress at the springs under combined torsion and bending is significantly higher. Further modifications on the optimized design *D1* were also implemented to design *D2* following the opto-mechanical optimization process. These modifications include an extension in the AVC structure and filleting at the gimbal-mirror links and the central torsion beams. The final layout of *D2* is presented in **Figure 8-4**.
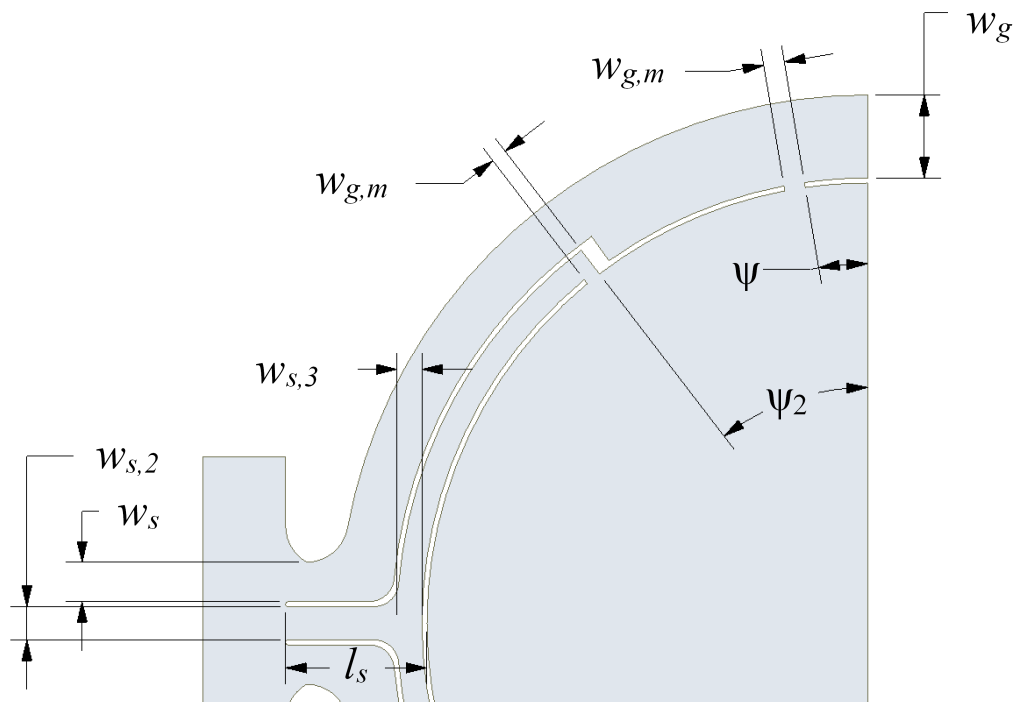
Figure 8-3: Definition of design parameters of design *D2*

Table 8-7: Nominal values and range of variation for the input parameters considered in the design optimization process of micro-scanner *D2*

Design Parameter, s_j	Symbol	Description	Nominal Value	Range of Variation
s_1	ψ	link angle	10°	± 5°
s_2	$w_{g,m}$	link width	25 μm	± 15 μm
s_3	w_g	gimbal frame width	80 μm	± 20 μm
s_4	w_s	torsional beam width	60 μm	± 20 μm
s_5	l_s	torsional beam length	130 μm	± 60 μm
s_6	ψ_2	second link angle	45°	± 15°
s_7	$w_{s,2}$	middle spring width	35 μm	± 15 μm
s_8	$w_{s,3}$	arm width	25 μm	± 10 μm

Table 8-8: Design optimization results for design *D2*

Design Parameter	Value		Output Parameter	Value
s_1	7.7°		F_1	0.636 μm
s_2	30.5 μm		F_2	24885 Hz
s_3	86.8 μm		F_3	1820.6 Hz
s_4	49.3 μm		F_4	2.098 GPa
s_5	157.0 μm			
s_6	49.9°			
s_7	22.3 μm			
s_8	14.8 μm			

Figure 8-4: Final layout of micro-scanner design *D2* based on the direct-drive concept and a multi-spring configuration exhibiting combined torsion and bending stiffness

144

8.3.2   Electrostatic-Fluidic Optimization

In order to determine the micro-scanner's energy loss, two CFD models were developed to simulate the air damping moments acting on the mirror plate and the AVC structure respectively. The modelling procedures discussed in Chapter 5, were applied to obtain the transient air pressure and shear loading on the moving structures. The total aerodynamic moment acting on the mirror plate and the gimbal-structure at the resonant frequency is plotted in **Figure 8-5**. The dynamic variation of the total moment is predominantly sinusoidal while the phase angle relative to the mirror velocity indicates that the inertia-component is greater than the drag component.
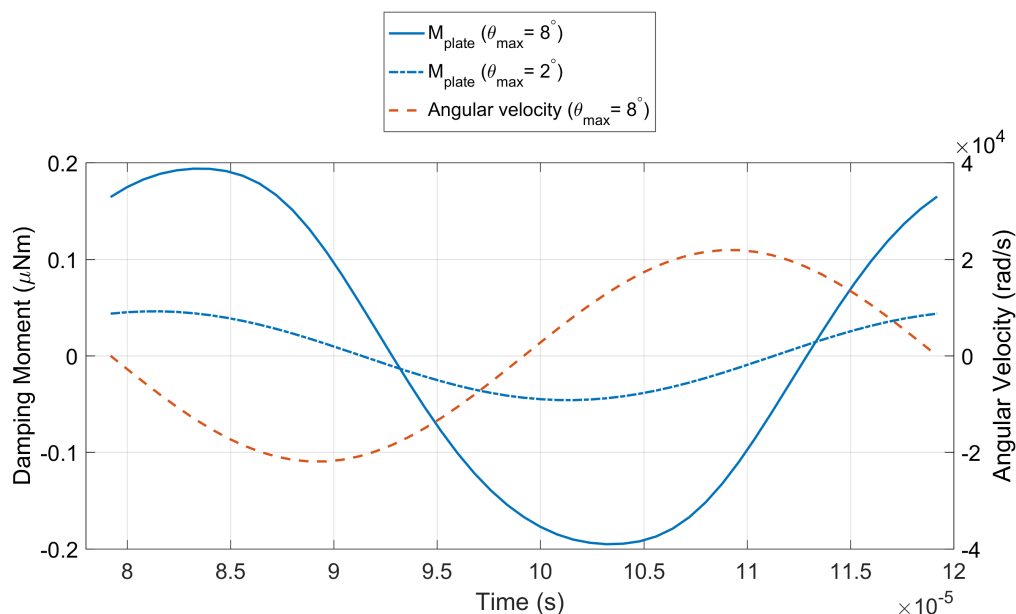
Figure 8-5: Variation of the damping moment acting on the mirror plate of *D1* relative to the applied angular velocity; obtained from transient N-S simulations (f_s = 25 kHz)

The total aerodynamic moment acting on a comb finger is displayed in **Figure 8-6**. A sharp peak in the total moment is observed when the moving comb finger is about to re-engage with the static comb finger. In contrast with **Figure 8-5**, the applied moment is approximately in-phase with the angular velocity indicating that the drag-component is predominant. At maximum velocity, a lower spike in damping moment is achieved when the finger length, f_l is reduced by 50 μm. CFD simulations demonstrate that the velocity at the tip of the moving comb finger determines the cyclic flow development. An increase in comb finger length or position from the rotational axis may result in the shift from predominantly laminar, attached flow to rotational, separated flow at the comb

145

finger edges. This in turn leads to a non-linear increase in the AVC structure energy loss due to air damping.
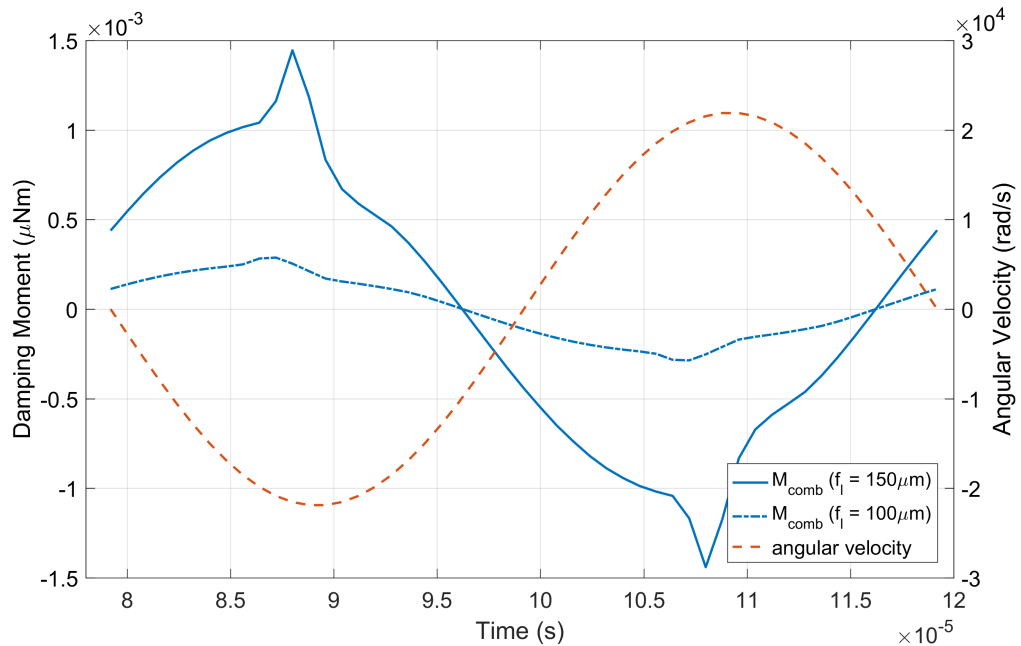
Figure 8-6: Variation of the damping moment acting on an AVC finger of *D1* located 450 μm from the rotational axis (f_s = 25 kHz; θ_{max} = 8°); obtained from transient N-S simulations (f_s = 25 kHz)

Given the limited area available to insert straight AVC structures, additional comb fingers are introduced at the gimbal-frame boundary as shown in **Figure 8-4**. This entails consideration to the variation of each comb finger position in the computation of the electrostatic energy and the energy loss over one oscillation. For this reason, the following look-up tables were generated from numerical simulations to evaluate the scanning efficiency of the direct-drive micro-scanner designs:

1) from transient fluid simulations (based on the *CFD_1* model of **Figure 7-6**), the variation of the mirror plate energy loss with scan angle amplitude is determined: $E_{plate}(\theta_{max})$ look-up table;

2) from transient fluid simulations (based on the *CFD_2* model of **Figure 7-7**, the variation of the energy loss with comb finger position and scan angle amplitude is determined: $E_{comb}(\theta_{max}, f_r)$ 2-D look-up table;

3) from electrostatic simulations, the comb finger capacitance variation with scan angle amplitude and comb finger position is determined: $C(\theta_{max}, f_r)$ 2-D look-up table.

The above look-up tables were compiled for the ranges of $0° < \theta_{max} < 20°$ in steps of $0.5°$ and $250 < f_r \, (\mu m) < 650$ in steps of 50 μm. The decay of the overall Q with scan angle amplitude, for design $D1$, is displayed in **Figure 8-7**. The out-of-plane oscillations of the mirror-plate and gimbal frame result in a higher energy loss contribution compared to the AVC structures. A comparison between **Figure 8-7(a)** and **(b)** shows that an increase in finger length has a negligible impact on the overall Q. In general, if the mirror plate damping is the dominant energy loss mechanism, the comb structure can be modified to extract more electrostatic energy without significant impact on Q.

(a) $f_l = 100$ μm   (b) $f_l = 150$ μm
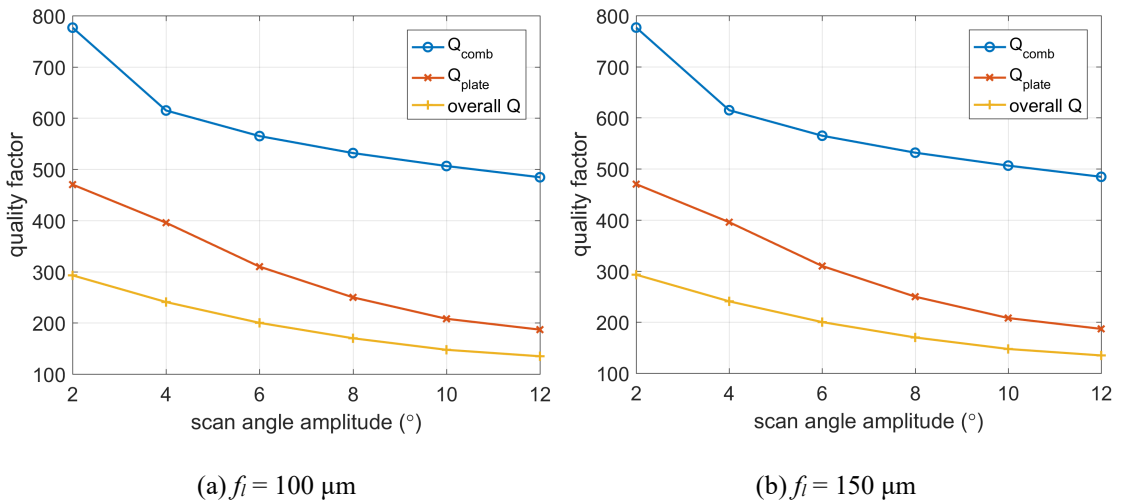
Figure 8-7: Q variation with scan angle amplitude, θ_{max} of $D1$ with different comb finger lengths; obtained from transient N-S simulations

The electrostatic energy input from the AVC structure is directly proportional to f_l as shown in **Figure 8-8**. The $dC/d\theta$ of a comb finger ($f_r = 250$ μm) decreases quadratically beyond $\theta = 3.5°$. In the case of the direct-drive micro-scanners, larger f_r combined with a low Si thickness, limit the available electrostatic moment during one oscillation.
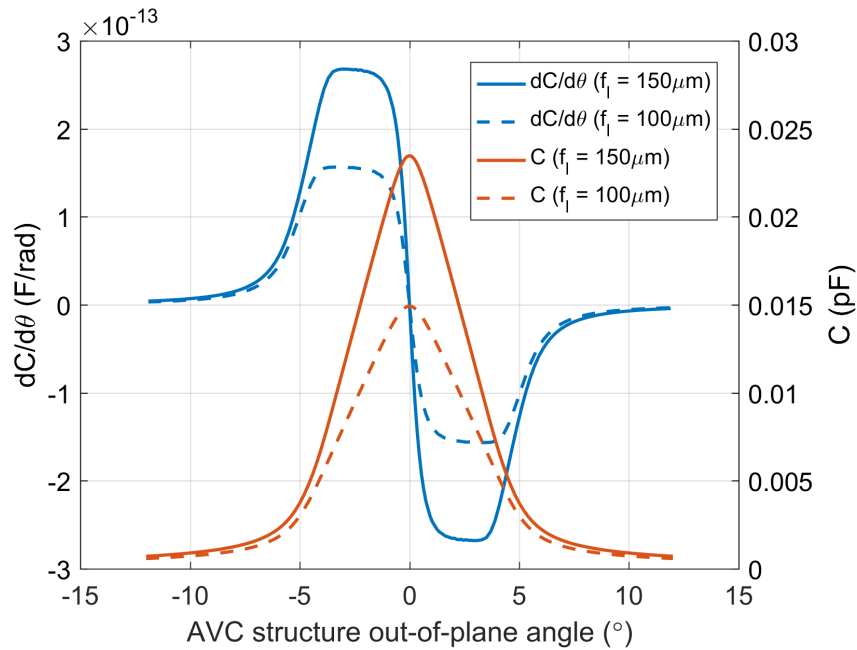
Figure 8-8: Capacitance and *dC/dθ* variation with micro-mirror scan angle of a comb finger with a length of 100 μm and 150 μm (design *D1*, f_r = 250 μm); obtained from electrostatic FE simulations

When a micro-scanner AVC structure is located on a straight path, (e.g. STM design of **Figure 2-14**), $θ_{max}$ is directly proportional to the number of comb fingers, N. This is confirmed in **Figure 8-9** whereby $θ_{max}$ can be increased by extending the straight section of the AVC structure displayed in **Figure 8-2**. However, with AVC structures located on a curved path, E_{el} and E_{comb} are dependent on a non-constant f_r. The applied electrostatic and damping moments of an AVC structure have a different dependency on f_r, leading to a more complex $θ_{max}$ - f_r relationship. Electrostatic-fluidic simulations suggest that an optimum number of comb-fingers exists for the curved section of the AVC structure and a further increase in *N* does not improve the scanning efficiency of the micro-mirror. Therefore, the scan angle amplitude of D1-C-150 is maximized by directly connecting not more than eight comb fingers on either sider of the gimbal frame. For the AVC structure geometry considered in D1-C-150, no improvement in performance is achieved if comb fingers are placed at a radial distance of more than 475 μm from the rotational axis as shown in **Figure 8-10**.

(a) straight AVC section

(b) curved AVC section
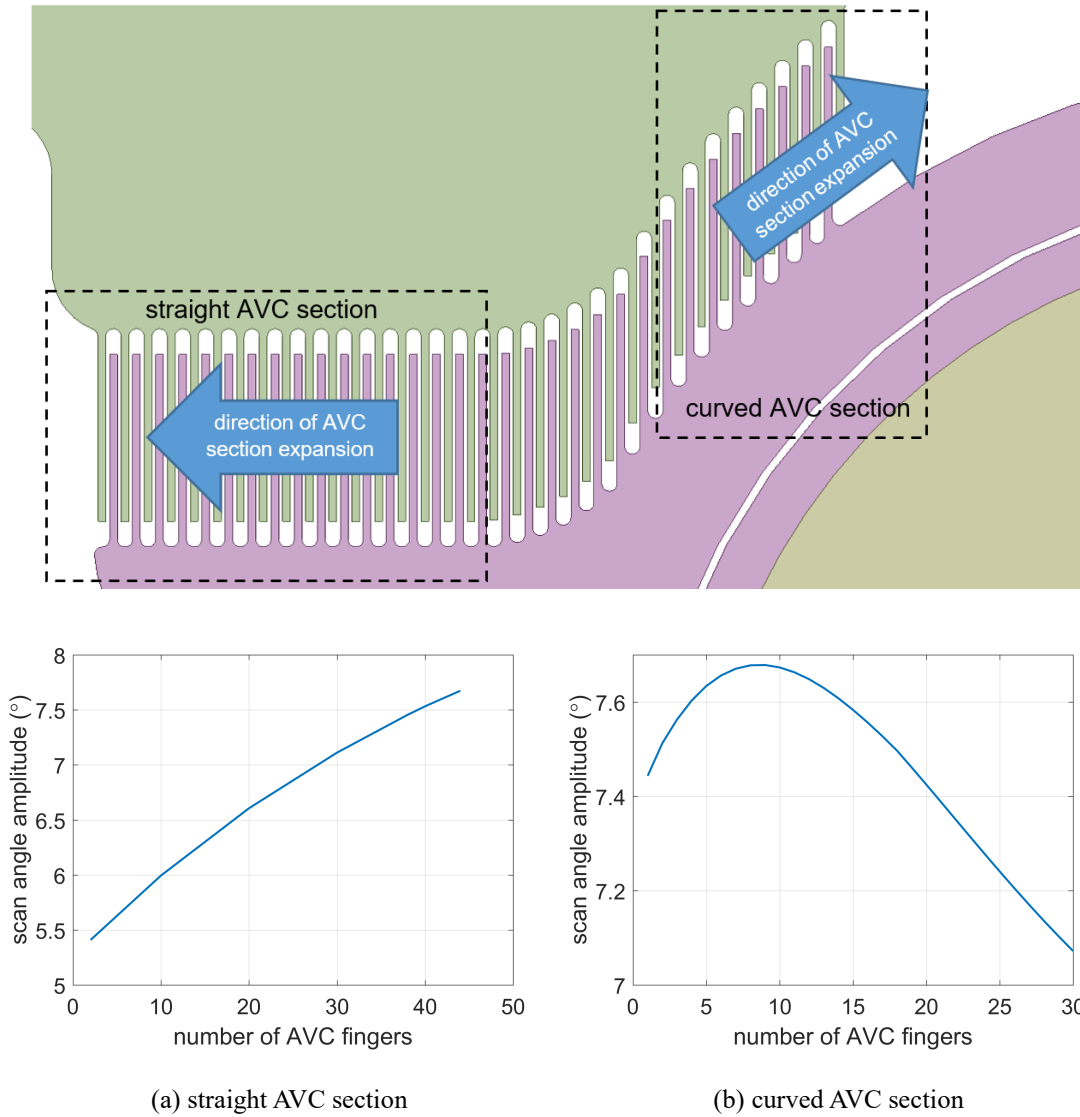
Figure 8-9: Scan angle amplitude, θ_{max} variation with size of the AVC structure when a 200V sinusoidal drive signal is applied to design *D1*; obtained from transient CFD simulations and electrostatic FE simulations
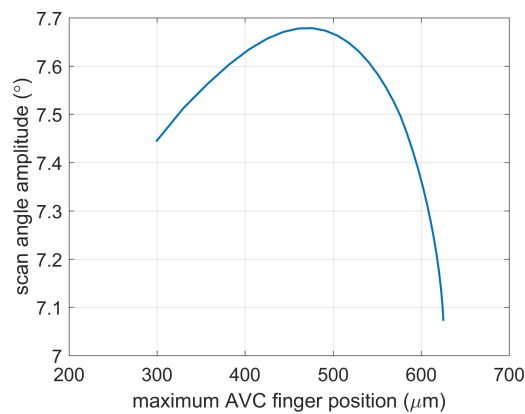
Figure 8-10: Scan angle amplitude, θ_{max} variation with size of the AVC structure (in terms of the maximum rotating comb finger position (f_r) from the rotational axis) when a 200V sinusoidal drive signal is applied to design *D1*; obtained from transient CFD simulations and electrostatic FE simulations

Figure 8-11 and **Figure 8-12** summarize the scanning performance of the final direct-drive micro-scanner designs: D1-C-150, D1-C-100 and D2-C-150 as predicted from FE and CFD simulations. The AVC structures of all scanner designs are optimized based on the electrostatic-fluidic simulations in order to achieve the maximum scan angle amplitude. A lower scanning performance is predicted from the variant of design *D1* with shorter comb fingers (100 µm). Given that the highest probability that fabrication defects occur as a result of comb finger breakage, prototype D1-C-100 is considered to determine whether a reduction in comb finger length is required to improve yield.
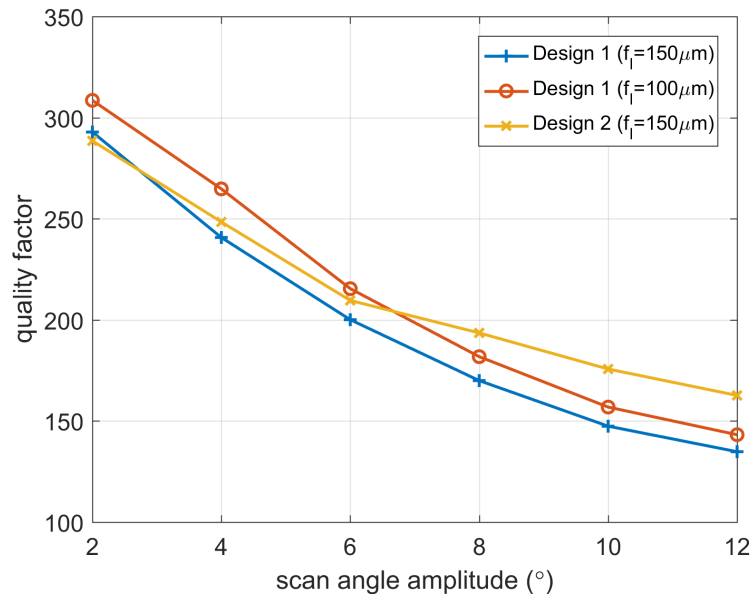
Figure 8-11: The *Q* variation with scan angle amplitude, θ_{max}, of the direct-drive micro-scanners *D1* and *D2* obtained from transient N-S simulations ($f_s = 25$ kHz)
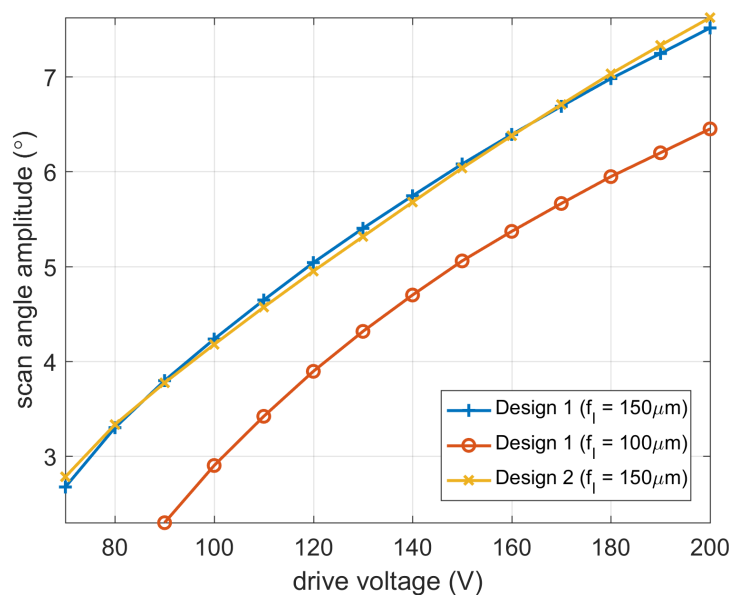
Figure 8-12: θ_{max} variation with drive voltage amplitude for the direct-drive micro-scanner designs *D1* and *D2* obtained from transient N-S and electrostatic FE simulations ($f_s = 25$ kHz)

8.4   Indirect-Drive Design (D3)

As part of the research questions outlined in Chapter 5, it is necessary to investigate the micro-scanner damping and dynamic deformation characteristics at high oscillating amplitudes. Due to the reduced Si layer thickness in the standard SOIMUMPs process (compared to the STM process), θ_{max} is limited to 5-7° with the direct-drive designs of Section 8.3. Consequently, the concept of mechanical amplification, discussed in Section 2.3.1, is applied in design $D3$ through the introduction of an outer frame as shown in **Figure 8-13**. The optimized $D1$ design is modified such that the gimbal structure is connected to an outer-frame. The outer frame is, in turn, connected to the substrate by means of a second set of torsional beams (B). The AVC structures are connected to the outer frame such that a small out-of-plane rotation of the movable comb fingers results in an amplified micro-mirror scan angle.
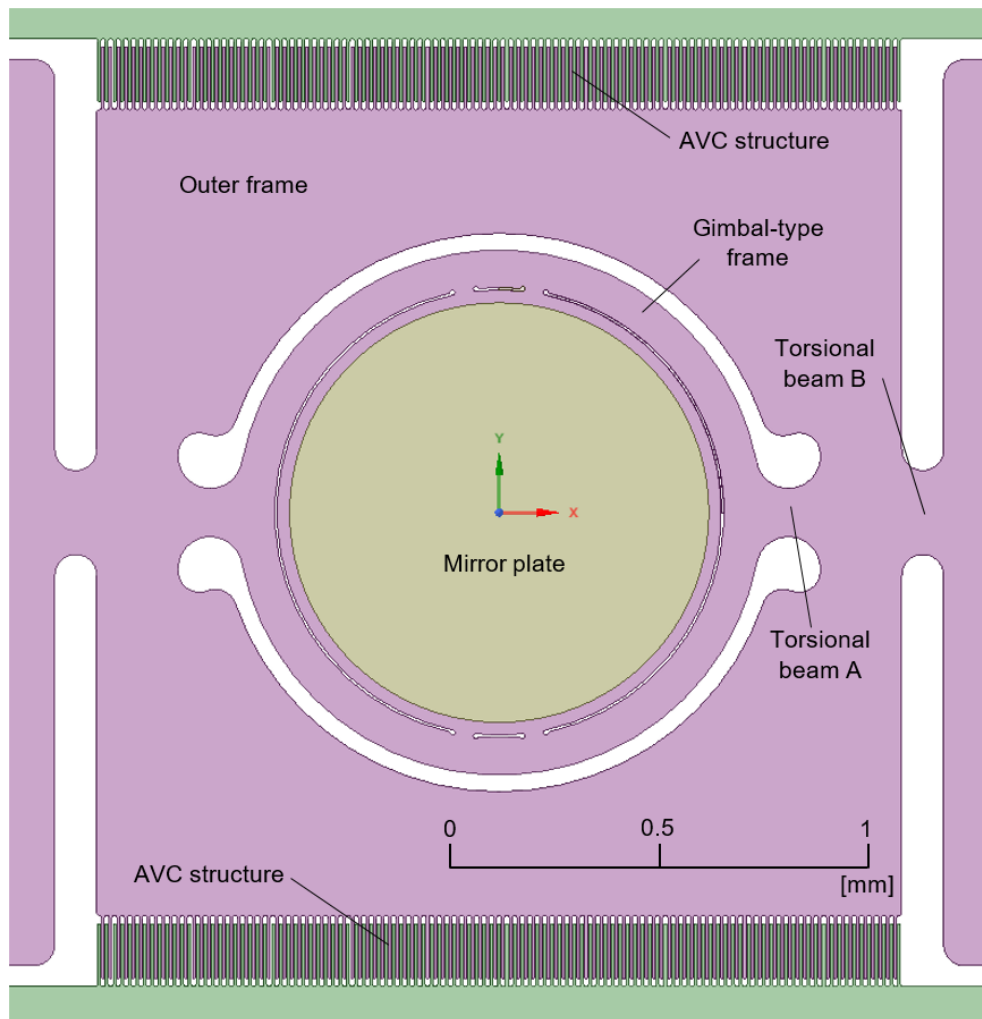
Figure 8-13 Final layout of micro-scanner design $D3$ based on the indirect-drive concept. The dimensions of the torsional beam A and the gimbal-type frame are identical to those of design $D1$

8.4.1   **Opto-Mechanical Optimization**

A modified version of the FE simulation set-up presented in Section 8.3.1 is implemented in the design process of the indirect-drive micro-scanner. The first four modal shapes of design *D3* are plotted in **Figure 8-14**. Mechanical amplification is exploited when the micro-scanner is operated at the out-of-phase torsional bending mode (mode 4). Optimization of *D3* is performed by introducing an additional partial objective to the design objectives listed in **Table 7-1**: maximizing the amplification factor, *A*. From **Figure 8-14**, *A* is defined as the ratio of maximum angular modal displacement between the mirror plate and the outer frame. Mechanical amplification can be increased by minimizing the frequency of the in-phase torsion mode: either by enlarging the outer frame area or by reducing the stiffness of the torsional beam set B. A wider outer frame area additionally allows for longer AVC structures and hence greater scanning efficiency. However, an increase in the overall micro-scanner area is limited by the available chip design area. Moreover, undesirable vibration modes may result from weaker torsional beams or a wider outer frame. The modal frequencies and the corresponding effective inertia of the optimized D3 design are listed in **Table 8-9**. The modal frequencies of the uncoated micro-scanner are also provided. Compared to the *BLANKETMETAL*-coated micro-scanners, a lower scanning frequency is expected at the out-of-phase torsional mode as a result of the spring-softening effect from the in-plane residual stress in the metal coating (σ_{res}).

The maximum torsional beam stress in the direct-drive designs can be numerically predicted by applying an angular acceleration equal to $\omega_s^2.\theta_{max}$ in a static structural FE simulation. However, at the out-of-phase torsional mode displayed in **Figure 8-14**, the angular acceleration of the outer plate is $\omega_s^2.\theta(t)/A$. The non-constant inertial torque acting on the indirect-drive micro-scanner at the frequency of operation can be applied using a harmonic response simulation in ANSYS Mechanical. Although the resonating system is driven by a non-linear electrostatic moment, a sinusoidal mechanical loading function is applied to obtain the equivalent stress state at the target micro-scanner response. Equal and opposite vertical harmonic loads were prescribed to the edges of the outer frame. The amplification factor and phase difference between the mirror plate and the outer frame can be observed from the linear harmonic response plot of **Figure 8-15**. The maximum principle stress and maximum shear stress at the torsional beams of the optimized scanner are plotted in **Figure 8-16** and **Figure 8-16** respectively. The

low oscillation amplitude of the outer frame results in an equally low stress state at the torsional beam set B. Moreover, the maximum stress is predicted to be lower than the critical Si stress (τ_{crit} = 1.4 GPa) at the target mirror scanning amplitude and frequency.

(a) in-phase torsional mode (12.7 kHz)　　　(b) in-phase bending mode (14.8 kHz)

(c) out-of-phase bending mode (18.2 kHz)　　　(d) out-of-phase torsional mode (25.3 kHz)

out-of-plane (vertical) displacement

Minimum　　　Maximum
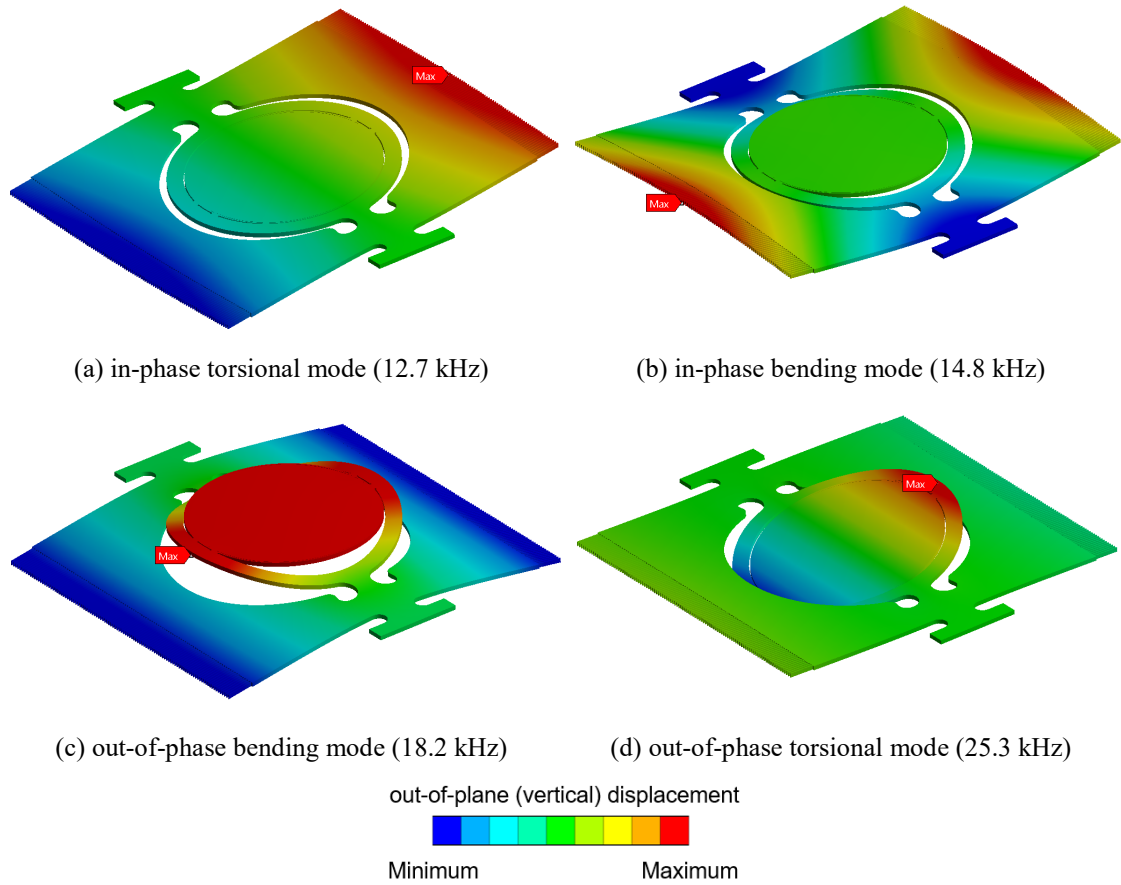
Figure 8-14: Results from modal analysis of the indirect-drive FE model

Table 8-9: Modal frequencies and effective inertia about the rotational axis for design *D3*

Mode	With *BLANKETMETAL* coating			Without *BLANKETMETAL* coating		
	Frequency (Hz)	Effective inertia (kgµm²)	Effective inertia/Total inertia ratio	Frequency (Hz)	Effective inertia (kgµm²)	Effective inertia/Total inertia ratio
1	12702	0.766×10^{-1}	0.989	12076	0.751×10^{-1}	0.990
2	14824	0.975×10^{-13}	0.127×10^{-11}	14871	0.491×10^{-9}	0.647×10^{-8}
3	18184	0.880×10^{-13}	0.115×10^{-11}	18694	0.414×10^{-11}	0.546×10^{-10}
4	25278	0.208×10^{-3}	0.272×10^{-2}	26583	0.774×10^{-4}	0.102×10^{-2}

153
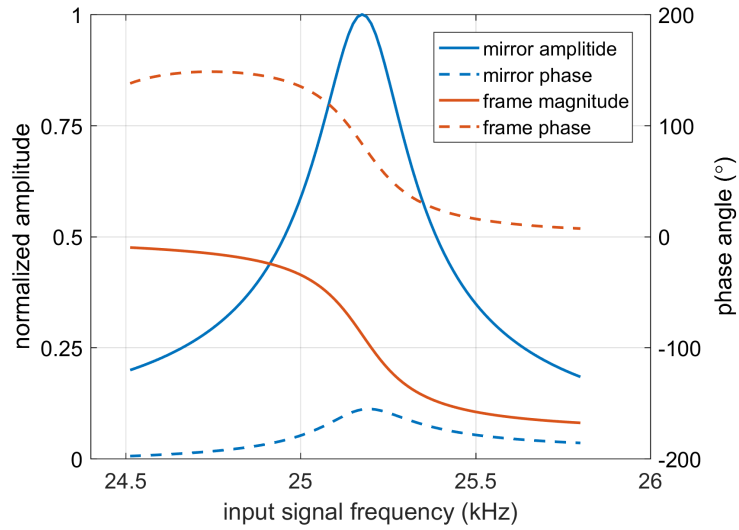
Figure 8-15: Linear harmonic response simulation of the indirect-drive micro-scanner FE model
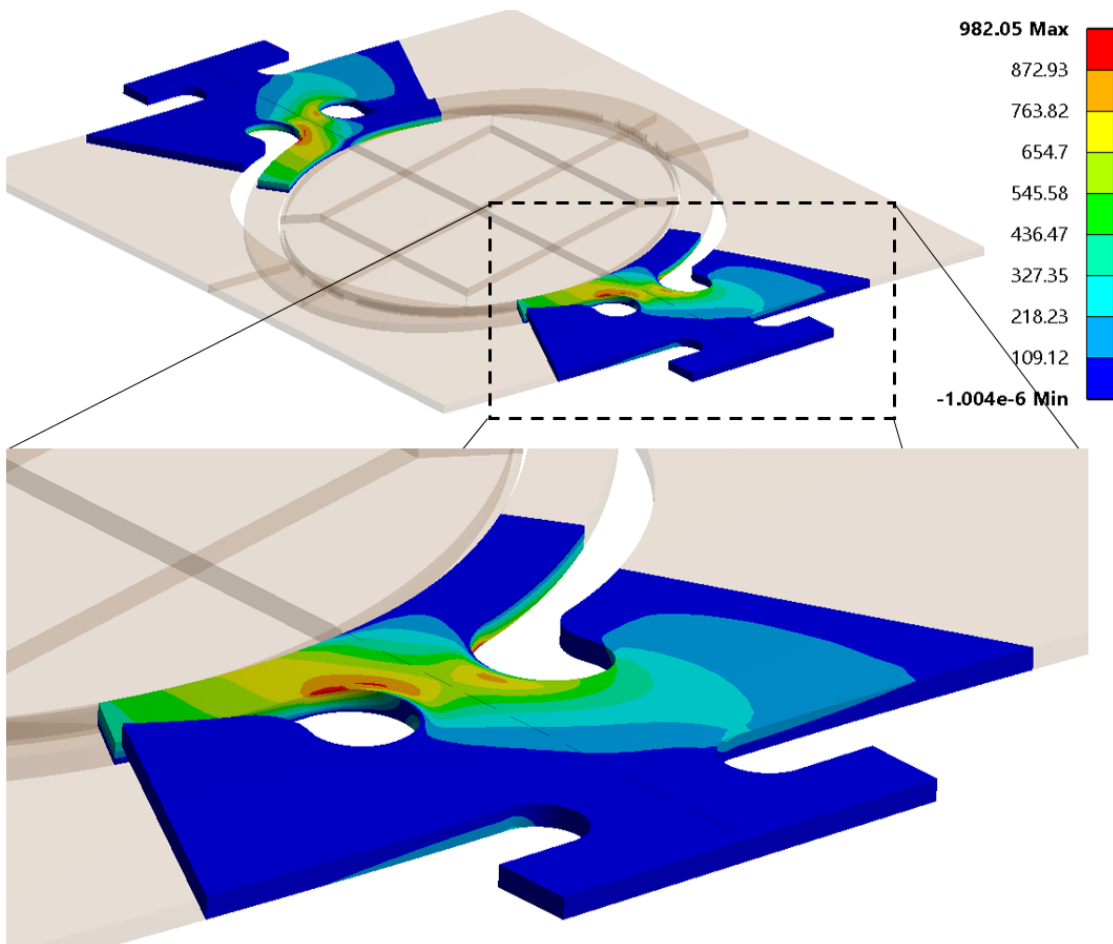
Figure 8-16: Maximum principal stress (in MPa) contour plot of indirect-drive micro-scanner *D3*; obtained from linear harmonic FE simulations to produce representative micro-mirror oscillations at the out-of-phase torsional resonant mode (25.3 kHz and θ_{max} of 12°)

154
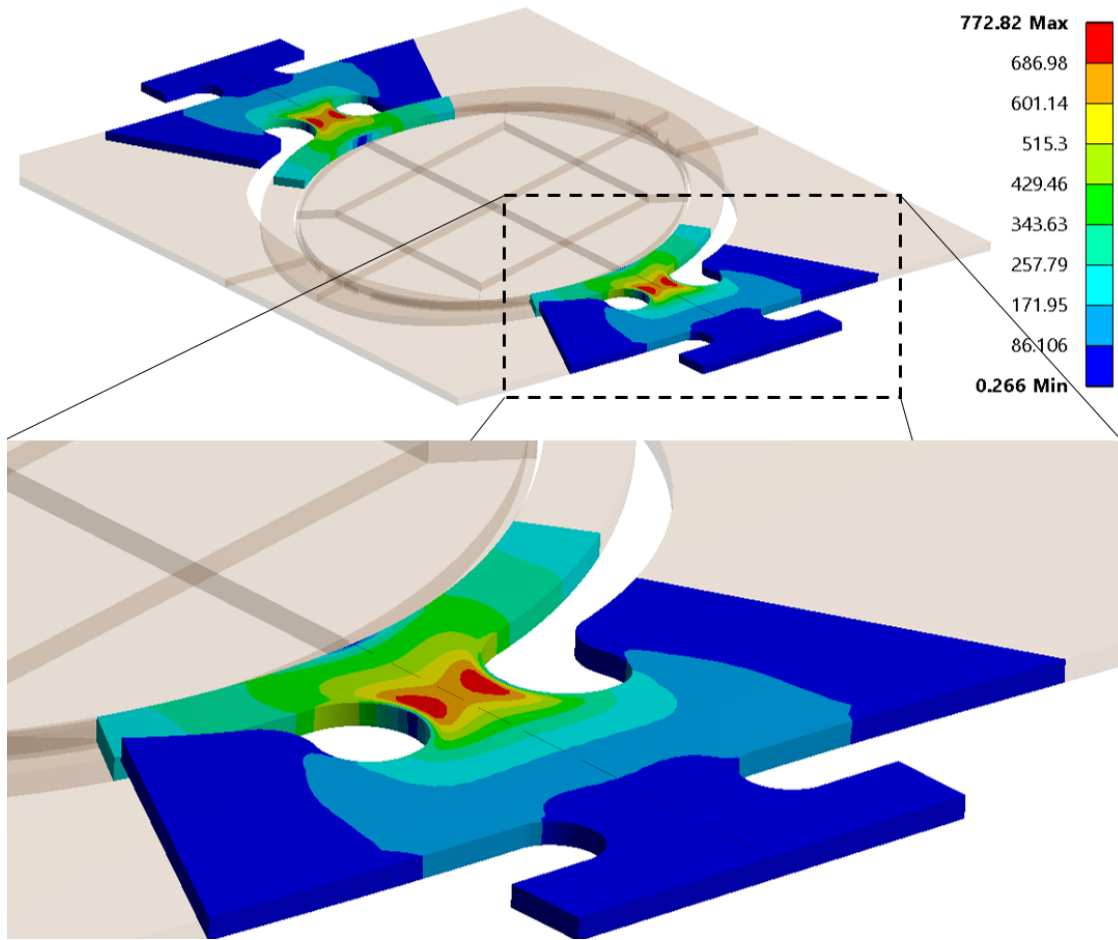
Figure 8-17: Maximum shear stress (in MPa) contour plot of the indirect-drive micro-scanner *D3*; obtained from linear harmonic FE simulation to produce representative micro-mirror oscillations at the out-of-phase torsional resonant mode (f_s = 25.3 kHz and θ_{max} of 12°)

8.4.2   Electrostatic-Fluidic Analysis

The CFD models defined in Section 8.4.2 were modified to investigate the mirror plate and comb structure damping characteristics of the indirect-drive micro-scanners. The relative motion between the mirror plate and outer frame eliminates the possibility of implementing the *sliding mesh* technique for the computation of the transient drag damping moment on the oscillating structure. Therefore, the more computationally-intensive *dynamic mesh* technique, depicted in **Figure 8-18**, is set-up in ANSYS Fluent. The *dynamic mesh* model allows the mesh to be adjusted in order to accommodate a prescribed movement of the fluid domain boundaries. Given the large out-of-plane displacement of the micro-scanner boundary, a combination of diffusion-based mesh smoothing and cell-zone re-meshing methods, in ANSYS Fluent, were necessary to impede against mesh degeneration during one oscillation. Unlike the *sliding mesh* method, the *dynamic mesh* method provides the possibility of including the cavity wall

155

boundary as shown in **Figure 8-18**. For simplicity, the air gap between the gimbal-frame and mirror plate was assumed to have a negligible effect on the overall damping and therefore was not included in the CFD model. A one-way coupled structural-fluid system was set-up to evaluate the transient air pressure and shear loading on the mirror-frame structure oscillating in the out-of-phase torsional resonant mode. At each time step, the motion of the micro-scanner boundary in the fluid domain is updated by the steady-state micro-scanner displacement data obtained from a transient structural analysis.

The static pressure distribution on the rotating boundary together with the air flow velocity streamlines are displayed in **Figure 8-19**. Vortex structures are generated at the mirror plate tips at high oscillation amplitudes. The presence of the outer frame forces a more rapid detachment of the tip vortex from the plate edge compared to the flow profile observed in **Figure 5-20**. This suggests that the gap between gimbal frame and the mirror plate can be optimized to drastically alter the flow development and hence the drag coefficient of the indirect-drive micro-scanner.

<table>
<tr><td>(a) CFD fluid domain at $\theta(t) = 0°$</td><td>(b) CFD fluid domain at $\theta(t) = \theta_{max}$</td></tr>
</table>

<table>
<tr><td>(c) CFD mesh at $\theta(t) = 0°$</td><td>(d) CFD mesh at $\theta(t) = \theta_{max}$</td></tr>
</table>
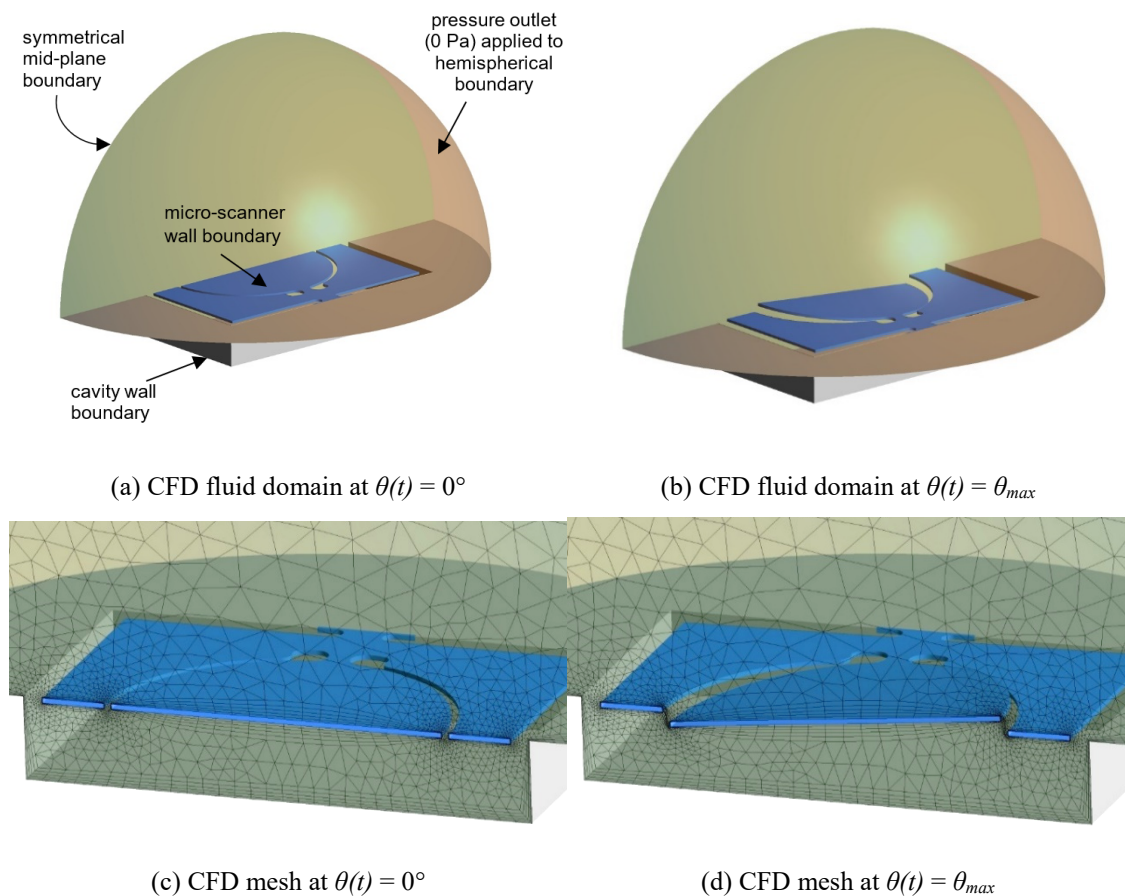
Figure 8-18: Computational fluid domain and dynamic mesh generation for transient N-S simulations performed to deduce the air damping losses acting on the mirror plate and outer frame structure of design *D3*
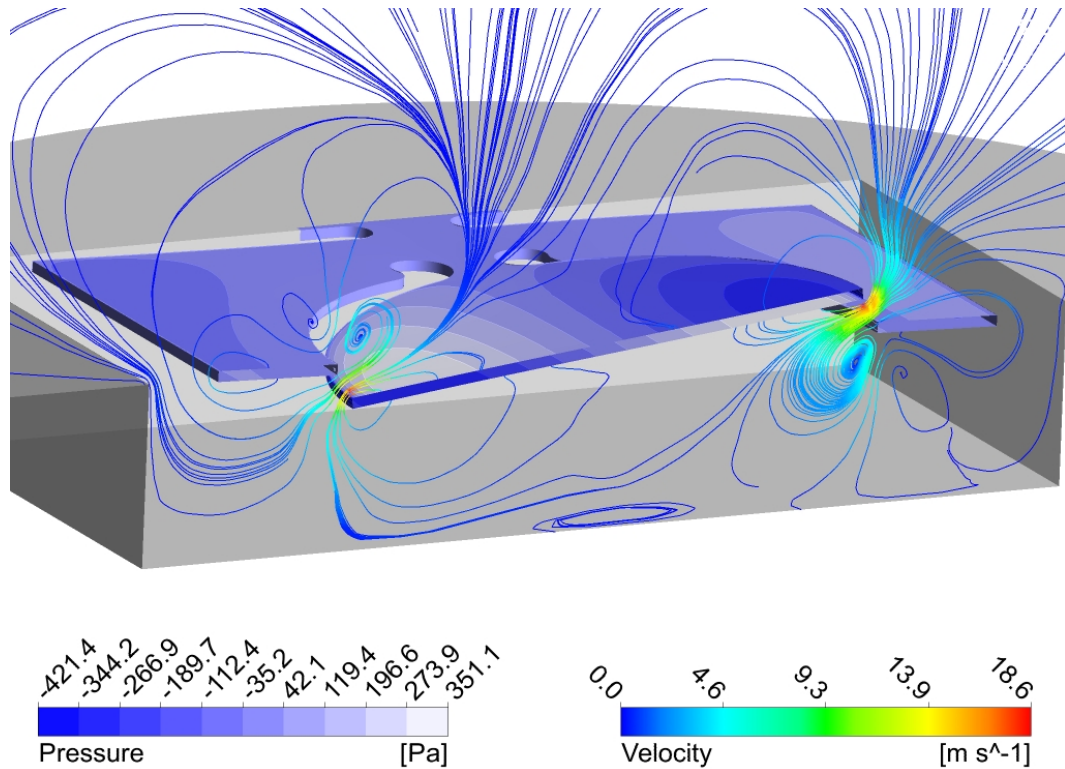
Figure 8-19: Static pressure distribution on the oscillating structure (design *D3*) and air velocity streamlines along the mid-plane at $\theta(t) = \theta_{max}$; obtained from one-way coupled fluid-structural simulations (f_s = 24.6 kHz; θ_{max} = 7°)

The placement of the AVC structures on the outer frame substantially increases the distance between the comb fingers and the rotational axis. This renders the CFD model of **Figure 5-2** computationally intensive for large AVC finger radial positions. A modified version of the *sliding mesh* model, displayed in **Figure 7-6** is proposed for the indirect-drive design. A section of the fluid domain shown in **Figure 8-20** is meshed whereby the moving fluid domain rotates about the *x*-axis and the fluid interface surfaces (shown in red) allow for flow continuation between the rotating and static fluid domains. The transient damping moment is extracted from the elemental pressure and shear stress acting on the rotating finger wall boundary shown in **Figure 8-21**. The wall shear stress distribution on the rotating finger together with the adjacent flow velocity profile is plotted in **Figure 8-22**.

157
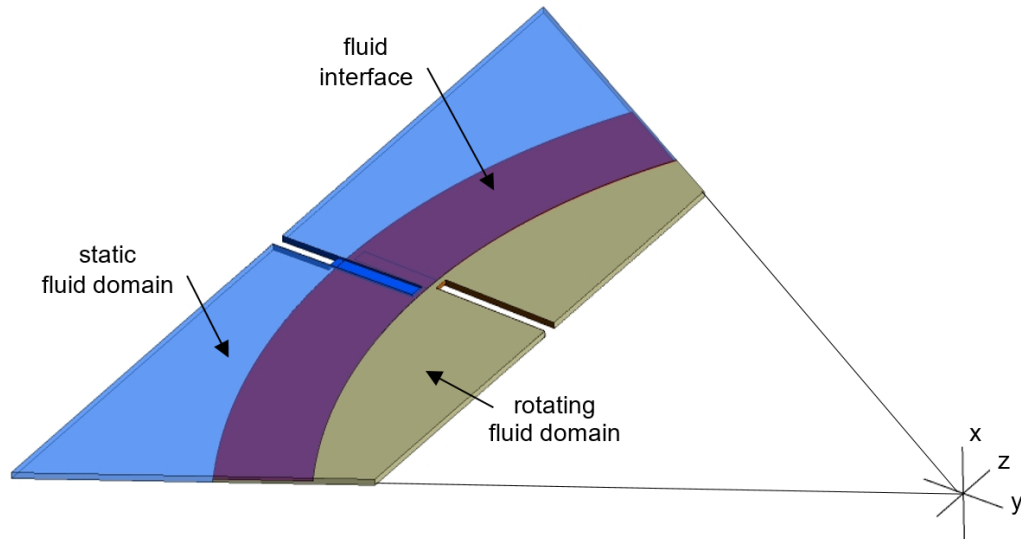
Figure 8-20: CFD model for the transient damping simulation of AVC structures in the indirect-drive micro-scanner design (*D3*)

The temporal variation of the damping moment components acting on the AVC structures (M_{comb}) and the mirror - outer frame structure (M_{plate}) are plotted in **Figure 8-23**. Although the damping moment on the outer frame is low compared to that acting on the mirror plate, a non-sinusoidal profile is observed. This is in contrast with the predicted M_{plate} of direct-drive micro-scanners (see **Figure 8-5**) and demonstrates the impact that the gap between the mirror plate and outer frame has on the flow development. The quality factor was derived using (5.15) whereby the energy stored over one cycle is calculated using the effective moment of inertia at the out-of-phase torsion mode deduced from modal analysis (see **Table 8-9**). **Figure 8-24** demonstrates that the AVC structure damping has negligible impact on the overall system energy loss. This signifies that the AVC structures, and hence the outer plane, can be extended to increase the electrostatic input energy without a significant reduction in the overall energy loss. The electrostatic moment shown in **Figure 8-26** was calculated using the $C(\theta)$ function of the AVC structure, plotted in **Figure 8-25**. The $C(\theta)$ is obtained using electrostatic FE simulations based on the same method discussed in Section 8.4.2. The predicted θ_{max} obtained at two drive voltage amplitudes is shown in **Figure 8-27**.

(a) $\theta(t) = \theta_{max}$

(b) $\theta(t) = 0°$
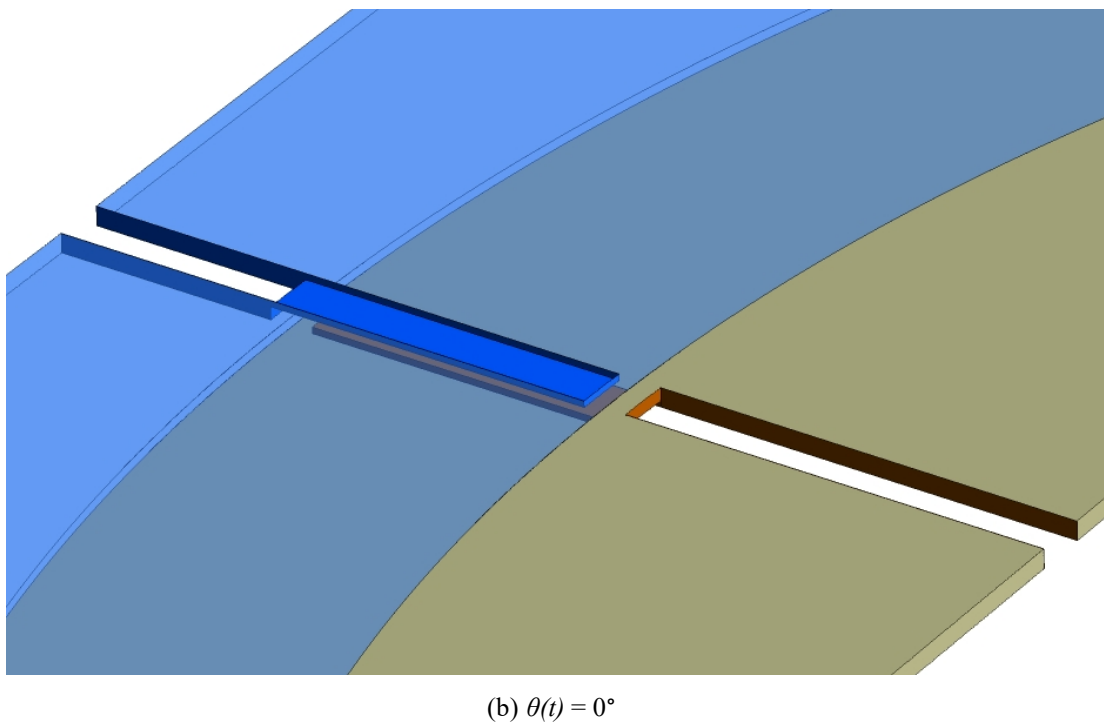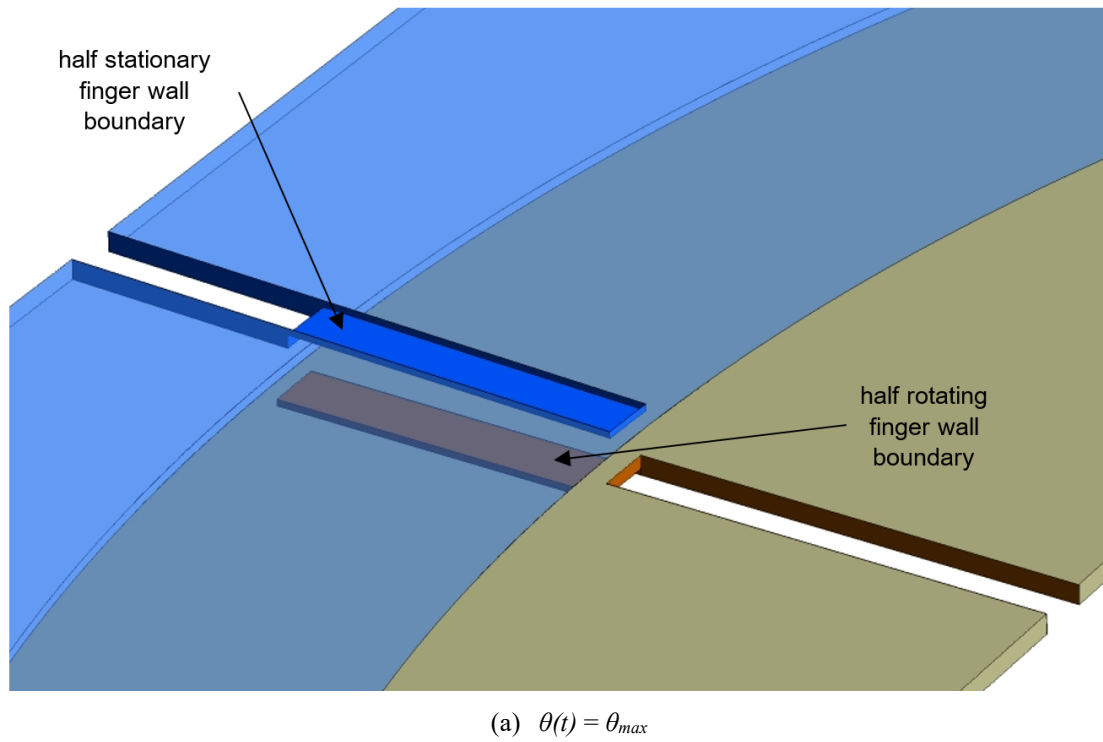
Figure 8-21: Relative motion between the stationary and rotating finger wall boundaries as part of the AVC structure CFD model for transient N-S simulations based on the *sliding mesh* method

159
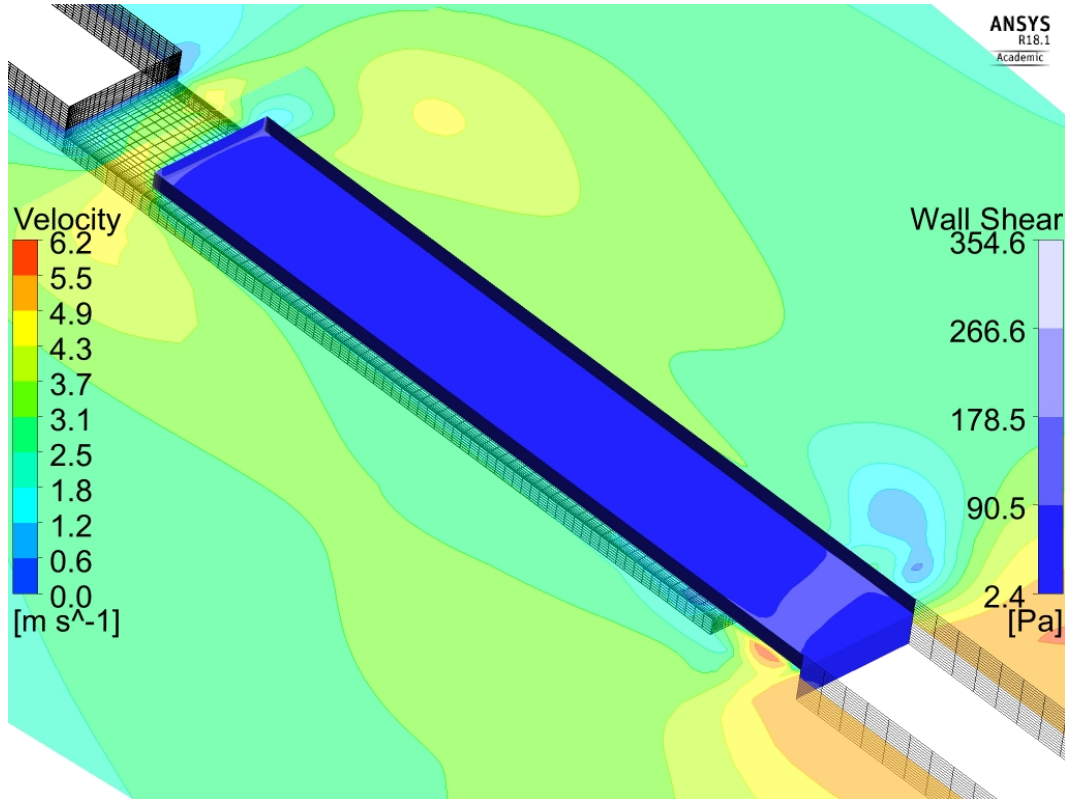
Figure 8-22: Instantaneous shear stress distribution on the rotating comb finger cell and air velocity contour plot at the mid-plane of the comb finger gap at $\theta(t) = \theta_{max}$; obtained from N-S simulations ($f_s = 24.6$ kHz; $\theta_{max} = 7°$)
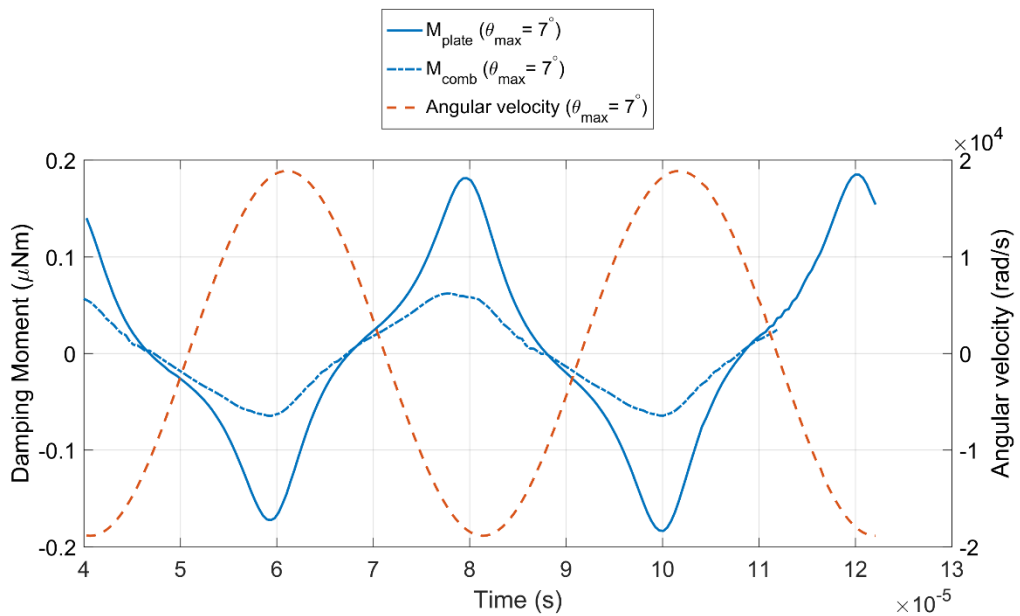
Figure 8-23: Transient damping moment response relative to the mirror plate angular velocity, $\dot{\theta}$ for the indirect-drive micro-scanner *D3*: mirror plate - outer frame structure (M_{plate}) and AVC structure damping (M_{comb})
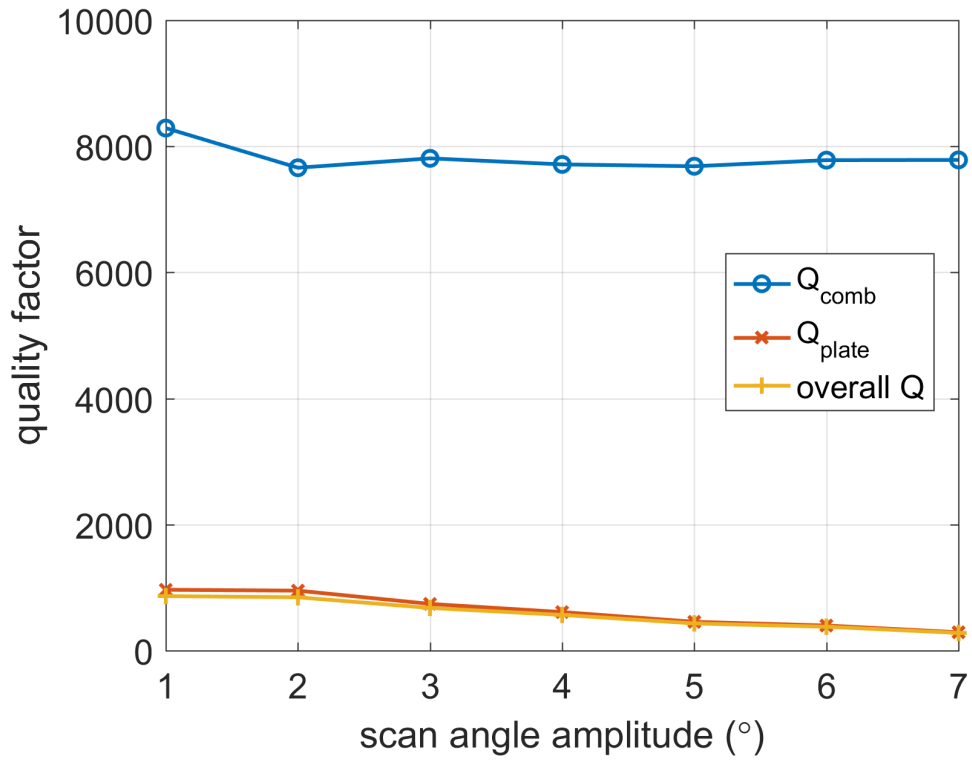
Figure 8-24: Q variation with θ_{max} for the indirect-drive micro-scanner $D3$ deduced from transient N-S simulation results
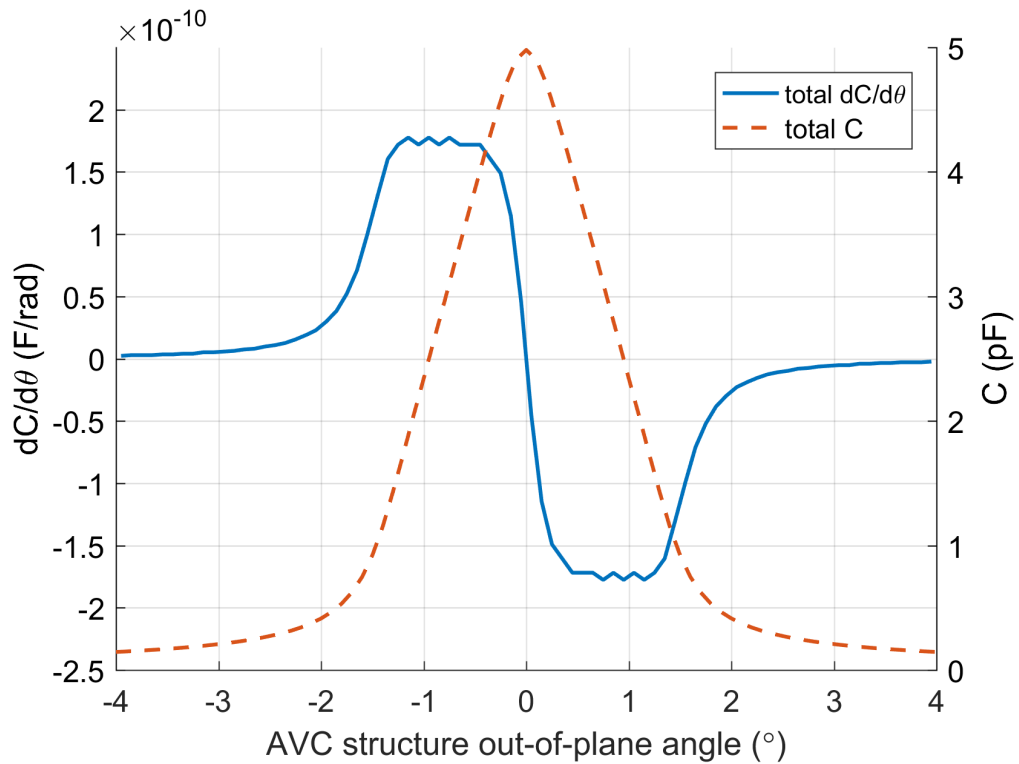
Figure 8-25: Variation of total AVC structure capacitance and $dC/d\theta$ in the indirect-drive micro-scanner $D3$; obtained from electrostatic FE simulations

161
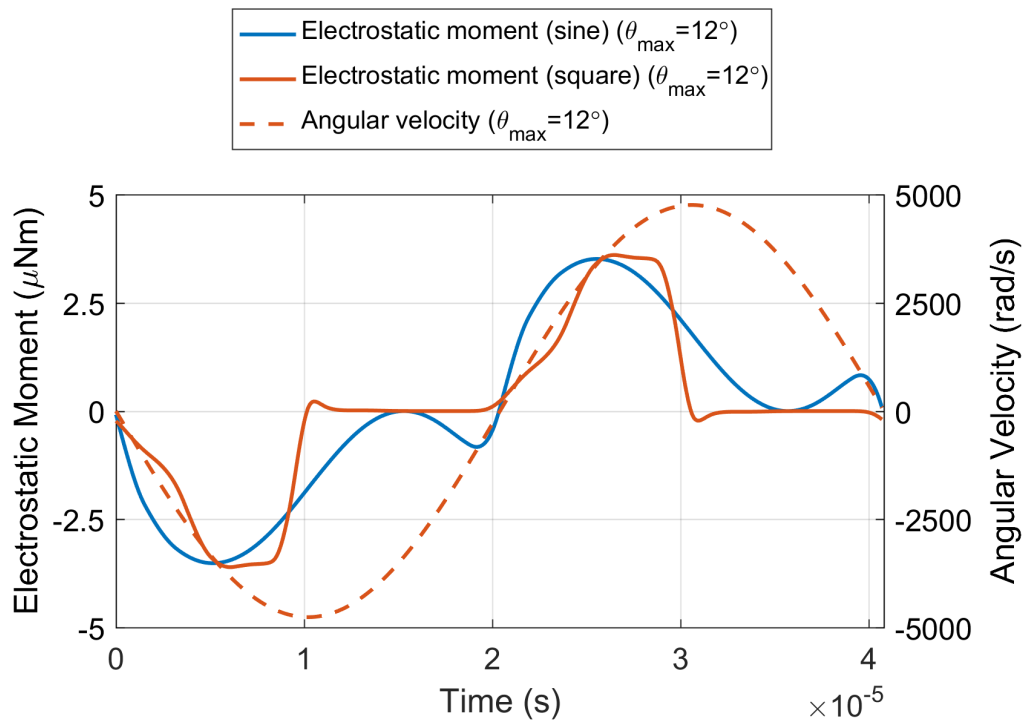
Figure 8-26: Comparison of the electrostatic moment profiles generated between a sine and a square wave drive voltage signal applied to the indirect-drive micro-scanner, *D3*
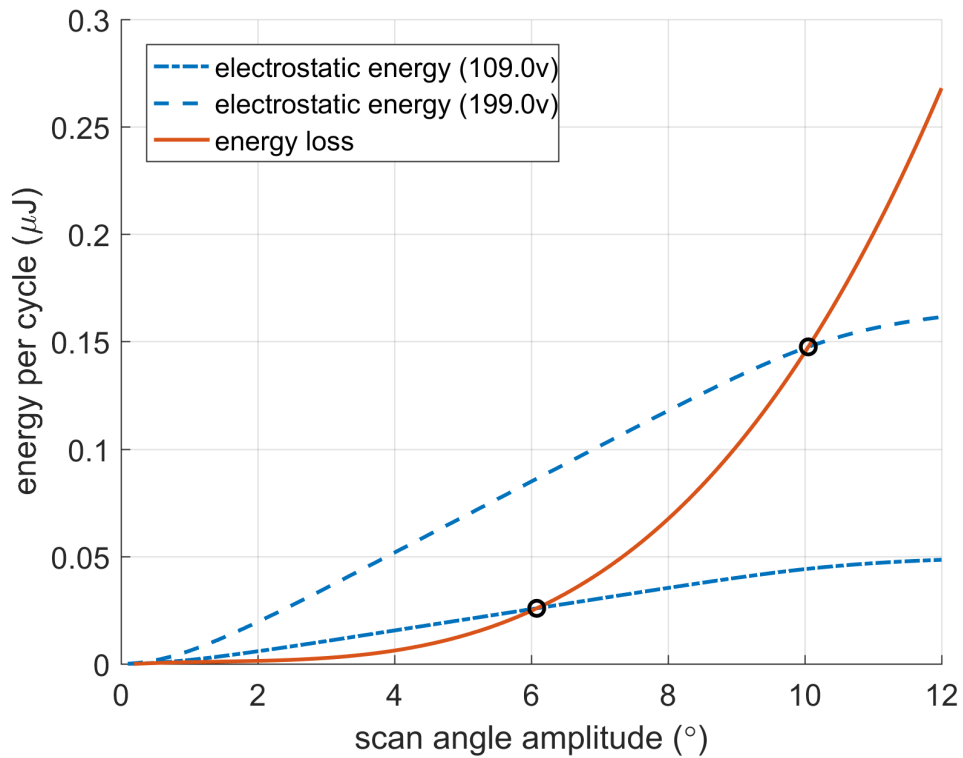
Figure 8-27: Energy input and output per cycle of the resonating electromechanical system (*D3*) highlighting the stable equilibrium points obtained at two sinusoidal drive voltage amplitudes; obtained from electrostatic FE and N-S simulations

162

8.5   Prototype Fabrication Issues

The seven design variations listed in **Table 8-4** were fabricated in a single SOIMUMPs MPW run in which a total of 12 identical dies were produced. Two critical flaws were observed from this initial run. The etch profile in the *Silicon* layer, following the TRENCH process step, results in a micro-scanner cavity with a non-negligible sidewall angle. In fact, the process design rules suggest that a TRENCH to SOI edge-to-edge bias of < 50 μm needs to be accounted for. However, an overcompensation for the cavity sidewall angle in *D1* and *D2* resulted in a mismatch between the cavity edge (*A*) and the micro-scanner end (*B*) as depicted in **Figure 8-28**. Consequently, a fraction of the torsional beams remained unreleased. A reduction of 20-30 μm in the effective torsional beam length, in turn results in an increase in the torsional resonant frequency. This issue was only observed in the direct-drive designs suggesting that the Silicon sidewall angle decreases significantly for small cavity areas. Complete release of the torsional beam was achieved in the second fabrication run by redesigning the TRENCH mask layout.

Additionally it was observed that at least one broken comb-finger was encountered in 80% of the micro-scanner prototypes despite adhering to the design rule limits. A visual check of the prototypes indicate that yield does not improve when the comb finger length is reduced from 150 μm to 100 μm. The majority of defects consist of missing comb-finger tips, while in other instances partial rupture resulted in bent fingers as shown in **Figure 8-29**. The foundry indicated that vibration at some point during the process may be a plausible explanation. For the second run, the die layout was placed at different locations and orientations on the SOI wafer and yield increased from 20% to 50%. Fewer breakages were observed in dies rotated 90° from the original layout however there is no significant evidence as to why the comb-structure yield substantially improves between the first and second run.
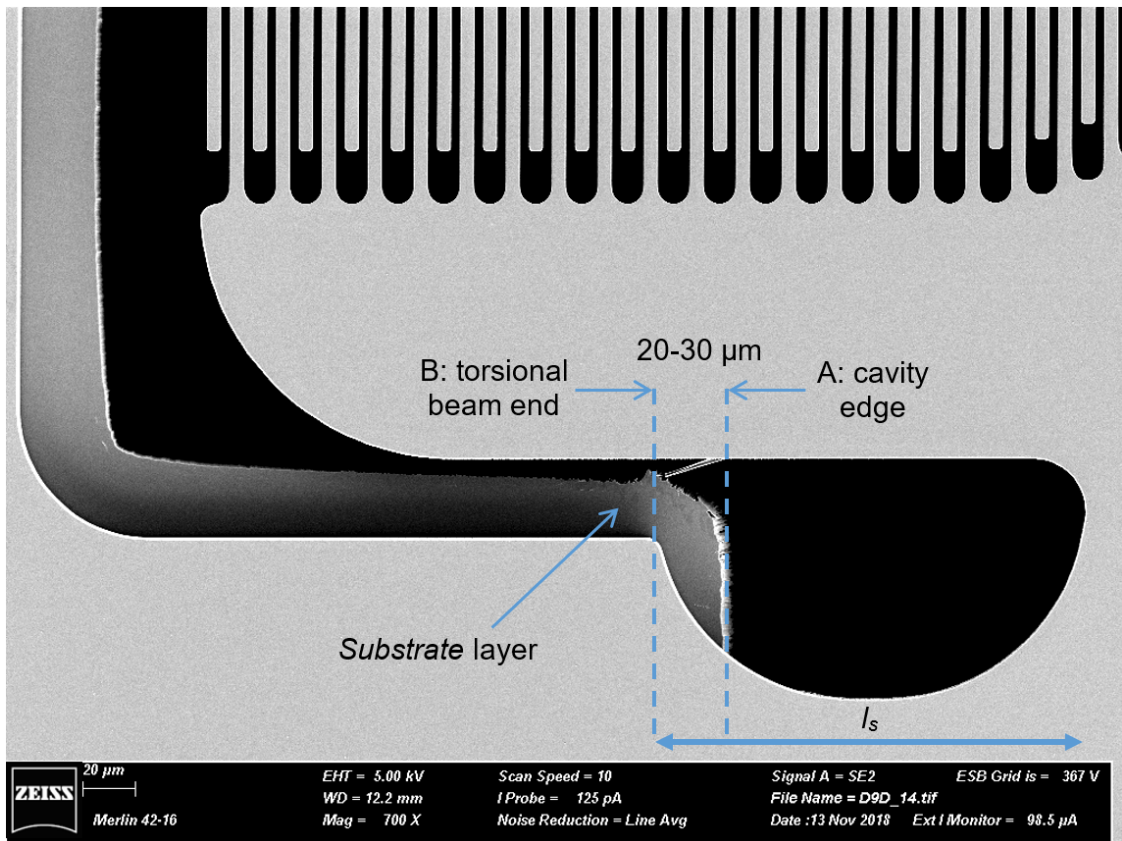
Figure 8-28: SEM image of design *D1* showing the offset between the cavity edge
and the torsional beam end
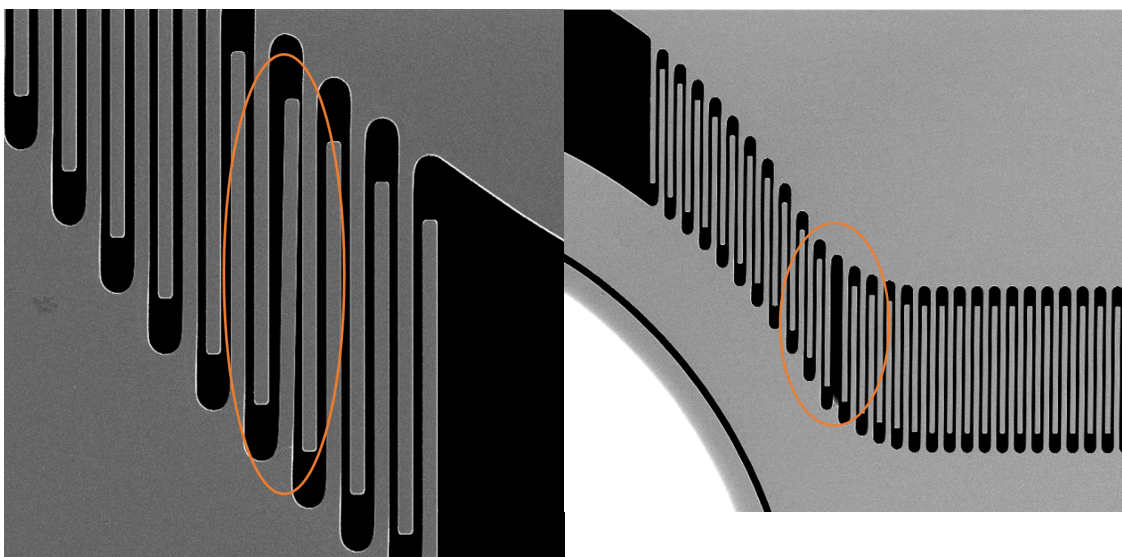
| (a) bent comb finger | (b) missing comb finger |

Figure 8-29: Observed defects in the AVC structures from the initial fabrication run

164

8.6   **Prototype Measurement Results**

Images of the prototypes fabricated in the second SOIMUMPs MPW run are presented in **Figure 8-30** and **Figure 8-31**.
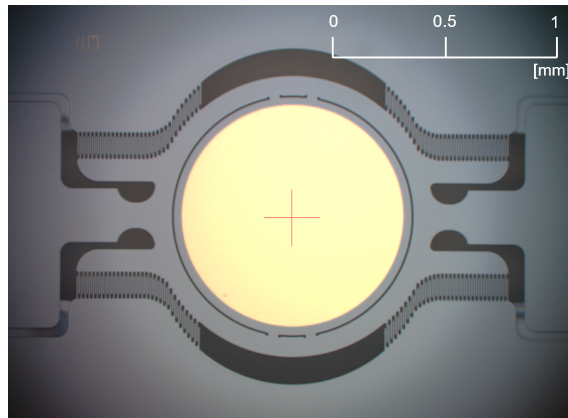
(a) D1-C-100
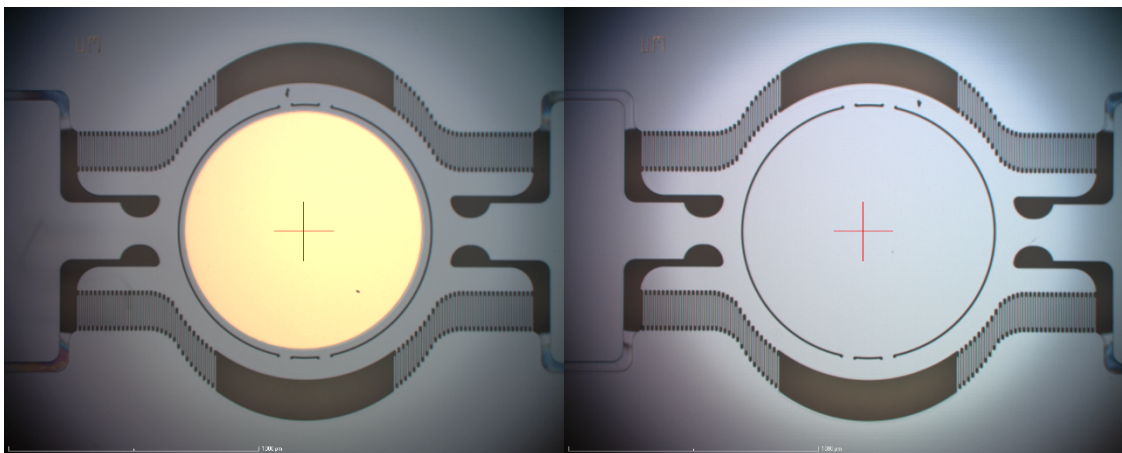
(b) D1-C-150

(c) D1-NC-150
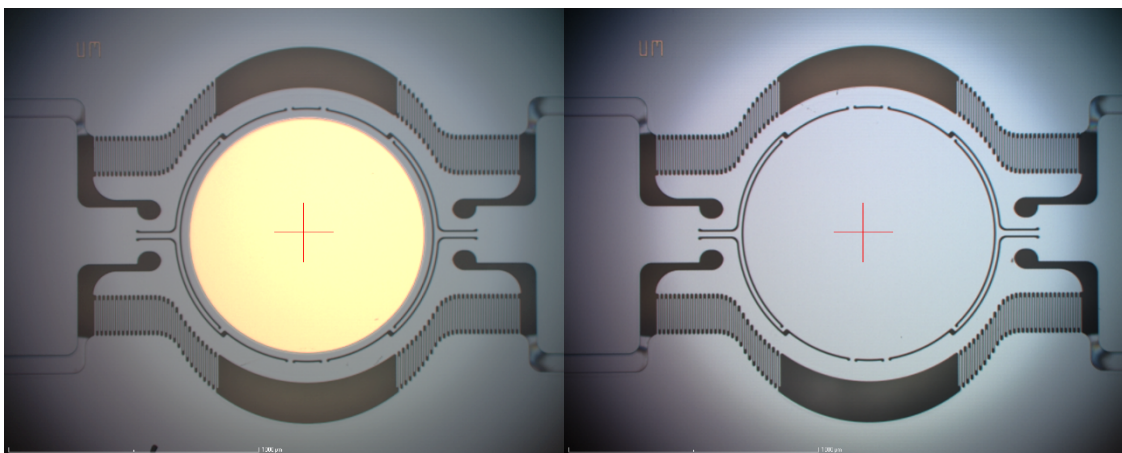
(d) D2-C-150

(e) D2-NC-150

Figure 8-30: Microscope images of the fabricated direct-drive micro-scanner designs

165
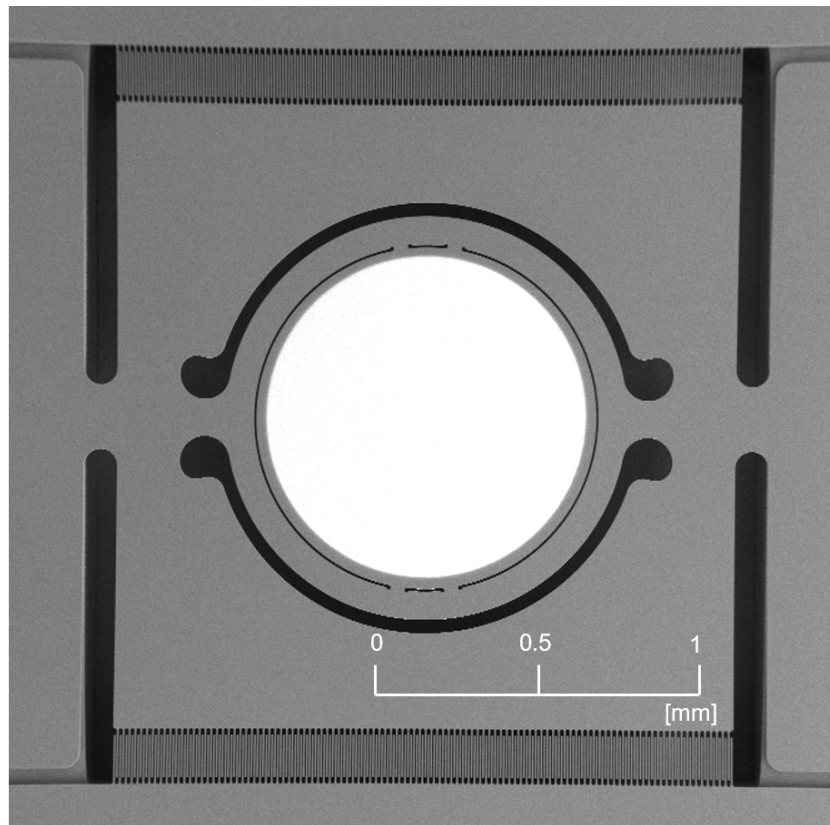
(a) D3-C-150
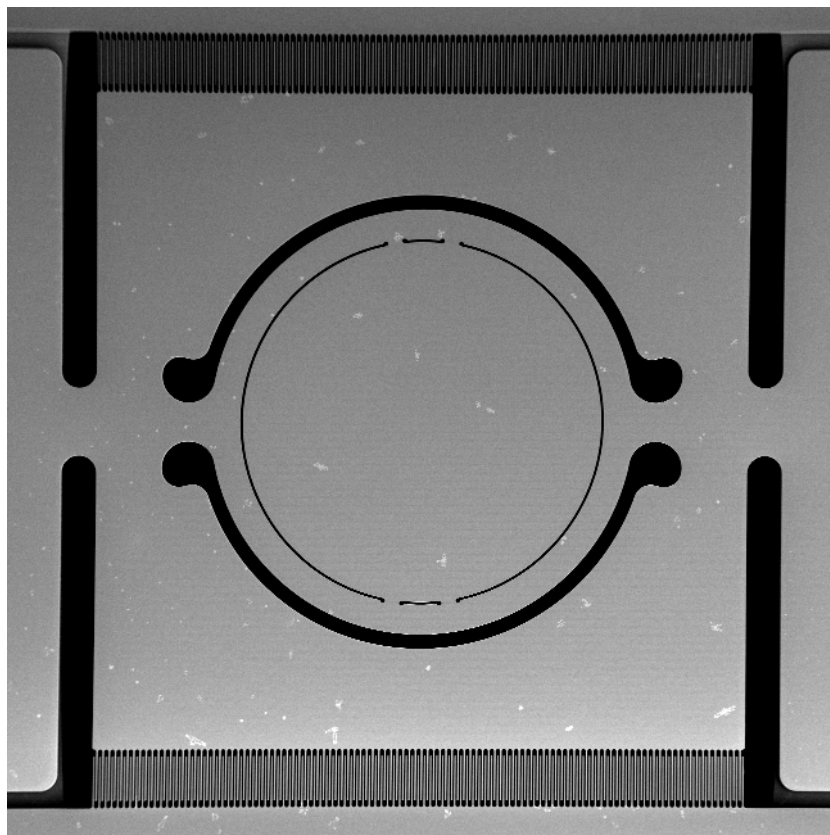
(b) D3-NC-100

Figure 8-31: SEM images of the fabricated indirect-drive micro-scanners

8.6.1   **Micro-Mirror Deformation**

In this section, the effectiveness of the gimbal-frame design in reducing micro-mirror dynamic deformation is evaluated. Initially, measurements from an optical profiler are presented in order to determine the out-of-plane deformation of the micro-mirror in the as-released condition, which, is being referred to as static deformation. The residual stress values for the SOIMUMPs process are also derived from the static curvature of the coated and uncoated micro-mirrors. Laser Doppler Vibrometry (LDV) measurements were subsequently performed on three scanning micro-mirrors: D1-NC-150, D3-C-150, D3-NC-150. The dynamic mirror deformation of the SOIMUMPs micro-scanners is compared to measurements performed on the STM micro-scanner introduced in Section 2.7.

8.6.1.1   Static deformation

Significant out-of-planarity in released MEMS structures may not only render them unsuitable as optical surfaces but can also affect the performance of coupled electrostatic components such as AVC structures. Static deformation in the SOIMUMPs micro-scanners is primarily determined by two process-related sources of stress:

- high temperature deposition of the metal reflective coating coupled with a mismatch in the coefficient of thermal expansion between the *Silicon* and *BlanketMetal* layers: inter-layer strain mismatch is generated and if no delamination occurs, an in-plane residual tensile stress, σ_{res}, develops in the metal layer [142];

- the doping process of the Si layer where phosphorous is driven into the top surface at a high temperature: the result is a through-thickness stress gradient, σ/z, tensile on the top surface and compressive at the bottom surface of the silicon layer.

It has to be noted that the in-plane residual stress is assumed to be laterally uniform and biaxial. However, the stress distribution is dependent on the homogeneity of the metal film thickness and microstructure. Additionally the through-thickness strain gradient in the *Silicon* layer largely depends on the lateral distribution of the doping rate on the top surface. Averaged values for the stress gradient in the *Silicon* layer, σ/z and the residual stress in *BlanketMetal* layer, σ_{res} illustrated in **Figure 8-32**, are deduced by measuring the mirror curvature of the non-coated and coated micro-scanners respectively. In addition to σ/z and σ_{res}, an in-plane residual stress in the *Silicon* layer has also been

observed and measured [139]. The *Silicon* in-plane residual stress does not contribute to the out-of-plane curvature of metal-free silicon structures. Moreover, FE simulations demonstrated that the measured in-plane residual stress value in the *Silicon* layer (listed in **Table 8-3**) has a negligible effect on the static deformation of coated micro-scanners.
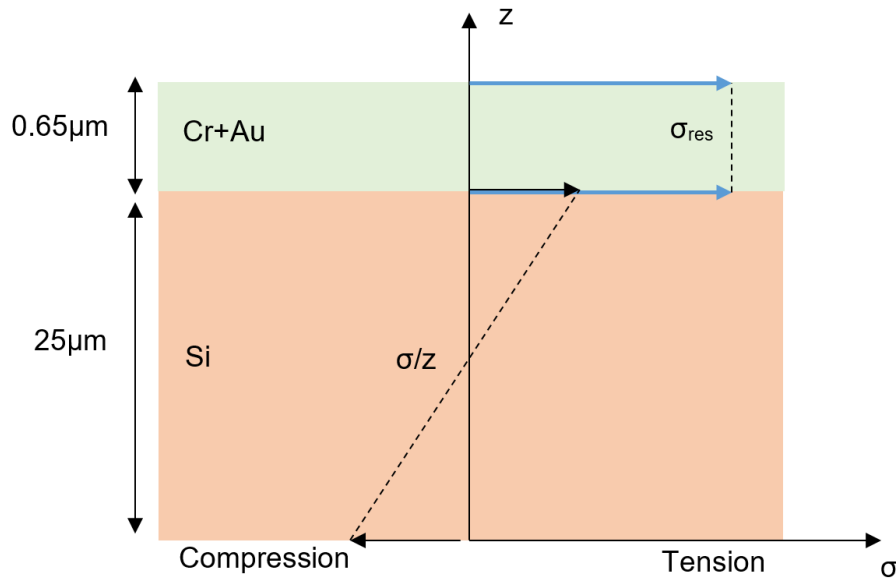
Figure 8-32: Simplified internal stress state of the micro-scanners contributing to static deformation

The planarity of the reflective mirror surface was measured using the *SENSOFAR S neox* noncontact 3-D optical profiler [143]. Sub-nanometer resolution is made possible with a phase shift interferometric (PSI) objective with specifications listed in **Table 8-10**. On the contrary to confocal objectives, very high resolution can be achieved with the PSI objective even at low magnifications, making it suitable for measuring very smooth, continuous surfaces. The entire 1 mm diameter mirror surface can be captured within the objective's field of view. This eliminates possible inaccuracies observed when stitching together multiple images.

Table 8-10: Specifications of the *SENSOFAR S neox* optical profiler with 10X interferometric objective [143]

Magnification	10X
Numerical aperture	0.30
Working distance, WD	7.4 mm
Field of view, FOV	1700 × 1420 μm
Optical resolution	0.47 μm
Vertical resolution (nm)	0.1 nm
Maximum slope on smooth surfaces	14°

The out-of-plane deflection of a coated and uncoated mirror surface is displayed in **Figure 8-33** and **Figure 8-34** respectively. A concave mirror surface profile is observed in all devices listed in **Table 8-4**, which confirms that σ/z and σ_{res} are positive.   The measured peak-to-peak and rms deformation values listed in **Table 8-11** demonstrate that the thin film metal deposition is the main contributor towards mirror curvature. However, measurements also indicate that around 22% of the mirror surface curvature results from the through-thickness stress gradient in the silicon layer. The curvature of the coated mirror surface was simulated using the FE models presented in Sections 8.3 and 8.3.2, whereby an initial stress of 360 MPa is applied to the *BlanketMetal* layer (**Table 8-3**). An overestimation in the simulated static deformation suggests a lower σ_{res} in the *BlanketMetal* layer. It has to be noted that variations in the residual stresses between runs are to be expected.
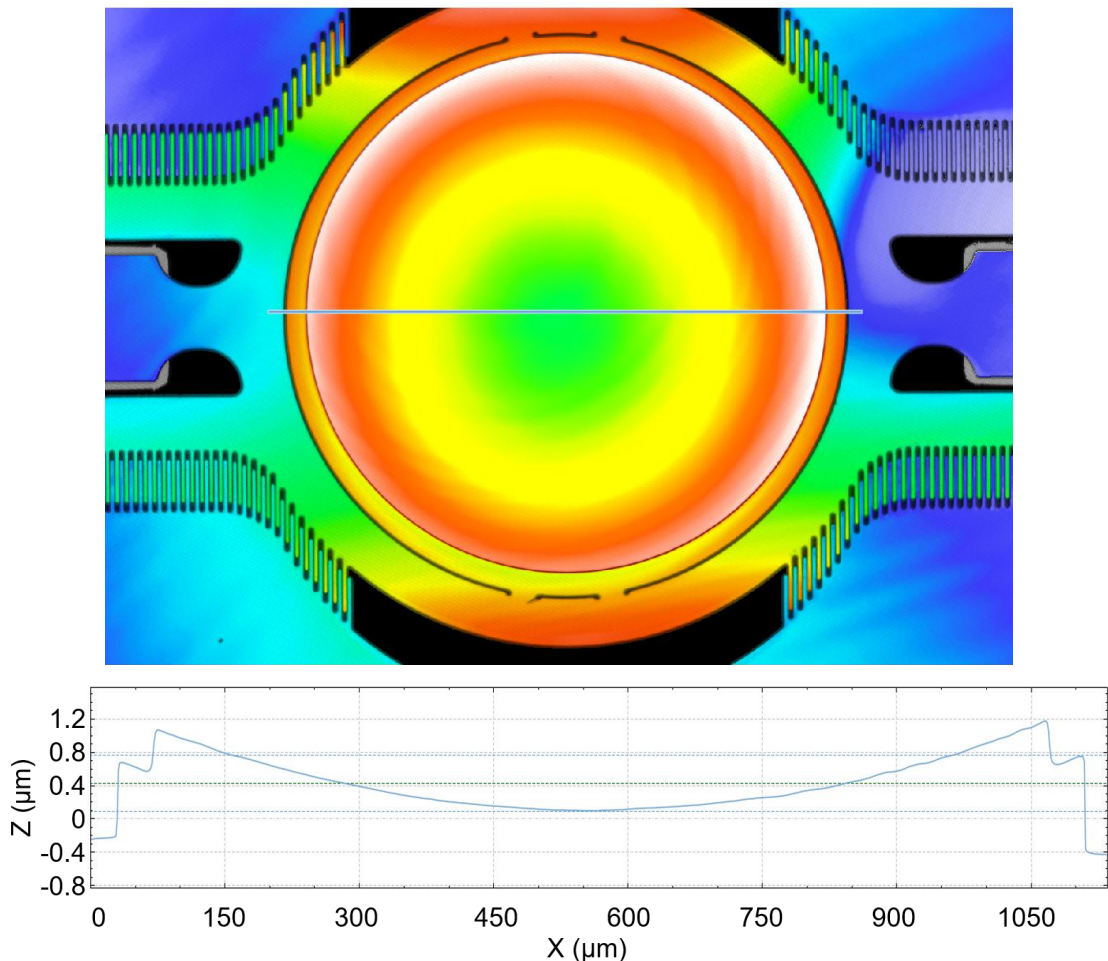
Figure 8-33: Out-of-plane surface profile of D1-C-100 micro-scanner measured with
SENSOFAR S neox 10x PSI objective
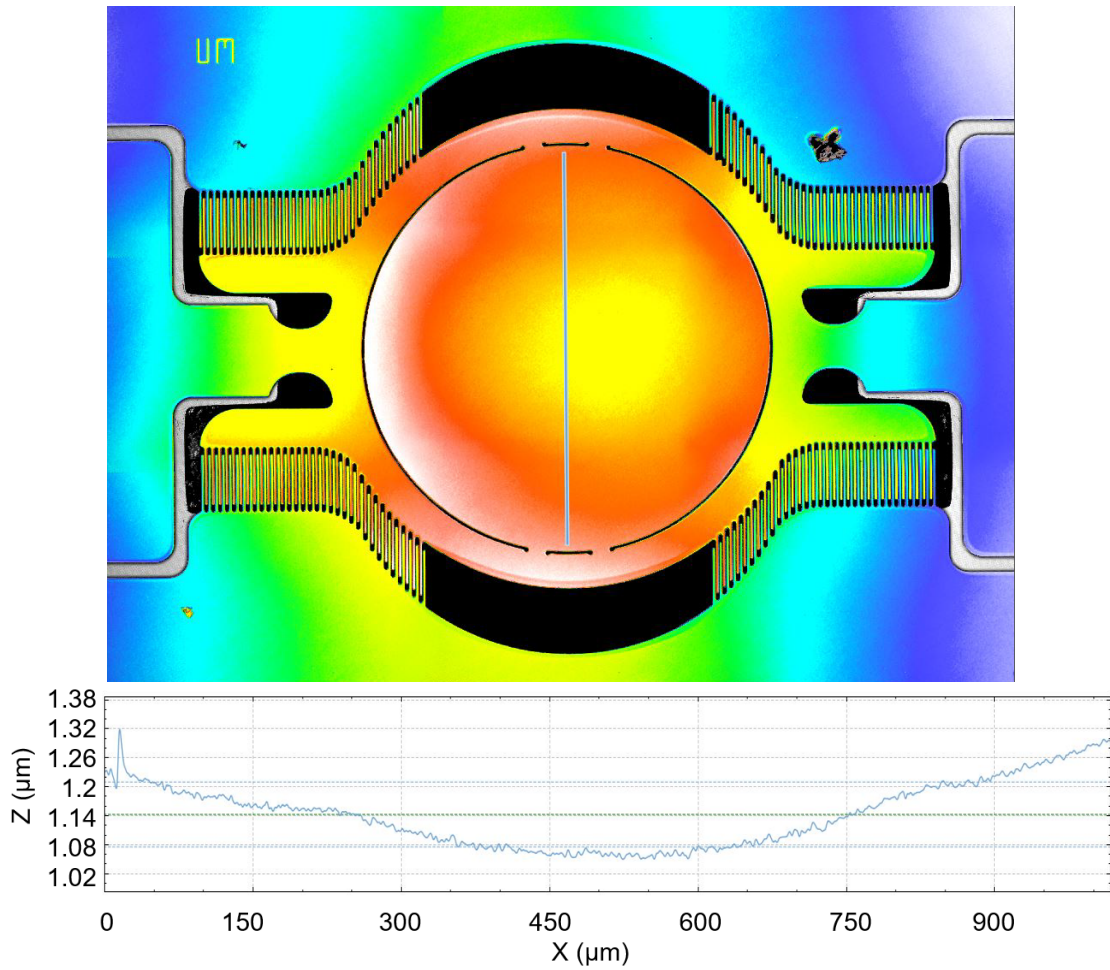
Figure 8-34: Out-of-plane surface profile of D1-NC-150 micro-scanner measured with
SENSOFAR S neox 10x PSI objective

Table 8-11: As-fabricated mirror surface flatness properties of the SOIMUMPs micro-scanners [σ_{res} of
360 MPa is applied in FE simulations while σ/z in the Silicon layer not considered]

Device Name	Measurements		Simulations	
	δ_{rms} (static) [nm]	δ_{max} (static) [nm]	δ_{rms} (static) [nm]	δ_{max} (static) [nm]
D1-C-100	475.1	860.5	636.6	1105.2
D1-C-150	466.7	854.1	622.1	1091.6
D1-NC-150	102.3	186.5	/	/
D2-C-150	480.8	854.8	734.7	965.4
D2-NC-150	96.8	176.2	/	/
D3-C-150	456.8	834.3	563.7	973.3
D3-NC-150	104.5	189.6	/	/

The linear variation of internal stress with thickness in the doped *Silicon* layer can be
deduced from (8.3) where the elastic modulus, E is 169 GPa. The curvature for the
uncoated mirror surface, k_{NC} is the mean of k_x and k_y, as defined in (8.4) and calculated

from a second order 3-D polynomial fit of the measured surface height. However, monocrystalline Si is orthotropic, that is, the 2-D distribution of E is not constant and varies between 169GPa and 130GPa [108]. Given that the micro-scanner is oriented in the [110] Si wafer reference plane, the orthogonal in-plane stress values, σ_x and σ_y, can be deduced from (8.5) and (8.6) respectively [108]. The estimated through-thickness stress gradient derived from isotropic (8.3) and orthotropic (8.7) elastic properties is listed in **Table 8-12**. Higher σ/z values are obtained when the orthotropic elastic property of Si is considered. It was generally observed that, k_x is marginally larger than k_y. This is not necessarily an indication of an inhomogeneous distribution of the Si dopant or *BlanketMetal* deposition. The location of gimbal-mirror links has a slight impact on the mirror surface curvature which could however explain the marginal difference between k_x and k_y. This is evident from the relatively lower discrepancy between k_x and k_y in the case of micro-scanner *D2*, which consists of a more uniform radial link distribution (see **Figure 8-30(b, d)**).

$$\sigma = Ekz \tag{8.3}$$

$$k_x = \frac{\partial^2 z}{\partial x^2} ; k_y = \frac{\partial^2 z}{\partial y^2} \tag{8.4}$$

$$\sigma_x[GPa] = 194.5k_xz + 35.7k_yz \tag{8.5}$$

$$\sigma_y[GPa] = 35.7k_xz + 194.5k_yz \tag{8.6}$$

$$\bar{\sigma} = \frac{\sigma_x + \sigma_y}{2} \tag{8.7}$$

Table 8-12: Uncoated mirror curvature measurements and the through-thickness stress gradient of the doped Silicon layer, σ/z, deduced from equations (8.3) and (8.7)

Device Name	k_x [1/m]	k_y [1/m]	k_{NC} [1/m]	Goodness of fit - R^2	σ/z (using Si isotropic properties - (8.3)) [MPa/µm]	$\bar{\sigma}$/z (using Si orthotropic properties - (8.7)) [MPa/µm]
D1-NC-150	1.65	1.64	1.64	0.9898	0.28	0.38
D2-NC-150	1.54	1.55	1.54	0.9822	0.26	0.36
D3-NC-150	1.72	1.67	1.70	0.9924	0.29	0.39

The residual stress in the metal coating can be estimated from the difference in curvature between the coated and uncoated mirror surfaces: $k_C - k_{NC}$. The Stoney equation of (8.8) is valid for a small film thickness, t_f, relative to the substrate thickness, t_m. A more general equation has been proposed by Dunn *et al.* [144], which accounts for the elastic properties of the film layer: E_f and ν_f. The results, summarized in **Table 8-13**, indicate a small discrepancy between the estimated σ_{res} derived from (8.8) and (8.9) respectively. This suggests that the Stoney equation is valid for residual stress estimations of the SOIMUMPs process (25 μm Si layer thickness).

$$\sigma_{res} = \frac{E_s}{6(1-\nu_s)} \frac{t_m^2}{t_f} (k_C - k_{NC}) \tag{8.8}$$

$$\sigma_{res} = \frac{E_s}{6(1-\nu_s)} \frac{t_m^2}{t_f} (k_C - k_{NC}) \left(\frac{1 + 2hm(2 - 3hm + 2h^2) + h^4 m^2}{1 + h} \right) \tag{8.9}$$

$$\text{where } h = t_f / t_m \; ; m = E_f / E_{Si} \left(\frac{1-\nu_s}{1-\nu_f} \right)$$

The design-independent estimate of σ_{res} is 226.29 MPa, which is deduced by averaging over the four micro-scanner designs listed in **Table 8-13**. In order to predict the overall out-of-plane deformation in the as-released condition, analytically or numerically, an equivalent σ_{res} can be applied to the *BlanketMetal* layer to include the additional effect of the Si-layer stress-gradient. By removing k_{NC} in (8.9), the equivalent σ_{res} for the SOIMUMPs *BlanketMetal-Silicon* (25 μm) stack is 284.36 MPa.

Table 8-13: Coated mirror curvature measurements and derived *BlanketMetal* residual stress due to the metallization process

Device Name	k_x [1/m]	k_y [1/m]	k_C [1/m]	Goodness of fit - R^2	σ_{res} (from (8.8)) [MPa]	σ_{res} (from (8.9)) [MPa]
D1-C-100	8.22	7.71	7.97	0.9993	222.15	225.92
D1-C-150	8.32	7.75	8.04	0.9993	223.29	227.08
D2-C-150	8.32	8.04	4.09	0.9993	232.06	236.00
D3-C-150	8.07	7.47	7.77	0.9992	212.56	216.17

8.6.1.2 Dynamic deformation

Dynamic deformation measurements were performed using the Polytec MSA-500 Micro System Analyzer in collaboration with the Department of Information Engineering at the University of Padova. The MSA-500 acquires non-contact real time measurements of the out-of-plane velocity and displacement at any sample point using a scanning Laser Doppler Vibrometer (LDV) [145]. This enables the characterization of out-of-plane vibrations in MEMS devices. A LDV consists of a two beam laser interferometer capable of measuring the frequency shift between a reference beam and a test beam. The amplitude and frequency of vibration can be deduced from the Doppler shift of the test beam frequency due to the motion of the surface under test. In order to characterize an entire surface, the vibrometer automatically moves to each sample point on a predefined scan grid.

Laser Doppler Vibrometry is normally used to assess the vibration modes of resonating MEMS devices [146, 147]. Theoretically, the out-of-plane displacement resolution at the micro-scanner oscillating frequency (see **Table 8-14**) enables the extraction of the dynamic deformation of the mirror surface. It has to be noted that dynamic deformation measurements are limited to scanning amplitudes of less that 2.5°. Additionally, the LDV measurement accuracy is dependent on the reflectivity of the target surface. The signal-to-noise ratio can be improved with increased reflectivity; however, the out-of-plane displacement magnitude may vary depending on the reflective material and deposition method [148].

Table 8-14: Specifications of the Scanning Laser Doppler Vibrometer
as part of the Polytec MSA-500 Micro System Analyser [149]

Velocity resolution	<1 μm/s
Displacement resolution	< 1 nm
Maximum velocity of vibration	1 m/s
Maximum out-of-plane displacement	approx. 20 μm
Maximum vibration frequency	1 MHz
Objective magnification	5x
Objective FOV	1.8 × 1.34 mm

Using the set-up depicted in **Figure 8-35**, the dynamic deformation was extracted by implementing the following procedure. The resonating micro-scanner is actuated using a sinusoidal waveform generator coupled (Agilent 33250A) to a high voltage amplifier (FLC A400). The characterization procedure is described in the following steps:

(a) initially, the topography of the micro-mirror surface was measured;

(b) a reference point on a non-movable surface was selected as shown in **Figure 8-36**, which is required for LDV measurements;

(c) a sample point at the micro-mirror tip was selected to acquire the harmonic scanning response during a frequency sweep of the drive voltage (this is performed to determine the drive frequency at which the maximum measurable out-of-plane displacement is reached);

(d) the micro-scanner was actuated at a fixed voltage and frequency and out-of-plane displacement measurements were performed after steady-state response is reached;

(e) at each sample point, a trigger signal from the waveform generator ensured that the out-of-plane displacement was measured at the required phase angle (measurements were acquired at $\theta(t) = \theta_{max}$; $\theta(t) = -\theta_{max}$ and $\theta(t) = 0°$);

(f) each displacement measurement was obtained by averaging over 25 successive acquisitions to minimize the impact of any temporal scanning variations on the measurements;

(g) steps (e) and (f) were repeated to scan the mirror surface sample points displayed in **Figure 8-36**.
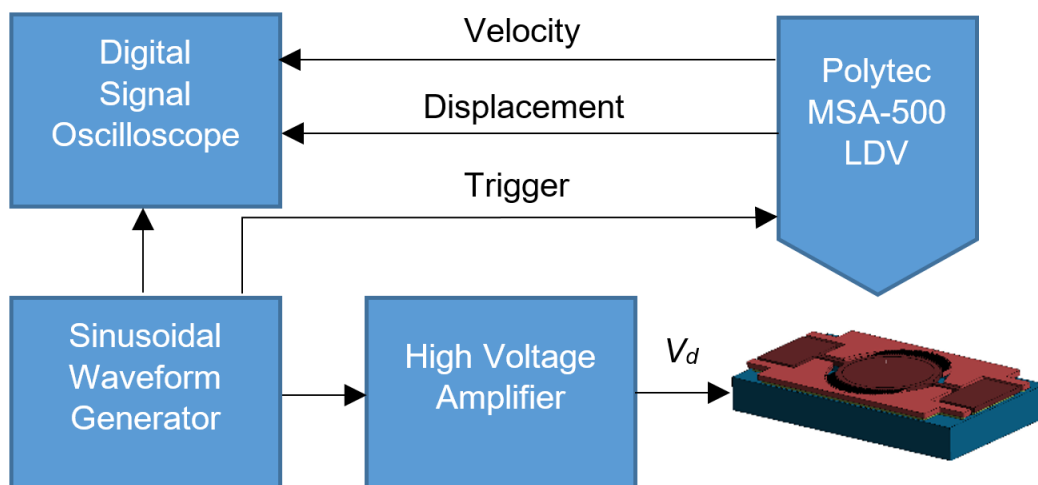
Figure 8-35: LDV dynamic deformation measurement system set-up at the University of Padova
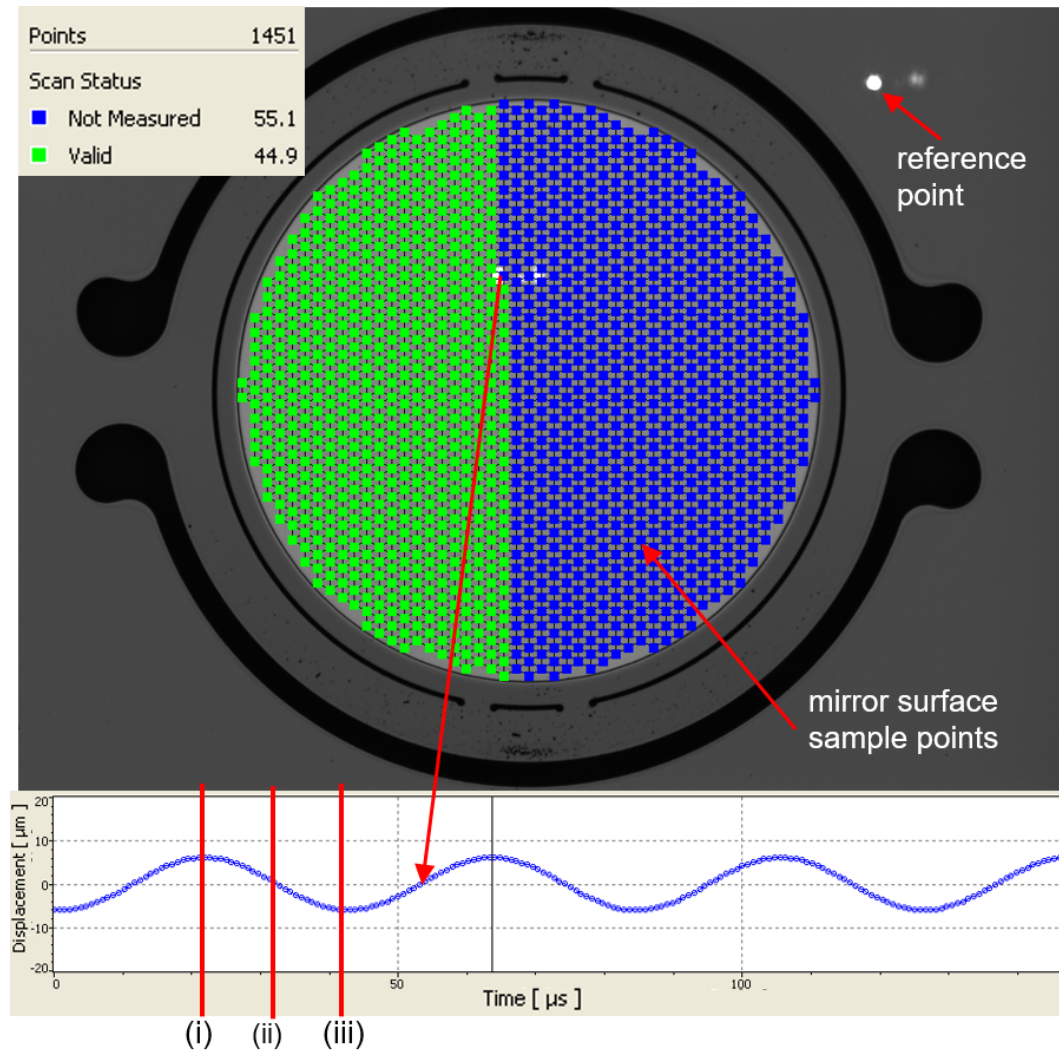
Figure 8-36: Dynamic out-of-plane displacement measurements at (i) $\theta(t) = \theta_{max}$ (ii) $\theta(t) = 0°$ and (iii) $\theta(t) = -\theta_{max}$ using the Polytec MSA-500 LDV (D3-C-150 micro-scanner)

The settings of the LDV measurement set-up are listed in **Table 8-15**. The variation of dynamic deformation with scan frequency and amplitude is also evaluated by taking measurements at three different drive frequencies: f_1, f_2 and f_3.

Table 8-15: LDV settings for the dynamic deformation measurements of the SOIMUMPs micro-scanners (*in the case of D3-NC-150, the scanned area also includes the gimbal-frame area)

Drive voltage	120 V_{pk} sinusoidal		
Acquisition time per point	200 µs		
Number of acquisitions per point	25		
Device	**D1-NC-150**	**D3-C-150**	**D3-NC-150**
Total scanned points	1671	1451	2227*
f_1 **(Hz)**	26694	23920	26694
f_2 **(Hz)**	26696	23925	26696
f_3 **(Hz)**	26701	23930	26701

In MATLAB, the dynamic deformation, $\delta(x,y)$ of the mirror surface is deduced from the 3-D displacement data as follows:

(a)   extract mirror deflection, $z(x, y)$ data for the sample points within a radial distance of 0.45 mm from the mirror centre defined by $\sqrt{(x^2+y^2)} <= 0.45$ mm;

(b)   prepare surface data for polynomial fit: MATLAB function *preparesurfacedata*;

(c)   fit linear surface function to obtain micro-mirror tilt:

$z_{tilt} = p00+p10x+p01y$

(d)   extract 3-D dynamic deformation surface: $\delta(x,y) = z - z_{tilt}$

(e)   fit third order surface polynomial function:

$\delta_{fit}(x,y) = q00+q10x+q01y+q20x^2+q11xy+q02y^2+q30x^3+q21x^2y+q12xy^2+q03y^3$

(f)   calculate the root-mean-square and peak-to-peak dynamic deformation from δ_{fit} : δ_{rms} and δ_{max}

(g)   Calculate R_{def} (defined in (6.10)) from δ_{rms}

The extraction of $\delta(x,y)$ from the out-of-plane displacement raw data is demonstrated in **Figure 8-37**. With the micro-scanner's axis of rotation aligned to the *x*-axis, the out-of-plane displacement of the mirror plate and outer gimbal-frame at maximum scan angle is plotted in **Figure 8-37(a)**. Dynamic deformation is proportional to the angular acceleration and therefore angular displacement of the micro-scanner. By eliminating the overall mirror tilt, the dynamic deformation of the mirror plate and gimbal-frame is plotted in **Figure 8-37(b)**. The dynamic flatness of the micro-mirror is approximately two orders of magnitude higher than that of the gimbal-frame. The measured gimbal-frame deformation is in agreement with the FE simulation results depicted in **Figure 8-38**. This demonstrates the principle behind the gimbal-framed micro-scanner design whereby the angle of twist of torsional beams is disengaged from the tilting mirror plate. It has to be noted that the 3-D surface plot of **Figure 8-37(b)** does not correspond to the actual mirror plate out-of-planarity. The overall mirror out-of-plane deformation can be obtained by combining the dynamic deformation to the static deformation, discussed in Section 8.6.1.1 .

The fitted dynamic deformation (δ_{fit}) profiles of micro-scanners D3-NC-150, D1-NC-150 and D3-C-150 are shown in **Figure 8-39**, **Figure 8-40** and **Figure 8-41** respectively. A change from a convex to a concave dynamic deformation profile can be observed

when the micro-mirror rotates from maximum to minimum scan angle. Close similarity exists between the dynamic deformation profiles of the uncoated micro-mirror samples (D1-NC-150 and D3-NC-150). However, a significant difference is present between the $\delta(x,y)$ profiles of the coated and uncoated indirect-drive micro-scanners. **Figure 8-42** shows the simulated dynamic deformation profiles of designs D3-C-150 and D3-NC-150 at the same experimental θ_{max} values. It has to be noted that the measurement results do not exhibit the symmetrical property inherent in the simulated $\delta(x,y)$ surface profiles of **Figure 8-42**. Simulation results indicate that higher dynamic deformation is attained with the introduction of the *Blanketmetal* reflective layer. However, the significant difference in shape between the measured surface profiles of the coated and uncoated micro-mirrors is not observed in the simulation results. The difference in dynamic deformation profiles between coated and uncoated micro-mirrors may result from an observed offset of the coating surface relative to the mirror plate. Given that deposition of the *Blanketlayer* is performed using the shadow mask technique, a wafer-to-wafer misalignment of up to 35 μm may occur between the shadow mask and the SOI wafer [140]. Moreover, the discrepancy between the measured (**Figure 8-39** and **Figure 8-40**) and simulated (**Figure 8-42**) dynamic deformation surface profiles may indicate other higher order effects such as plate buckling due to the initial micro-mirror curvature.

(a)   (b)
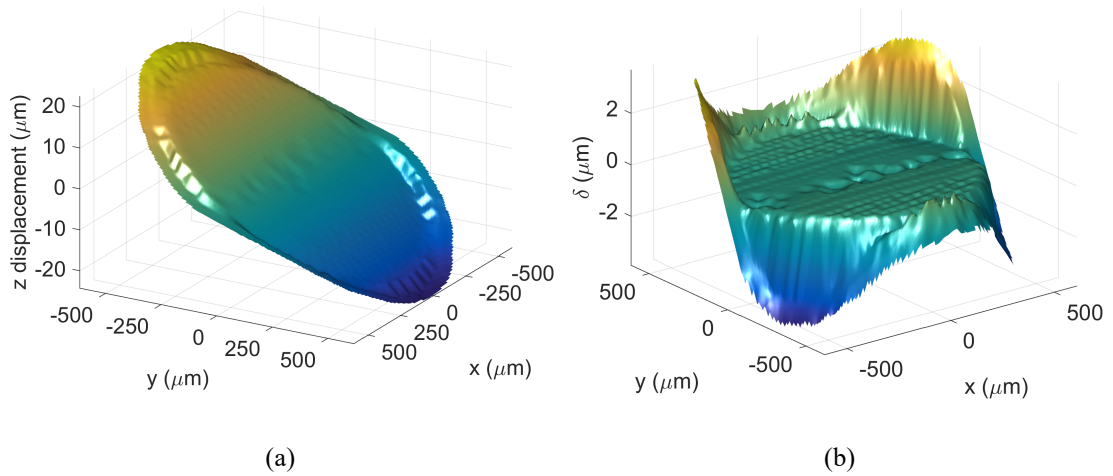
Figure 8-37: (a) out-of-plane displacement and (b) out-of-plane deformation of D3-NC-150 mirror and gimbal-frame surface oscillating at maximum scan angle (f_s = 24.92 kHz; θ_{max} = 2.23°) [raw data from Polytec LDV measurements]

(a)   (b)
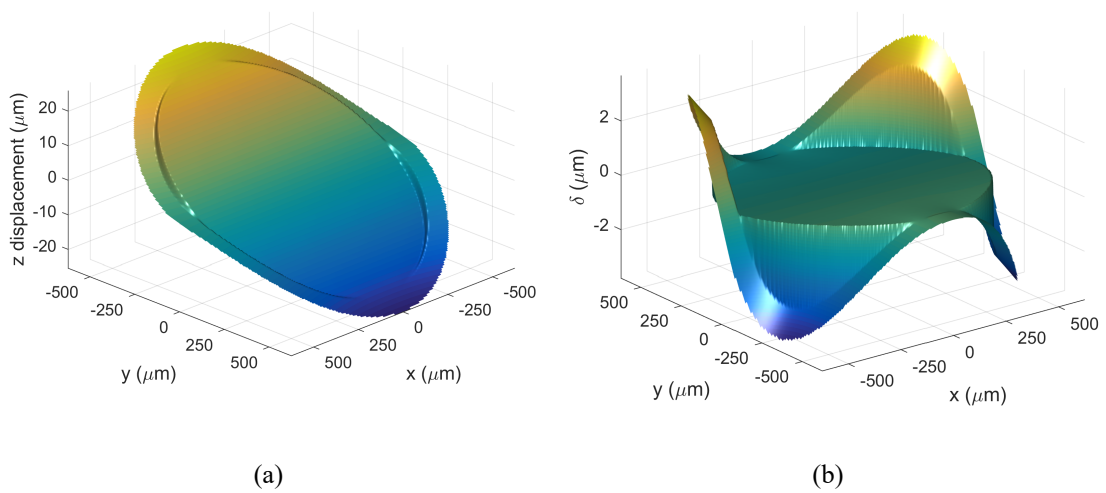
Figure 8-38: (a) out-of-plane displacement and (b) out-of-plane deformation of D3-NC-150 mirror and gimbal-frame surface oscillating at maximum scan angle (f_s = 24.92 kHz; θ_{max} = 2.23°) [FE simulations]

(a) $\theta(t) = \theta_{max}$

(b) $\theta(t) = -\theta_{max}$
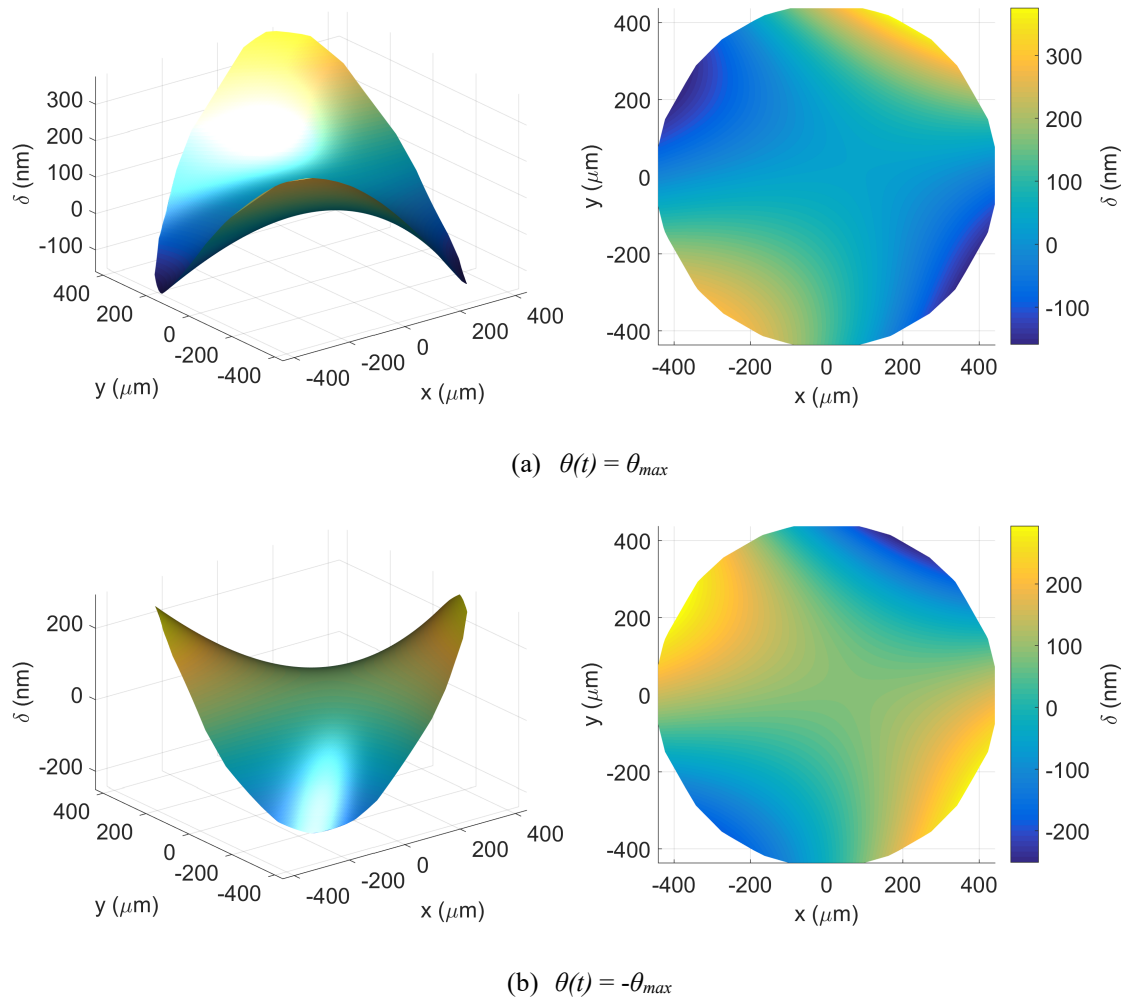
Figure 8-39: Out-of-plane deformation of the D3-C-150 mirror surface oscillating at 23.93 kHz and θ_{max} of 2.27° [surface fit from Polytec LDV measurements]

179

(a) $\theta(t) = \theta_{max}$

(b) $\theta(t) = -\theta_{max}$
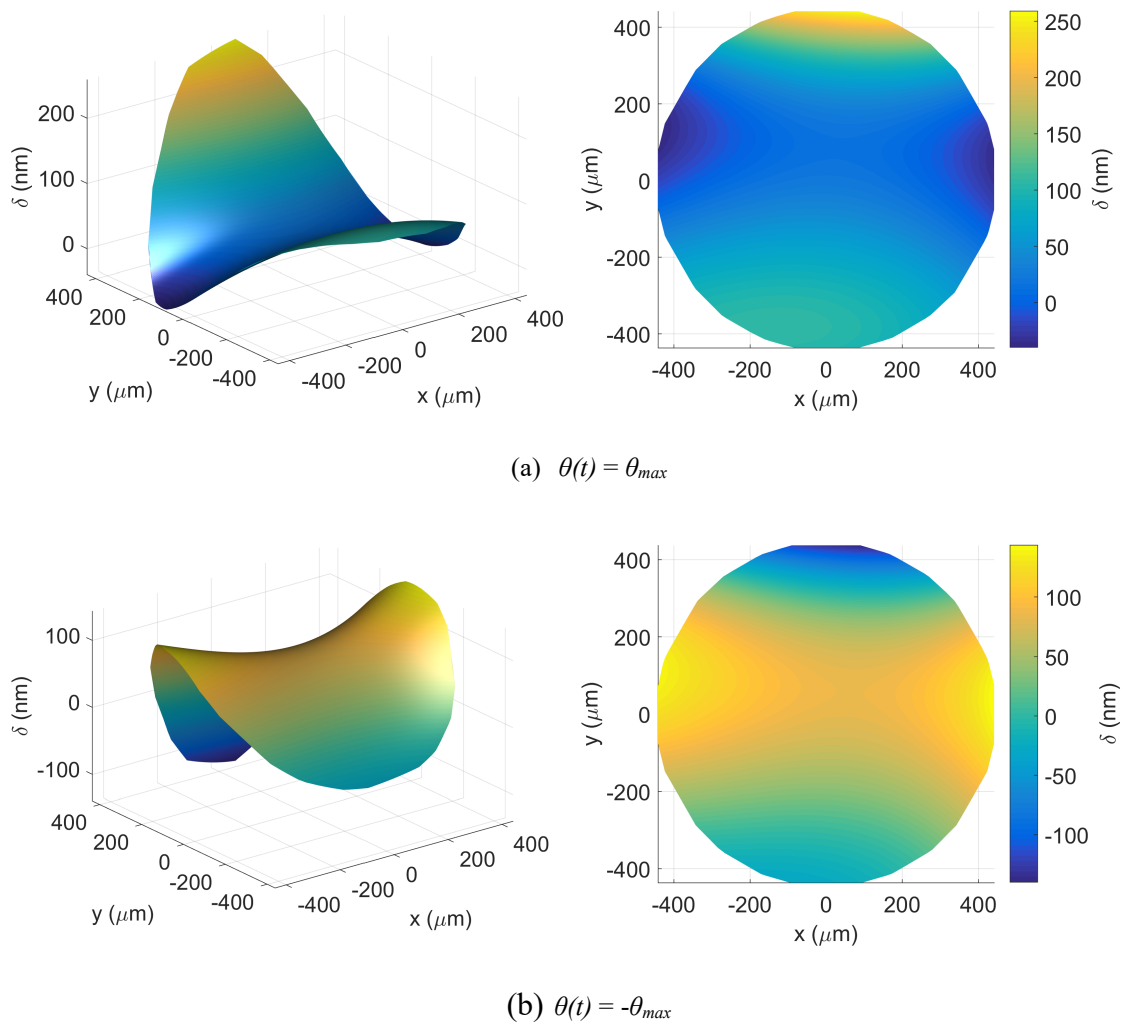
Figure 8-40: Out-of-plane deformation of the D3-NC-150 mirror surface oscillating at f_s = 24.92 kHz and θ_{max} of 2.23° [surface fit from Polytec LDV measurements]

180

(a) $\theta(t) = \theta_{max}$

(b) $\theta(t) = -\theta_{max}$
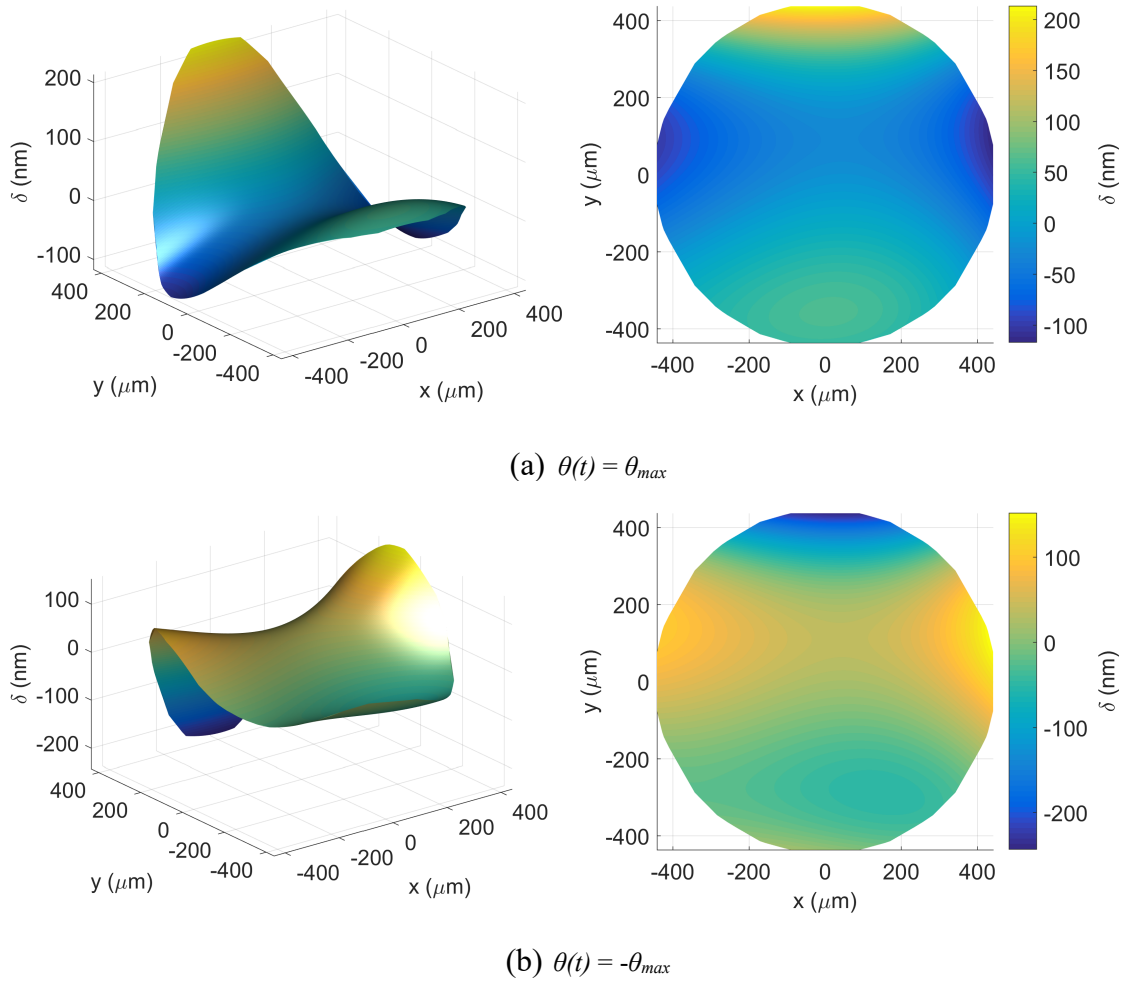
Figure 8-41: Out-of-plane deformation of the D1-NC-150 mirror surface oscillating at $f_s = 26.701$ kHz and θ_{max} of 2.35° [surface fit from Polytec LDV measurements]

(a) D3-C-150 ($\theta_{max} = 2.27°$)

(b) D3-NC-150 ($\theta_{max} = 2.44°$)
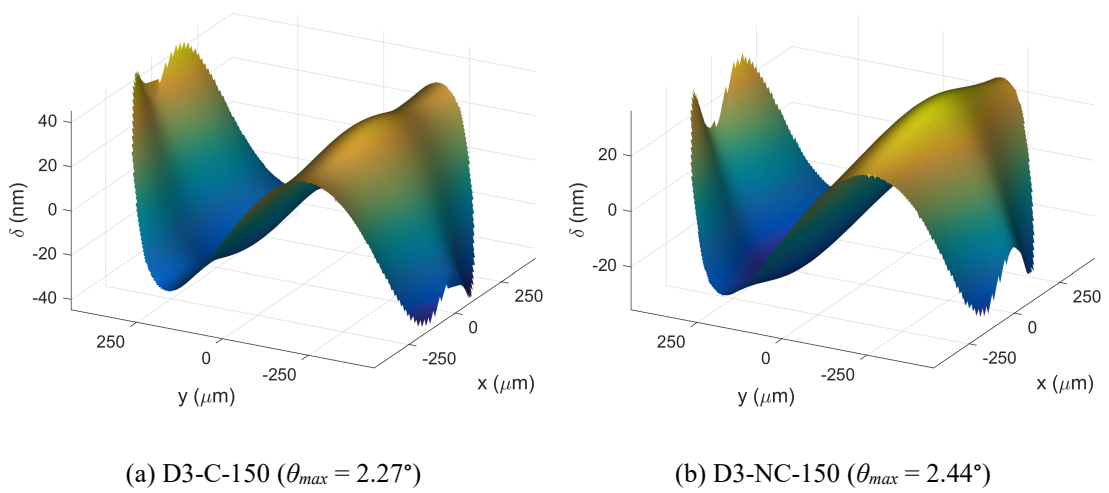
Figure 8-42: Dynamic deformation surface profile obtained from FE simulations

The measurement results of **Figure 8-43** demonstrate that for all micro-scanners, the surface-averaged δ_{rms} increases with scanning frequency and amplitude. In spite of variations in the actuation configuration, comparable dynamic deformation magnitudes can be observed between the two un-coated micro-scanners (D1-NC-150 and D3-NC-150). This is in agreement with the numerical predictions obtained from FE simulations. Higher dynamic deformation is achieved with the Au-Cr coated micro-scanner (D3-NC-150). This can be observed when considering either rms or peak-to-peak dynamic deformation values, which are listed in **Table 8-16**. A higher δ can be the result of increased mirror reflectivity, which improves the LDV signal-to-noise ratio [148], or higher static deformation. The static micro-mirror deformation significantly increases following the deposition of the *BlanketMetal* coating (see **Table 8-11**). This may lead to a different parasitic mirror surface vibration mode compared to that of the uncoated micro-scanners. The difference in the dynamic deformation surface profile between coated and uncoated mirrors (**Figure 8-39** and **Figure 8-40**) may be indicative of this hypothesis.
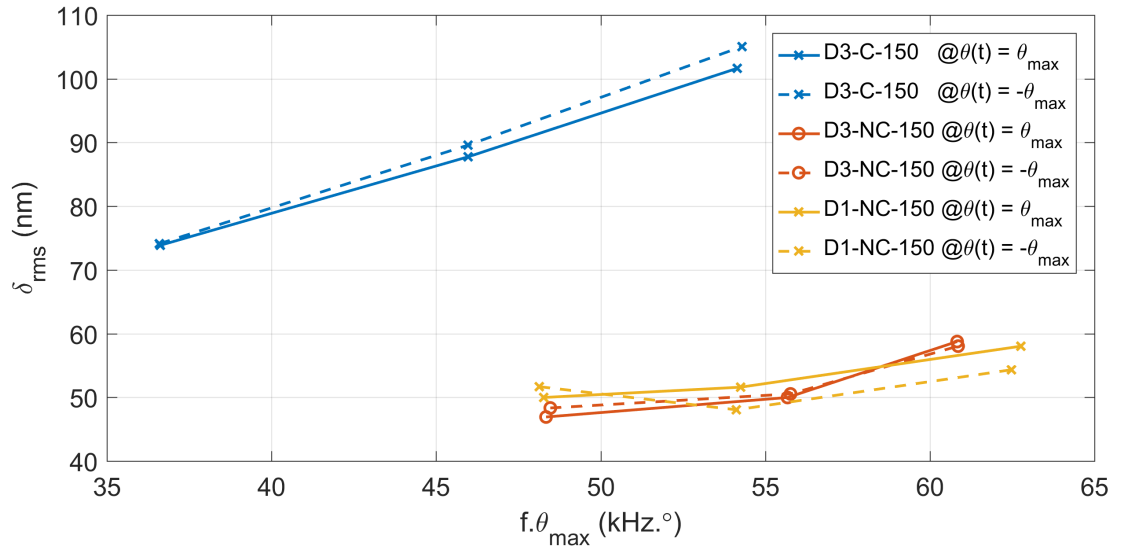
Figure 8-43: Dynamic deformation as a function of the $f_s.\theta_{max}$ product for the three fabricating micro-scanners obtained from LDV measurements

Table 8-16: Dynamic deformation results of the fabricated micro-scanners driven at resonance (obtained from Polytec LDV Measurements)

Device	f_s range (Hz)	θ_{max} range (°)	δ_{rms} range (nm) @$\theta(t) = 0°$	δ_{rms} range (nm) @$\theta(t) = \theta_{max}$	δ_{max} range (nm) @ $\theta(t) = \theta_{max}$
D1-NC-150	26694-26701	1.80-2.35	9.35-3.60	41.48-52.58	289.41-395.23
D3-C-150	23920-23930	1.53-2.27	2.07-10.63	71.93-92.72	407.14-534.73
D3-NC-150	24915-24923	1.95-2.44	1.85-5.07	45.79-52.58	280.29-363.80

In order to quantify improvements in dynamic flatness of the SOIMUMPs gimbal-frame micro-scanners, out-of-plane deformation is presented in normalized form, R_{def} (see (6.10)) in **Table 8-17** and **Table 8-18**. In comparison to the conventional mirror-to-torsional beam linkage design (**Figure 2-14**), measurements demonstrate that the optimized gimbal-framed design leads to an 80% reduction in the dynamic deformation of a circular mirror plate. The measured gain in dynamic flatness is in agreement with FE simulations. The simulated dynamic deformation profile is deduced from the difference between the overall deformation profile (static-equivalent inertial load and initial residual stress) and the static deformation profile (initial residual stress). Thus, any possible effects of initial mirror curvature on the dynamic deformation surface profile is also considered. By comparing the normalized dynamic deformation of D3-C-150 and D3-NC-150, measurements and simulations indicate that the residual stresses resulting from reflective layer deposition lead to a marginal amplification in dynamic deformation of the mirror plate. The results of **Table 8-17** show a consistent underestimation of dynamic deformation from FE simulations. This may be linked to (i) the impact of the mirror surface optical characteristics (ex: reflectivity) on the measured displacement resolution or (ii) the low vibrational velocity at maximum displacement amplitude which diminishes the signal-to-noise ratio of the LDV. The Polytec MSA-500 LDV measurements of the oscillating 1 mm diameter circular plate are limited to θ_{max} values of less than 2.5°. Within this scanning range the simulations predict δ_{rms} values in the range of tens of nanometers.

Table 8-17: Normalized mirror surface deformation of oscillating micro-scanners fabricated using the STM and SOIMUMPS processes

Design type	Circular mirror with gimbal-type support (SOIMUMPs process)			Circular mirror with conventional support (STM process)
Device name	D1-NC-150	D3-C-150	D3-NC-150	Horizontal
R_{def} (measured)	0.1056	0.1751	0.0831	0.9349
R_{def} (simulated)	0.0418	0.0518	0.0383	0.3067

Table 8-18: Ratios of normalized dynamic deformations as an indication of the effects of design configuration and the reflective layer deposition on the dynamic flatness of a 1 mm diameter circular micro-mirror

Ratio of normalized dynamic deformation		
R_{def} (conventional mirror support: STM design)	Measurements	5.34
R_{def} (gimbal-type frame mirror support: D3-C-150)	Simulations	5.92
R_{def} (*BLANKETMETAL* coating: D3-C-150)	Measurements	1.66
R_{def} (no *BLANKETMETAL* coating: D3-NC-150)	Simulations	1.34

8.6.2   **Quality Factor**

The optical test bench set-up discussed in Section 5.3 was used to measure the quality factor, harmonic response and scanning efficiency of the fabricated micro-scanners. The superior Q of the indirect-drive micro-scanner, compared to the direct-drive designs, can be observed in **Figure 8-44**. This is primarily a result of the lower oscillation amplitudes and hence negligible energy loss from the AVC structures in the indirect-drive configuration. The measured Q of the indirect-drive micro-scanner is in agreement with the CFD simulation results, as shown in **Figure 8-45**. Therefore, PSD-based measurements validate the predicted damping characteristics of a scanning circular plate, namely the non-linear aerodynamic drag variation with θ_{max} (see Section 5.5.2). A strong correlation between numerical and experimental results outline two potential benefits of resonating micro-scanners based on the indirect-drive concept:

- a comprehensive analysis on the aerodynamics of micro-plates oscillating in out-of-plane rotation can be achieved using low-cost MEMS processes and conventional AVC structures;

- a predominant damping source enables the development of more accurate system-level models in the design stage of electrostatically-actuated 1-D resonating micro-scanners.

Measurements performed on D1 prototypes demonstrate an improvement in Q when the comb finger length, f_l is reduced from 150 μm to 100 μm. This implies that the AVC structure energy loss has a more significant weighting on the overall Q when compared to the D3 prototypes. While the observed effect of f_l on Q is in agreement with the simulation results of **Figure 8-11**, a considerable offset between the measured and simulated decay profile can be seen in **Figure 8-46** for *D1*. This may suggest that the applied CFD models are only valid in electrostatic micro-scanner designs where there is

negligible aerodynamic interference between the AVC structures and mirror plate. The direct-drive designs of **Figure 8-2** and **Figure 8-4** consist of comb fingers that are directly connected to a structure resonating at large displacement amplitudes as opposed to the indirect-drive and STM horizontal scanner designs.

Although simulations predict a negligible difference in Q between *D1* and *D2*, as shown in **Figure 8-46**, a significantly lower Q is observed in *D2* from measurements. This can be attributed to the fact that the natural frequencies of the torsional mode and the parasitic out-of-plane bending mode (see **Figure 7-5**) are very close to each other. FE simulations performed on the final D2-C-150 design demonstrate that the modal separation between the torsional and out-of-plane bending mode is 1.21 kHz, in contrast with the modal separation of 5.01 kHz for the final D1-C-150 design. In general, the non-coated prototypes are characterized by a lower Q. This can be linked to the shift to lower scanning frequencies as a result of metallization, which will be discussed in Section 8.6.3. A reduction in the scanning frequency of around 1 kHz as a result of metallization may be sufficient to cause a non-negligible increase in Q.
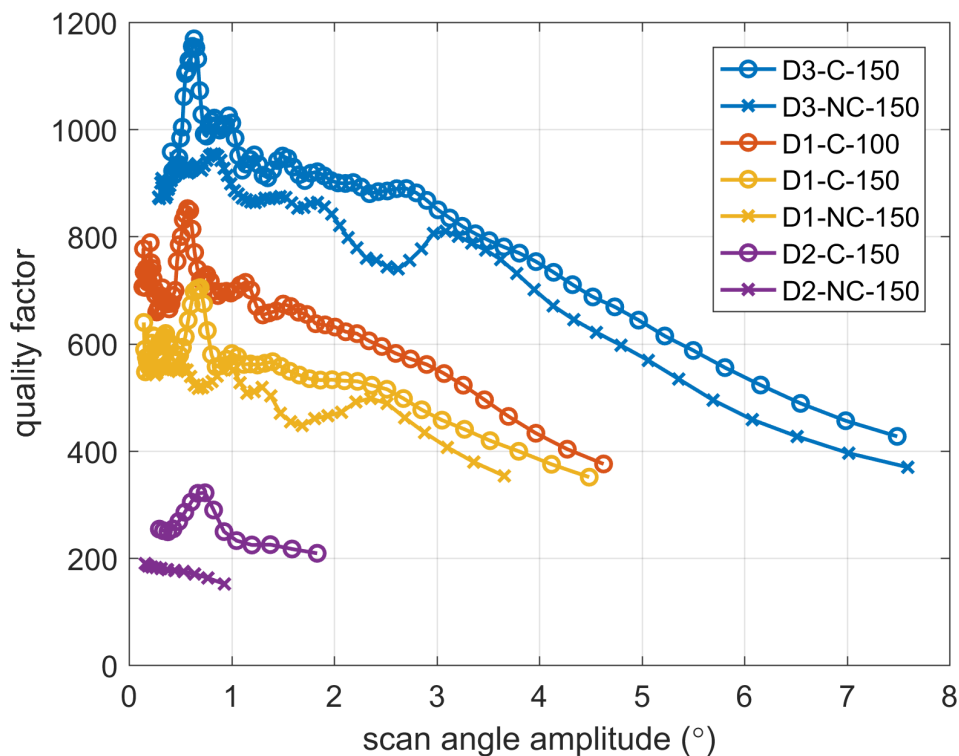
Figure 8-44: Variation of quality factor with scan angle amplitude, θ_{max}, obtained from PSD-based measurements
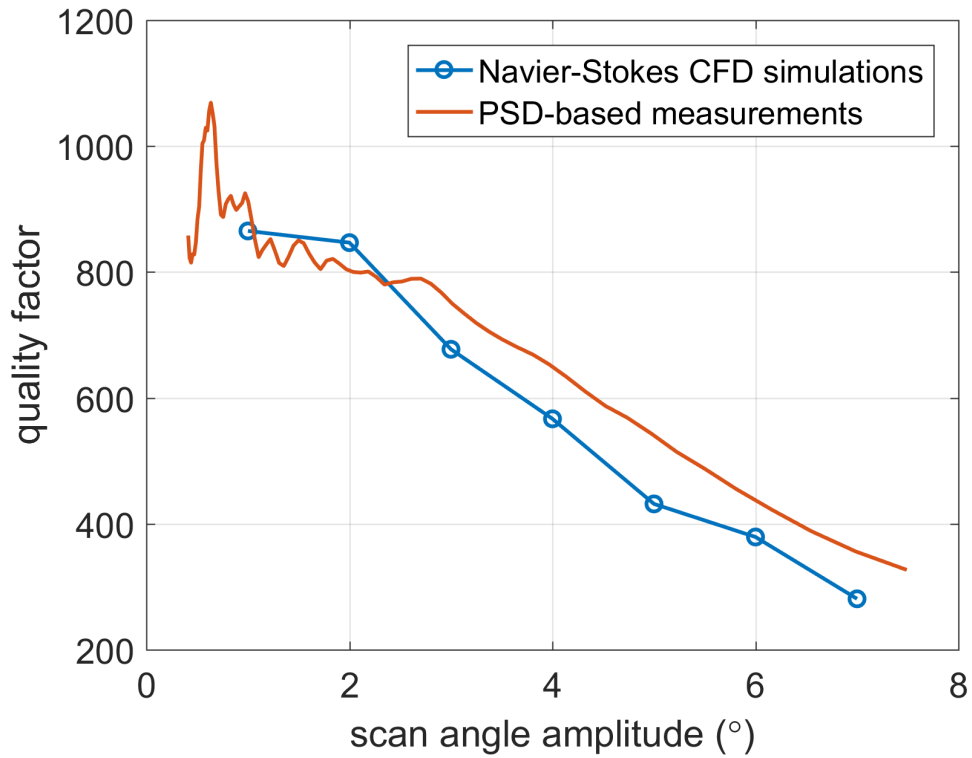
Figure 8-45: Quality factor variation with scan angle amplitude, θ_{max} for the indirect-drive design: a comparison between measurements and numerical simulation results (D3-NC-150)
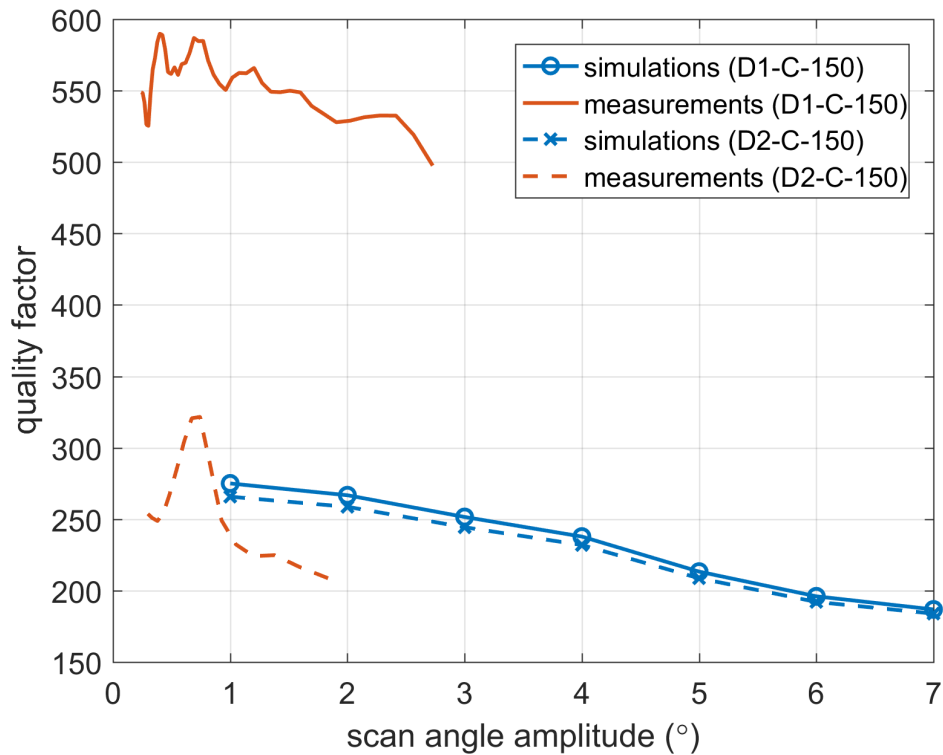
Figure 8-46: Quality factor variation with scan angle amplitude for the direct-drive micro-scanner designs: a comparison between measurements and numerical simulation results

Based on the micro-scanner dynamic equation of (2.7), the non-linear damping ratio, ζ, defined in (3.10), can be deduced from the above damping measurements. The Q_0 (defined as the intercept when $\theta_{max} = 0°$) and the non-linear quality factor, Q_{nl} are obtained from a linear fit of (3.10). For each prototype, the coefficients and quality of the polynomial fit are listed in **Table 8-19**.

$$2\zeta = \frac{1}{Q} = \frac{1}{Q_0} + \frac{\theta_{max}^{\;2}}{Q_{nl}} \tag{3.10}$$

Table 8-19: Least mean squares fit to quality factor measurement results
(*nrmse* is defined as the root mean squared error as a percentage of full-scale)

Device Name	Q_0	Q_{nl}	%*nrmse**
D1-C-100	733.9	5.29	2.19
D1-C-150	604.2	5.27	1.90
D1-NC-150	549.8	4.52	2.89
D2-C-150	280.3	0.77	3.19
D2-NC-150	186.6	0.22	2.93
D3-C-150	927.4	10.92	7.79
D3-NC-150	1017.9	12.66	0.86

8.6.3   Scan Angle Amplitude versus Drive Voltage

Drive voltage frequency sweeps were performed using the set-up described in Section 5.4 in order to analyse the micro-scanner harmonic response at different drive voltage amplitudes. The resonant micro-scanners are non-linear dynamic systems and consequently both upsweep and downsweep of the vibration frequency are necessary to characterize the bi-stable scanning response as shown in **Figure 8-47**. The resonant frequency is defined as the point where the scan angle amplitude is maximum.

The peak θ_{max} and f_s during frequency upsweep and downsweep are equal for all direct-drive prototypes at a drive voltage of 110V, which is an indication that the AVC structures remain in the engaged state during oscillation. On the other hand, peak θ_{max} is greater during upsweep when 189V is applied to D1-C-100 and D1-C-150. Peak performance during frequency upsweep is also achieved with indirect-drive designs (**Figure 8-47(e, f)**).The latter exhibits a smooth amplitude profile during frequency upsweep, which contrasts with the abrupt changes in the response of direct-drive micro-scanners. Therefore, the harmonic response of the indirect-drive micro-scanners provides drive control circuitry with a wider bandwidth for resonant frequency tracking.

The peak amplitude and corresponding frequency of all micro-mirror prototypes are given in **Table 8-20** and **Table 8-21** for two sinusoidal drive voltage amplitudes: 100V and 180V. The peak amplitude of the indirect-drive micro-scanner is 45% higher than that of an equivalent direct-drive micro-scanner albeit achieved at a lower resonant frequency. The lowest scanning performance is achieved by D2-C-150, as expected following the Q measurements of **Figure 8-44**. This may be a consequence of insufficient modal separation between the out-of-plane torsion mode and the parasitic out-of-plane piston bending mode (see **Figure 7-5b**) of the numerically-optimized design, resulting in a fraction of the electrostatic energy being diverted into the parasitic mode. Comparisons between **Figure 8-47(b, c)** and **(e, f)** indicate that the residual stresses resulting from *BlanketMetal* layer deposition influence the scanning response during drive voltage frequency sweeps. Moreover, the 0.65 μm thick metal coating results in an average reduction of 1 kHz in the resonant frequency.

Table 8-20: Results from a frequency sweep at 100 V_{pk} sinusoidal drive amplitude

Device Name	Upsweep		Downsweep		torsional modal frequency (FE Simulations)
	peak amplitude (°)	peak frequency (Hz)	peak amplitude (°)	peak frequency (Hz)	
D1-C-100	2.9	24607.3	2.9	24607.7	26055
D1-C-150	3.3	24221.3	3.3	24221.3	25692
D1-NC-150	3.5	25419.1	3.5	25419.3	26744
D2-C-150	1.5	23657.5	1.5	23652.4	25567
D2-NC-150	0.4	24587.2	0.4	24578.9	26656
D3-C-150	4.2	23649.8	3.4	23610.9	25278
D3-NC-150	4.5	24522.7	3.4	24464.4	26583

Table 8-21: Results from a frequency sweep at the intended 180 V_{pk} sinusoidal drive amplitude

Device Name	Upsweep		Downsweep	
	peak θ_{max} (°)	frequency at peak θ_{max} (Hz)	peak θ_{max} (°)	frequency at peak θ_{max} (Hz)
D1-C-100	5.5	24756.5	5.2	24731.3
D1-C-150	5.7	24341.0	5.3	24320.6
D3-C-150	8.3	23907.4	5.5	23727.8
D3-NC-150	9.2	24894.7	6.0	24639.0
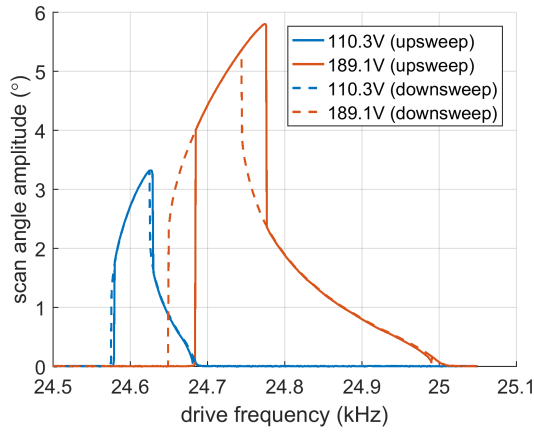
(a) D1-C-100
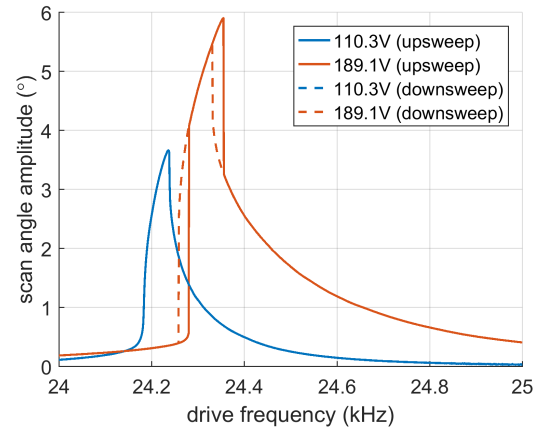
(b) D1-C-150
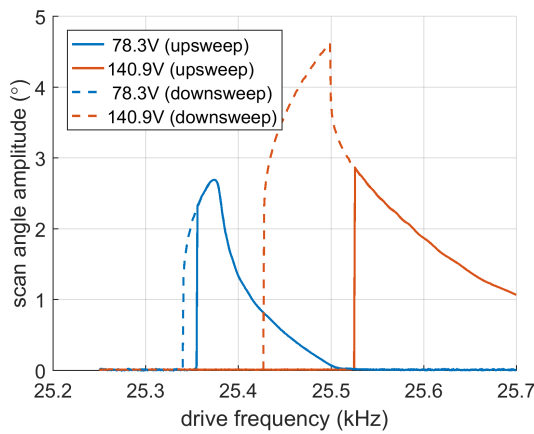
(c) D1-NC-150
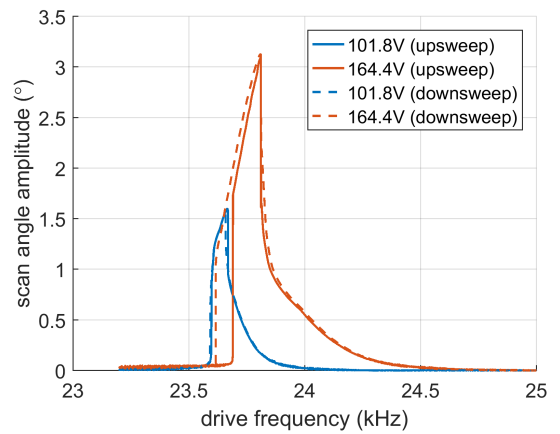
(d) D2-C-150
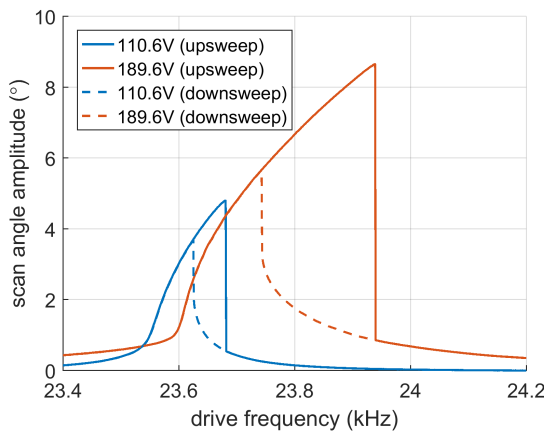
(e) D3-C-150
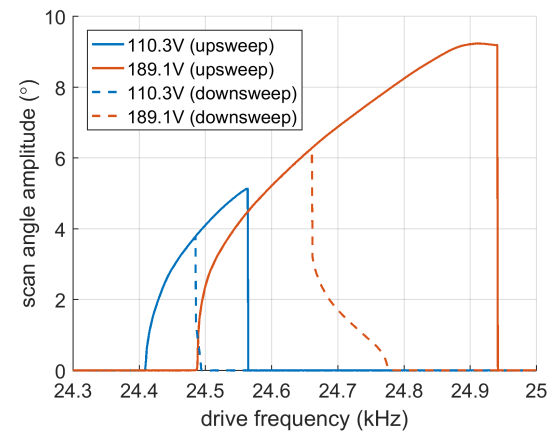
(f) D3-NC-150

Figure 8-47: Micro-scanner frequency response at different drive voltage amplitudes

189

A detailed analysis on the phase shift between the drive voltage and measured scan angle response is presented in **Figure 8-48**. The phase angle at the resonant frequency, φ_{res} is acquired for a range of drive voltage amplitudes. The theoretical maximum input energy transfer for an AVC-actuated micro-scanner occurs at φ_{res} of 45° when a sinusoidal drive signal is applied. It can be seen that the measured φ_{res} during drive frequency upsweep corresponds to the theoretical value for all three designs. Measurements show the φ_{res} remains relatively constant irrespective of the applied voltage and scan angle amplitudes.

The variation of the scan angle amplitude with drive voltage amplitude is plotted in **Figure 8-49** and **Figure 8-50**. A marginal improvement in scanning performance is achieved when f_l is increased from 100 μm to 150 μm, in-line with the electrostatic-fluidic simulation results of Section 8.4.2 as shown in **Figure 8-53**. A degradation in performance is observed due to the deposition of the metallization layer, despite exhibiting a higher Q compared to the uncoated mirror (see **Figure 8-44**). The residual stress due to the metal coating, results in a positive out-of-plane displacement of the rotating comb fingers. An initial comb finger angle alters the $dC/d\theta$ function in such a way that electrostatic energy input over one cycle is reduced. The stiffening effect as a result of the non-linear electrostatic moment can be observed in **Figure 8-51** and **Figure 8-52** through the increase in resonant frequency with input voltage.
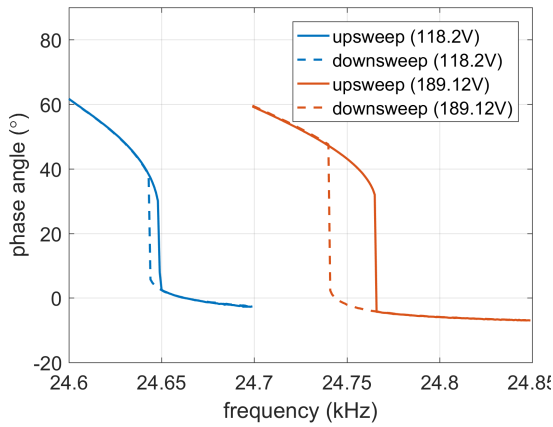
(a) D1-C-150: phase response
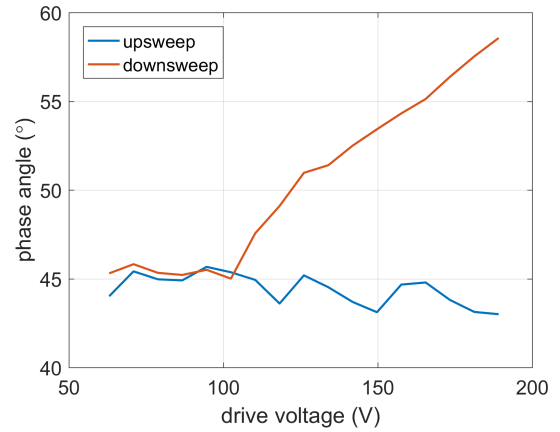
(b) D1-C-150: φ_{res} - V_d
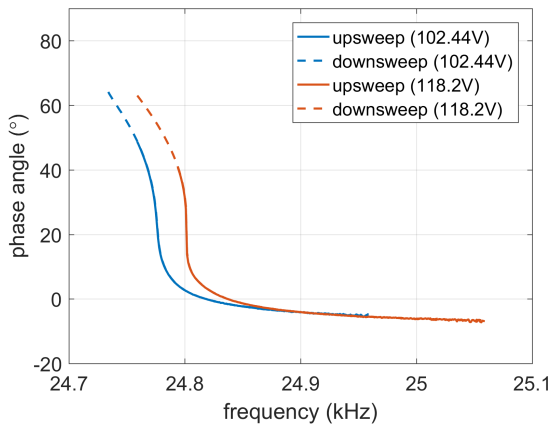
(c) D2-C-150: phase response
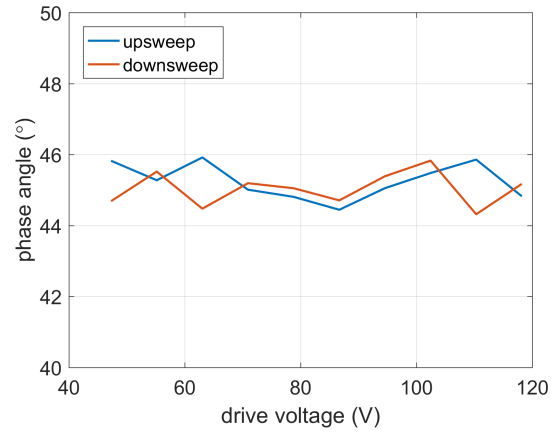
(d) D2-C-150: φ_{res} - V_d
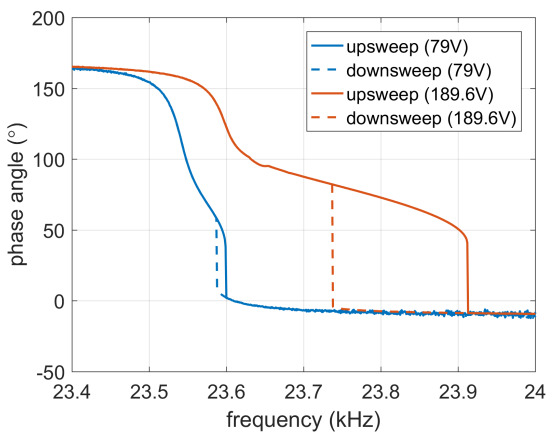
(e) D3-C-150: phase response
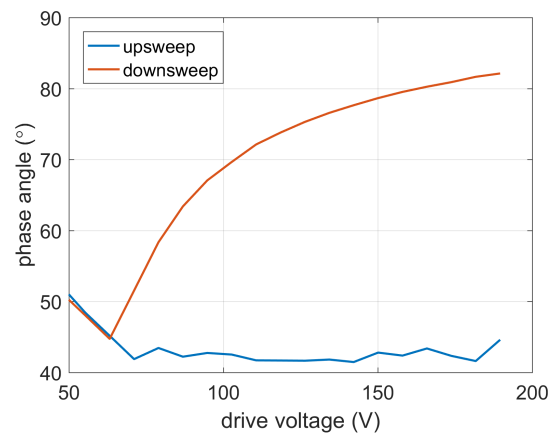
(f) D3-C-150: φ_{res} - V_d

Figure 8-48: Micro-scanner phase response and the variation of φ_{res} (the phase angle at peak θ_{max}) with drive voltage amplitude, V_d from PSD-based measurements

191
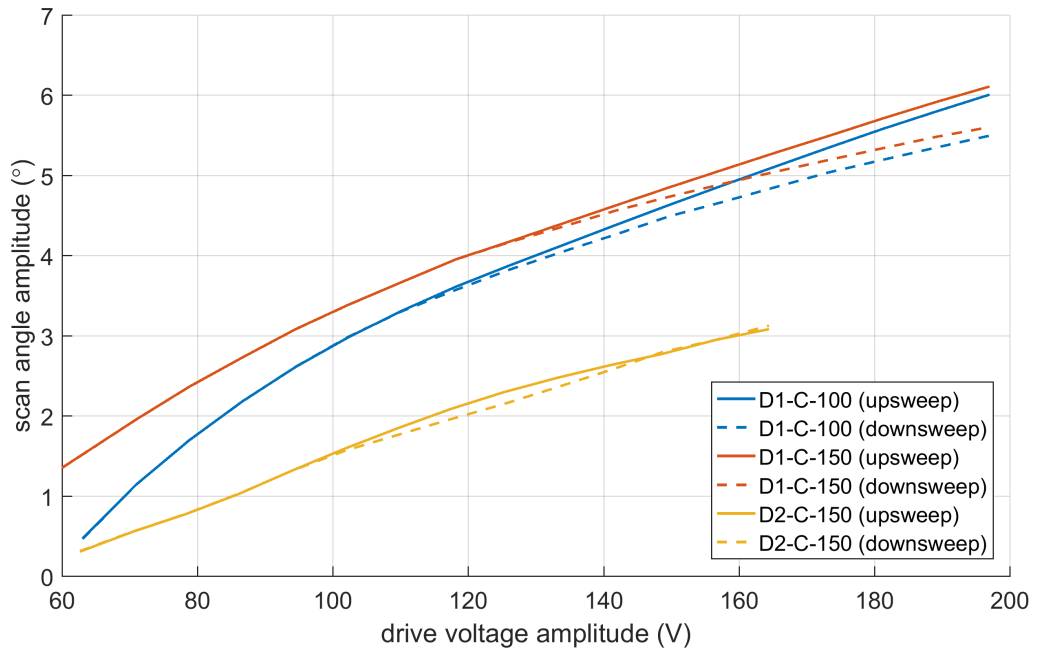
Figure 8-49: Peak micro-scanner response measurements during drive voltage frequency sweeps: a comparison among direct-drive designs
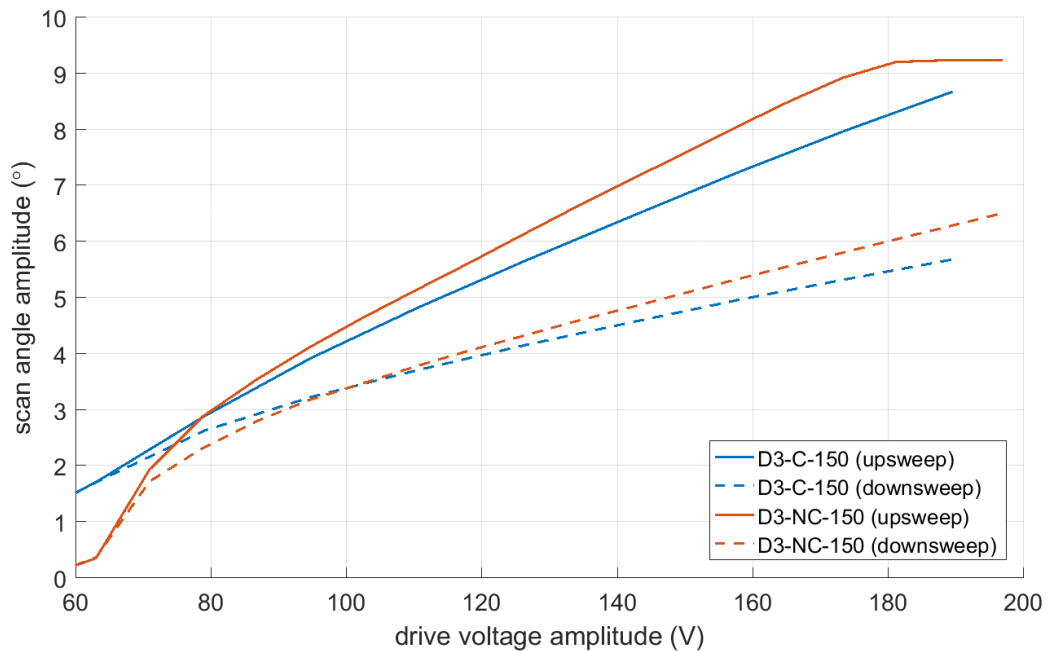
Figure 8-50: Peak micro-scanner response measurements during drive voltage frequency sweeps: a comparison between indirect-drive designs with and without the reflective metal coating
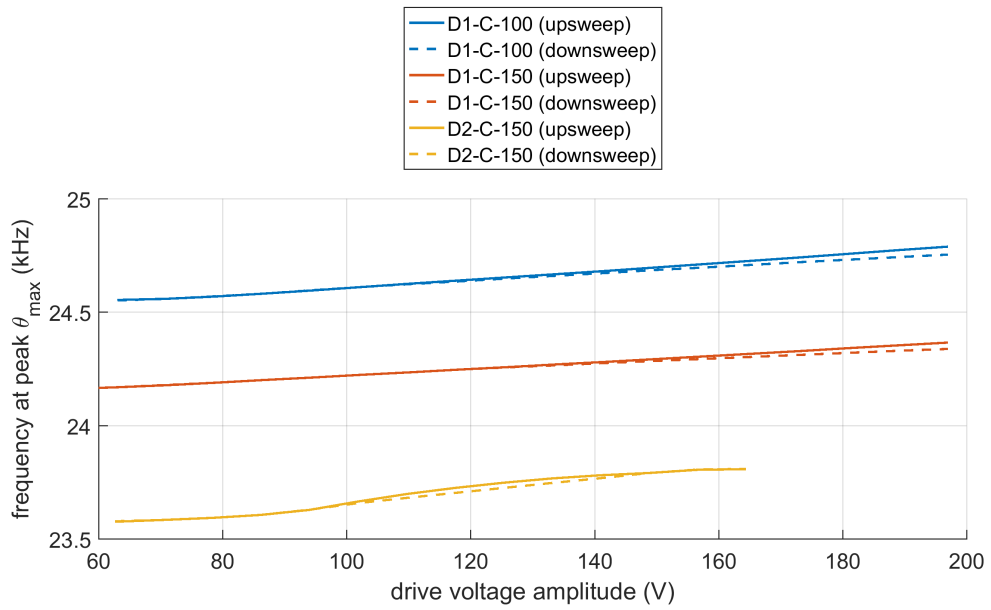
Figure 8-51: Variation of micro-scanner resonant frequency with drive voltage amplitude: a comparison among direct drive designs
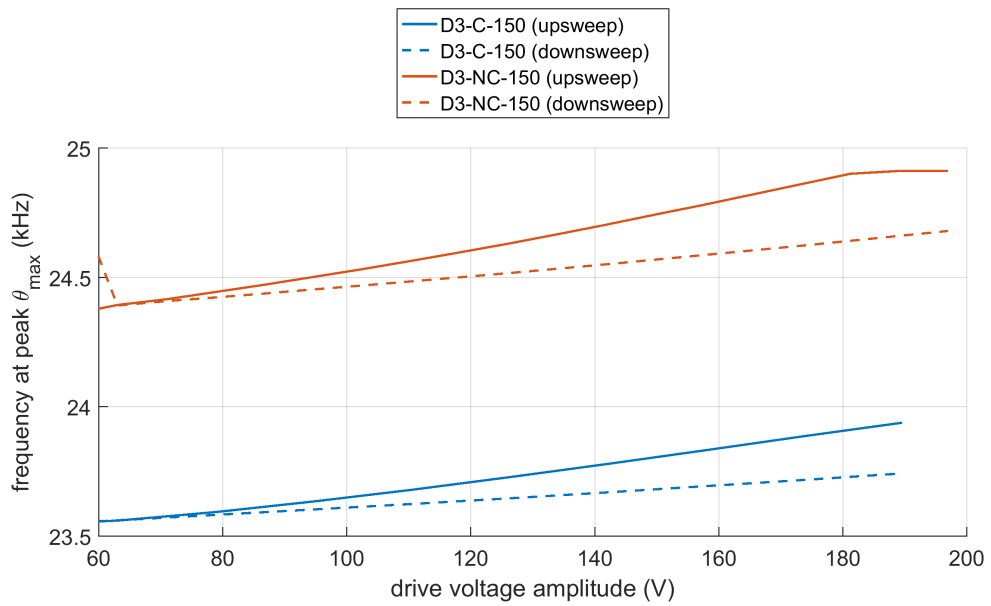
Figure 8-52: Variation of micro-scanner resonant frequency with drive voltage amplitude: a comparison between indirect-drive designs with and without the reflective metal coating

193

A comparison between simulation and measurement results is provided in **Figure 8-53** and **Figure 8-54**. Good agreement is achieved in the actuator sensitivity of all prototypes. An offset between the two sets of data, in the case of the direct-drive micro-scanners may originate from the discrepancy between the simulated and measured Q values shown in **Figure 8-46**. Improved correlation between the numerical and experimental results of **Figure 8-54** validate the electrostatic energy predictions obtained from FE electrostatic simulations.
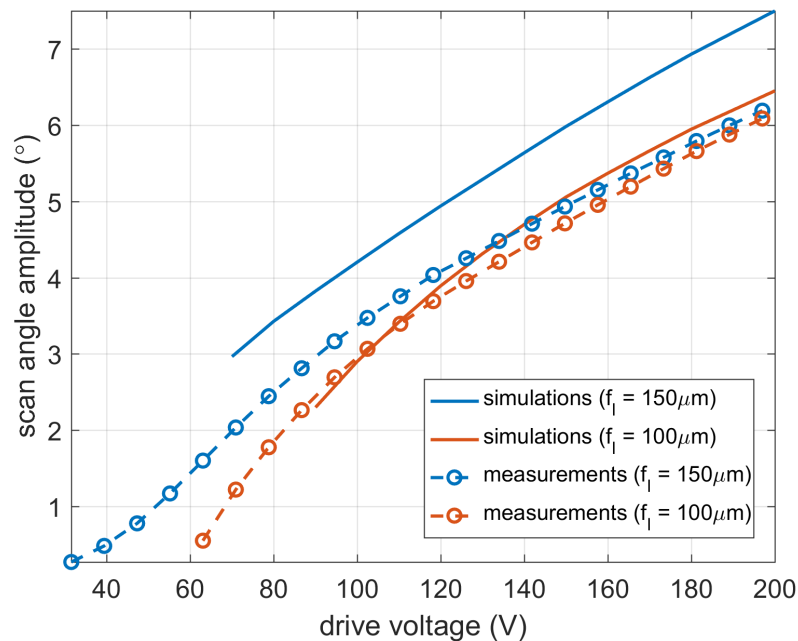
Figure 8-53: Performance comparison between D1-C-150 and D1-C-100 micro-scanners deduced from electrostatic/fluid dynamic simulations and PSD-based measurements

Up to this point, only a sinusoidal voltage input has been considered to evaluate the micro-mirror scanning efficiency. However such a waveform does not maximize the available electrostatic force generated by an oscillating AVC structure [72]. This can only be achieved by applying a unipolar square waveform at twice the micro-scanner's resonant frequency such that maximum voltage is applied during the recoil phase of the mirror oscillation. The increase in scanning efficiency with a square voltage signal is demonstrated from both simulation and measurement results as shown in **Figure 8-54**.
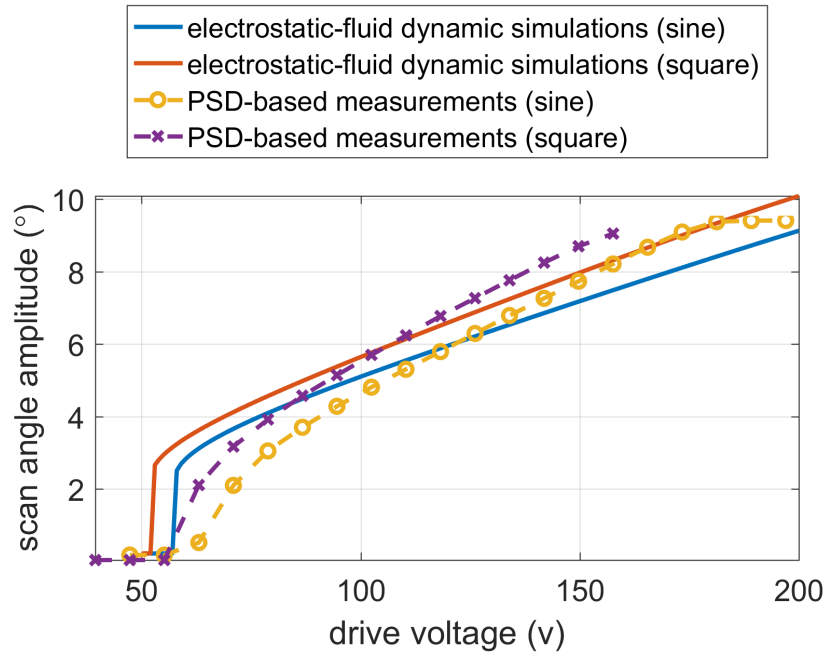
Figure 8-54: D3-C-150 micro-scanner efficiency deduced from electrostatic/fluid dynamic simulations and PSD-based measurements: a comparison between applied sinusoidal and square-wave drive voltages

In order to assess the amplification factor *A*, between the mirror plate and outer frame angles, of the indirect-drive micro-scanners, a laser beam was directed onto the outer frame and its harmonic response was measured using the PSD. A long frequency sweep was performed to verify whether the scan angle amplitude of the outer frame corresponds to that of the mirror plate at the in-phase torsional mode (depicted in **Figure 8-14(a)**). **Figure 8-55** displays the input drive frequencies, which correspond to the first four mode shapes of the indirect-drive micro-scanner design. All resonant modes of **Figure 8-14** were verified using stroboscopic microscope imaging. The amplification factor is deduced from the ratio in peak amplitude response between the mirror plate and outer frame at the intended out-of-phase torsional mode (mode 4). **Table 8-22** demonstrates good agreement between FE modal analysis and PSD-based optical measurements. Moreover, results indicate that the deposition of the reflective coating degrades the mechanical amplification obtained from the indirect-drive concept.
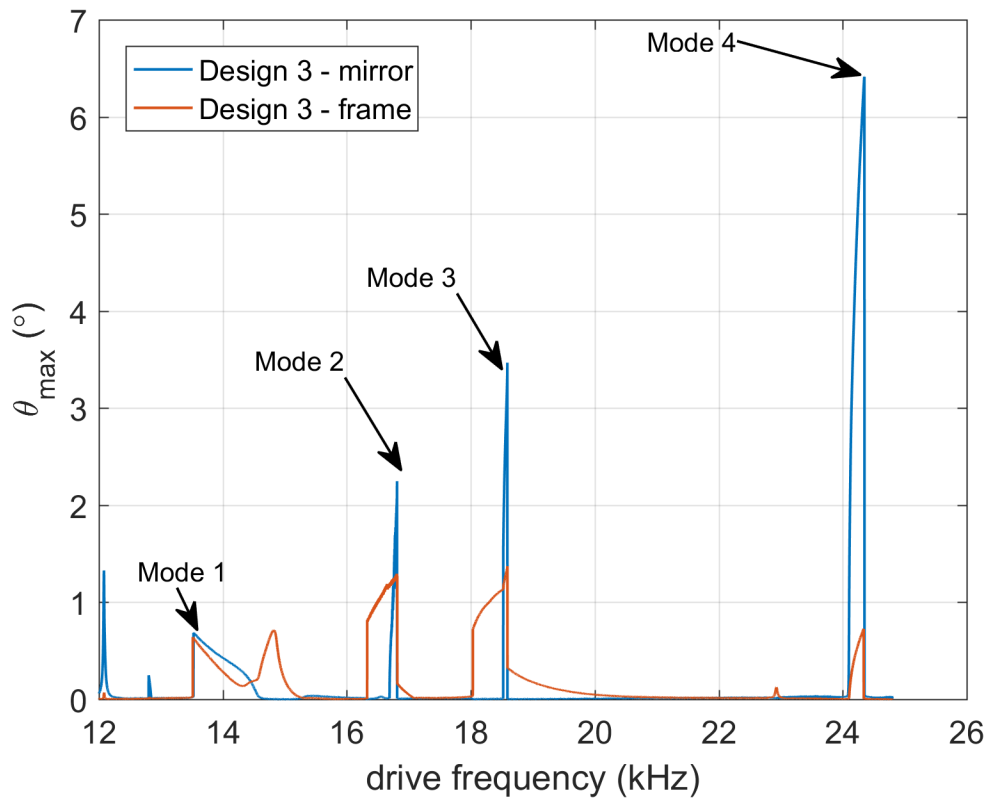
Figure 8-55: Comparison of the mirror plate and outer frame frequency responses at a $141V_{pk}$ sinusoidal drive voltage (D3-C-150)

Table 8-22: Simulated and measured amplification factor of the indirect-drive micro-scanner design (D3)

Device	D3-150-C	D3-150-NC	
Result set	FE simulations	FE simulations	Measurements
Amplification factor, A	9.04	10.20	8.82

9   CONCLUSIONS, RESEARCH OUTCOMES AND RECOMMENDATIONS

In this dissertation, an in-depth analysis was presented on the multi-physical characteristics of high performance resonating micro-scanners. Numerical models were developed and measurement techniques were set up in order to investigate the structural, fluidic and electrostatic properties of such devices. The numerical simulation methods were experimentally validated using a resonating micro-scanner provided by STM. The structural properties of the micro-mirror torsional beams were evaluated in Chapter 3. In Chapter 4, the electrostatic torque generated by an AVC actuator was analysed through the simulation and measurements of the capacitance change with scan angle amplitude. Experimentally-validated transient Navier-Stokes simulations of the air damping in resonating micro-scanners were presented in Chapter 5. Design solutions for the minimization of micro-mirror dynamic deformation were evaluated in Chapter 6 using FE simulations. A design optimization scheme based on FE and CFD numerical simulations was proposed in Chapter 7 in order to maximize the electro-mechanical performance of a resonating micro-scanner. The design optimization scheme was implemented in Chapter 8 to design three micro-scanner layouts which were fabricated using the SOIMUMPs MPW process.

The scanning performance plot of **Figure 9-1** demonstrates that the indirect-drive micro-scanner design ($D3$) is suitable for projection display applications with SVGA resolution requirements. A superior $\theta_{max}.D.f_s$ product (at a $V_d = 200V$) is achieved with $D3,$ in comparison to the electrostatic micro-scanner designs, reported in literature, which are fabricated from a device layer thickness of less than 30 μm. Higher performance electrostatic micro-scanners have been reported, however these utilise a device layer thickness which is significantly greater than 30 μm. Additionally, measurements demonstrate that the optimized gimbal-framed design leads to an 80% reduction in the dynamic deformation of a circular mirror plate. The main research outcomes from this work are discussed in Section 9.1 while recommendations for future work are presented in Section 9.2.
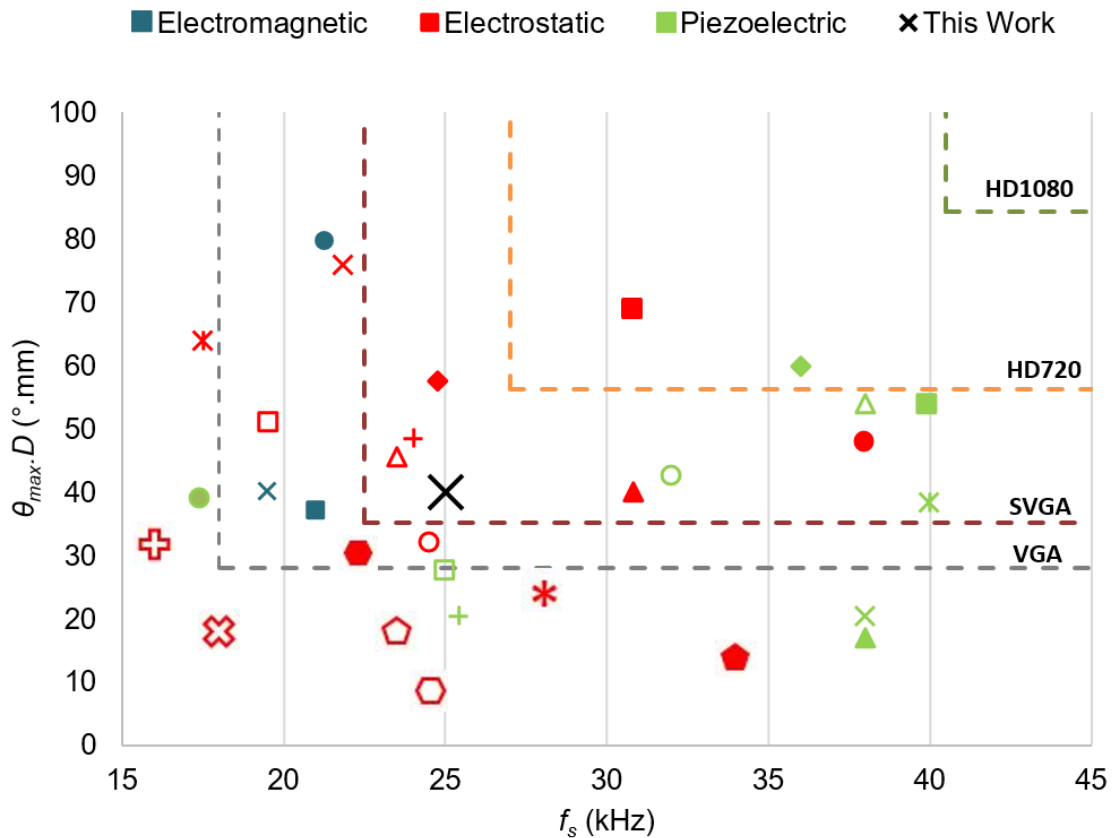
Figure 9-1: Comparison of scanning characteristics between design *D3* and the highest performing resonating micro-mirrors reported in literature (refer to **Table 2-2**)

9.1 Research Outcomes

In this section, a summary of all the novel results which were discussed in Chapters 3-8 is provided. The research outcomes are grouped according to the following sub-sections: (i) electrostatic and structural analyses, (ii) dynamic deformation, (iii) air damping and (iv) design, fabrication and testing.

9.1.1 Electrostatic and Structural Analyses

a. The development of FE models is essential for the evaluation of the scanning frequency, modal frequency separation, maximum torsional beam stress and dynamic deformation as part of the design optimization process of high performance resonating micro-scanners. The implemented finite element type will have an impact on the computational efficiency of the design optimization scheme and the accuracy of the structural simulation results. The selection of the appropriate finite element in resonant micro-scanners largely depends on the aspect ratio of the torsional beam members.

b.   Non-linearity in the torsional beam stiffness of a scanning micro-mirror can be investigated using the proposed micro-force probing method. However prior checks are necessary to ensure that the measurement accuracy is not compromised by lateral bending and slip of the micro-force probe. Minor modifications can be implemented to the micro-scanner prototypes in order to facilitate the force and displacement measurement acquisition.

c.   The issues related to parasitic capacitances and low signal-to-noise ratios encountered in dynamic capacitance measurement techniques can be overcome by the proposed static capacitance measurement technique. Static measurements obtained from micro-force probe actuation and a high precision LCR meter read-out can be a useful tool to validate the accuracy of theoretical and numerical capacitance calculations of AVC structures.

9.1.2   Dynamic Deformation

a.   FE simulations demonstrated that the dynamic deformation of representative scanning micro-mirror designs is not accurately described using one-dimensional classical bending theory. An analytical equation has been proposed, based on combined 2-D plate bending and twist theory, for the dynamic deformation predictions of rectangular mirror plates with a conventional torsional beam configuration. The improved accuracy was verified for a range of mirror plate aspect ratios using FE simulations.

b.   A limited improvement in micro-mirror dynamic flatness has been attained from the consideration of a number of non-rectangular mirror plate geometries. It was demonstrated that the introduction of a gimbal-type support structure is the most effective method to substantially reduce dynamic deformation in high performance micro-scanners fabricated from a single silicon layer. The gimbal-type support structure refers to a design feature which uncouples the twist present in the torsional beams from the out-of-plane rotation of the mirror plate. The effectiveness of gimbal-type support structures in reducing dynamic deformation of single-layer micro-scanners was confirmed from Laser Doppler Vibrometer measurements and FE simulations. The optimal geometric configuration of such a support structure is dependent on the micro-scanner layout and dimensions. A

δ_{rms} reduction of around 20% was obtained in a 1 mm circular mirror plate when an optimized gimbal-type structure is introduced in the design.

c. Optimized gimbal-frame design configurations have been established to minimize dynamic deformation in 1 mm circular mirror plates. It was observed that the optimum configuration consists of a total of four links connecting the gimbal-type structure to the mirror plate. This is valid for single torsion beam type designs and for a device layer thickness ranging from 25 μm to 65 μm.

9.1.3   Air Damping

a. In-depth air damping analysis of electrostatically-actuated micro-scanners was performed using transient N-S simulation results in ANSYS Fluent. The overall system damping was deduced by developing separate CFD models for the AVC structure and the mirror plate. The *sliding mesh* method and the *dynamic mesh* method were implemented in the AVC structure and mirror plate models respectively as part of the aim of developing computationally efficient N-S simulations, without comprising on solution accuracy. The numerical results were successfully validated against Q-θ_{max} measurements performed on a resonant micro-scanner test case using a custom-built PSD-based measurement system. Numerical verification analyses demonstrate that the less computationally-intensive *sliding mesh* method can be considered for mirror plate damping simulations with $\theta_{max}.R/h$ ratios lower than $\pi/12$. Moreover, the method of deducing the overall micro-scanner damping using separate CFD models for the AVC structure and mirror plate is not recommended in the case of designs where the AVC structures are located on the edges of the mirror plate itself.

b. The amplitude-dependent damping losses resulting from the out-of-plane oscillations of AVC structures can be accurately predicted from three-dimensional transient N-S simulations using the *sliding mesh* method. The pressure drag moment acting on the rotating comb finger is not negligible, thus rendering the analytical Couette flow model not suitable for the evaluation of AVC structure damping. On the other hand, the three-dimensional Stokes model is only valid for very small amplitudes: $\theta_{max} < 1°$.

c. Transient N-S simulations indicate that aerodynamic pressure drag acting on the mirror plate is the predominant damping mechanism in high performance resonating micro-scanners even in the case where actuation is performed using

electrostatic AVC structures. The air flow surrounding a circular plate oscillating in out-of-plane rotation, is characterised by the periodic development and dissipation of strong vortices emanating from the plate edges. The viscous fluid shear moment is a negligible fraction of the overall aerodynamic moment acting on the mirror plate. On the other hand, the moment resulting from the dynamic fluid pressure acting on the AVC structure is significant and has to be considered during the computation of the overall energy dissipation.

d. Transient N-S simulations confirmed that the aerodynamic drag on a circular plate is proportional to θ_{max}^2 within the typical operating region of high performance resonating micro-scanners: $200 < Re_m < 2300$. This implies that the air damping in high performance micro-scanners is highly non-linear. Mirror plate damping can, in general, be described by the form drag equation for high frequency and amplitude oscillations. On the other hand, the unsteady Stokes flow equation is only valid for high frequency oscillations at very low amplitudes $\theta_{max} < 1°$.

e. Consequently, a drag damping moment equation was proposed for millimetre-sized circular plates oscillating in out-of-plane rotation, whereby an expression for the drag coefficient as a function of Re_m was deduced from an extensive parametric evaluation exercise using transient N-S simulations. Apart from f_s, θ_{max} and R, the effect of the plate thickness, t_m and the underlying cavity depth, h on the drag coefficient were evaluated. It was demonstrated that damping losses increase with reduced t_m and h.

f. A numerical model was proposed for the analysis of aerodynamic pressure drag acting on the mirror plate and outer frame of an indirect-drive micro-scanner design. A fluid-structural one-way coupled model was developed in ANSYS whereby the instantaneous displacement deduced from a FE model of the oscillating structure is transferred to a CFD model of the fluid flow surrounding the same structure in order to update the boundary surface displacement of the dynamic mesh. The transient N-S simulation results were successfully validated against Q measurements of the fabricated indirect-drive micro-scanner design *D3*.

9.1.4 Design, Fabrication and Testing

a. A design optimization scheme has been proposed for high performance resonating micro-scanners on the basis of dynamic deformation, torsion beam stress, scanning frequency, air damping and scanning efficiency ($= \theta_{max}/V_d$). The design

201

optimization is applicable to single-layer micro-scanner designs which incorporate a gimbal-type structure and are actuated using electrostatic AVC structures.

b. Dynamic deformation can be integrated in a multi-physics design optimization scheme for high performance micro-scanners. The most computationally-efficient method for the evaluation of dynamic deformation in direct-drive designs is to perform static structural FE simulations and apply the maximum inertial load to the micro-scanner body which is equal to $\omega_s^2.\theta_{max}$.

c. The electrostatic and damping characteristics of AVC structures lying on a curved path were investigated as part of the optimization process for the direct-drive designs, *D1* and *D2.* Electrostatic FE and transient N-S simulation results demonstrate that a non-linear relationship exists between the scanning efficiency and the maximum distance of the AVC structure from the micro-scanner's rotational axis (f_r). This implies that for particular micro-scanner designs, no improvement in the scanning efficiency is achieved by increasing the number of comb fingers along the curved mirror plate edge beyond a certain value of f_r.

d. Three designs of high performance one-directional resonating micro-scanners were fabricated using the SOIMUMPs process. Measurements demonstrated that although the process is limited to a device layer thickness of 25 μm, dynamic deformation and scanning efficiency on par with the state-of-the-art in electrostatic micro-scanners can be achieved by incorporating an optimized gimbal-type structure and the indirect-drive concept.

e. The fabrication of three micro-scanner designs with and without a reflective metal coating provided a detailed assessment of the post-released stress state of the SOIMUMPs process stack, namely the through-thickness stress gradient in the doped-Si layer and the residual stress in the metallization layer. An equivalent residual stress value for the pre-fabrication predictions of the process-related out-of-plane curvature in *BlanketMetal*-coated devices was also deduced.

f. A detailed analysis on the effect of the SOIMUMPs *BlanketMetal* coating on the micro-scanner performance was presented. From a comparison of the measurement results of the coated and uncoated micro-scanners, the impact of the *BlanketMetal* layer on the following performance indicators were deduced: scanning frequency, quality factor, scanning efficiency and the amplification factor in indirect-drive micro-scanners.

9.2   Recommendations

After summarizing the main outcomes from this research work, a list of recommendations for future work is provided in this section:

1) A drag moment equation for circular mirror plates with respect to f_s, θ_{max}, and R was proposed. However, t_m and h were found to have a non-negligible impact on C_d. An exhaustive parametric analysis is necessary to fully investigate the dependence of C_d on inter-relations between all the mentioned parameters for a wide range of Re flows.

2) The measurement validation results of designs *D1* and *D2* damping simulations indicated that when the AVC structure is directly connected to the boundary edges of the mirror plate, the overall micro-scanner damping is not accurately deduced without considering the mutual impact between the mirror plate and the electrostatic actuator. For this reason, further analysis is required to determine an efficient method of how micro-scanner damping can be accurately predicted without simulating the entire AVC structure and the mirror plate in one CFD model.

3) The proposed gimbal-frame structure supporting the mirror plate has been proposed and optimized with the aim of minimizing dynamic deformation. Although the structure has been considered in the damping simulations, its impact on E_{loss} and Q has not been investigated. While it can be assumed that damping losses increase with the introduction of the gimbal-frame, the air gap between the gimbal-frame and the mirror plate (referred to as the gimbal-mirror link length) is expected to alter the flow development around the oscillating structure. Therefore, optimal values for the gimbal frame width and the link length, can be deduced with the objective of minimizing both dynamic deformation and the damping loss. From this analysis, it can be determined whether the gimbal-frame structure can be purposely introduced to reduce the mirror plate drag.

4) In-depth analysis of the effect of several dimensions and operating parameters on micro-scanner damping has been presented. N-S simulations demonstrated that the aerodynamic moment acting on the oscillating mirror plate is dominated by the added inertia component. Results show that at $\theta_{max} = 12°$ and $f_s = 25$ kHz, the added inertia of D3-C-150 is approximately 0.25% of I which translates into a non-negligible frequency reduction of 32 Hz. Therefore although the damped

frequency of oscillation can be assumed to be equal to the natural frequency at the measured Q values, the added inertia effect on the resonant frequency needs to be considered. Further investigation is necessary to determine the dependence of the added inertia moment on f_s, θ_{max}, R, t_m and h.

5) Chapter 8 exposes the limitations of acquiring dynamic deformation measurements using laser Doppler vibrometry. While an upgraded version of the Polytec MSA-500 is currently available (MSA-600) [150], allowing for the measurement of higher vibration velocities and improved displacement resolution, other measurement techniques can be investigated: stroboscopic scanning white light interferometry and the static-slit profiling method [95].

6) An analytical expression for the dynamic deformation of rectangular micro-mirror plates was deduced from classical plate theory by considering the combined effect of bending and twisting moments. A similar expression can be derived for circular mirror plates.

7) Where possible, the mutual interactions among all physical domains (electrostatic, fluidic and structural) were neglected due to the significant computational resources necessary to perform fully coupled transient FE and N-S simulations. The damping and electrostatic moments are, in general, weakly coupled to the structural dynamic deformation allowing for a rigid body representation of the structure in electrostatic and fluidic simulations. However, with this technique the following effects are not taken into consideration:

   a. initial out-of-planarity of the rotating comb fingers due to the static mirror deformation, which was later observed to be significant in the SOIMUMPs prototypes from interferometric measurements;

   b. dynamic deformation of the oscillating structures (mirror plate, gimbal frame and outer frame) induced by the periodic aerodynamic pressure loading.

Analysis of these phenomena entail structural-electrostatic FE simulations and transient fluid-structural interaction simulations with two-way coupling.

8) Non-linear structural, electrostatic and fluid characteristics of an AVC-actuated resonating micro-scanner have been deduced from experimentally-validated simulations. These findings enable the implementation of the Duffing-Mathieu-van-der-Pol dynamic model (given in (2.19)) for the computation of the non-linear

204

harmonic frequency response and transient analysis of such systems. The availability of more accurate system-level models is beneficial in the design and simulation process of micro-scanner drive and feedback control circuitry.

REFERENCES

[1]   P. R. Patterson, D. Hah, M. Fujino, W. Piyawattanametha and M. C. Wu, "Scanning micromirrors: An overview," *Proc. SPIE 5604, Optomechatronic Micro/Nano Components, Devices, and Systems,* pp. 195-207, 2004.

[2]   A. Wolter, H. Schenk, E. Gaumont and H. Lakner, "The MEMS micro scanning mirror for barcode reading: from development to production," *Proc. SPIE 5348, MOEMS Display and Imaging Systems II,* pp. 32-39, 2004.

[3]   Y. Wang, M. Ray, H. McGuff, G. Bhave, B. Yang, T. Shen and X. Zhang, "Portable oral cancer detection using a miniature confocal imaging probe with a large field of view," *Journal of Micromechanics and Microengineering,* vol. 22, no. 6, 2012.

[4]   J. Liu, M. Mandella, N. Loewke, H. Haeberle, H. Ra, W. Piyawattanametha, O. Solgaard, G. Kino and C. Contag, "Micromirror-scanned dual-axis confocal microscope utilizing a gradient-index relay lens for image guidance during brain surgery," *Journal of Biomedical Optics,* vol. 15, no. 2, 2010.

[5]   A. Hung, H. Lai, T. Lin, S. Fu and M. Lu, "An electrostatically driven 2D micro-scanning mirror with capacitive sensing for projection display," *Sensors and Actuators A: Physical,* no. 222, pp. 122-129, 2015.

[6]   C.-D. Chen, Y.-J. Wang and P. Chang, "A novel two-axis MEMS scanning mirror with a PZT actuator for laser scanning projection," *Optics Express,* vol. 20, no. 24, pp. 27003-27017, 2012.

[7]   C. Fan and S. He, "Micromirror based virtual image automotive head-up display," *Microsystem Technologies,* vol. 22, pp. 1-6, 2016.

[8]   E. Pengwang, K. Rabenorosoa, M. Rakotondrabe and N. Andreff, "Scanning Micromirror Platform Based on MEMS Technology for Medical Application," *Micromachines,* vol. 7, no. 24, 2016.

[9]   G. Silva, F. Carpignano, F. Guerinoni, S. Costantini, M. D. Fazio and S. Merlo, "Optical Detection of the Electromechanical Response of MEMS Micromirrors Designed for Scanning Picoprojectors," *IEEE Journal of Selected Topics in Quantum Electronics,* vol. 21, no. 4, 2015.

[10] R. Ben-Mrad and D. Pasiliao, " A MEMS Micromirror Based Head-Up Display System," in *Symposium on Design Test Integration and Packaging of MEMS and MOEMS*, Montpeiller, 2015.

[11] L. Ye, G. Zhang and Z. You, "Large-Aperture kHz Operating Frequency Ti-alloy Based Optical Micro Scanning Mirror for LiDAR Application," *Micromachines,* vol. 8, no. 120, 2017.

[12] V. Milanović, A. Kasturi, J. Yang and F. Hu, "Closed-Loop Control of Gimbal-less MEMS Mirrors for Increased Bandwidth in LiDAR Applications," in *SPIE Conference on Laser Radar Technology and Applications XXII*, Anaheim, 2017.

[13] F. Senger, T. Wantoch, M. C, J. Janes, U. Hofmann, B. Wagner and W. Benecke, "MEMS scanning mirrors for high power laser display and lighting applications," in *4th Laser Display and Lighting Conference*, Yokohama, 2015.

[14] G. Kloppenburg, A. Wolf and R. Lachmayer, "High-resolution vehicle headlamps: technologies and scanning prototype," *Advanced Optical Technologies,* vol. 5, no. 2, pp. 147-155, 2016.

[15] K. Hwang, Y. Seo and K. Jeong, "Microscanners for optical endomicroscopic applications," *Micro and Nano Systems Letters,* vol. 5, no. 1, 2017.

[16] T. Bieniek, "Lab4MEMSII Micro-Optical MEMS, micro-mirrors and pico-projectors," [Online]. Available: http://www.lab4mems2.ite.waw.pl/demonstrators.html. [Accessed 10 12 2019].

[17] R. Bogue, "MEMS Laser Scanners in Automotive Head-up Displays," 22 7 2013. [Online]. Available: https://www.novuslight.com/mems-laser-scanners-in-automotive-head-up-displays_N1400.html. [Accessed 10 12 2019].

[18] I. Underwood, "Introduction to Microdisplays," in *Handbook of Visual Display Technology*, Springer Heidelberg, 2012, pp. 2034 - 2044.

[19] S. Holmstrom, U. Baran and H. Urey, "MEMS Laser Scanners: A Review," *Microelectromechanical Systems,* vol. 23, no. 2, pp. 259-275, 2014.

[20] C. Liao and J. Tsai, "The Evolution of MEMS Displays," *IEEE Transactions on Industrial Electronics,* vol. 56, no. 4, pp. 1057 - 1065, 2009.

[21] V. Duma and A. Podoleanu, "Polygon mirror scanners in biomedical imaging: a review," in *Optical Components and Materials*, San Francisco, 2013.

[22] G. Reddy and P. Saggau, "Fast three-dimensional laser scanning scheme using acousto-optic deflectors," *Journal of Biomedical Optics,* vol. 10, no. 6, p. 064038, 2005.

[23] J. Xie, S. Huang, Z. Duan, Y. Shi and S. Wen, "Correction of the image distortion for laser galvanometric scanning system," *Optics and Laser Technology,* vol. 37, no. 4, pp. 305-311, 2005.

[24] H. Urey, D. W. Wine and J. R. Lewis, "Scanner design and resolution tradeoffs for miniature scanning displays," in *IS&T/SPIE Conference on Flat Panel Display Technology*, San Jose, 1999.

[25] M. Freeman, M. Champion and S. Madhavan, "Scanned Laser Pico-Projectors: Seeing the Big Picture (with a Small Device)," *Optics & Photonics News,* pp. 28-34, May 2009.

[26] J. Grahmann, M. Wildenhain, T. Grasshoff, C. Gerwig, H.-G. Dallmann, A. Wolter and H. Schenk, "Laser projector solution based on two 1-D resonant scanning micro mirrors assembled in a low vertical distortion scan head," in *MOEMS and Miniaturized Systems XI*, San Francisco, 2012.

[27] W. Du, G. Zhang and L. Ye, "Image Quality Analysis and Optical Performance Requirement for Micromirror-Based Lissajous Scanning Displays," *Sensors,* vol. 16, no. 675, 2016.

[28] U. Hofmann, M. Oldsen, H.-J. Quenzer, J. Janes, M. Heller, M. Weiss, G. Fakas, L. Ratzmann, E. Marchetti, F. D'Ascoli, M. Melani, L. Bacciarelli, E. Volpi and F. Battini, "Wafer-level vacuum packaged micro-scanning mirrors for compact laser projection displays," *Proc. SPIE 6887,* 2008.

[29] K.-U. Roscher, H. Grätz, H. Schenk, A. Wolter and H. Lakner, "Low cost projection device with a 2-dimensional resonant microscanning mirror," *Proc. SPIE Vol. 5348, MOEMS Display and Imaging Systems II,* pp. 22-31, 2004.

[30] A. Geiger, J. Newman, S. Sreehari, S. Sullivan, C. Bouman and G. Simpson, "Sparse sampling image reconstruction in Lissajous trajectory beam-scanning multiphoton microscopy," in *High-Speed Biomedical Imaging and Spectroscopy: Toward Big Data Instrumentation and Management*, San Francisco, 2017.

[31] H. Zappe , Fundamentals of Micro-optics: Technology, devices and applications, Cambridge: Cambridge University Press, 2010.

[32] H. Urey, D. Wine and T. Osborn, "Optical performance requirements for MEMS-scanner based microdisplays," in *MOEMS and Miniaturized Systems Conference*, Santa Clara, 2000.

[33] C. Tsai, C. Tsai, H. Chang, S. Liu and J. Tsai, "Electrothermally-Actuated Micromirrors with Bimorph Actuators - Bending-type and Torsion-Type," *Sensors,* vol. 15, pp. 14745-14756, 2015.

[34] Y. Eun, H. Na, J. Choi, J. Lee and J. Kim, "Angular vertical comb actuators assembled on-chip using in-plane electrothermal actuators and latching mechanisms," *Sensors and Actuators A: Physical,* vol. 165, pp. 94-100, 2011.

[35] D. W. Wine, M. P. Helsel, L. Jenkins, H. Urey and T. D. Osborn, "Performance of a Biaxial MEMS-Based Scanner for Microdisplay Applications," *Proc. SPIE Vol. 4178, MOEMS and Miniaturized Systems,* pp. 186-196, 2000.

[36] R. Schroedter, T. Sandner, K. Janschek, M. Roth and C. Hruschka, "Real-time closed-loop control for micro-mirrors with quasistatic comb drives," *Proc. of SPIE,* vol. 9760, p. 976009, 2016.

[37] R. A. Conant, J. T. Nee, K. Y. Lau and R. S. Muller, "A Flat High-Frequency Scanning Micromirror," in *Solid-State Sensor and Actuator Workshop*, Hilton Head , 2000.

[38] J. Cho, Y. Park, Y. Ko, B. Lee, S. Kang, S. Chung, W. Choi, Y. Cho, S. Chang, J. Lee and J. Sunu, "Electrostatic 1D Micro Scanner with Vertical Combs for HD Resolution Display," *Proc. SPIE Vol. 6466, MOEMS and Miniaturized Systems VI,* 2007.

[39] Y.-C. Ko, J.-W. Cho, Y.-K. Mun, H.-G. Jeong, W. K. Choi, J.-W. Kim, Y.-H. Park, J.-B. Yoo and J.-H. Lee, "Eye-type scanning mirror with dual vertical combs for laser display," *Sensors and Actuators A,* vol. 126, no. 1, pp. 218-226, 2006.

[40] P. R. Patterson, D. Hah, H. Nguyen, H. Toshiyoshi, R. Chao and M. C. Wu, "A Scanning Micromirror with Angular Comb Drive Actuation," in *Micro Electro Mechanical Systems*, Las Vegas, 2002.

[41] Y. Eun, J. Kim and L. Lin, "Resonant-frequency tuning of angular vertical comb-driven microscanner," *Micro and Nano Systems Letters,* vol. 2, no. 4, 2014.

[42] J. Kim and L. Lin, "Electrostatic scanning micromirrors using localized plastic deformation of silicon," *Journal of Micromechanics and Microengineering,* vol. 15, pp. 1777-1785, 2005.

[43] H. Zuo, F. H. Nia and S. He, "SOIMUMPs micromirror scanner and its application in laser line generator," *Journal of Micro/Nanolithography, MEMS, and MOEMS,* vol. 16, no. 1, 2017.

[44] S. Hsu, T. Klose, C. Drabe and H. Schenk, "Fabrication and characterization of a dynamically flat high resolution micro-scanner," *Journal of Optics: Pure and Applied Optics,* vol. 10, no. 4, 2008.

[45] J. Kim, H. Jeong, S. Lee, C. Ji and J. Park, "Electromagnetically actuated biaxial scanning micromirror fabricated with silicon on glass wafer," *Microsystem Technologies,* vol. 23, pp. 2075-2085, 2017.

[46] T.-L. Tang, C.-P. Hsu, W.-C. Chen and W. Fang, "Design and implementation of a torque-enhancement 2-axis magnetostatic SOI optical scanner," *Journal of Micromechanics and Microengineering,* vol. 20, 2010.

[47] A. D. Yalcinkaya, H. Urey, D. Brown, T. Montague and R. Sprague, "Two-Axis Electromagnetic Microscanner for High Resolution Displays," *Journal of Microelectromechanical Systems,* vol. 15, no. 4, pp. 786 - 795, 2006.

[48] A. Cho, A. Han, S. Ju, H. Jeong, J. Park, I. Kim, J. Bu and C. Ji, "Electromagnetic biaxial microscanner with mechanical amplification at resonance," *Optics Express,* vol. 23, no. 13, pp. 16792-16802, 2015.

[49] D. Raboud, T. Barras, F. L. Conte, L. Fabre, L. Kilcher, F. Kechana, N. Abele and M. Kayal, "MEMS Based Color-VGA Micro-Projector System," in *Eurosensors XXIV*, Linz, 2010.

[50] M. Tani, M. Akamatsu, Y. Yasuda, H. Fujita and H. Toshiyoshi, "A combination of fast resonant mode and slow static deflection of SOI-PZT actuators for MEMS image projection display," in *International Conference on Optical MEMS and their Applications*, Big Sky, 2006.

[51] F. Filhol, E. Defay, C. Divoux, C. Zinck and M.-T. Delaye, "Resonant micro-mirror excited by a thin-film piezoelectric actuator for fast optical beam scanning," *Sensors and Actuators A,* vol. 124, pp. 483-489, 2005.

[52] S. Zhang, C. Ataman and H. Zappe, "Compact Architecture for High-Frequency Resonant Microscanners with Low Dynamic Deformation," in *International Conference on Optical MEMS and Nanophotonics*, Singapore, 2016.

[53] F. Casset, P. Poncet, B. Desloges, B. Neff, F. D. D. Santos, J. Danel, M. Vimercati, L. Zanotti and S. Fanget, "Development of a resonant asymmetric micro mirror using an electro active polymer actuation," *Journal of Physics: Conference Series,* vol. 922, no. 1, 2017.

[54] T. Iseki, M. Okumura and T. Sugawara, "High-Speed and Wide-Angle Deflection Optical MEMS Scanner Using Piezoelectric Actuation," *IEEJ Transactions on Electrical and Electronic Engineering,* vol. 5, pp. 361-368, 2010.

[55] U. Baran, D. Brown, S. Holmstrom, D. Balma, W. O. Davis, A. Mazzalai, P. Muralt and H. Urey, "High Frequency Torsional MEMS Scanner for Displays," in *MEMS*, Paris, 2012.

[56] A. Wolter, T. Klose, S. Hsu, H. Schenk and H. Lakner, "Scanning 2D micromirror with enhanced flatness at high frequency," in *MOEMS Display, Imaging, and Miniaturized Microsystems IV*, San Jose, 2006.

[57] C.-H. Ji, M. Choi, S.-C. Kim, S.-H. Lee, S.-H. Kim, Y. Yee and J.-U. Bu, "An electrostatic scanning micromirror with diaphragm mirror plate and diamond-shaped reinforcement frame," *Journal of Micromechanics and Microengineering,* vol. 16, no. 5, p. 1033–1039, 2006.

[58] A. Arslan, D. Brown, W. O. Davis, S. Holmström, S. K. Gokce and H. Urey, "Comb-Actuated Resonant Torsional Microscanner With Mechanical Amplification," *Journal of Microelectromechanical Systems,* vol. 19, no. 4, pp. 936-944, 2010.

[59] M. Yoda, K. Isamoto, C. Chong, H. Ito, A. Murata, S. Kamisuki, M. Atobe and H. Tohiyoshi, "A MEMS 1-D Optical Scanner for Laser Projection Display using Self-assembled Vertical Combs and Scan-angle Magnifying Mechanism," in *13th International Conference on Solid-state Sensors, Actuators and Microsystems*, Seoul, 2005.

[60] H. Soemers, K. Krastev and D. van Lierop, "Design of a High Frequency MEMS Scanning Mirror," in *American Society for Precision Engineering 23rd Annual Meeting*, Portland, 2008.

[61] D. Jung, T. Sandner, D. Kallweit and H. Schenk, "Vertical Comb Drive Microscanners for Beam Steering, Linear Scanning and Laser Projection Applications," *Proc. of SPIE Vol. 8252,* 2012.

[62] S. Kurth, C. Kaufmann, R. Hahn, J. Mehner, W. Dötzel and T. Gessner, "A novel 24 kHz resonant scanner for high resolution laser display," *Proc. SPIE Vol. 5721, MOEMS Display and Imaging Systems III,* pp. 23-34, 2005.

[63] C. H. Manh and K. Hane, "Vacuum operation of comb-drive micro display mirrors," *Journal of Micromechanics and Microengineering,* vol. 19, 2009.

[64] S. K. Gokce, S. Holmstrom, D. Brown, W. O. Davis and H. Urey, "A high-frequency comb-actuated resonant MEMS scanner for microdisplays," in *Optical MEMS and Nanophotonics*, Istanbul, 2011.

[65] U. Hofmann, J. Janes and H. Quenzer, "High-Q MEMS Resonators for Laser Beam Scanning Displays," *Micromachines,* vol. 3, pp. 509-528, 2012.

[66] H. Schenk, J. Grahmann, T. Sandner, M. Wagner, U. Dauderstädt and J. Schmidt, "Micro Mirrors for high-speed Laser Deflection and Patterning," in *8th International Conference on Photonic Technologies LANE*, Fürth, 2014.

[67] J. G. Smits, K. Fujimoto and V. F. Kleptsyn, "Microelectromechanical flexure PZT actuated optical scanner: static and resonance behavior," *Journal of Micromechanics and Microengineering,* vol. 15, no. 6, pp. 1285 - 1293, 2005.

[68] S. Gu-Stoppel, J. J. D. Kaden, H. J. Quenzer, U. Hofmann and W. Benecke, "Piezoelectric resonant micromirror with high frequency and large deflection applying mechanical leverage amplification," *Proc. of SPIE Vol. 8612,* 2013.

[69] T. Iseki, M. Okumura and T. Sugawara, "Shrinking design of a MEMS optical scanner having four torsion beams and arms," *Sensors and Actuators A,* vol. 164, pp. 95-106, 2010.

[70] U. Baran, D. Brown, S. Holmstrom and D. Balma, "Resonant PZT MEMS Scanner for High-Resolution Displays," *Journal of Microelectromechanical Systems,* vol. 21, no. 6, pp. 1303-1310, 2012.

[71] U. Nabholz, W. Heinzelmann, J. Mehner and P. Degenfeld-Schonburg, "Amplitude- and gas pressure-dependent nonlinear damping of high-Q oscillatory MEMS micro mirrors," *Journal of Microelectromechanical Systems ,* vol. 27, no. 3, pp. 383-391, 2018.

[72] A. Frangi, A. Guerrieri, R. Carminati and G. Mendico, "Parametric Resonance in Electrostatically Actuated Micromirrors," *IEEE Transactions on Industrial Electronics,* vol. 64, no. 2, pp. 1544-1551, 2017.

[73] D. Brunner, H. Yoo, T. Thurner and G. Schitter, "Data based modelling and identification of nonlinear SDOF MOEMS mirror," in *Proc. SPIE 10931, MOEMS and Miniaturized Systems XVIII*, San Francisco, 2019.

[74] H. Li, P. Barnes, E. Haring, X. Duan, T. Wang and K. Oldham, "Large-Displacement Vertical Electrostatic Microactuator Dynamics Using Duty-Cycled Softening/Stiffening Parametric Resonance," *Journal of Microelectromechanical Systems,* vol. 28, no. 3, pp. 351-361, 2019.

[75] G. Duffing, "Forced oscillations with variable natural frequency and their technical relevance," *Sammlung Vieweg,* vol. 41/42, 1918.

[76] J. Warminski, "Frequency locking in a nonlinear MEMS oscillator driven by harmonic force and time delay," *International Journal of Dynamics and Control,* vol. 3, pp. 122-136, 2015.

[77] J. Rhoads, C. Guo and G. Fedder, "Parametrically Excited Micro- and Nanosystems," in *Resonant MEMS*, Weinheim, Wiley-VCH Verlag GmbH & Co. KGaA., 2015, pp. 73-95.

[78] J. Rhoads, S. Shaw, K. Turner, J. Moehlis, B. DeMartini and W. Zhang, "Generalized parametric resonance in electrostatically actuated microelectromechanical oscillators," *Journal of Sound and Vibration,* vol. 296, pp. 797-829, 2009.

[79] R. Mirzazadeh, S. Mariani and M. De Fazio, "Fluid damping in compliant, comb-actuated torsional micromirrors," in *EuroSimE*, Belgium, 2014.

[80] W. O. Davis, "Empirical analysis of form drag damping for scanning micromirrors," *Proc. of SPIE,* vol. 7208, 2009.

[81] T. Klose, T. Sandner, H. Schenk and H. Lakner, "Extended Damping Model for Out-Of-Plane Comb driven Micromirrors," in *MOEMS Display, Imaging, and Miniaturized Microsystems IV*, San Jose, CA, 2006.

[82] T. Klose, H. Conrad, T. Sandner and H. Schenk, "Fluidmechanical Damping Analysis of Resonant Micromirrors with Out-of-plane Comb Drive," in *COMSOL Conference*, Hannover, 2008.

[83] A. Fornari, M. Sullivan, H. Chen and C. Harrison, "Experimental Observation of Inertia-Dominated Squeeze Film," *Journal of Fluids Engineering,* vol. 132, no. 12, 2010.

[84] C. Xia, D. Qiao, Q. Zeng and W. Yuan, "The squeeze-film air damping of circular and elliptical micro-torsion mirrors," *Microfluidics and Nanofluidics,* vol. 19, no. 3, pp. 585-593, 2015.

[85] J. D. Sherwood, "Stokes drag on a disc with a Navier slip condition," *Fluid Dynamics Research,* vol. 45, no. 5, 2013.

[86] W. Zhang and H. Stone, "Oscillatory motions of circular disks and nearly spherical particles in viscous flows," *Journal of Fluid Mechanics,* vol. 367, pp. 329-358, 1998.

[87] H. C. Chu and M.-U. Kim, "Oscillatory Stokes flow due to motions of a circular disk parallel to an infinite plane wall," *Fluid Dynamics Research,* vol. 34, pp. 77-97, 2004.

[88] R. J. Clark, P. Williams and O. E. Jensen, "The drag on a microcantilever oscillating near a wall," *Journal of Fluid Mechanics,* vol. 545, pp. 397-426, 2005.

[89] M. Kim, K. Kim, Y. Cho and B. Kwak, "Hydrodynamic force on a plate near the plane wall.Part II: plate in squeezing motion," *Fluid Dynamics Research,* vol. 29, pp. 171-198, 2001.

[90] A. Sorger, M. Freitag, A. Shaporin and J. Mehner, "CFD analysis of viscous losses in complex microsystems," in *9th International Multi-Conference on System, Signals and Devices*, Chemnitz, 2012.

[91] S. Choi, H. Choi and S. Kang, "Characteristics of flow over a rotationally oscillating cylinder at low Reynolds number," *Physics of Fluids,* vol. 14, no. 8, pp. 2767 - 2777, 2002.

[92] X. Tian, L. Xiao, X. Zhang, J. Yang, L. Tao and D. Yang, "Flow around an oscillating circular disk at low to moderate Reynolds numbers," *Journal of Fluid Mechanics,* vol. 812, pp. 1119-1145, 2017.

[93] L. Koay, M. Ratnam and H. Gitano-Briggs, "An Approach for Nonlinear Damping Characterization for Linear Optical Scanner," *Experimental Techniques,* vol. 39, pp. 38-46, 2015.

[94] T. Sandner, T. Klose, A. Wolter, H. Schenk and H. Lakner, "Damping Analysis and Measurement for a Comb-Drive Scanning Mirror," *Proc. of SPIE,* vol. 5455, pp. 147-158, 2004.

[95] A. A. Elhady, Y. M. Sabry and D. Khalil, "Optical characterization of high speed microscanners based on static slit profiling method," *Optics and Lasers in Engineering,* vol. 88, pp. 129-168, 2017.

[96] S. Hsu, T. Klose, C. Drabe and H. Schenk, "Fabrication and characterization of a dynamically flat high resolution micro-scanner," *Journal of Optics: Pure and Applied Optics,* vol. 10, no. 4, 2008.

[97] R. Conant, Micromachined Mirrors, New York: Springer Science+Business Media, 2003.

[98] P. Brosens, "Dynamic Mirror Distortions in Optical Scanning," *Applied Optics,* vol. 11, no. 12, pp. 2987-2990, 1972.

[99] P. Benham, R. Crawford and C. Armstrong, "Stress and Strain Transformations," in *Mechanics of Engineering Materials*, Essex, Pearson Education Limited, 1996, pp. 301-302.

[100] P. Benham, R. Crawford and C. Armstrong, "Yield Criteria and Stress Concentration," in *Mechanics of Engineering Materials*, Essex, Pearson Education Limited, 1996, pp. 292-366.

[101] D. Chong, W. Lee, J. Pang, T. Low and B. Lim, "Mechanical failure strength characterization of silicon dice," in *5th Electronics Packaging Technology Conference*, Singapore, 2003.

[102] A. Wolter, H. Schenk, H. Korth and H. Lakner, "Torsional stress, fatigue and fracture strength in silicon hinges of a micro scanning mirror," *Proceedings of SPIE Vol. 5343,* 2004.

[103] T. Klose, D. Kunze, T. Sandner, H. Schenk, H. Lakner, A. Schneider and P. Schneider, "Stress Optimization of a Micromechanical Torsional Spring," *Nanotech,* vol. 3, pp. 602-605, 2005.

[104] S. Timoshenko and J. Goodier, "Torsion," in *Theory of Elasticity*, London, McGraw-Hill Book Company Inc., 1951, pp. 258-315.

[105] W. Young and R. Budynas, "Torsion," in *Roark's Formulas for Stress and Strain*, New York, McGraw-Hill Companies, Inc., 2002, pp. 381-427.

[106] A. Ugural and S. Fenster, Advanced Strenght and Applied Elasticity, New Jersey: Prentice Hall, 2003.

[107] *ANSYS® Academic Research, Release 18.0, Help System, Element Reference,* ANSYS, Inc., 2018.

[108] M. A. Hopcroft, W. D. Nix and T. W. Kenny, "What is the Young's Modulus of Silicon?," *Journal of Microelectromechanical Systems,* vol. 19, no. 2, pp. 229-238, 2010.

[109] FemtoTools, "Combined Electro-Mechanical MEMS Testing," [Online]. Available: https://www.femtotools.com/fileadmin/pdf/Product_Brochures/FT-MPS02_Broschure.pdf. [Accessed 31 10 2019].

[110] A. Frangi, A. Guerrieri and N. Boni, "Accurate Simulation of Parametrically Excited Micromirrors via Direct Computation of the Electrostatic Stiffness," *Sensors,* vol. 17, no. 4, 2017.

[111] B. Portelli, R. Farrugia, I. Grech, O. Casha, J. Micallef and E. Gatt, "Capacitance measurement techniques in MOEMS angular vertical comb-drive actuators," in *Symposium on Design, Test, Integration and Packaging of MEMS/MOEMS*, Bordeaux, 2017.

[112] D. Hah, P. R. Patterson, H. D. Nguyen, H. Toshiyoshi and M. C. Wu, "Theory and experiments of angular vertical comb-drive actuators for scanning micromirrors," *IEEE Journal of Selected Topics in Quantum Electronics,* vol. 10, no. 3, pp. 505-513, 2004.

[113] M. Naftali and D. Elata, Towards a Linear Response of Vertical Comb-drive Actuators, Technion - Israel Institute of Technology, Faculty of Mechanical Engineering, 2004.

[114] C. Ataman and H. Urey, "Nonlinear frequency response of comb-driven microscanners.," *Micromachining and Microfabrication. International Society for Optics and Photonics,* pp. 166-174, 2004.

[115] A. Hunga, H. Laia, T. Lina, S. Fuc and M. Lu, "An Electrostatically Driven 2D Micro-scanning Mirror and Capacitive Sensing for Projection Display," *Sensors and Actuators A: Physical.,,* vol. 222, pp. 122-129, 2015.

[116] R. Farrugia, B. Portelli, I. Grech, D. Camilleri, J. Micallef, O. Casha and E. Gatt, "Air damping of high performance resonating micro-mirrors with angular vertical comb-drive actuators," *Microsystem Technologies,* 2019.

[117] R. Farrugia, B. Portelli, I. Grech, D. Camilleri, O. Casha, J. Micallef and E. Gatt, "Air damping analysis in resonating micro-mirrors," in *Symposium on Design, Test, Integration and Packaging of MEMS/MOEMS*, Rome, 2018.

[118] R. Farrugia, I. Grech, D. Camilleri, O. Casha, J. Micallef and E. Gatt, "CFD analysis of aerodynamic drag on resonating MEMS micro-scanners," in *Symposium on Design, Test, Integration and Packaging of MEMS/MOEMS*, Paris, 2019.

[119] R. Barber and D. Emerson, "A numerical study of low Reynolds number slip flow in the hydrodynamic development region of circular and parallel plate ducts," Daresbury laboratory technical report DL-TR-01-001, 2001.

[120] A. Fargas Marques and R. S. A. M. Costa Castello, "Modelling the electrostatic actuation of MEMS: state of the art," 2005.

[121] T. Veijola, H. Kuisma, J. Lahdenpera and T. Ryhanen, "Equivalent-circuit model of the squeezed gas film in a silicon accelerometer," *Sensors and Actuators A,* vol. 48, pp. 239-248, 1995.

[122] *ANSYS® Academic Research, Release 18.0, Help System, Sliding Mesh Theory,* ANSYS Inc., 2016.

[123] G. A. Bird, Molecular Gas Dynamics and the Direct Simulation of Gas Flows, Clarendon Press, 1998.

[124] *ANSYS® Academic Research, Release 18.0, Help System, Mechanical APDL, Fluids Analysis Guide, Chapter 5: Slide Film Damping,* ANSYS, Inc., 2016.

[125] G. Haller, "An objective definition of a vortex," *Journal of Fluid Mechanics,* vol. 525, pp. 1-26, 2005.

[126] R. Farrugia, I. Grech, O. Casha, J. Micallef and E. Gatt, "Analysis of dynamic deformation in 1-D resonating micro-mirrors," in *Symposium on Design, Test, Integration and Packaging of MEMS/MOEMS*, Montpeiller, 2016.

[127] R. Farrugia, I. Grech, D. Camilleri, O. Casha, E. Gatt and J. Micallef, "Theoretical and finite element analysis of dynamic deformation in resonating micromirrors," *Microsystem Technologies,* pp. 1-11, 2017.

[128] S. Timoshenko, Theory of Plates and Shells, McGraw-Hill Book Company, 1987.

[129] W. Schock, J. Mehner and J. Fritz, "FEM based modeling and optimization of a 2D micro mirror," in *12th International Conference on Thermal, Mechanical and Multi-Physics Simulation and Experiments in Microelectronics and Microsystems (EuroSimE)*, Linz, 2011.

[130] M. M. Saleem, U. Farooq, U. Izhar and U. S. Khan, "Multi-Response Optimization of Electrothermal Micromirror Using Desirability Function-Based Response Surface Methodology," *Micromachines,* vol. 8, no. 4, 2017.

[131] S. Younis, M. M. Saleem, M. Zubair and S. M. T. Zaidi, "Multiphysics design optimization of RF-MEMS switch using response surface methodology," *Microelectronics Journal,* vol. 71, pp. 47-60, 2018.

[132] A. Martowicz and T. Uhl, "Reliability- and performance-based robust design optimization of MEMS structures considering technological uncertainties," *Mechanical Systems and Signal Processing,* vol. 32, pp. 44-58, 2012.

[133] M. M. Saleem and A. Somá, "Design of experiments based factorial design and response surface methodology for MEMS optimization," *Microsystem Technologies,* vol. 21, pp. 263-276, 2015.

[134] R. Farrugia, I. Grech, D. Camilleri, O. Casha, J. Micallef and E. Gatt, "Design optimization of a dynamically flat resonating micro-mirror for pico-projection applications," *Microsystem Technologies,* 2018.

[135] R. Farrugia, I. Grech, D. Camilleri, O. Casha, J. Micallef and E. Gatt, "Design optimization of a high frequency resonating micro-mirror with low dynamic

deformation," in *Symposium on Design, Test, Integration and Packaging of MEMS/MOEMS* , Budapest, 2017.

[136] *ANSYS® Academic Research, Release 18.0, Help System, DesignXplorer User's Guide,* ANSYS Inc., 2016.

[137] J. Mehner, Enwurf in der Mikrosystemtechnik, Dresden Univ. Press, 1999.

[138] ANSYS Inc., "ANSYS App Store," 2017. [Online]. Available: https://appstore.ansys.com/shop/ACTApps_act%20apps#. [Accessed 17 April 2017].

[139] D. C. Miller, B. L. Boyce, M. Dugger, B. T.E and K. Gall, "Characteristics of a commercially available silicon-on-insulator MEMS material," *Sensors and Actuators A,* vol. 138, pp. 130-144, 2007.

[140] A. Cowen, G. Hames, D. Monk, S. Wilcenski and B. Hardy, *SOIMUMPS Design Handbook: Revision 8,* MEMSCAP Inc., 2011.

[141] S. Chang and J. Kempisty, "Lift-off Methods for MEMS Devices," *Material Research Society Proceedings,* vol. 729, p. U2.3, 2002.

[142] D. Miller, H. C.F, H. Maier, S. George, K. Stoldt and K. Gall, "Thermo-mechanical evolution of multilayer thin films. Part 1. Mechanical of Au/Cr/Si microcantilevers," *Thin Solid Films,* vol. 515, pp. 3208-3223, 2007.

[143] SENSOFAR, "S neox 3D Optical Profiler," [Online]. Available: https://www.sensofar.com/wp-content/uploads/2019/03/Brochure-S-neox-090-v4-EN-web-1.pdf. [Accessed 22 11 2019].

[144] M. L. Dunn, Y. Zhang and M. Bright, "Deformation and Structural Stability of Layered Plate Microstructures Subjected to Thermal Loading," *Journal of Microelectromechanical Systems,* vol. 11, no. 4, pp. 372-383, 2002.

[145] E. Lawrence, K. Speller and D. Yu, "MEMS Characterization using Laser Doppler Vibrometery," in *Micromachining and Microfabrication*, San Jose, 2003.

[146] F. Senger, U. Hofmann, P. Herwig and A. Wetzig, "Centimetre-scale MEMS scanning mirrors for high power laser application," in *Proc. SPIE 9375*, San Francisco, 2015.

[147] J. Janes and U. Hofmann, "Studies on the Dynamics of Vacuum Encapsulated 2D MEMS Scanners by Laser Doppler Vibrometry," *Proc. of SPIE,* vol. 8975, 2014.

[148] M. Hasanian and C. Lissenden, "Assessment of coating layers on the accuracy of displacement measurement in laser Doppler vibrometry," in *44th Annual Review of Progress in Quantitative Nondestructive Evaluation*, Utah, 2017.

[149] Polytec GmbH, "MSA-500 Micro System Analyzer," [Online]. Available: www.polytec.com/fileadmin/d/Vibrometrie/OM_BR_MSA-500_E_42121.pdf. [Accessed 26 11 2019].

[150] Polytec GmbH, "MSA-600 Micro System Analyzer," [Online]. Available: https://www.polytec.com/fileadmin/d/Vibrometrie/OM_PB_MSA-600_E_42497.pdf. [Accessed 11 12 2019].

[151] H. Urey, "Torsional MEMS scanner design for high-resolution display systems," *Proeceedings of SPIE Vol. 4773,* 2002.